Conformable Cardiac Patch for Myocardial Infarction Repair and Sensing

by

Xingying Zhang

Thesis submitted to the Faculty of Graduate and Postdoctoral Studies of

the University of Manitoba

in partial fulfillment of the requirements of the degree of

DOCTOR OF PHILOSOPHY

Department of Mechanical Engineering

University of Manitoba

Winnipeg, Manitoba

Abstract

The ischemic myocardium resulting from myocardial infarction becomes a region where the electrical communication across the myocardium is disrupted. Conductive cardiac patches (CCPs) can rebuild the electroactive microenvironment of the infarcted myocardium. This study contains two projects that tackle two prominent challenges encountered by current CCPs:1) it's difficult for polymeric CCPs scaffolds to form gapless attachment on spherical myocardium, and 2) the healing efficacy of current CCPs heavily relies on the carried drugs and cells. CCPs prepared using emerging printing techniques can be imparted with unique patterns to improve their conformability. However, insufficient conductivity, modulus mismatch, and compromised healing efficacy remain unresolved in these printed CCPs. In the first project, an ultrathin moisture-responsive polydopamine-coated rGO/GO microlattice (DrGOM) was developed using graphene oxide (GO) aqueous ink through direct ink writing (DIW) printing. The ultrathin thickness and unique microlattice morphology provide flexibility that enables conformal contact with the spherical myocardium. The moisture-responsive actuation allows the DrGOM to spontaneously encapsulate the spherical myocardium. The DrGOM improves cardiac function and reduces the infarcted myocardial area in rat models. The integration of electrical stimulation (ES) into CCPs has emerged as a promising approach to improving the healing efficacy of bioagent-free CCPs. In the second project, a trinity triboelectric nanogenerator-based CCP (TRI-TENG) was developed, integrating three functionalities into a single device: energy harvesting, in situ ES therapy, and real-time cardiac monitoring. The TRI-TENG improves cardiac function and reduces the infarcted area in both rat and porcine myocardial infarction models. In addition, the TRI-TENG can monitor cardiac abnormalities by analyzing heart rate and contractility both in vitro and in vivo.

Acknowledgments

First and foremost, I would like to thank my supervisor, Dr. Malcolm Xing, for recognizing my potential, emphasizing the importance of self-learning, enhancing my problem-solving skills, and giving me the freedom to explore my research projects, which enabled me to grow as an independent researcher.

I would also like to express my sincere gratitude to my committee members, Dr. Zhong and Dr. Liang, for their guidance in my research and for serving on my candidacy examination committee.

I am very thankful to my colleagues, Dr. Leyu Wang and Dr. Chen Song, for their contributions to the in vivo and in vitro experiments as well as manuscript preparation. I would also like to thank my colleague, Dr. Yuqing Liu, for his guidance on standard operating procedures.

I also wish to thank my partner, Qian Liu, and all my lab colleagues who provided me with encouragement and support throughout this journey.

Finally, I would like to express my deepest gratitude to my parents for their financial support with my living expenses and tuition fees.

Foreword

This thesis comprises five chapters, including two published papers. It begins with an introduction (Chapter 1), which consists of the following sections: General Overview, Problem Definition, Objective, and Summary of Experimental Methods and Major Findings. The General Overview provides background information on engineered cardiac patches for myocardial infarction repair. The Problem Definition highlights the key challenges associated with current engineered cardiac patch technologies. The Objective outlines the overarching goal of this thesis. The Summary of Experimental Methods and Major Findings presents the experimental approaches and summarizes the key results of each study.

Chapter 2 reviews recent advances in engineered cardiac patches for post-myocardial infarction management. Chapters 3 and 4 present two independent research studies written in journal article format, each detailing the materials and methods, results, discussion, and conclusions.

Chapter 5 presents the Conclusion of the thesis, which consolidates the key findings from the research work, and outlines Future Work, proposing potential research directions for further improving engineered cardiac patches for myocardial infarction management.

List of Authors of Each Manuscript

1. **Paper 1** (Published as the title of *Development of an Asymmetric Hydrophobic/Hydrophilic Ultrathin Graphene Oxide Membrane as Actuator and Conformable Patch for Heart Repair* in the Journal of Advanced Functional Materials)

Xingying Zhang#, Chen Song#, Huijia Nong, Kaige Xu, Xiao Zhuo Wu, Wen Zhong, Malcolm Xing*, and Leyu Wang*

X. Zhang contributed to material design, synthesis, and characterization, and participated in manuscript preparation. C. Song performed the in vitro and in vivo experiments and contributed to manuscript preparation. H. Nong and K. Xu contributed to the in vitro experiment. M. Xing, L. Wang, X. Zhang, C. Song, X. Wu, and W. Zhong verified data integrity and performed statistical analysis. L. Wang and M. Xing conceived the research and supervised the project.

2. **Paper 2** (Published as the title of *E-cardiac patch to sense and repair infarcted myocardium* in the Journal of Nature Communications)

Renjie Qiu[#], **Xingying Zhang**[#], Chen Song[#], Kaige Xu, Huijia Nong, Yi Li, Xianglong Xing, Kibret Mequanint, Qian Liu, Quan Yuan, Xiaomin Sun, Malcolm Xing*, and Leyu Wang*

X. Zhang contributed to material design, synthesis, and characterization, and participated in manuscript preparation. C. Song and H. Nong contributed to manuscript preparation. R. Qiu, X. Zhang, C. Song, K. Xu, and Q. Yuan performed in vitro experiments. R. Qiu, X. Zhang, C. Song, H. Nong, Y. Li, Q. Liu, X. Xiang, and X. Sun performed the in vivo experiments. X. Zhang, C. Song, K. Xu, H. Nong, and K. Mequanint interpreted data and performed statistical analysis. L. Wang and M. Xing conceived the research and supervised the project.

Contribute equally to the work

* Corresponding Author

Table of Contents

List of Figures

List of Equations

List of Abbreviations

PLGA	polylactic-co-glycolic acid
ac	alternating current
AFM	atomic force microscope
Au	gold
CM	cardiomyocyte
DOPA	dopamine
PDA	Polydopamine
ECM	extracellular matrix
dECM	Decellularized extracellular matrix
ES	electrical stimulus
GFM	graphene family materials
GO	graphene oxide
MA	methacrylate group
MI	myocardial infarction
NIR	near-infrared
OCG	oxygen-containing functional groups
PDMS	polydimethylsiloxane
PMMA	polymethylmethacrylate
PPy	polypyrrole
PVA	poly(vinyl alcohol)
PVP	polyvinylpyrrolidone

rGO	reduced graphene oxide
SEM	scanning electron microscope
VEGF	vascular endothelial growth factor
CCPs	Conductive cardiac patch
TRI-TENG	Trinity triboelectric nanogenerator conductive cardiac patch
ECP	Engineered cardiac patch
DIW	Direct ink writing
I-TENGs	Implantable triboelectric nanogenerators
PLA	polylactic acid
PVDF	polyvinylidene fluoride
GelMA	methacrylated gelatin
UV	Ultraviolet
cTn	Cardiac troponin
PCI	Percutaneous coronary intervention
EF	Ejection fraction
FS	Fractional shortening
CPCs	Cardia progenitor cells
ESCs	Embryonic stem cells
iPSCs	Induced pluripotent stem cells
DCM	Dichloromethane
PANI	Polyaniline
PEDOT: PSS	Poly(3,4-ethylenedioxythiophene) polystyrenesulfonate

ECG	Electrocardiogram
MEMSs	Microelectromechanical systems
LV	Left ventricular
LVIDd	left ventricular internal diameter at end-diastole
LVIDs	left ventricular internal diameter at end-systole
V_{oc}	Open-circuit voltage
I_{sc}	Short-circuit current

1 Chapter 1 Introduction

1.1 General overview

Myocardial infarction (MI), pathologically defined as myocardial necrosis caused by prolonged ischemia resulting from coronary artery occlusion,[1] affects more than 7 million individuals worldwide each year.[2] The ischemia typically results from the coronary artery occlusion caused by atherosclerotic plaque rupture or superficial erosion of the coronary artery.[3] The cardiomyocytes (CMs) possess limited regenerative capacity; thus, impaired vasculature leads to irreversible CMs necrosis and the formation of stiff scar tissue, leading to disrupted electrical coupling, deterioration of cardiac function, and heart failure.[4,5] Direct transplantation of therapeutic cells (CMs or stem cells) into the infarcted myocardium has been explored clinically. However, this approach has shown limited improvement in cardiac function, mainly due to the low survival rate of transplanted cells under ischemic conditions and the hostile cardiac microenvironment.[6-8] Engineered cardiac patches (ECPs), composed of biomaterial scaffolds and therapeutic cells, have emerged as a promising strategy for myocardial repair and cardiac function improvement after MI.[9,10] Functional ECPs can preserve the viability of transplanted cells, enabling them to exert paracrine effects on the infarcted myocardium, and facilitate microenvironment reconstruction, including restoration of electroactivity and provision of mechanical support to the infarcted myocardium. [9,11,12] Our previous studies have demonstrated that conductive scaffolds as ECPs, which mimic the electrical conductivity and elasticity of native myocardium, can significantly improve cardiac function in infarcted hearts.[13]

1.2 Problem Definition

1.2.1 Conformable Cardiac Patch that Forms Seamless Attachment

Recently, the seamless spatial alignment between ECPs and epicardial topography has been recognized as a crucial factor in achieving optimal cardiac repair outcomes.[14,15] The high compliance of scaffolds with the epicardial topography can promote the physiological adaptability of ECPs to the host myocardium, as it favors mechanical support, electrical integrity, and the paracrine signaling in the infarcted hearts. However, it remains a challenge to develop an ECP scaffold that satisfies all the following requirements: high compliance with epicardial geometry, high conductivity, low cytotoxicity, and high flexibility. To improve ECPs' flexibility and their ability to conform to the epicardial topography, patterned ECPs with microarchitectures have been fabricated through emerging printing techniques;[14] however, they are not able to fulfill all the requirements simultaneously. Owing to the shear-thinning and thermoplastic behavior of some polymers, patterned polymeric scaffolds can be fabricated through direct ink writing (DIW) and 3D printing.[16-18] However, these polymeric scaffolds generally lack sufficient conductivity for electrical signal propagation. In addition, the mechanical modulus of thermoplastic polymers is typically too high. Photolithography-patterned metallic electronics have been applied to cardiac tissue monitoring and regulation.[19,20] Nonetheless, issues such as modulus mismatch and compromised biocompatibility remain unresolved.

Graphene family materials (GFM), including graphene oxide (GO) and reduced graphene oxide (rGO), have attracted significant attention due to their metal-like conductivity,[21] low cytotoxicity, and excellent mechanical flexibility. Ultra-thin patterned GO structures can be achieved through several low-cost printing methods, such as ink-jet printing,[22-24] aerosol-jet printing,[25,26] direct ink writing (DIW),[27] screen printing,[28,29], and gravure printing.[30] However,

there are still several challenges associated with these methods. Graphene family inks used for printing are usually dispersed in hazardous solvents and require complex, intricate processing steps.

1.2.2 Cardiac Patch that Provides Electrical stimulus

Aside from their inability to achieve seamless attachment, current bioagent-free conductive cardiac patches (CCPs) have several additional limitations: 1) the healing efficacy of current CCPs is heavily dependent on the loaded cells and drugs,[31] 2) remote monitoring capability is essential for successful treatment due to the high readmission rate of cardiac patients. Inspired by the electroactive property of cardiac tissue, electrical stimulation is an effective strategy to induce CM maturation[32,33] and has even been used to reduce ischemic size of the myocardium after ischemia-reperfusion injury using an invasive electrode implanted in the rat's ventricular wall[34]. Furthermore, the synergy of electrical stimulation (ES) and conductive scaffolds can significantly improve cell-cell coupling and synchronous contraction of CMs, compared with the conductive scaffolds alone.[31] Recently, as an alternative to traditional battery-powered stimulation devices, implantable TENGs (I-TENGs) with high energy conversion efficiency can convert in vivo biomechanical motion into electricity, providing power for biomedical devices or electrical stimulation for therapeutic electrodes. TENG-powered interdigital electrodes can promote the maturation of neonatal CMs, as well as increase and synchronize the beating rate of CMs,[35,36] demonstrating strong potential to aid the recovery of infarcted hearts. On the other hand, the electrical output signals of TENGs, including open-circuit voltage, short-circuit current, and frequency, are highly sensitive to mechanical motions and other stimuli, making them an excellent candidate for miniaturized cardiac monitoring systems. Implantable TENGs (I-TENG) have thus been transplanted into hearts for the detection of heart rate[37,38] and endocardial pressure.[39] The

therapeutic electrodes for TNEG-based cardiac healing systems are typically constructed of inert metals such as gold. These electrode materials are stiffer than myocardium by several orders of magnitude, resulting in a significant stiffness mismatch.[40] Moreover, sophisticated surface modification strategies are necessary to improve the effective contact area of the dielectric layers and the electrodes of TENG,[41] which limits scalability. Accordingly, for myocardial infarction treatment and diagnosis, a cost-effective miniaturized CCP that unifies three functions in one device, including CCP therapy, self-powered electrical stimulation for treatment, and real-time cardiac monitoring, is called for but absent.

1.3 Objectives

The overall objective of this thesis is to develop cardiac patches to address the abovementioned issues.

First, to develop a highly conductive and flexible cardiac patch fabricated by direct ink writing (DIW) that can conform to the spherical epicardial geometry, a heat-processed multifunctional GO ink is utilized.

Second, to develop a cost-effective triboelectric nanogenerator (TENG)-based conductive cardiac patch capable of directly delivering electrical stimulation (ES) to the myocardium and enabling real-time cardiac signal monitoring, a unique double-spacer design, along with biomimetic surface structures such as a leaf-vein architecture and mussel-inspired polydopamine (PDA) coating, is employed.

1.4 Summary of Experimental Methods and Major Findings

1.4.1 Summary of Experimental Methods

1.4.1.1 DIW Printed Conformable Conductive Cardiac Patch

The rheological behavior of the GO aqueous solution was modified by heating the solution at 90 ℃ without the aid of any additives to facilitate DIW printing. The printed structure was air-dried to form a GO microlattice. The GO microlattice was exposed to hydroiodic acid vapor for controlled reduction, producing a hydrophobic rGO surface with high conductivity. The combination of hydrophilic GO and hydrophobic rGO results in humidity sensitivity. A mussel-inspired PDA was decorated onto the conductive rGO surface to improve the bioaffinity of the rGO surface. The GO ink can be directly deployed in our "masked spin coating" technique without any modifications for the fabrication of microscale wearable electronics. The incomplete reduction by hydroiodic acid was employed again to impart these microscale wearable electronics with the distinct rGO/GO asymmetric hydrophobicity, rendering them sensitive to multiple signals such as temperature, pH, and strain. The flexibility and fitness on curved surfaces of the unique microlattice structure were investigated. The actuation of rGO/GO structures with different degrees of reduction in response to different humidity levels was tested. The sensitivities of rGO/GO electronic modules in response to different signals were also tested. The healing efficacy of DIW-printed PDA-coated rGO/GO microlattice (DrGOM) for infarcted myocardium was tested both in vivo and in vitro.

1.4.1.2 Trinity-TENG as a Repair Patch and Sensor for Infarcted Myocardium

A GO aqueous solution and mixed elastomer precursor were drop cast on a 3D printed polylactic acid (PLA) mold with a polyvinylpyrrolidone (PVP) sacrificial layer to prepare a

patterned GO membrane, elastomer spacer, and an elastomer package. GO films were subjected to thermal annealing to prepare rGO electrodes. PDA coatings were deposited on some rGO electrodes to prepare PDA-rGO electrodes, improving both biocompatibility and surface roughness. The PVDF solution prepared in a mixed solvent system (DMF/Acetone = 2:1) was drop-cast on a polydimethylsiloxane (PDMS) mold with a negative leaf-vein structure and vacuum dried to prepare a leaf-vein structured PVDF layer. A trinity-TENG (TRI-TENG) was fabricated by assembling the following components in the following order: an elastomer package layer, an rGO electrode, a leaf-vein structured PVDF layer, an elastomer spacer layer, a PDA-rGO electrode, and another elastomer spacer layer. To fit the myocardium of the minipig, whose epicardium has a large curved surface, the TRI-TENGs were assembled into an array design by connecting the rGO electrodes from neighboring TRI-TENGs, and the PDA-rGO electrodes with ultraviolet (UV) crosslinked GelMA/ PEDOT: PSS hydrogel. The effects of the PDA coating and the leaf-vein structure on the power output of the TRI-TENG were studied. The potential of the TRI-TENG as a sensor was also investigated. The ability of the TRI-TENG array to distinguish between healthy and ischemic hearts was investigated in vitro and in vivo.

1.4.2 Summary of Major Findings

1.4.2.1 DIW Printed Conformable Conductive Cardiac Patch

The resultant PDA-coated rGO (hydrophobic)/GO (hydrophilic) microlattice (DrGOM) exhibits high conductivity, an ultrathin thickness (approximately 500 nm), and excellent flexibility. The DIW-printed microlattice structure endows the DrGOM with sufficient flexibility to conform to the spherical geometry of the epicardium. Moreover, the partial reduction imparts the DrGOM with moisture-responsive asymmetric hydrophobicity/hydrophilicity. The humid epicardial

environment triggers spontaneous curvature of the DrGOM, enabling seamless attachment to the curved epicardium by forming a gapless encapsulation once placed on the epicardial surface. The DrGOM preserves high cardiomyocyte (CM) viability, conducts external physiological electrical impulses, and enhances intracellular calcium signaling in CMs. In addition, the DrGOM promotes microvascular structure formation both in vitro and in vivo. When the DrGOM and CM-loaded DrGOM ECPs were transplanted onto infarcted hearts in rat MI models for four weeks, the grafts significantly improved cardiac repair by promoting revascularization of the infarcted myocardium and enhancing cardiac function. Furthermore, rGO/GO sensing modules fabricated using the "masked spin-coating" method demonstrate the capability to detect a range of cardiac physiological signals, including temperature, pH, and strain. The sensitivity of the asymmetric rGO/GO hydrophobic–hydrophilic structure to different stimuli, such as humidity, pH, temperature, and strain, depends on the extent of reduction, which can be tuned by controlling the HI vapor exposure time. The sensitivity of the rGO/GO structure to moisture increases with the degree of reduction. Depositing a PDA coating on the rGO surface of GO/rGO90 has no significant effect on either the conductivity or the moisture sensitivity. In addition, the degree of reduction influences the sensing stability of the rGO/GO structure in response to changes in temperature and pH. A higher reduction extent results in improved sensing stability for both temperature and pH. However, the temperature sensitivity of the rGO/GO structure decreases as the reduction extent increases. In contrast, for strain sensing, rGO/GO structures with a higher degree of reduction exhibit greater sensitivity.

1.4.2.2 Tri-TENG as a Repair Patch and Sensor for Infarcted Myocardium

The two surface modifications inspired by nature, namely, the PDA coating and leaf-vein structure, increased the short circuit current (I_{sc}), open-circuit voltage (V_{oc}), and power output of the TRI-TENG. The TRI-TENG demonstrated the ability to monitor human activities at various levels due to the high sensitivity of the output V_{oc} to the frequency and magnitude of the applied stress and strain. The TRI-TENG array was also shown to effectively monitor cardiac abnormalities in terms of heart rate and contractility.

1.5 Thesis layout

This thesis consists of six chapters, organized as follows,

- Chapter 1 provides a brief introduction, including a general overview, problem definitions, research objectives, and a summary of the experimental methods and major findings.
- Chapter 2 presents a literature review on engineered cardiac patches for post-myocardial infarction management.
- Chapter 3 describes the experimental procedures, results, and discussion of the DIW-fabricated and "masked spin-coating" ultrathin GO/rGO membrane with asymmetric hydrophobicity/hydrophilicity, which functions as a sensor, actuator, and conformable cardiac patch.
- Chapter 4 details the experimental procedures, results, and discussion of the TRI-TENG for infarcted myocardium repair and cardiac monitoring.
- Chapter 5 summarizes the major findings and conclusions of the research.
- Chapter 6 outlines potential directions for future work.

2 Chapter 2: Literature Review

2.1 MI and Cardiac Remodeling after MI

In clinical practice, myocardial injury is characterized by elevated levels of cardiac troponin (cTn), a contractile protein exclusively expressed in the heart. The pathological definition of myocardial infarction (MI) refers to cardiomyocyte (CM) necrosis resulting from prolonged ischemia. According to the Fourth Universal Definition of MI,[42] MI can be classified into several types based on the underlying cause of acute ischemia. Coronary arteries deliver oxygen- and nutrient-rich blood to CMs (Figure 2-1A, B). Plaque, which consists of accumulated cholesterol, lipids, calcium, and fibrin in the inner lining of the artery, often leads to atherosclerosis, a condition characterized by the stiffening and narrowing of arteries. When a plaque ruptures or erodes, thrombosis—the formation of a blood clot—may occur. Myocardial injury caused by thrombosis-associated ischemia is defined as type 1 MI (Figure 2-1C). Type 2 MI refers to ischemic myocardial injury resulting from an imbalance between oxygen supply and demand. Acute stressors, such as gastrointestinal bleeding or sustained tachyarrhythmia, can increase oxygen demand and precipitate this condition. Type 3 MI manifests as sudden cardiac death before elevated cTn levels or abnormal electrocardiogram (ECG) findings can be detected. The incidence of type 3 MI is relatively low compared with other MI types. Type 4 MI and type 5 MI are myocardial injuries associated with coronary procedures. Type 4 MI occurs in association with percutaneous coronary intervention (PCI), including procedures such as angioplasty and stent placement. The subtype type 4a MI is defined by a cTn concentration exceeding five times the baseline level. If stent or scaffold thrombosis occurs as a complication of PCI, the resulting MI is classified as type 4b MI. Type 4c MI occurs without thrombosis, and the elevation in cTn

concentration does not necessarily exceed five times the baseline level. Type 5 MI refers to myocardial infarction associated with coronary artery bypass graft (CABG) surgery.

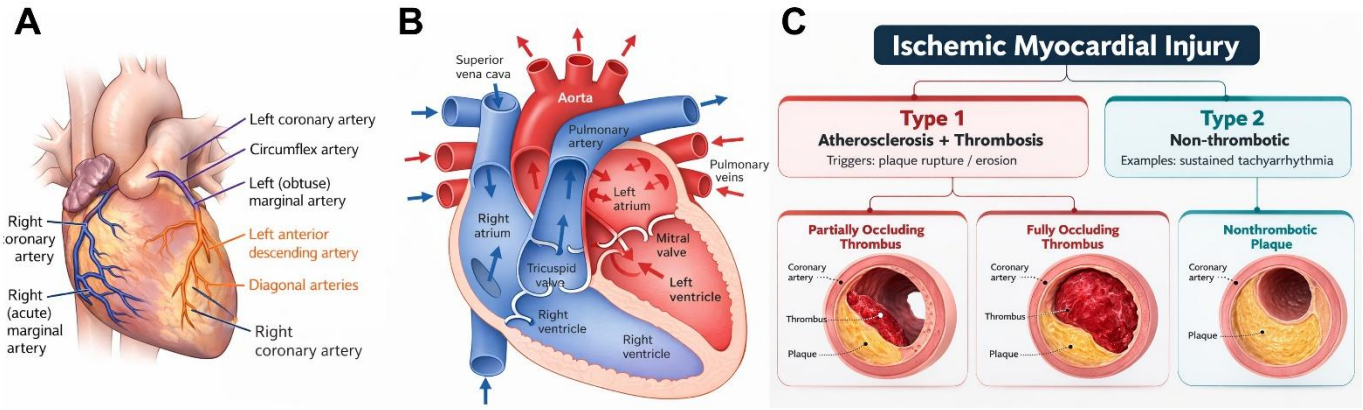

Figure 2-1 Schematic illustration of the parthenogenesis and classification of MI.

(A) Diagram of the coronary arteries in the heart. (B) human heart anatomy. (C) Classification of MI.[43,44]

CMs lack sufficient regenerative capacity to compensate for the large-scale tissue loss following myocardial infarction (MI). The loss of CMs after MI creates abnormal loading conditions that initiate a cascade of intracellular signaling pathways involved in myocardial remodeling until the distending force is balanced by the tensile strength of the collagen scar.[45] Cardiac remodeling is defined as a complex set of molecular, cellular, extracellular, and geometric changes occurring in both the infarcted and non-infarcted regions of the ventricles and arteries as a result of MI-induced hemodynamic stress, neurohormonal factors, and epigenetic regulation.[46,47] Cardiac remodeling is generally considered adverse, as these maladaptive responses exacerbate diastolic filling impairment, worsen systolic dysfunction, and contribute to the progression of heart failure.[48] Post-infarction remodeling can be divided into two phases: an early phase (≤72 h),

characterized by expansion of the infarct zone, and a late phase (>72 h), which involves ventricular dilation, alterations in ventricular architecture, and hypertrophy of the left ventricle.

2.1.1 Early Remodeling

Within hours to days after myocardial infarction, the cytokine transforming growth factor-β1 released by injured CMs triggers the recruitment of immune and inflammatory cells, including macrophages, monocytes, and neutrophils, into the infarct zone to remove necrotic cellular debris through phagocytosis.[49] The infiltrating neutrophils also secrete elevated levels of matrix metalloproteinases (MMPs), which degrade collagen,[50] the most abundant protein in the extracellular matrix (ECM). Degradation of collagen in the ECM by proteases leads to regional wall thinning and elongation within the infarcted zone.[51] This process is termed infarct expansion (Figure 2-2).[52] Infarct expansion results in early ventricular dilation, defined as the enlargement of the heart's ventricular chambers. Early ventricular dilation after infarction can initially serve as a compensatory mechanism to maintain stroke volume (SV), the volume of blood pumped out of the left ventricle. The non-injured myocardium exhibits apparent hyperfunction through augmented segment shortening to compensate for the loss of contractile myocardium in the ischemic region.[53] According to the Frank–Starling mechanism, a higher end-diastolic volume (EDV), which represents the volume of blood filling the ventricle, results in a higher SV. The non-ischemic myocardium increases EDV through acute dilation, thereby increasing total segment shortening. However, these acute compensatory responses are ultimately insufficient to maintain SV.

2.1.2 Late Remodeling

The late remodeling phase can extend from weeks to months and, in some cases, persist for years after the initial myocardial infarction. Long-term ventricular dilation increases the size of the ventricular cavity and may partially restore SV. However, the ejection fraction ($EF = \frac{SV}{EDV}$), which serves as an indicator of cardiac function, continues to decline after myocardial infarction despite this compensatory dilation. In addition, the increase in ventricular radius caused by dilation leads to elevated diastolic and systolic wall stress, according to the Laplace law ($wall\ stres = \frac{presure \times radius}{2 \times wall\ thickness}$).[51] The increased wall stress in the dilated ventricle stimulates hypertrophy of non-injured CMs. This hypertrophic response acts as an adaptive mechanism that helps counterbalance the increased workload, limit further dilation, and temporarily stabilize contractile function. However, this compensatory hypertrophy is insufficient to fully offset ventricular dilation, ultimately resulting in progressive global dilation and deterioration of cardiac function.

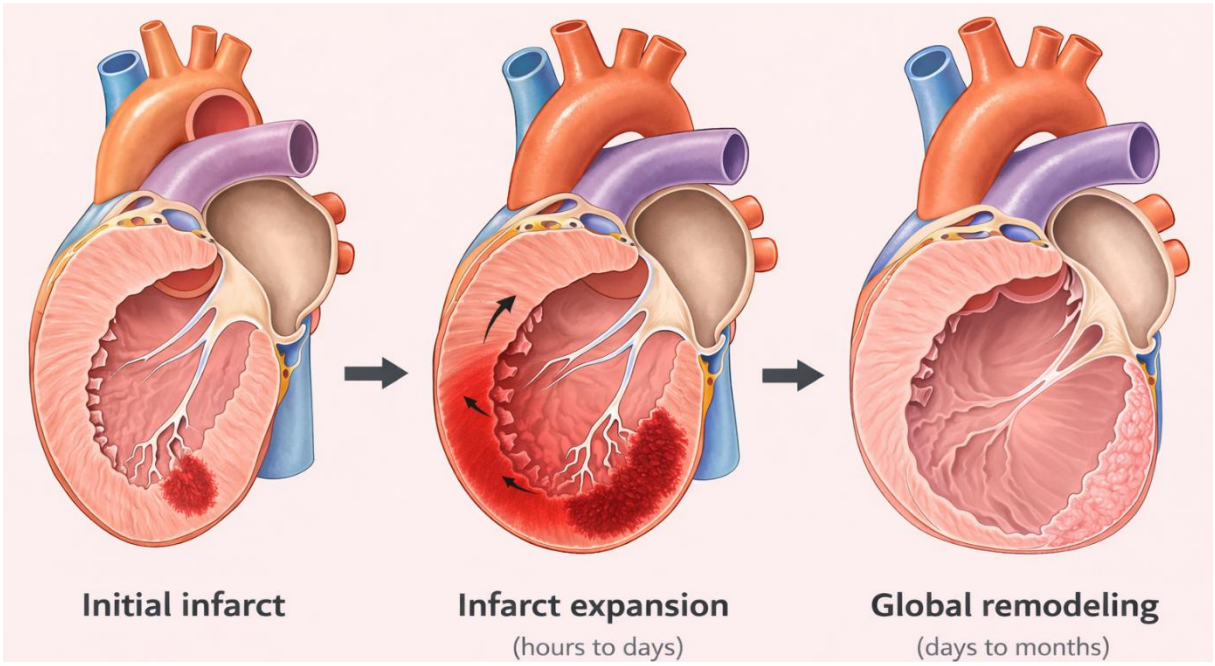

Figure 2-2 Ventricular remodeling after acute myocardial infarction.[54]

2.1.3 Changes in Extracellular Matrix

Cardiac fibroblasts, the most prevalent cell type in the heart, play a key role in maintaining the extracellular matrix (ECM) and regulating myocardial remodeling.[55] Following infarct expansion, cardiac fibroblasts are recruited to the injury site, where they proliferate and contribute to scar formation in the early post-infarct period by depositing a new collagen matrix. Changes in the mechanical microenvironment, together with elevated levels of proinflammatory cytokines secreted by inflammatory cells, vasoactive peptides, and growth factors, stimulate the differentiation of cardiac fibroblasts into myofibroblasts.[56] Myofibroblasts, regulated by multiple factors, increase ECM collagen turnover, thereby promoting scar maturation and fibrosis. The resulting scar replaces the necrotic CMs and provides tensile strength to the remodeled ECM. These inflammatory responses and healing processes are analogous to wound healing in the skin. However, they become maladaptive because myofibroblasts in myocardial infarcts may persist for many years, whereas myofibroblasts in the skin typically undergo apoptosis once the scar matures. The persistence of myofibroblasts in myocardial infarcts leads to a net accumulation of collagen, cardiac fibrosis, and eventual loss of cardiac function.[55,56] In addition, collagen deposition by myofibroblasts can also occur in the non-infarcted myocardium when intercellular signaling is enhanced by extensive CM necrosis resulting from chronic ischemia and pressure overload.[45,50,56] Collagen accumulation in the ECM of the non-infarcted myocardium increases cardiac stiffness and contributes to cardiac dysfunction. Moreover, the contraction generated by myofibroblasts differs fundamentally from that of CMs. Myofibroblasts generate sustained tonic contraction regulated by circulating factors and neurohormones, resembling smooth muscle cells (SMCs). In contrast, CM contraction and relaxation are regulated by electrical stimuli from the cardiac conduction system. Cardiac fibroblasts can electrically couple with CMs and enhance CM

excitability by forming gap junctions with them.[57,58] However, depolarization of cardiac fibroblasts within scar tissue can disrupt cardiac excitation and conduction, creating a substrate that favors sustained arrhythmias.[59]

2.2 Critical Properties of ECPs for MI

Due to the limited regenerative capacity of CMs and the persistence of myofibroblasts, the heart undergoes maladaptive responses following myocardial infarction, including adverse remodeling and extensive collagen deposition in the extracellular matrix (ECM). These processes ultimately lead to mechanical dysfunction, electrical uncoupling, structural distortion, and eventual heart failure. Pharmaceutical management and percutaneous coronary intervention (PCI) can significantly extend patients' lifespans and reduce mortality after MI; however, they cannot fully restore cardiac function.[45,54] Heart transplantation remains the gold-standard treatment for patients with end-stage heart failure. Nonetheless, the widespread application of heart transplantation is limited by the scarcity of suitable donors and the requirement for lifelong immunosuppression. Stem cells derived from various sources have been shown to promote regenerative processes such as angiogenesis, neovascularization, and enhanced cell survival.[60] However, the clinical application of cell-based therapies faces several challenges, including difficulties in cell preservation, high laboratory and material costs, uncontrolled cell growth and activity, potential immunogenicity, and low cell retention due to the lack of an appropriate microenvironment. Advances in biomaterials have enabled the development of ECPs, which offer a promising strategy for enhancing cardiac regeneration and restoring cardiac function.

Within the field of tissue engineering, biomaterials are designed to achieve an appropriate combination of physical properties that match those of the target tissue, suitable chemical

properties, and bioactive characteristics that stimulate regeneration while inducing minimal toxicity to the host.[61-63] Post-MI remodeling generates a complex microenvironment that presents significant challenges for the design of ECPs. ECPs are applied directly onto the surface of the infarcted myocardium, either alone or in combination with therapeutic cells or bioactive factors.[64] Due to their intimate interaction with both the myocardium and therapeutic cells, ECPs must conform to the architecture of the myocardium, provide mechanical support, withstand continuous cycles of contraction and relaxation, promote cell adhesion, and facilitate electrophysiological functionality. Furthermore, establishing an appropriate three-dimensional (3D) microenvironment for therapeutic cells requires ECPs to possess several key properties that enable cell assembly and the formation of functional myocardial tissue.[65]

2.2.1 Biocompatibility and Biodegradability

Biocompatibility refers to the ability of a material to perform a specific function in a biological environment while eliciting only a limited host response. In the context of ECPs, biocompatibility requires promoting the survival of CMs both in vitro and in vivo without inducing cytotoxic effects, while also supporting the contractile function of the myocardium and avoiding excessive foreign-body responses. Although inflammatory and immune responses from the host are inevitable, minimizing these reactions is crucial to prevent additional tissue damage and functional impairment. In addition, biocompatible materials should exhibit resistance to blood clot formation and bacterial colonization. Moreover, if a material elicits an immune response, it should promote the recruitment of reparative cells, such as M2 macrophages, rather than cell types that exacerbate pathological remodeling, thereby supporting a favorable healing environment.

Biodegradability refers to the limited inherent lifespan of an implanted material and its ability to degrade through various mechanisms within the biological environment. The degradation of implanted materials generally occurs through three main mechanisms: (1) bioerosion, which includes chemical decomposition of the material through hydrolysis as well as physical dissolution; (2) bioresorption, which involves the removal of the material or its degradation products by body fluids and cellular activities such as phagocytosis; and (3) biodegradation, in which biological agents (e.g., enzymes, microbes, or cells) are responsible for the degradation process. A material is considered biodegradable if it undergoes degradation through these mechanisms in the in vivo environment and if the resulting degradation products meet the criteria for both biocompatibility and biodegradability. Biodegradability is particularly important for ECPs, as it eliminates the need for surgical removal of the patch after tissue repair. Although biocompatibility and biodegradability are distinct concepts, they are typically considered simultaneously during biomaterial design. The design of a biocompatible ECP must therefore also ensure that its degradation products are non-toxic and safe for the surrounding tissue.

2.2.2 Mechanical Stimulation and Mechanical Support

Mechanical support is a crucial criterion for ECPs. An ideal ECP must possess sufficient mechanical strength to withstand the persistent mechanical demands of the continuously beating ventricle. At the same time, it must be sufficiently flexible to respond synchronously to the dynamic contractions of the myocardium. The mechanical properties of ECPs should also enable the transmission of mechanical stimulation to CMs, which are the primary therapeutic cells within ECPs. Unidirectional cyclic stretching plays a vital role in CM differentiation, promoting a phenotypic shift toward mature cardiac tissue,[66] and guiding the formation of cardiac organoids

that exhibit the contractile and electrophysiological properties of native myocardium.[67,68] Under mechanical stimulation, CMs develop key ultrastructural hallmarks of differentiation, including organized sarcomeres assembled into myofibrils with distinct Z, I, A, H, and M bands, specialized cell–cell junctions, and well-defined basement membranes.

In addition, the stiffness of an ideal ECP should not disrupt the mechanical microenvironment of the surrounding tissue. A mismatch in stiffness may impose excessive strain on the injured myocardium if the ECP is too rigid. The stiffness of ECPs can significantly influence cellular behaviors, including morphology, proliferation, apoptosis, differentiation, migration, spreading, and cell–scaffold adhesion. Cells cultured on rigid substrates exhibit increased spreading, enhanced adhesion, reduced motility,[69] increased contractility,[70] reduced cell volume,[71] elevated metabolic activity,[72] and higher proliferation rates. The substrate stiffness is a pivotal regulator of stem cell fate.[73,74] As a mechanical cue, stiffness can be sensed and integrated by cells, ultimately influencing gene expression and determining cell fate.[73] For example, soft matrices that mimic brain tissue ($0.1 \sim 1$ kPa) tend to promote neuronal differentiation. Matrices with intermediate stiffness (8∼17 kPa), which resemble striated muscle, favor myogenic differentiation, whereas stiffer matrices (25∼40 kPa), with stiffness comparable to collagenous bone, promote osteogenic differentiation toward osteoblasts.[74] Similarly, muscle stem cells cultured on hydrogels with stiffness mimicking that of native muscle exhibit enhanced self-renewal[75] and demonstrate improved regenerative potential after transplantation.[76] The stiffness of a cell's prior physical environment and the duration of previous culture conditions can also influence gene expression and lineage commitment when human mesenchymal cells are subsequently cultured on softer substrates.[77] On matrices with stiffness gradients, cells tend to migrate toward regions of higher stiffness,[78] a phenomenon known as durotaxis. However, their ultimate fate remains strongly

influenced by the stiffness of the environment in which they previously resided.[79] In the context of cardiac repair, the stiffness of ECPs plays an important role in cardiac function and regeneration. Lower stiffness can promote cardiomyocyte proliferation and tissue repair, whereas higher stiffness is often associated with tissue maturation and fibrosis.[80]

Moreover, recent reviews have highlighted that cells can sense and respond to the viscoelastic properties of tissue engineering scaffolds.[81] Viscoelasticity plays a significant role in regulating fundamental cellular processes. Scaffolds with higher loss modulus and faster stress relaxation rates can promote cellular behaviors that are not typically observed in purely elastic scaffolds.[82,83] Viscoelasticity has also been shown to promote the differentiation of mesenchymal stem cells toward adipogenic, osteogenic, and smooth muscle cell lineages.[83,84] Cells cultured on viscoelastic scaffolds can more easily overcome the mechanical confinement imposed by the matrix compared with those cultured on elastic scaffolds. This allows cells to alter their morphology, expand in volume, and deposit extracellular matrix during proliferation and migration.[85,86] Cell–matrix remodeling, which involves changes in pore size, viscoelasticity, matrix architecture, and degradability,[87] is also enhanced in scaffolds with higher viscoelasticity. The remodeling process and the forces exerted by cells on the matrix occur in a highly dynamic manner. In response, viscoelastic matrices exhibit complex time-dependent mechanical behaviors that can alter their original architecture and structural features. The scaffolds with these altered characteristics subsequently interact with cells and trigger further cellular responses. Consequently, cell–matrix interactions develop into a dynamic and iterative process.[81]

2.2.3 Electrical Stimulation and Conductivity

Electrical signaling is a fundamental property of native cardiac tissue, playing a crucial role in coordinating heartbeat rhythms and serving as a key therapeutic target for arrhythmia management through pacing and defibrillation.[88] The electrical excitation generated by pacing cells propagates rapidly along the membranes of adjoining CMs and triggers calcium release that stimulates myofibril contraction. This process ultimately drives synchronized cardiac muscle contraction. Following MI, the accumulation of condensed collagen in scar tissue disrupts the electrical signal propagation between healthy myocardium and surviving islands of intact CMs within the scarred region due to the lack of electrical connectivity. This interruption contributes to desynchronized cardiac contraction and eventually leads to progressive ventricular dysfunction.

In vitro models face similar challenges, as conventional culturing systems fail to recapitulate the electrical microenvironment necessary for CM maturation. Culturing neonatal CMs or human pluripotent stem cell–derived cardiomyocytes (hPSC-CMs) without electrical stimulation exhibits deficient ultrastructural organization, asynchronous contraction, and immature functional characteristics.[89-91] To address this limitation, pulsatile electrical field stimulation has been incorporated into 3D culture systems, enhancing synchronous contractile activity, promoting sarcomere ultrastructure formation, and improving electrophysiological maturation.[88,89,92] Consequently, conductive scaffolds that can electrically bridge healthy myocardium and viable CMs within scar tissue are being pursued in the development of ECPs.

Electromechanical stimulation also demonstrates superior efficacy in promoting CM maturation compared with either electrical or mechanical stimulation alone. In a recent study, combined electromechanical stimulation was applied to human pluripotent stem cells cultured on a 3D printed conductive scaffold.[31] This dual stimulation paradigm significantly improved

structural and functional maturation, as evidenced by enhanced cell alignment, increased cell elongation, greater sarcomere length, and well-organized parallel myofibril arrangement. These findings have driven the development of conductive scaffolds that simultaneously electrically bridge healthy myocardium with viable CMs within scar tissue while providing mechanical support to the infarct border zone.

2.2.4 Surface Characteristics

Surface chemistry, including surface charge and wettability, as well as surface roughness and topography, are important factors to consider in the design of ECPs because they influence cell adhesion, proliferation, differentiation, and apoptosis. Many proteins, including immunoglobulins, fibronectin (FN), vitronectin, fibrinogen, and von Willebrand factor, rapidly adsorb onto the surface of implanted biomaterials and form a coating layer immediately after the biomaterial is introduced into physiological fluids.[93] These adsorbed proteins act as ligands for integrin receptors on cells such as neutrophils, macrophages, and other inflammatory cells, regulating their adhesion, spreading, proliferation, and differentiation through receptor–ligand interactions.[94] The type,[95] quantity,[96] and conformation[97] of the adsorbed proteins are strongly influenced by the surface chemistry of the implanted biomaterial. Among these proteins, FN alone is sufficient to mediate cell adhesion and other cellular activities and has therefore been extensively studied.[98] The saturated adsorption amount of FN on surfaces with different chemical functionalities follows the trend: $–NH_2 > –CH_3 > –COOH \geq –OH$.[95,99,100] However, the binding affinity of $\alpha_5\beta_1$ integrins to the adsorbed FN follows the order: $–OH > –COOH = –NH_2 > –CH_3$. Cell adhesion to adsorbed FN on these surfaces is mediated by $\alpha_5\beta_1$ integrins integrins and therefore follows a similar trend. Surface chemistry–dependent cell adhesion and integrin binding

can be explained by adsorption-induced structural changes in the binding domains of FN. The FN–integrin interaction induces conformational changes that activate integrin-mediated signaling pathways controlling cell proliferation and differentiation.[101] In addition, structural proteins in focal adhesions, as well as signaling proteins in adherent cells, are significantly affected by surface chemistry.[102] The highest recruitment of these proteins to adhesion plaques occurs on–OH-terminated surfaces, whereas the lowest recruitment is observed on –CH3-terminated surfaces. Bone-specific gene expression, alkaline phosphatase enzymatic activity, and mineralization in immature osteoblast-like cells cultured on –OH and $–NH_2$ modified surfaces are upregulated compared to those cultured on –COOH and $–CH_3$- modified surfaces. Hydrophilic and anionic surfaces can also mitigate implant-related inflammatory responses by restricting monocyte adhesion and macrophage fusion into foreign-body giant cells, as well as by promoting apoptosis of adherent macrophages.[103]

Surface energy typically exerts a more significant influence on cellular adhesion strength and proliferation than surface roughness.[104] The relationship among surface energy, surface roughness, and fibroblast adhesion is complex. For materials with low surface energy, such as polymers, surface roughness plays a dominant role in cell adhesion, and adhesion strength increases with increasing surface roughness. In contrast, for materials with high surface energy, such as metals, cellular adhesion strength increases primarily with surface energy, while the effect of surface roughness becomes negligible. On a per-cell basis, the amount of secreted ECM on polymer surfaces is more than twice that on metal surfaces. However, cell proliferation on polymers is nearly half of that observed on metals.

2.3 Cell-Based ECPs

Exogenous cells, including pluripotent cells such as embryonic stem cells (ESCs) and induced pluripotent stem cells (iPSCs), as well as adult cells with restricted potential, such as cardiac progenitor cells (CPCs) and cells native to other tissues, have been investigated in clinical trials.[105] CPCs represent a heterogeneous population of cells with self-renewing, clonogenic, and multipotent capabilities that reside within terminally differentiated hearts.[106,107] Giacomello's group demonstrated that small, round, phase-bright cells isolated from explants of postnatal atrial or ventricular tissue obtained from human biopsies or murine hearts express stem cell and endothelial cell markers.[108] These cells subsequently self-assemble into 3D spherical clusters in suspension culture, termed cardiospheres. This study highlights the potential for obtaining CPCs from postnatal hearts. It has been shown that CPCs can differentiate into CMs both in vitro and in vivo after transplantation, thereby improving cardiac function following infarction.[109] However, the behavior of CPCs in different contexts, such as development, homeostasis, aging, and response to injury after transplantation, remains poorly understood, which has led to ongoing controversy regarding their therapeutic potential. One population of CPCs used in clinical trials is cardiosphere-derived cells (CDCs). Marban's group generated CDCs by replating cardiospheres onto adherent culture flasks (Figure 2-3A).[110] Patients treated with CDCs exhibited reduced scar mass and enhanced regeneration of healthy myocardial tissue compared with control groups.

The iPSCs are generated by reprogramming somatic cells, such as fibroblasts, through the introduction of four defined factors.[111] ESCs and iPSCs are considered promising sources of human CMs due to their capacity for indefinite propagation while retaining the ability to differentiate into nearly all cell types. However, iPSCs are prone to teratoma formation and may elicit host immune responses after transplantation.[112] In addition, differentiated ESCs in culture

tend to form aggregates known as embryoid bodies, which contain less than 1% myocytes. Both ESCs and iPSCs require tightly controlled induction processes, including treatment with defined factors and chemical cues, and are often combined with patch scaffolds to maximize CM yield and optimize therapeutic outcomes.[113-116] Fibroblasts can also be transdifferentiated into functional myocytes through defined factor–mediated direct reprogramming, making them potential alternative sources of CMs.[117,118] A scaffold that provides a biomimetic microenvironment capable of directing cell behavior is therefore crucial for the successful repair of MI using stem cell–based therapies.

Human mesenchymal stem cells (hMSCs) are considered promising candidates for cardiac therapy due to their ability to secrete a wide range of paracrine factors, including cytokines, chemokines, and growth factors, that influence neighboring cells.[119] The paracrine growth factors produced by hMSCs, such as vascular endothelial growth factor (VEGF), basic fibroblast growth factor (bFGF), hepatocyte growth factor (HGF), and angiopoietin, play important roles in promoting angiogenesis, neovascularization, and cell survival.[60] Mesenchymal stem cells (MSCs), particularly those with Akt1 survival gene overexpression or those subjected to hypoxic treatment, have been shown to exert cytoprotective effects on ischemic CMs through the enhanced release of paracrine factors.[120,121] The paracrine factors released by injected hMSCs can positively influence post-infarction remodeling, as evidenced by decreased fibrosis and apoptosis, reduced left ventricular (LV) dilation, increased myocardial thickness, and preservation of both systolic and diastolic cardiac function.[122]

Decellularized extracellular matrix (dECM) scaffolds are biomaterials primarily composed of ECM, obtained by removing immunogenic cellular components from human or animal organs or tissues using detergents, enzymes, and/or salts.[105] The decellularization process preserves the

complex composition, structure, and biological activity of the ECM, including collagen, non-collagenous proteins, glycosaminoglycans, proteoglycans, glycoproteins, and growth factors. The dECM can be solubilized and subsequently self-assembled into injectable hydrogels through controlled processing, enabling both in vivo and in vitro applications. The typical preparation of dECM hydrogels involves two main steps: (1) solubilization of dECM using pepsin, an enzyme that cleaves the telopeptide bonds of the collagen triple-helix structure to dissociate collagen fibril aggregates; and (2) hydrogel formation triggered by neutralization to physiological pH, adjustment of salt concentration, and temperature control.[123] Cell behaviors such as cell viability, proliferation, migration, morphology, differentiation, and phenotype can be regulated by dECM through multiple mechanisms.[124-126] These mechanisms involve the physical and mechanical properties of the hydrogel, embedded cytokines and chemokines, the presentation of cryptic peptides, exposure of bioactive motifs, and signaling mediated by matrix-bound nanovesicles.[127,128] Injectability is another advantage of dECM hydrogels as deliverable scaffolds for stem cells. The dECM hydrogels can be injected through syringes or catheters with gauges ranging from 18 to 27, which are compatible with the catheters commonly used for cell transplantation into the myocardium.[129] Consequently, dECM hydrogels provide a promising platform for mechanical support and serve as a biological 3D carrier for cell delivery.

A dual stem cell therapy strategy that leverages the synergistic effects of iPSCs and MSCs has been developed by Park's group (Figure 2-3B).[130] In this approach, human iPSC-derived CMs were administered via intramyocardial injection, while hMSCs were seeded onto a dECM hydrogel patch (hMSC-P) that was subsequently implanted epicardially. The dECM used for the patch was derived from porcine heart tissue. hMSCs isolated from bone marrow were compared with hMSCs derived from other tissues in terms of their ability to secrete VEGF and were found to exhibit

superior secretion capacity. The hMSC-P exerted multiple beneficial effects, including the secretion of paracrine factors, upregulation of growth factor expression in the MI heart, and enhanced angiogenesis. However, epicardial implantation of hMSC-P alone was insufficient to improve cardiac function, as indicated by the lack of significant improvement in EF, FS, and other echocardiographic parameters. Notably, the hMSC-P enhanced the retention of intramyocardially injected CMs and promoted their maturation and survival. This dual-therapy strategy highlights the complementary advantages of different stem cell types. Specifically, hMSCs promote vascularization in the infarcted myocardium and support the engraftment and viability of the injected CMs, ultimately contributing to improved cardiac function.

As mentioned previously, fibroblasts can transdifferentiate into CMs through transcription factor- and microRNA-mediated direct reprogramming, thereby promoting functional recovery after MI.[131,132] However, delivering transcription factors using viral methods is not ideal for clinical applications due to safety concerns and regulatory limitations.[133] Small molecules have therefore emerged as alternative tools capable of efficiently reprogramming fibroblasts into chemically induced CMs.[134] It has been reported that culturing fibroblasts within fibrin hydrogels, which provide a 3D microenvironment, improves the efficiency of cardiac reprogramming mediated by microRNAs. Cho's group further demonstrated that both chemical reprogramming and cardiac maturation of chemically induced CMs were enhanced in a 3D microenvironment provided by porcine heart–derived dECM hydrogels.[135] Compared with both 3D Matrigel and dECM-coated 2D substrates, 3D dECM hydrogels exhibited greater improvements in fibroblast reprogramming efficiency, CM maturation, and the electrical functionality of the induced CMs. Furthermore, dECM hydrogels derived from heart tissue were more effective in enhancing fibroblast reprogramming than dECM hydrogels derived from other tissues, demonstrating a

tissue-specific effect in promoting cardiac reprogramming. The induced CMs generated in 3D dECM hydrogels were subsequently injected into a rat MI model to evaluate their therapeutic efficacy. As a result, cardiac contractility and overall cardiac function were significantly improved, while cardiac fibrosis was reduced.

Although dECM hydrogels provide an ideal 3D bioactive carrier for stem cells, long-term storage of cell-loaded cardiac patches remains challenging, thereby limiting their widespread clinical application. Cheng's group developed an off-the-shelf artificial cardiac patch (artCP) loaded with synthetic cardiosphere-derived cells (synCSCs) that is fully acellular and capable of maintaining therapeutic potency after long-term cryopreservation.[136] CDCs, similar to MSCs, secrete paracrine factors that promote cardiac regeneration, inhibit fibrosis, reduce inflammation, and interact directly with injured CMs.[110,137,138] The cardiac patch was prepared from lyophilized heart tissue–derived dECM. The heart tissues used to produce dECM were harvested from market-weight pigs. Human heart tissues were used to prepare cardiospheres, which were subsequently collected and replated onto fibronectin-coated surfaces to generate CDCs. The CDCs were cultured in fetal bovine serum–free medium for 14 days, after which the cells were removed by centrifugation to obtain CDC-conditioned medium. synCSCs were then fabricated using a water/oil/water (w/o/w) emulsion technique. The CDC-conditioned medium containing 0.1% (w/v) polyvinyl alcohol (PVA) served as the internal aqueous phase and was mixed with the oil phase consisting of dichloromethane (DCM) containing polylactic-co-glycolic acid (PLGA). The mixture was first emulsified and then added to a 0.7% (w/v) PVA aqueous solution to generate a secondary emulsion. The solvent was subsequently removed by continuous stirring at room temperature, resulting in the formation of solidified synCSCs. The synCSCs were then loaded onto the dECM scaffold through vacuum filtration to produce the off-the-shelf artCPs. It was

demonstrated that the paracrine factor–releasing capability, mechanical properties, and in vitro therapeutic efficacy of the artCPs were not affected after 28 days of cryostorage, indicating the cryostability of the artCPs.

To avoid open-chest surgery during cardiac patch administration, injectability is a highly desirable property. The pericardial cavity, a space between the pericardium and epicardium, can serve as a natural mold for injectable CPs. Dashuai et al. demonstrated an intrapericardial procedure for administering an iPSC-loaded dECM hydrogel (Figure 2-3C).[139] As shown in Figure 2-3C, two small incisions were made on the left side of the chest to serve as ports for the introducer needle and camera. The intrapericardial injection of iPSC-derived CPC-loaded dECM hydrogel elicited a lower immune response in the host compared with the intramyocardial injection of iPSC-derived CPCs.

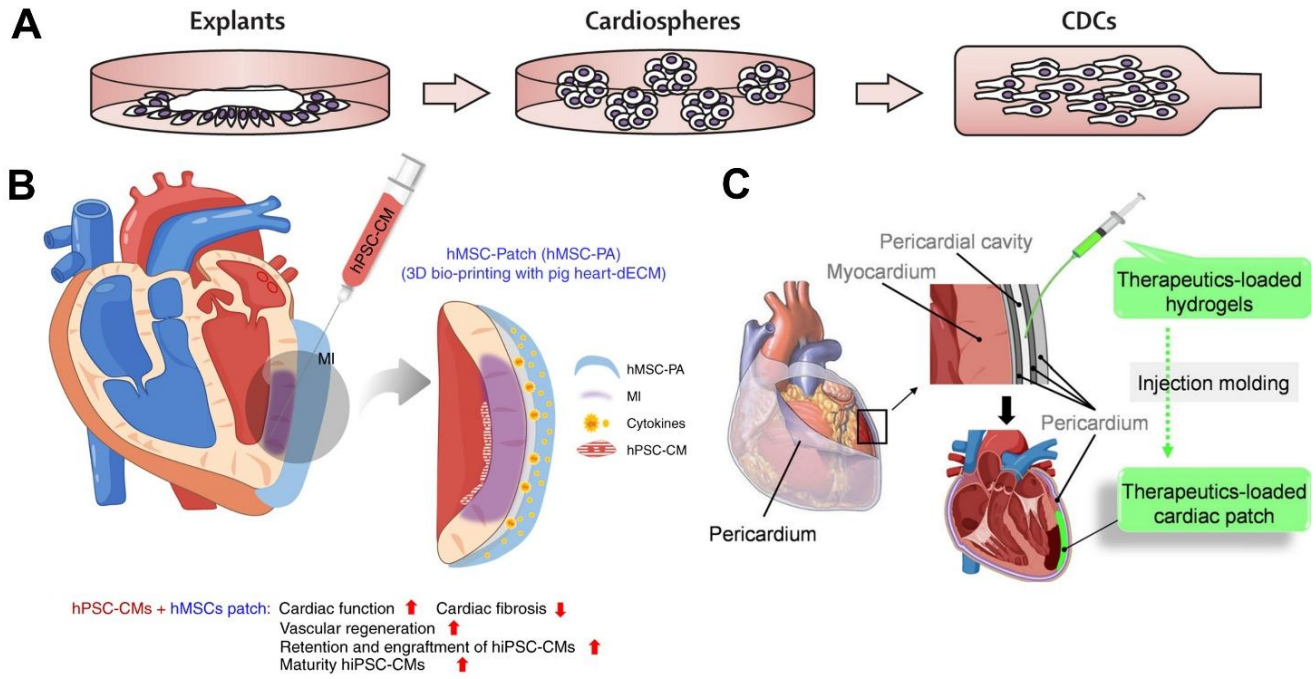

Figure 2-3 Schematic illustration of a cell-loaded scaffold for MI repair.

(A) Manufacturing process of cardiosphere-derived cells.[110] Schematic illustration of (B) Synergistic dual treatment strategy involving intramyocardial injection of hiPSC-derived CMs and epicardial implantation of hMSC-loaded dECM hydrogel.[130] (C) Intrapericardial injection of dECM hydrogel loaded with therapeutic cells.[139] Reprinted with permission.

2.4 ECPs Prepared with 3D Printing Techniques

3D printing, an additive manufacturing technique, enables the precise construction of multiscale 3D architectures across a wide range of resolutions, typically from 10 to 10,000 μm. Printing technologies hold great promise in tissue engineering because of their ability to fabricate complex anatomical structures, tailor mass distribution, and tune material properties through a structural approach. Several 3D printing techniques have been widely applied in tissue engineering, including inkjet printing, extrusion-based printing, and laser-assisted printing.[140] These techniques can fabricate 3D objects from digital models designed using CAD software. The digital model is typically converted into STL format, which represents the object as a triangular mesh. The STL file is then sliced into multiple two-dimensional layer profiles that are translated into machine instructions known as G-code. The G-code contains coordinates in the X, Y, and Z directions that guide the movement of the extrusion nozzle or laser across the fabrication platform. Each layer is deposited sequentially on top of the previous one until the entire 3D structure is completed. The term “direct write” was first proposed by Lewis et al. to describe a class of additive manufacturing techniques that use pattern-generating devices, such as ink extrusion nozzles or laser-emitting systems, to create designed architectures through computer-controlled motion.[141]

Inkjet printing for biomaterials originates from commercial two-dimensional digital inkjet printing used in graphic arts, newspapers, and industrial manufacturing. This technique generally involves two key processes: (1) the ejection of ink droplets and (2) the behavior of the ejected droplets. Inkjet printing can be categorized into continuous inkjet (CIJ) printing and drop-on-demand (DOD) inkjet printing. Ink viscosity and surface tension are critical parameters for successful printing. The viscosity of a typical bioink is usually lower than 2 cP, although some printers can accommodate viscosities up to 100 cP.[142] The surface tension of the ink is typically greater than 35 $mN \cdot m^{-1}$.[143] CIJ printing operates based on the Rayleigh–Plateau instability, in which a vertically falling liquid stream breaks into droplets when the relationship between its length and diameter reaches an unstable condition. In CIJ, a continuous stream of ink is ejected and subsequently breaks into droplets due to the Rayleigh–Plateau instability. The droplets are then electrically charged by a charging electrode and pass through an applied electric field. Uncharged droplets travel directly to their designated positions on the substrate, while charged droplets are deflected into a gutter for recirculation.[144] CIJ printing is widely used in high-speed graphic applications, such as textile printing and labeling. However, its application in biomaterials is limited because ink recirculation can compromise sterility.

DOD printing is the preferred inkjet method for biomaterials due to its smaller droplet size and higher placement accuracy. In DOD printing, droplets are generated only when the drop generator is precisely positioned above the target location. Based on the mechanism of droplet formation, DOD printing can be classified into several types, including thermal, piezoelectric, electrostatic, and acoustic inkjet printing.[145] In thermal inkjet printing, ink is vaporized by heat generated from a resistive film, producing a vapor bubble that generates pressure to eject small droplets from the nozzle. The heating temperature in this method can exceed 200 °C, making

thermal inkjet printing less suitable for tissue engineering because the high temperature may denature biological components. In addition, nozzle clogging is a common issue in thermal inkjet printers. Piezoelectric inkjet printing relies on a piezoelectric actuator. When voltage is applied, the actuator deforms, generating a pressure pulse in the ink chamber that ejects ink droplets. In electrostatic inkjet printing, the trajectory of charged ink droplets is controlled by varying the electric potential applied to the electric field through which the droplets pass. Acoustic inkjet printing uses a high-frequency transducer located behind the ink chamber and operates without a nozzle. The acoustic waves generated by the transducer expel droplets from the surface of the ink chamber. Electrohydrodynamic jet printing (EHD) is an advanced form of electrostatic inkjet printing. In EHD printing, ink is first extruded from a syringe to form a droplet at the nozzle tip, which is then ejected by modulation of an electric field between the nozzle and the substrate. This dual-controlled mechanism allows EHD printing to achieve nanoscale deposition. Inkjet printing techniques are commonly used for two-dimensional biomaterial patterning, such as fabricating biomolecule microarrays and sensors.[143,146] To fabricate 3D soft tissue engineering scaffolds using an inkjet-based system, a direct 3D inkjet printing approach can be employed. In this system, a crosslinking agent or other solidification reagent is ejected from the printer nozzle onto a build platform that moves along the Z-axis and is immersed in a precursor solution.[147]

There are three major variations of laser-assisted 3D printing: selective laser sintering (SLS), direct laser writing (DLW), and laser-induced forward transfer (LIFT). In SLS, successive layers of solid polymer particles are deposited in a powder bed and selectively heated and sintered by a computer-controlled laser.[148] The addition of each new layer of polymer particles is facilitated by a powder deposition system. In LIFT, a pulsed laser beam is focused and scanned across a three-layer structure arranged from top to bottom as follows: a donor substrate, an absorbing layer,

and a layer of ink. The absorbing layer absorbs the laser radiation and rapidly vaporizes, forming a high-pressure bubble that propels the ink toward a receiving substrate.[149,150] In addition to vaporizing the absorbing layer to eject ink droplets, laser irradiation can also be used for localized polymerization of transparent precursors. This mechanism forms the basis of direct laser writing (DLW).[151]

Based on the photon absorption event that leads to material synthesis, the localized fabrication process in DLW can be categorized into single-photon and two/multi-photon reactions. In single-photon reactions, a single photon excites an electron to a higher energy state, initiating localized chemical reactions. For the fabrication of tissue engineering scaffolds, a liquid resin containing photoinitiators, photosensitizers, and monomeric building blocks is typically used. The laser light, usually in the UV range, is absorbed by the photosensitizer, and the absorbed energy is transferred to the photoinitiator. This process generates reactive species such as free radicals or cations that initiate polymerization. Because single-photon absorption has a limited penetration depth, the effective reaction zone in single-photon DLW is typically confined to a thin liquid layer near the resin surface. To enable 3D fabrication, a layer-by-layer approach, similar to that used in direct 3D inkjet printing systems, is commonly employed. In this approach, DLW is repeatedly performed on a thin resin layer above a platform that moves along the Z-axis. After a two-dimensional microstructure is formed in each layer, the platform is translated upward or downward to expose a fresh resin layer for fabrication of the next layer. Single-photon DLW is also referred to as micro-stereolithography (μSLA) in some literature. Stereolithography (SLA) is likewise based on spatially controlled photopolymerization and uses a similar setup to single-photon DLW, achieving layer-by-layer fabrication through a bottom-up process.

A variant of SLA is digital light projection (DLP)**,** which uses a masked projection system to fabricate microstructures within each layer. The key component of a DLP system is a digital micromirror device (DMD), which can contain up to millions of microscopic mirrors. Each mirror tilts independently between on and off states, allowing the DMD to function as a dynamic mask. When an illumination beam strikes the DMD, a two-dimensional pixel pattern is projected through a transparent window/plate into a vat of liquid resin (typically from the bottom), selectively curing a patterned microstructure for that layer. After the layer is formed, the build platform moves upward to expose fresh resin for the next exposure, enabling 3D fabrication via a layer-by-layer process.

In two- or multi-photon reactions, two or more photons are absorbed nearly simultaneously at the focal point where the laser intensity is highest. This multiphoton absorption excites an electron to a higher energy state, with the total excitation energy equal to the sum of the photon energies, thereby activating photoinitiators that generate reactive species and initiate polymerization. Two- or multi-photon absorption is a nonlinear optical process that restricts the reaction to the focal region while leaving surrounding areas unaffected. Because two-/multi-photon absorption is a nonlinear optical process, it strongly confines the reaction to the focal volume while leaving surrounding regions largely unaffected. As a result, 3D structures can be written directly within the liquid resin without requiring a layer-by-layer process.[152,153] Moreover, this nonlinear confinement enables fabrication at resolutions that can surpass the optical diffraction limit. The polymerization volume ("voxel") produced via two-photon absorption is substantially smaller than that produced by single-photon absorption, allowing extremely fine structural features. More broadly, laser-assisted 3D printing techniques are nozzle-free, which eliminates issues such as nozzle clogging and avoids direct contact between the dispensing system and bioinks. These

techniques also offer broader material compatibility than inkjet printing because they do not impose strict requirements on liquid viscosity or surface tension. In addition, they provide higher fabrication resolution, with multiphoton laser direct writing capable of reaching nanoscale features (~100 nm).[154]

Extrusion-based 3D printing can be categorized into two main groups based on the type of material used as ink: fused deposition modelling (FDM) and hydrogel-based 3D bioprinting. In FDM, a thermoplastic filament is fed by a motor-driven mechanism into a heated nozzle, where it is softened/melted and deposited onto a build platform. Because the processing temperature is high, FDM is generally unsuitable for most cell-laden or protein-based bioinks; therefore, it is often used to fabricate molds, supportive frameworks, or sacrificial templates rather than directly printing bioactive scaffolds. Direct ink writing (DIW) is an extrusion-based printing technique that leverages the shear-thinning behavior of the ink. This rheological property allows the ink to flow readily through the nozzle under applied pressure, while rapidly increasing in viscosity after extrusion to maintain the printed geometry. In general, DIW inks require a viscosity greater than 10^{-1} Pa·s to provide sufficient self-supporting capability and preserve structural fidelity before curing or crosslinking.[155] In DIW systems, the ink is typically loaded into a syringe and extruded through a nozzle using either pneumatic pressure or a screw-extrusion mechanism. Extrusion-based 3D printing, particularly DIW, together with laser-assisted 3D printing, has recently emerged as a promising fabrication approach in cardiac tissue engineering and will be discussed further in the following sections.

The ability of 3D printing to recapitulate intricate natural architectures, particularly functional vascular-like structures, represents a critical advancement for tissue engineering. These vascular-like structures can integrate with host vasculature and serve as perfusable microvessels,

sustaining oxygen and nutrient delivery to therapeutic cells located deep within thick scaffolds.[156,157] This strategy can reduce early post-implantation cell death, which often arises from the limited diffusion distance of oxygen and the slow rate of vascular ingrowth during tissue repair.[157-160] Chen's group developed a tissue engineering scaffold containing embedded, multiscale sacrificial filament networks that dissolve to form perfusable channels (Figure 2-4A). (Figure 2-4A).[156] A "carbohydrate glass" (liquid glass) was prepared by heating a mixture of glucose, sucrose, dextran, and water to 165 °C, and thermal extrusion-based 3D printing was used to fabricate a carbohydrate-glass lattice. To assess compatibility with different scaffold materials and gelation mechanisms, the printed lattice was encapsulated within various cellularized hydrogels. In this process, a parenchymal cell–containing precursor solution was cast around the glass lattice in a rectangular mold, followed by gelation via multiple mechanisms. After dissolution of the carbohydrate-glass lattice in culture medium, endothelial cells were injected through the inlet into the resulting channel network and rapidly lined the lumen walls (Figure 2-4B). Scaffolds containing channels exhibited higher cell viability in the core region than bulk hydrogels (Figure 2-4C). Moreover, endothelial cells lining the lumens formed both single-cell and multicellular sprouts extending into the surrounding hydrogel matrix (Figure 2-4D). Overall, Chen's study demonstrates a straightforward strategy for fabricating vascularized tissue engineering scaffolds using thermal extrusion-based 3D printing. However, many existing approaches for generating microfluidic networks in tissue scaffolds still rely on layer-by-layer stacking of prefabricated structures.

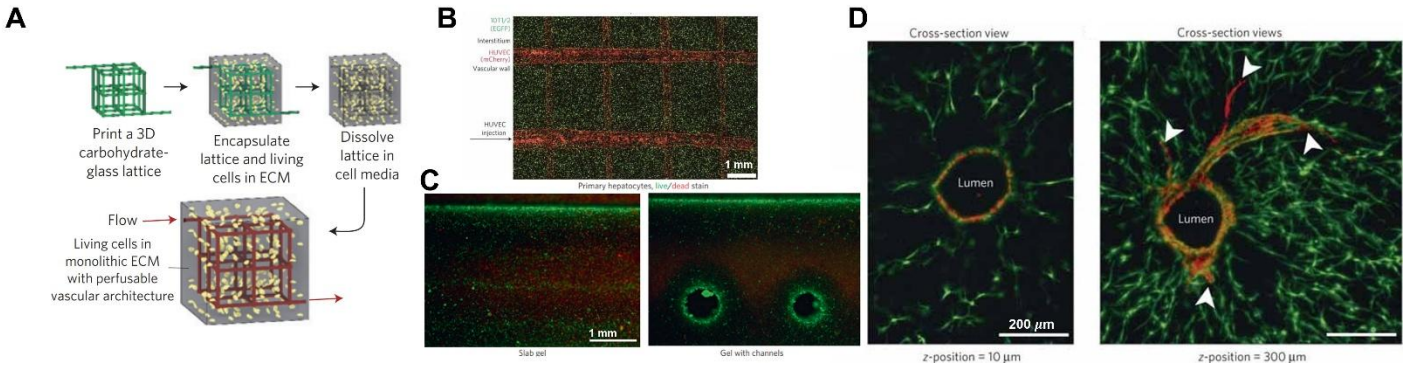

Figure 2-4 Hydrogel scaffold with a 3D printed sacrificial carbohydrate glass network.[156]

(A) Schematic illustration of the fabrication process. (B) Fluorescence image of the hydrogel scaffold showing EGFP-expressing 10T1/2 cells (green) encapsulated within the hydrogel and mCherry-expressing HUVECs (red) lining the walls of the vascular network. (C) Fluorescence Live/dead assay results for cells encapsulated within bulky agarose gel and within agarose gel containing a vascular network. (D) Fluorescence image showing the cross-section of the vascular lumen seeded with HUVECs in a hydrogel containing 10T1/2 cells. Reprinted with permission.

Steinhoff's group developed a cardiac patch incorporating vascular-like structures by patterned seeding of human umbilical vein endothelial cells (HUVECs) and human mesenchymal stromal cells (hMSCs) onto a porous cardiac scaffold.[161] The scaffold was fabricated from polyester urethane urea with interconnected micropores produced using thermally induced phase separation. It then served as the receiving substrate for layer-by-layer cell printing via LIFT. For LIFT printing, glass slides were used as donor substrates and coated with a laser-absorbing gold layer by plasma-enhanced sputter deposition. HUVEC and hMSC suspensions were prepared separately in endothelial medium and individually spread onto the gold-coated surface using a

blade coater as bioinks. During LIFT, the gold layer absorbs laser energy and vaporizes locally, generating a high-pressure bubble that propels the bioink toward the cardiac scaffold positioned on a glass slide serving as the collector. Using this approach, two layers of HUVEC mesh and two layers of hMSC mesh were sequentially printed onto the scaffold (Figure 2-5A). As a control, a "MIX" patch was prepared by randomly seeding HUVECs and hMSCs through co-culture on the scaffold. Immunofluorescence microscopy showed that LIFT-patterned HUVECs and hMSCs formed capillary-like structures (Figure 2-5B), whereas cells on the MIX patch did not develop organized patterns. Both the MIX and LIFT-fabricated patches were sutured onto infarcted rat hearts to evaluate in vivo efficacy. Compared with the control, the LIFT-fabricated cardiac patches achieved improved therapeutic outcomes, including greater recovery of cardiac function, reduced fibrosis, and increased vascular density.

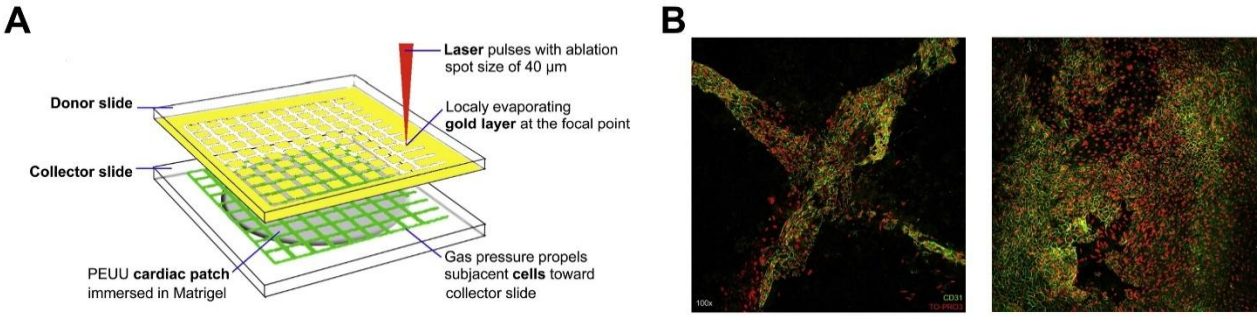

Figure 2-5 Bioprinting of HUVECs and hMSCs on a cardiac patch through LIFT.[161]

(A) Schematic illustration of the bioprinting process. (B) Immunofluorescence microscopy images of the LIFT patch (left) and MIX patch (right), showing HUVECs stained in red and hMSCs stained in green on the two patches. Reprinted with permission.

A 3D cardiac patch composed of layer-by-layer stacked compartments that mimic the vascular structure, parenchymal space, and vascular–parenchymal interface of native cardiac tissue

was developed using stereolithography (Figure 2-6A).[162] To each compartment, the corresponding material was deposited onto molds through spin-coating or casting on molds, which were prepared specifically by stereolithography. Poly(glycerol-co-sebacate) (PGS) was selected for the interface layer because it provides rubber-like elasticity and strength, along with controllable biodegradation (Figure 2-6B).[163,164] By tuning curing time,[165] curing temperature,[166] and monomer composition,[167] the mechanical properties of PGS can be adjusted to better match myocardial tissue, and its degradation rate can be finely controlled. To improve permeability, a sacrificial maltose layer (later dissolved) was spin-coated onto the mold before PGS deposition, yielding a porous PGS interface. Introducing an amino alcohol monomer into the PGS reaction forms a biodegradable elastomer, poly(1,3-diamino-2-hydroxypropane-co-polyol sebacate) (APS), with a slower degradation rate (Figure 2-6C).[168] APS with a lower amino-alcohol ratio was used for the heart-cell scaffold layers, whereas APS with a higher amino-alcohol ratio was used for the microfluidic base. As illustrated in Figure 2-6D, one microfluidic base layer, one interface layer, and two heart-cell scaffold layers were dip-coated with PGS prepolymer and assembled, followed by curing to yield a four-layer cardiac patch. For cellularization, neonatal heart cells were pipetted onto the upper two heart-cell scaffold layers, while culture medium was continuously perfused through the vascular layer. Tissue-like structures developed within the patch after four days of culture (Figure 2-6E).

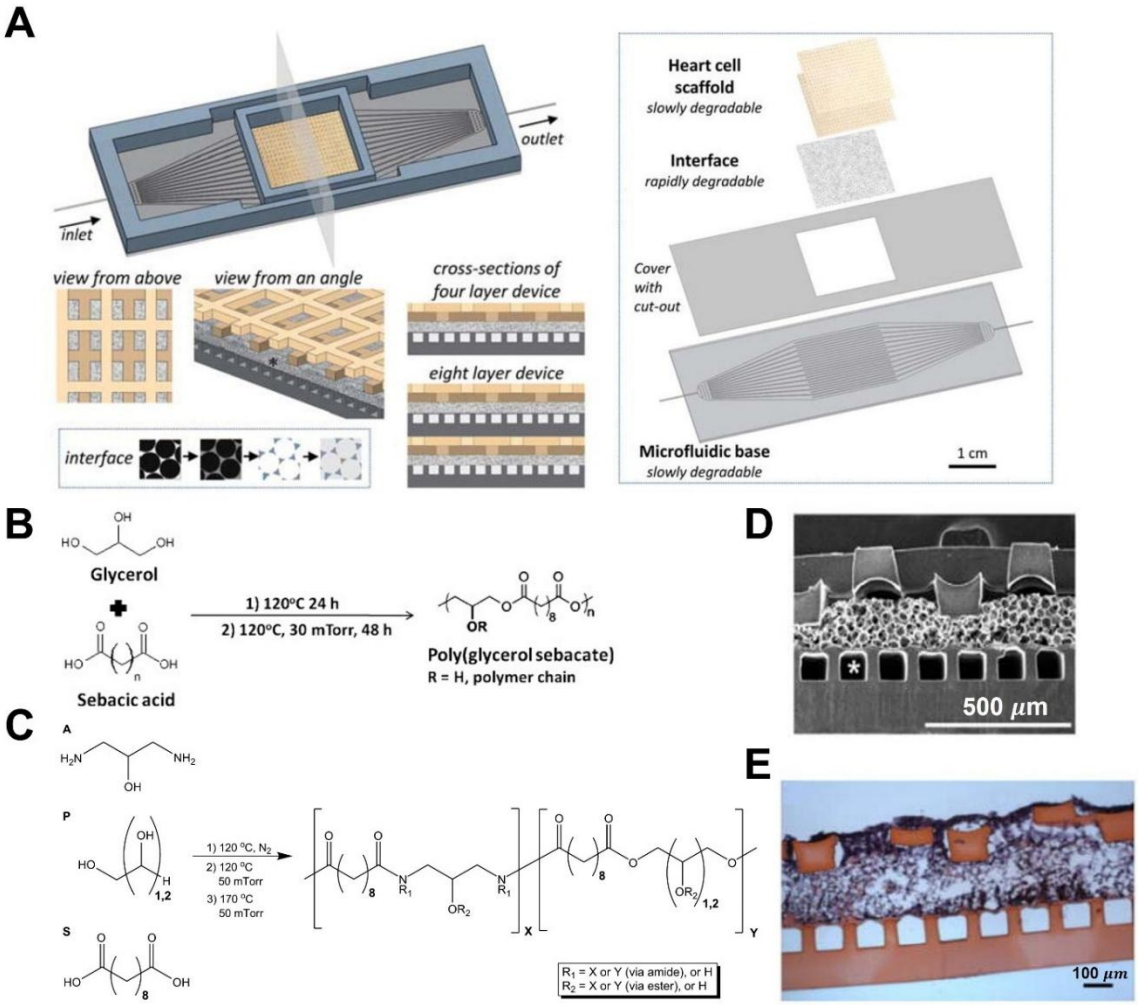

Figure 2-6 Design and composition of the multilayer cardiac patch.[162]

(A) Schematic illustration of the patch design. (B) Synthesis scheme of PGS. (C) Synthesis scheme of APS polymer. (D) SEM image of the cross-section of the four-layer cardiac patch. (E) Cross-sectional H&E-stained histological image of heart cells cultured on the four-layer cardiac patch. Reprinted with permission. Reprinted with permission.

Riboflavin, also known as vitamin B2, has been widely used in ophthalmology as a photoinitiator for crosslinking collagen fibrils within the corneal stroma under UV irradiation, thereby enhancing tissue stiffness and stability. Owing to its low toxicity and its ability to promote crosslinking between carbonyl groups,[169] riboflavin is considered a promising photoinitiator for 3D printing tissue engineering scaffolds composed of collagen and decellularized extracellular matrix (dECM).[170,171] Jinah et al. developed a 3D-printed cell-laden dECM scaffold using vitamin B2 as a photoinitiator for post-crosslinking (Figure 2-7A).[172] To achieve dual cellular patterning, the scaffold was fabricated by alternately printing two dECM-based bioinks using a multi-head extrusion-based 3D printer: Bioink I, containing CPCs, and Bioink II, containing MSCs and VEGF. All bioinks contained vitamin B2. After printing each layer, the structure was exposed to UV light to induce riboflavin-mediated crosslinking. After printing was completed, the entire scaffold, referred to as the patterned C/M patch, was further thermally crosslinked at 37 °C. For comparison, a CPC patch was printed using Bioink I, while a mixC/M patch was fabricated using Bioink III, which contained CPCs, MSCs, and VEGF. These three patches were implanted onto infarcted rat hearts to evaluate their therapeutic efficacy (Figure 2-7B). To secure the patches, they were placed on the infarcted region and covered with fibrin glue, rather than applying the glue at the interface between the patch and myocardium. This approach enabled better investigation of the direct interaction between the patch and cardiac tissue. The patterned C/M patch exhibited the best therapeutic performance. It significantly enhanced vascularization, as evidenced by the highest blood vessel density and the largest vessel diameter (Figure 2-7C). It also achieved greater reductions in infarct size and fibrosis, demonstrated by the largest muscle area, the thickest LV wall, and the lowest fibrosis level (Figure 2-7D). Furthermore, its superior ability to restore cardiac function was reflected by the highest EF among the treatment groups (Figure 2-7E).

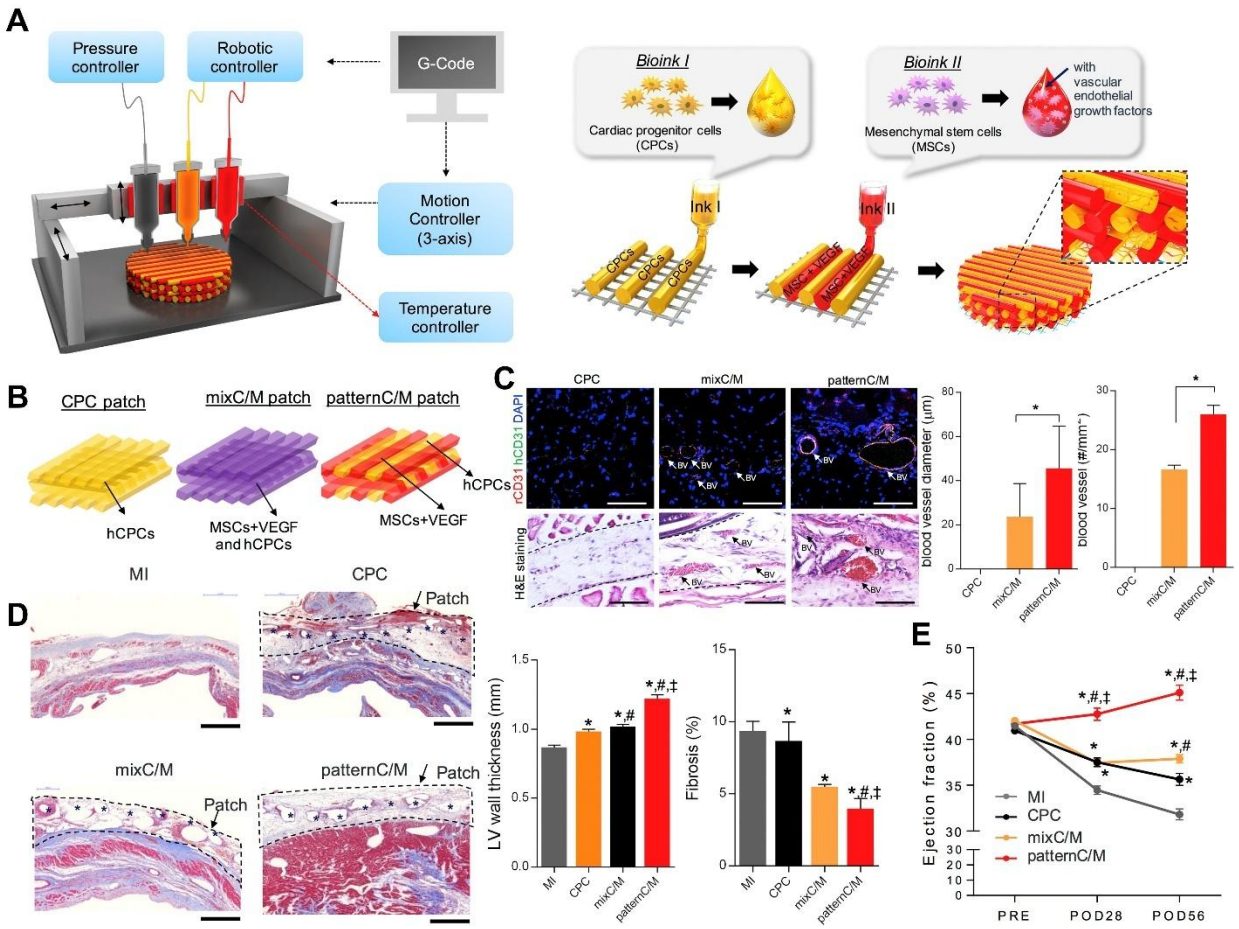

Figure 2-7 Multi-head extrusion-based 3D printing of two different bioinks.[172]

(A) Schematic illustration of the fabrication process. (B) Schematic illustration of the three types of printed cardiac patches. (C) Histological sections showing vascular formation in hearts treated with different patches and quantitative analysis of blood vessel diameter and vessel number. (D) Masson's trichrome-stained histological sections and quantitative analysis of wall thickness and fibrosis. (E) EF of the different groups. Reprinted with permission.

Beyond vascular structures, features of the ECM can also be recapitulated through 3D printing. Ling et al. developed a cell-laden, native-like 3D-printed cardiac patch with submicron resolution using multiphoton DLW.[173] To investigate the native distribution of fibronectin in myocardial tissue, the authors used multiphoton microscopy to scan sections of adult murine myocardium in which fibronectin was stained with an immunofluorescent dye (Figure 2-8A). Based on the analysis of the native myocardium, a computational model was generated to create a template for 3D printing. Multi-photon DLW was then conducted using a liquid resin consisting of methacrylated gelatin (GelMA) and the photoinitiator 4-[2-(4-morpholino)benzoyl-2-dimethylamino]-butylbenzenesulfonate (MBS) on a glass slide (Figure 2-8B). In native myocardial tissue, CMs reside in 15 × 100 μm channels, which were accurately recapitulated by the printed scaffold (Figure 2-8C). hiPSCs-derived CMs, hiPSCs-derived SMCs, and hiPSCs-derived endothelial cells were seeded onto the printed gelatin scaffold in a 2:1:1 ratio. The cell-loaded cardiac patch (hCMP) demonstrated high reproducibility as well as high fidelity in both coverage area and intensity variation (Figure 2-8C). Calcium transients and synchronous contraction were observed on the cell-loaded cardiac patch within one day after seeding (Figure 2-8D). To evaluate the *in vivo* healing effects of the hCMP, the patch was placed on the infarct site of a mouse heart and secured using a piece of decellularized bovine pericardium sutured to the heart. The cell-loaded cardiac patch demonstrated significant therapeutic effects, including restoration of cardiac function (Figure 2-8E) and reduction in infarct size (Figure 2-8F).

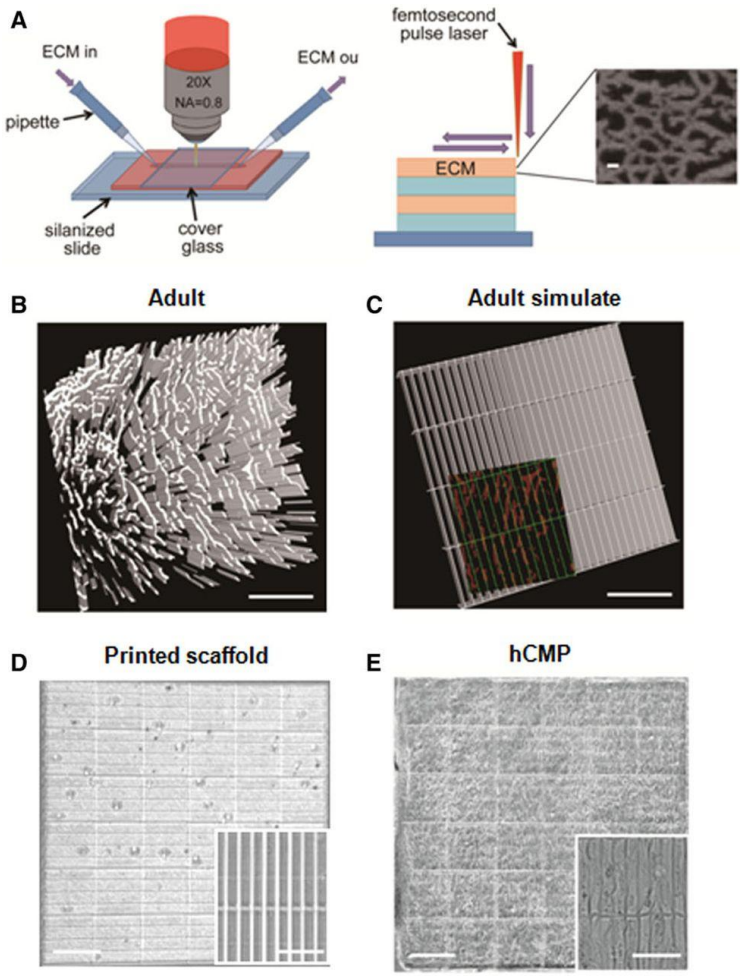

Figure 2-8 3D printed cardiac patch that recapitulates submicron features of native myocardium.[173]

(A) Schematic illustration of the multiphoton laser direct writing process. Scale bar:1 μm. (B) Reconstruction of multiphoton scanning results of heart sections with fibronectin staining. Scale bar: 200 μm. (C) Simulated template based on fibronectin distribution. Scale bar: 100 μm. (D) Printed scaffold. Scale bar: 500 μm (overall structure) and 50 μm (individual channels) (E) Cll-loaded scaffold. Scale bar: 500 μm (overall structure) and 50 μm (individual channels). Reprinted with permission.

In addition to complex tissue constructs such as vascular structures and ECM features, highly organized and anisotropic components are also essential characteristics of native cardiac tissue. The anisotropically aligned cardiac muscle fibers are critical for ensuring efficient and coordinated electromechanical activity in the ventricles, characterized by directionally dependent myocardial contraction and excitation wave propagation.[174] Cardiac tissue engineering scaffolds incorporating biomimetic topographical cues that mimic this cardiac anisotropy can significantly enhance cardiac tissue regeneration and functional restoration.[165,175] Although the anisotropic alignment of scaffold fibers can be achieved using 3D printing, replicating other topographical features, such as surface curvature, solely through conventional 3D printing remains challenging. As an extension of 3D printing, 4D printing, which produces structures capable of shape or functional transformation upon exposure to predetermined stimuli after fabrication,[176] offers the potential to generate tissue engineering scaffolds with more comprehensive topographical cues that better resemble the myocardium.

Zhang's group developed a 4D cardiac patch using SLA that features oriented fibers mimicking the anisotropy of cardiac muscle fibers. This patch also possesses self-morphing capability, allowing it to undergo a conformational change that mimics the surface curvature of the heart.[177] The detailed organization of myofibers in the left ventricle has been studied using diffusion tensor imaging (DTI), which revealed that myofibers are oriented from +60° to −60° across the ventricular wall and are arranged in a sheet-like structure [178,179] Based on this analysis, a 3D printing template was designed, and a wavy-patterned microstructure was used instead of a conventional mesh pattern. The bioink for SLA consisted of methacrylated gelatin, polyethylene glycol diacrylate (PEGDA) as the crosslinker, and Irgacure 2959 as the photoinitiator. SLA employs a bottom-up fabrication process, in which the laser repeatedly scans the upper layer,

leading to a higher crosslink density in the bottom layer. Because the bottom layer adheres to the substrate and cannot shrink freely, while the top layer can shrink spontaneously, the printed structure tends to bend toward the top layer, resulting in a curved 4D architecture after printing. The curvature of the structure increases with printing speed. hMSCs have been co-cultured with CMs and endothelial cells to improve cell viability, myogenesis, angiogenesis, and cardiac contractility through their paracrine activity. Accordingly, a triculture system consisting of hiPSC-CMs, human endothelial cells, and hMSCs was seeded onto the 4D-printed cardiac patch. The hiPSC-CMs on the patch exhibited synchronous contraction seven days after seeding, and calcium oscillation waveforms were observed. The cellularized patch was then placed on the infarcted mouse heart, where strong adhesion formed between the epicardium and the patch without the need for fibrin glue or sutures.

Bioinspired strategies offer a promising alternative to 3D printing for reconstructing the 3D structural organization of native myocardium. Leaf venation is a particularly compelling model because of its hierarchical branching architecture and highly efficient nutrient transport system, which closely resembles mammalian vascular networks. Mao et al. developed a leaf-venation-inspired PDMS negative mold containing microchannels with amphiphilic surface treatment to guide the self-assembly of cell-laden fibrin hydrogel into large-scale engineered tissue.[180] The amphiphilic modification involved octafluorocyclobutane coating, plasma treatment, and Pluronic F127 coating. Due to the amphiphilic surface, the cell-laden hydrogel detached from the PDMS surface as a result of cell-spreading-induced shrinkage, compacting into a thin rod-like structure (Figure 2-9A). Over time, HUVECs migrated toward the periphery, forming a tubular endothelial structure, while the fibrin matrix condensed into a dense core (Figure 2-9B). This strategy has been successfully applied to both neonatal rat CMs and hiPSC-CMs, producing cardiac tissues with

aligned sarcomeres, synchronous contraction, and electrophysiological functionality (Figure 2-9C). To enable deployment onto the heart, the researchers further developed an injectable cardiac patch by sandwiching an electrohydrodynamically printed polycaprolactone serpentine mesh between the engineered HUVEC tissue and cardiac tissue (Figure 2-9D). This design provides tunable mechanical properties and injectability (Figure 2-9E).

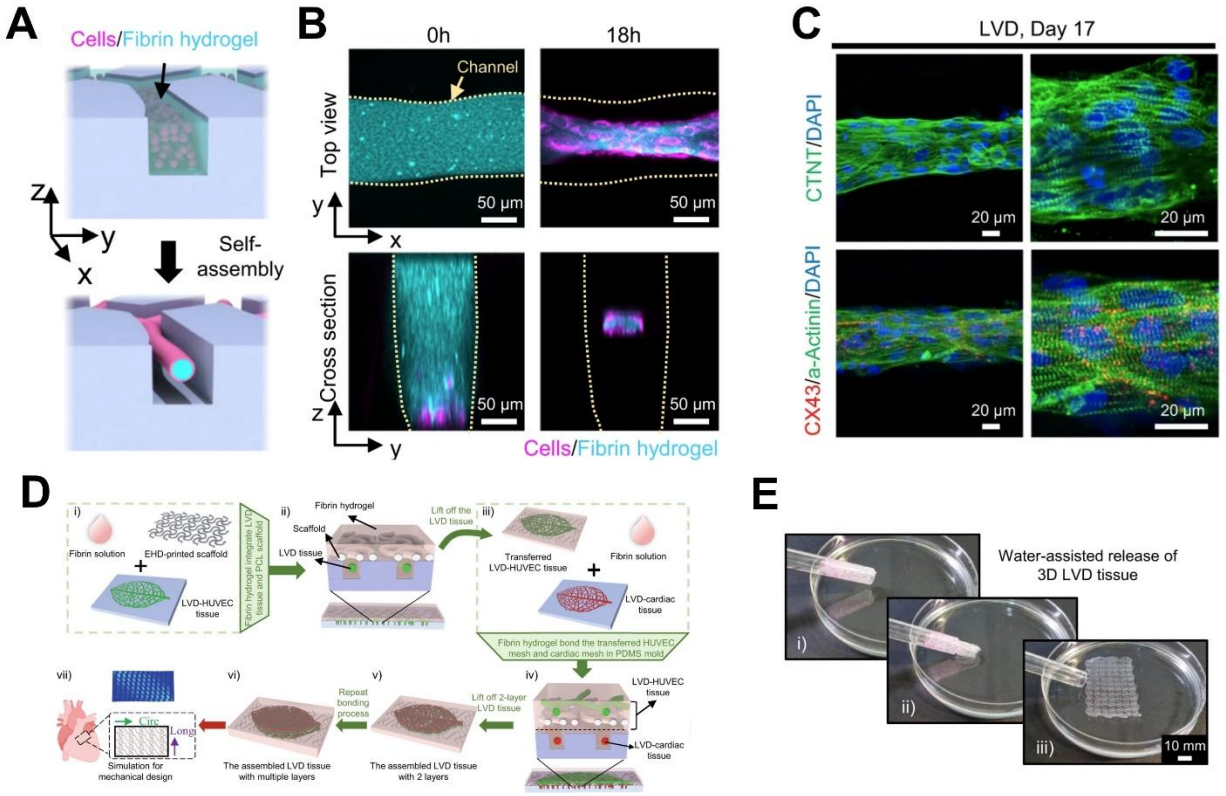

Figure 2-9 Leaf-venation directed (LVD) assembly of cell-laden hydrogels.[180]

(A) Schematic illustration of the self-assembly of cell-laden hydrogel directed by leaf-venation channels. (B) Self-assembly of HUVECs/fibrin hydrogel into tubular structures. (C) Immunofluorescence staining of self-assembled hiPSC-CMs/fibrin hydrogel showing sarcomeric structures with CX43 and cTn staining. (D) Schematic illustration of the fabrication of the cardiac patch. (E) Demonstration of the injectability of the cardiac patch. Reprinted with permission.

2.5 Functional Hydrogel as ECPs

A successful ECP typically possesses multiple material attributes simultaneously, including injectability, self-healing capability, structural stability, stimulus responsiveness, and underwater adhesion. Functional hydrogels have emerged as promising candidates to meet these requirements. To minimize the invasiveness associated with open-chest surgery, injectability is a particularly desirable property for ECPs. As discussed in Chapter 1, matrix metalloproteinases (MMPs) are overexpressed during the early remodeling phase following MI, contributing to the degradation of the cardiac ECM. To address this issue, researchers have developed smart hydrogels with MMP-responsive behavior for targeted therapeutic intervention. Elastin-like recombinamers (ELRs) are synthetic polypeptides that mimic elastin, a key structural component of the ECM. Pandit's group developed an MMP-sensitive ELR hydrogel using an innovative genetic engineering approach.[181] Two distinct ELR variants were engineered through bacterial expression in *E. coli*. One variant was functionalized with alkyne groups, while the other contained azide groups, enabling crosslinking through click chemistry. Upon injection into the peri-infarct region, the two ELRs rapidly formed a stable scaffold in situ. Notably, one of the ELR backbones contained MMP-cleavable bioactive sites, which can sequester and deplete MMPs, thereby inhibiting further degradation of the cardiac ECM.

Fan et al. also engineered an MMP-responsive hydrogel using a genetically engineered peptide fusion strategy (Figure 2-10).[182] The recombinant peptide, produced in *E. coli* BL21A, consisted of glutathione-S-transferase (GST), basic fibroblast growth factor (bFGF), and an MMP-cleavable peptide sequence PLGLAG (TIMP). Collagen was modified with glutathione groups, with Sulfo-SMCC serving as the linker, enabling crosslinking with the recombinant peptide to form an injectable hydrogel. Within the MI microenvironment, the TIMP peptide is cleaved by the

overexpressed MMPs in the infarct region, triggering the on-demand release of bFGF to promote tissue repair.

Chen et al. developed an MMPs-responsive hydrogel for the on-demand delivery of interleukin-4 plasmid DNA (IL4-pDNA).[183] The IL4-pDNA was electrostatically complexed with carbon dots to form stable nanocomposites that function as nanocarriers, enhancing cellular uptake while protecting the nucleic acid from degradation. The carbon dots were synthesized via microwave-assisted pyrolysis of polyethyleneimine and glycerol. The IL4-pDNA–carbon dot nanocarriers were incorporated into an injectable MMPs-sensitive hydrogel formed through thiol–norbornene click chemistry between norbornene-modified tetra-PEG and MMPs-cleavable peptides containing thiol groups. After injection into the infarcted myocardium, the hydrogel degrades in response to elevated MMP levels, enabling the controlled release of the gene nanocarriers. The released IL4-pDNA can be internalized by macrophages, inducing macrophage polarization to promote cardiac repair.

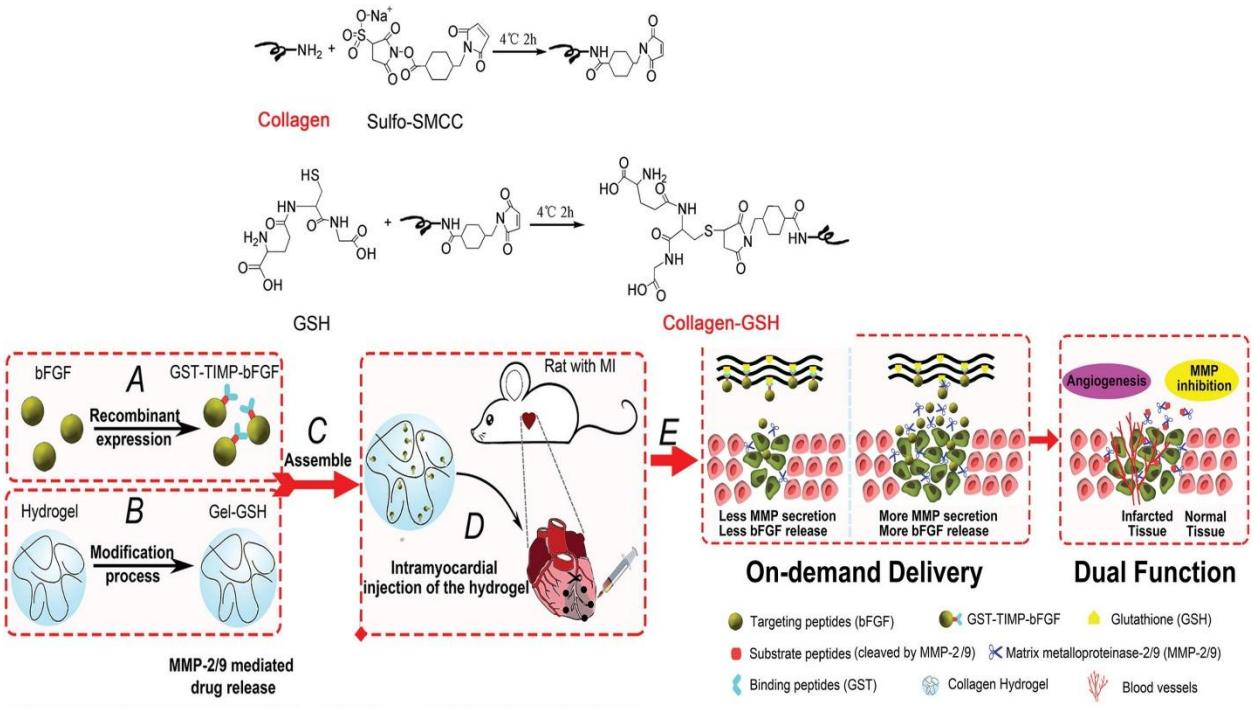

Figure 2-10 Schematic illustration of the synthesis and therapeutic application of metalloproteinases-responsive hydrogels.[182]

Design of MMP-sensitive hydrogels for controlled release of therapeutic growth factors in response to pathological MMP overexpression.[182] Reprinted with permission.

2.6 Conductive ECPs for Treatment and Diagnosis

Therapeutic cells, growth factors, chemical cues, and dECM help mimic the composition, physiological signals, and biomechanical properties of the native cardiac 3D microenvironment. Advanced printing techniques can recapitulate the structural complexity of native cardiac tissue, including vascular, ECM, and parenchymal architectures. However, electrical conductivity is another critical property of native cardiac tissue, as it coordinates heartbeat rhythms and plays an essential role in the understanding and management of arrhythmias, particularly through approaches such as pacing and defibrillation.[88] Following MI, the accumulation of condensed collagen within scar tissue disrupts electrical signal propagation between healthy myocardium and surviving islands of intact CMs within the infarct region due to the lack of electrical connectivity. This interruption leads to desynchronized cardiac contraction and ultimately contributes to progressive functional deterioration of the heart. Conventional culture of CMs or hiPSC-CMs without electrical stimulation fails to reproduce the synchronous contraction, ultrastructural organization, and functional characteristics of mature adult CMs.[89-91] To address this limitation, electrical stimulation systems have been developed to apply pulsatile electrical field stimulation to 3D cardiac cell cultures.[88] Such stimulation can enhance synchronous contraction and improve ultrastructural organization.[89] Consequently, conductive scaffolds capable of electrically bridging

healthy myocardium and viable CMs within scar tissue are actively being explored for the development of ECPs.

Carbon-based nanomaterials, such as carbon nanotubes (CNT) and graphene, along with conductive polymers including polyacetylene, polypyrrole (PPy), polyaniline (PANI), and poly(3,4-ethylenedioxythiophene):polystyrenesulfonate (PEDOT: PSS), as well as metal-based nanomaterials such as metal nanoparticles, nanowires, nanorods, nanoflakes, and quantum dots, have been incorporated into hydrogel-based ECPs as conductive fillers to enhance their electrical conductivity. Mihic et al. grafted PPy onto chitosan through Fe^{3+}-induced oxidative polymerization, followed by crosslinking of the grafted chitosan with glutaraldehyde to form a hydrogel.[184] For comparison, chitosan without PPy grafting was also crosslinked into hydrogels using the same method (Figure 2-11A). To evaluate whether the PPy–chitosan hydrogel could support electrical signal conduction, Mihic et al. designed an ex vivo assay. In this experiment, two pieces of skeletal muscle tissue isolated from adult rats were placed on dishes coated with either PPy–chitosan hydrogel or chitosan hydrogel, positioned 25 mm apart. Electrical stimulation was applied to one muscle sample, while the action potential of the second muscle sample was recorded using an electromyogram (EMG) system (Figure 2-11B). The PPy–chitosan hydrogel produced a significantly higher action potential amplitude in the measured muscle tissue (Figure 2-11C), indicating enhanced electrical signal conduction through the hydrogel. In addition, CMs cultured on the PPy–chitosan hydrogel exhibited faster Ca^{2+} transient propagation, further demonstrating its improved electrical conductivity.

MI rats were treated with PPy-chitosan hydrogel, saline, or chitosan hydrogel to assess the therapeutic efficacy of the PPy-chitosan hydrogel. ECG recordings from rats treated with the PPy-chitosan hydrogel exhibited narrower QRS intervals, resembling those of healthy rats. Following

excision, the hearts were Langendorff-perfused for electrophysiological assessment. Hearts from the PPy-chitosan hydrogel-treated group showed faster transverse conduction velocities, comparable to those of non-MI rats, along with higher conduction velocities in the border zone and scar region. These findings indicate that the PPy-chitosan hydrogel enhanced cardiac conduction. Furthermore, MI rats treated with the PPy-chitosan hydrogel displayed improved cardiac function and reduced scar size.

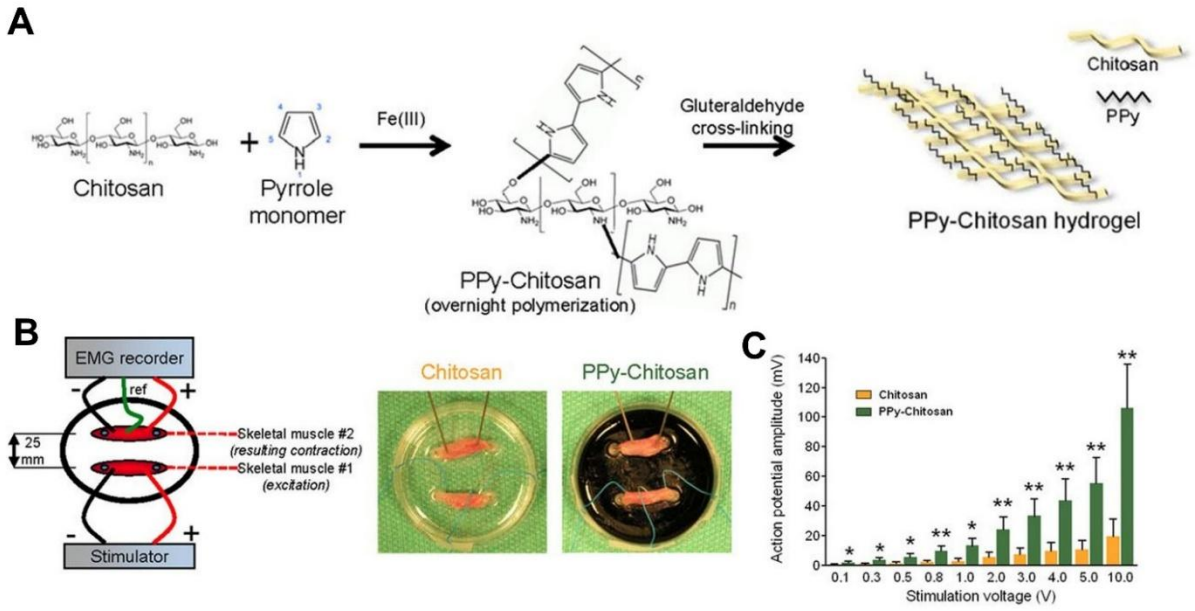

Figure 2-11 Conductive hydrogel for MI repair.[184]

(A) Schematic illustration of the synthesis of PPy-grafted chitosan and its crosslinking. (B) Schematic illustration and photograph of the ex vivo skeletal muscle excitation assay. (C) Action potential amplitudes recorded from unstimulated muscle.

To minimize the invasiveness associated with open-chest surgery, injectability is a desirable property for ECPs. Wang et al. developed a conductive cryogel with shape-memory-enabled injectability and high compressibility for myocardial infarction (MI) repair (Figure 2-12A).[185] These properties arise from the cryogel's hierarchical porous architecture. The cryogel was fabricated by gelation of a mixture containing F127-stabilized CNTs, methacrylated gelatin, and methacrylated elastin at −20 °C. During freezing, ice crystals served as templates for the crosslinked polymer network, generating macropores (Figure 2-12B). Subsequent removal of F127 produced nanopores along the scaffold walls.

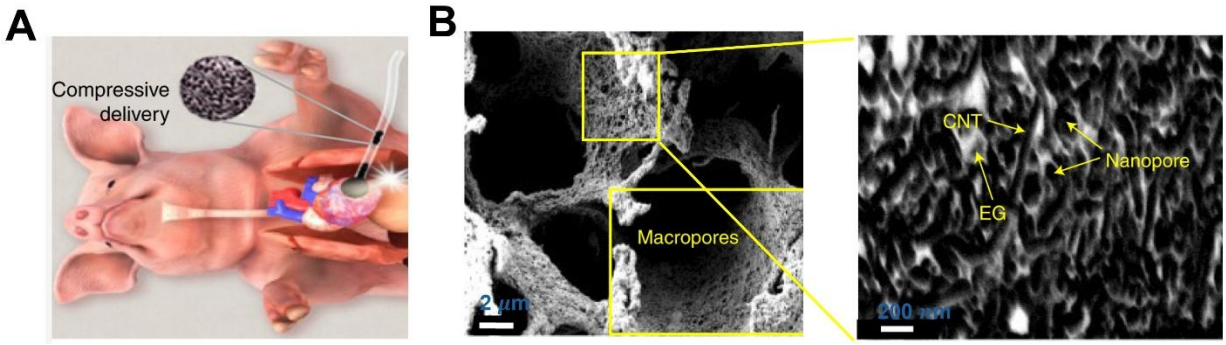

Figure 2-12 Injectable conductive cryogel.[185]

(A) Injectable delivery of the conductive cryogel. (B) SEM images of the cross-section of the cryogel showing ice crystal–templated macropores and a magnified view of nanopores along the walls of the macropores. Reprinted with permission.

He et al. developed a conductive Janus adhesive hydrogel designed to simultaneously address two major challenges associated with cardiac surgery: myocardial repair and the prevention of postoperative tissue adhesion.[186] The bottom layer, which interfaces with the myocardium, is a catechol-functionalized ionic hydrogel reinforced with cellulose nanocrystals

(CNCs). In this layer, 3-sulfopropyl methacrylate potassium salt (MASEP) provides ionic conductivity and facilitates electrostatic interactions with cardiac tissue. Aldehyde-modified CNCs enhance mechanical strength and promote tissue adhesion through dynamic covalent interactions, including Schiff base formation and Michael addition with amine groups in native tissue proteins. In addition, catechol groups derived from caffeic acid further strengthen the interfacial bonding through multiple interactions such as hydrogen bonding, π–π stacking, and Michael addition. N, N′-bis(acryloyl)cystamine (BAC) functions as a dynamic crosslinker that is cleavable by glutathione, enabling on-demand degradation and removal of the hydrogel, while also acting as a reactive oxygen species scavenger in the infarcted myocardium. Furthermore, polyethylenimine–poly(acrylic acid) complexes contribute additional electrostatic interactions that enhance the adhesion strength of the hydrogel to cardiac tissue. In contrast, the top layer of the Janus hydrogel is designed to prevent postoperative tissue adhesion. This anti-adhesive layer consists of carboxylated cellulose nanocrystals (CNCs-COOH) embedded within a poly(acrylic acid) matrix crosslinked with polyethylene glycol diacrylate (PEGDA). The presence of PEG chains provides anti-fouling and anti-cell-adhesion properties, thereby minimizing undesirable tissue attachment to the external surface of the patch.

Monitoring and modulating the electrophysiological state of the heart are essential for the diagnosis and treatment of cardiovascular diseases. The funny current (If) plays a critical role in regulating the spontaneous contraction and relaxation of the heart by controlling pacemaker activity in cardiac muscle cells.[187] Reduced electrophysiological signals and local conduction delays are key indicators of myocardial infarction (MI). In addition, real-time monitoring of other cardiovascular parameters and biomarkers, including blood pressure, local contractility, stroke volume, cardiac output, glucose levels, and blood lactate concentration, can significantly improve

diagnostic accuracy and enable more targeted therapeutic interventions.[188] Furthermore, evaluating the electrical maturation of therapeutic cells cultured on engineered cardiac patches (ECPs), as well as the electrical activity of the patches themselves, is a crucial step in the development and optimization of ECP-based therapies. Conventional electronic devices fabricated from metals and silicone have been applied to monitor and modulate cardiac electrical activity for the diagnosis and treatment of heart diseases.[189] However, these devices are typically composed of rigid materials. Consequently, they struggle to establish gapless and conformal contact with the dynamically beating and curved surface of the heart due to significant mechanical mismatch. This limitation restricts their ability to achieve high-resolution spatiotemporal mapping, which is essential for accurate cardiac signal detection and monitoring.

The intrinsic rigidity of materials such as metals can be substantially reduced by decreasing their thickness to the micrometer scale or below.[190] In addition, structural engineering strategies, including the fabrication of devices into mesh-shaped arrays, serpentine interconnection patterns, spring-like helical structures, and origami- or kirigami-inspired architectures, can significantly enhance device flexibility and deformability.[191] These design approaches enable otherwise rigid bulk materials to better accommodate the dynamic motion and curved geometry of the heart surface. Recent advances in microfabrication techniques, including microelectromechanical systems (MEMS), ion-beam lithography, layer-by-layer deposition, and holographic lithography, have enabled the fabrication of ultrathin 2D electronic devices with micro- and nanoscale features. However, despite these advances, such techniques still face challenges in producing complex 3D morphologies that are necessary to achieve fully conformal integration with the dynamically beating and curved surface of the heart.

Deterministic microfolding has emerged as a promising strategy for the fabrication of free-standing 3D microelectronic devices.[192] In this approach, a two-dimensional (2D) microelectronic precursor fabricated using techniques such as magnetron sputtering, laser cutting, photolithography, and spin coating is transferred onto a folding host to enable the transformation into a 3D configuration . The folding host consists of three sequentially spin-cast layers, including a PDMS substrate, a poly(methyl methacrylate) (PMMA) sacrificial layer, and a poly(lactic-co-glycolic acid) (PLGA) layer. A central trench is introduced into the folding host via laser cutting, and controlled folding along the trench axis induces the transformation of the planar device into a 3D architecture. A petal-shaped 2D electronic device was fabricated as the precursor structure for a 3D epicardial bioelectronic platform capable of monitoring local electrophysiological signals. The device consists of an ultrathin polyimide (PI) base layer (~10 μm), a layer of Au serpentine resistors (~50 nm), and a parylene encapsulation layer (~2 μm). Through deterministic folding, the planar device transforms into a fully bloomed 3D epicardial bioelectronic structure. The ultrathin architecture provides exceptional mechanical flexibility, enabling minimally invasive delivery to the heart via catheter insertion. Upon release, the device returns to its predesigned blooming configuration, allowing it to establish conformal contact with the geometrically irregular and dynamically beating cardiac surface. In vivo experiments demonstrated the device's capability for spatially resolved cardiac monitoring. After deployment, the four petal-like sensing elements extended to four distinct regions of a rat heart, where their relative resistance changes ($\Delta R/R_0$) were recorded and compared with simultaneously measured electrocardiogram (ECG) signals. To simulate myocardial ischemia, the left coronary artery was ligated. Sensors positioned on the left side of the heart (C2 and C3) exhibited stronger responses than those on the right side (C1 and

C4), highlighting the device's ability to detect localized electrophysiological abnormalities associated with myocardial ischemia.

Multilayer thin films composed of silver nanowires (AgNWs) and polydimethylsiloxane (PDMS) have been assembled into multifunctional electronic platforms, including transistor arrays, strain sensors, and temperature sensors, enabling spatiotemporal mapping of biopotential signals, cardiac motion, and temperature.[193] Patterned electronic structures were fabricated using Kapton tape masks prepared with a programmable cutting machine. The patterned AgNW thin films coated with gold nanoparticles (AuNPs-AgNWs) served as electrodes in the various device components. To prepare the AgNWs thin film, a solution of AgNWs was drop-cast on a clean glass slide covered with a patterned Kapton-tape mask. The AgNWs in the thin film were solidified at 60℃, then welded at 200℃ to enhance conductivity. A double-sided electrode design was adopted by the transistor arrays. To prepare the double-sided AgNWs electrode, PDMS was spin-coated on the patterned AgNMs film. Another prepared patterned AgNWs thin film attached to a glass slide was laminated on top of the PDMS. After the PDMS was cured, the double-sided electrode was peeled off the glass slides. AuNPs were then deposited onto the AgNW films through a galvanic exchange reaction by dropping a $HAuCl_4$ solution onto the AgNW network. The P3HT-NF/PDMS composite, consisting of poly(3-hexylthiophene-2,5-diyl) nanofibrils (P3HT-NFs) dispersed in PDMS, served as both the semiconducting layer in the transistors and the sensing layer in strain sensors. An ion-gel dielectric composed of 1-ethyl-3-methylimidazolium bis(trifluoromethylsulfonyl)imide ([EMIM][TFSI]) and poly(vinylidene fluoride-co-hexafluoropropylene) (PVDF-HFP) functioned as the gate dielectric in the transistors. Patterned P3HT/PDMS composites and ion-gel layers were fabricated by spin-coating onto masked glass substrates, followed by curing. Each transistor within the array employed a three-electrode

configuration consisting of source, drain, and gate electrodes formed from patterned double-sided AuNPs-AgNWs films (Figure 2-13A). The P3HT/PDMS semiconductor layer was positioned between the source and drain electrodes, while the ion-gel dielectric covered the semiconductor and gate electrode. The AuNPs-AgNWs electrodes located on the bottom side of the PDMS, which directly contacted the epicardial surface, were electrically connected to the top electrodes using conductive rubber paste (Figure 2-13B). A 5 × 5 transistor array was fabricated and attached to the surface of a porcine heart using surgical adhesive (Figure 2-13C). Biopotentials recorded from each transistor at sequential time points enabled spatiotemporal mapping of cardiac electrophysiological signals (Figure 2-13D). In addition to the transistor array, the P3HT-NF/PDMS composite and AuNPs-AgNWs electrodes were assembled into a strain sensor by laminating the composite layer between two electrodes (Figure 2-13E). The strain sensor exhibited stable linear responses up to 30 % strain. The AgNW electrodes also functioned as temperature sensors, demonstrating stable temperature responses that were minimally affected by mechanical deformation (Figure 2-13F). Furthermore, a triboelectric nanogenerator (TENG) was fabricated by inserting a PDMS spacer between two AgNW electrodes, providing a potential self-powered energy source (Figure 2-13G). All these functional components, including the transistor array, strain sensor, temperature sensor, and TENG, were integrated into a single multifunctional epicardial electronic platform (Figure 2-13H).

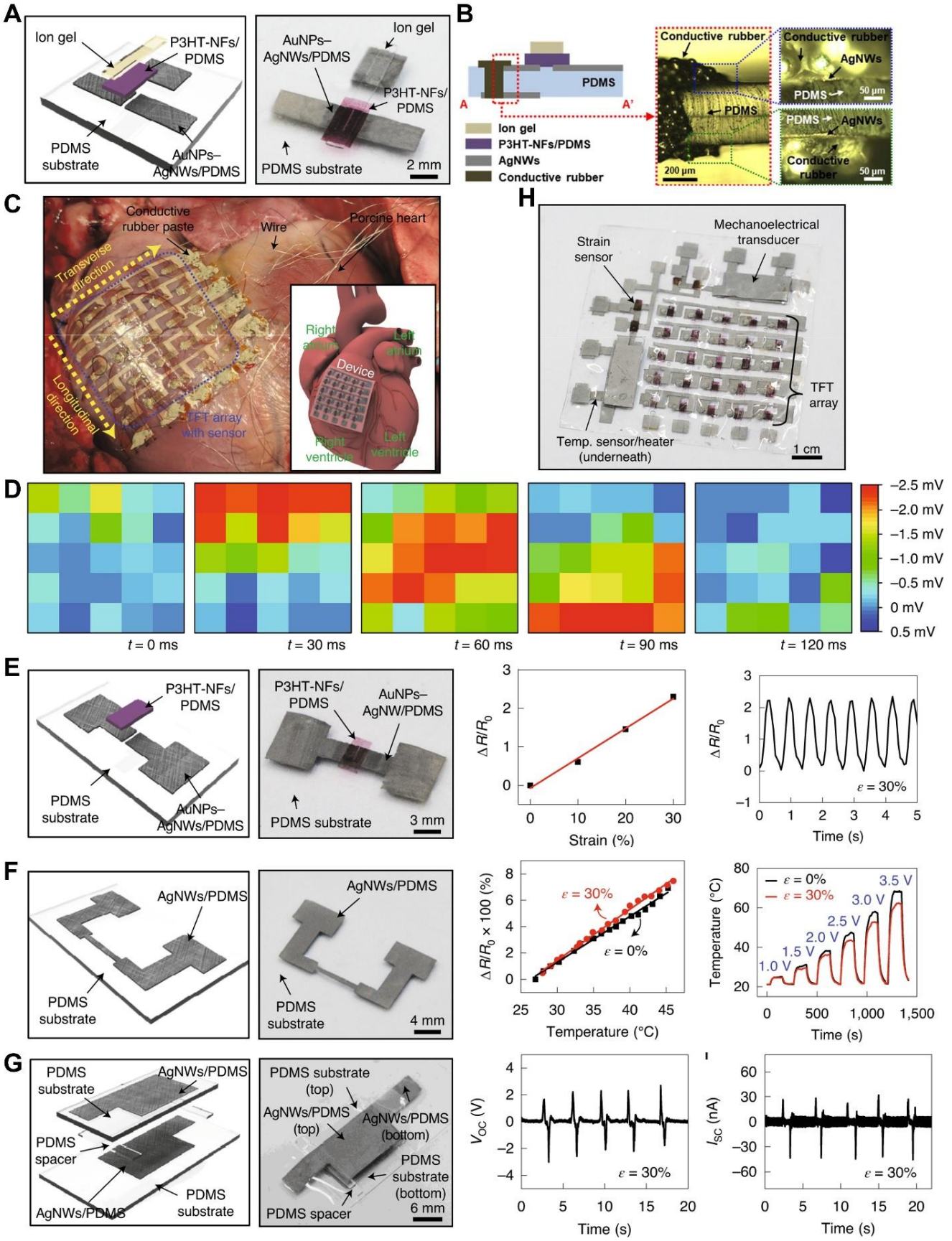
A
Ion gel
P3HT-NFs/ PDMS
PDMS substrate
AuNPs–AgNWs/PDMS
AuNPs–AgNWs/PDMS
Ion gel
P3HT-NFs/ PDMS
PDMS substrate
2 mm
B
PDMS
A
A'
Ion gel
P3HT-NFs/PDMS
AgNWs
Conductive rubber
Conductive rubber
PDMS
200 μm
Conductive rubber
AgNWs
PDMS
50 μm
PDMS
AgNWs
Conductive rubber
50 μm
C
Conductive rubber paste
Wire
Porcine heart
Transverse direction
Longitudinal direction
TFT array with sensor
Right atrium
Left atrium
Device
Right ventricle
Left ventricle
H
Strain sensor
Mechanoelectrical transducer
TFT array
Temp. sensor/heater (underneath)
1 cm
D
−2.5 mV
−2.0 mV
−1.5 mV
−1.0 mV
−0.5 mV
0 mV
0.5 mV
t = 0 ms
t = 30 ms
t = 60 ms
t = 90 ms
t = 120 ms
E
P3HT-NFs/ PDMS
PDMS substrate
AuNPs–AgNWs/PDMS
P3HT-NFs/ PDMS
AuNPs–AgNW/PDMS
PDMS substrate
3 mm
ΔR/R0
Strain (%)
ε = 30%
Time (s)
F
AgNWs/PDMS
PDMS substrate
AgNWs/PDMS
PDMS substrate
4 mm
ΔR/R0 × 100 (%)
ε = 30%
ε = 0%
Temperature (°C)
Temperature (°C)
ε = 0%
ε = 30%
3.5 V
3.0 V
2.5 V
2.0 V
1.5 V
1.0 V
Time (s)
G
PDMS substrate
AgNWs/PDMS
PDMS spacer
AgNWs/PDMS
PDMS substrate
PDMS substrate (top)
AgNWs/PDMS (top)
AgNWs/PDMS (bottom)
PDMS substrate (bottom)
PDMS spacer
6 mm
VOC (V)
ε = 30%
Time (s)
ISC (nA)
ε = 30%
Time (s)

Figure 2-13 Epicardial transistor array.

(A) Schematic illustration and image of a transistor. (B) Schematic cross-section of the transistor. (C) Image of the transistor array attached to the heart surface. (D) Spatiotemporal mapping of biopotentials at five sequential time points. (E) Schematic illustration and image of the strain sensor, including its calibration curve and relative resistance changes under cyclic stretching. (F) Schematic illustration and image of the temperature sensor, showing relative resistance changes in response to temperature variation with and without mechanical strain, and temperature changes in response to applied voltage with and without mechanical strain. (G) Schematic illustration and image of TENG and its V_{oc}, and I_{sc}. Reprinted with permission.

Although spatiotemporal mapping of cardiac activity has been demonstrated, several challenges remain. The continuous mechanical motion of the beating heart subjects implanted devices to repetitive cyclic strain, which increases the risk of device fracture or delamination. In addition, conventional device–tissue interfaces may trigger adverse biological responses, including bleeding, persistent shear stress, and acute or chronic inflammation. To address these issues, Choi et al. developed a conformable, fatigue-resistant, and adhesive bioelectronic system capable of instantaneous adhesion to the epicardium. Their strategy employs a self-healing conductive nanocomposite prepared by dispersing eutectic gallium–indium (EGaIn) liquid metal within a PDMS-based self-healing polymer matrix. The conductive nanocomposite is coated with a dopamine-conjugated alginate adhesive layer and subsequently transferred onto an electrospun self-heating polymer substrate. Upon contact with the epicardium, the dopamine-conjugated alginate undergoes spontaneous gelation, enabling rapid and robust adhesion to cardiac tissue. In

another approach, Hwang and Kim et al. developed a multilayer transistor-based cardiac patch capable of simultaneous in situ cardiac disease diagnosis and therapy.[194] The cardiac patch consists of three functional components: (i) an array of multilayer pressure-sensitive transistors for mapping cardiac mechanical activity, (ii) therapeutic electrodes that deliver electrical stimulation, and (iii) a catechol-functionalized alginate hydrogel adhesive layer that enables stable attachment of the patch to the wet epicardial surface.

2.7 Implantable Triboelectric Nanogenerators in ECPs for Therapeutic and Diagnostic Purposes

Electrical stimulation plays an important role in promoting the differentiation and maturation of cardiomyocytes (CMs). However, directly applying electrical stimulation to infarcted myocardium in vivo remains challenging. To overcome this limitation, implantable energy-harvesting systems, particularly triboelectric nanogenerators (TENGs), have emerged as promising platforms for generating in situ electrical stimulation. TENGs operate based on the coupling of the triboelectric effect and electrostatic induction, enabling the conversion of biomechanical energy into electrical energy. A biodegradable TENG fabricated from natural bioresorbable polymers, including cellulose, chitin, rice paper, silk fibroin, and egg white, was developed to power an electrical stimulation system composed of a rectifier and a PDMS-packaged Au interdigital electrode (Figure 2-14A).[35] When CMs were seeded on the surface of the interdigital electrodes, the electrical stimulation system generated a direct-current (DC) electric field that increased the beating rate of CM clusters and improved the synchronization of their contractions. In another study, a flexible TENG was directly coupled with a PDMS-packaged Au interdigital electrode to provide electrical stimulation for cultured cardiomyocytes (Figure 2-14B).[36] The generated electrical signals promoted the maturation of neonatal rat cardiomyocytes.

Both studies further demonstrated that the TENG could be effectively driven by biomechanical energy generated from respiratory motion, highlighting its potential as an implantable power source for medical electronic devices.

The energy harvested by implantable triboelectric nanogenerators (TENGs) can support not only therapeutic applications but also the operation of diagnostic devices. For example, a wireless cardiac monitoring system has been developed that utilizes an implantable TENG to track heartbeats in real time (Figure 2-14C).[195] In this system, the electrical energy generated by the TENG is first stored in a power management unit and subsequently transmitted through an implantable wireless transmitter. The transmitted signals are received by an external coil as electromagnetic waves, and the received electrical signals are then recorded by an oscilloscope for further analysis.

Beyond energy harvesting, TENGs exhibit exceptional sensitivity to mechanical stimuli through their output characteristics, including open-circuit voltage (V_{oc}), short-circuit current (I_{sc}), and signal frequency. These features enable TENGs to function as ultrasensitive sensors for biomechanical signals. In a representative demonstration, researchers successfully monitored the heart rate of a rat using a TENG implanted on the pericardium (Figure 2-14D).[38] The pericardium-implanted TENG detected subtle myocardial movements, and the peaks in V_{oc} showed strong synchronization with electrocardiogram (ECG) R-waves. The device also clearly detected abnormal cardiac activity induced by epinephrine administration. In another study, a TENG was implanted into the left ventricle of a swine to monitor endocardial pressure (Figure 2-14E).[39] The peaks in V_{oc} exhibited a linear correlation with pressure changes and responded sensitively to small fluctuations in femoral arterial pressure. The system successfully detected variations in arterial

pressure induced by epinephrine injection, demonstrating the potential of TENGs for real-time cardiovascular monitoring.

Our group has developed a multifunctional Trinity TENG that integrates energy harvesting, in situ electrical stimulation therapy, and real-time cardiac monitoring within a single cardiac patch (Figure 2-14F).[196] Owing to its innovative double-spacer architecture, the Trinity TENG is able to generate a localized electric field directly on the myocardium, thereby eliminating the need for additional therapeutic electrodes. This multifunctional platform not only harvests biomechanical energy from cardiac motion but also delivers electrical stimulation to the infarcted myocardium, leading to significant improvements in cardiac function and reductions in scar size. In addition, the Trinity TENG enables wireless monitoring of cardiac contractility through analysis of its V_{oc} signals.

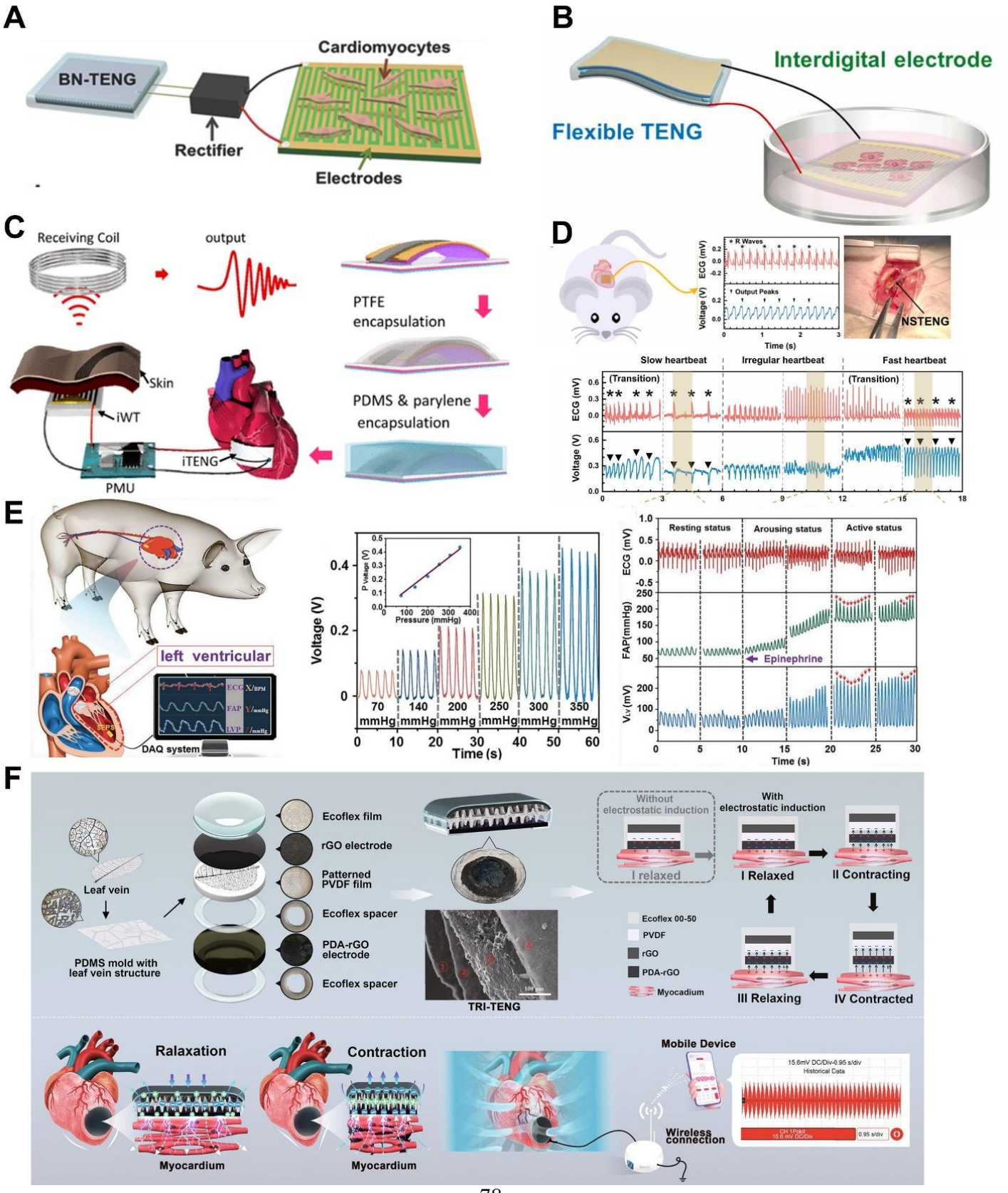
A
BN-TENG
Rectifier
Cardiomyocytes
Electrodes
B
Interdigital electrode
Flexible TENG
C
Receiving Coil
output
PTFE
encapsulation
PDMS & parylene
encapsulation
Skin
iWT
iTENG
PMU
D
R Waves
Output Peaks
ECG (mV)
Voltage (V)
Time (s)
NSTENG
Slow heartbeat
Irregular heartbeat
Fast heartbeat
(Transition)
E
left ventricular
DAQ system
Voltage (V)
Pressure (mmHg)
70 mmHg
140 mmHg
200 mmHg
250 mmHg
300 mmHg
350 mmHg
Time (s)
Resting status
Arousing status
Active status
ECG (mV)
FAP(mmHg)
Epinephrine
Time (s)
F
Leaf vein
PDMS mold with
leaf vein structure
Ecoflex film
rGO electrode
Patterned
PVDF film
Ecoflex spacer
PDA-rGO
electrode
Ecoflex spacer
TRI-TENG
Without
electrostatic induction
With
electrostatic induction
I relaxed
I Relaxed
II Contracting
III Relaxing
IV Contracted
Ecoflex 00-50
PVDF
rGO
PDA-rGO
Myocadium
Ralaxation
Contraction
Myocardium
Myocardium
Mobile Device
Wireless
connection
Historical Data

Figure 2-14 Schematic illustration and functional characterization of TENG-based therapeutic and diagnostic cardiac patch.

(A) Biodegradable TENG-powered electrical stimulation system for CMs.[35] (B) Electrical stimulation of CMs through interdigital electrodes powered by a flexible TENG.[36] (C) Wireless heart rate monitoring system enabled by wireless transmission of TENG-generated electrical power.[195] (D) Implanted TENG for heartbeat sensing through V_{oc} signal analysis.[38] (E) Calibration curve of the TENG V_{oc} response to liquid pressure sensing and the demonstration of endocardial pressure monitoring via V_{oc} analysis.[39] (F) Structural architecture and working mechanism of the Trinity TENG, demonstrating its wireless sensing capability.[196] Reprinted with permission.

2.8 Microneedle Patches as ECPs

Microneedles have emerged as a transformative platform for painless transdermal delivery of therapeutic agents, including drugs, nucleic acids, and proteins. These minimally invasive devices create microscale channels in tissues, enabling enhanced therapeutic delivery efficiency, homogeneous distribution, and prolonged local retention of therapeutic agents. The fabrication of microneedles typically follows a standardized protocol. A precursor solution is first cast into a microneedle mold, followed by vacuum treatment or centrifugation to remove trapped air bubbles and ensure complete filling of the mold cavities. The precursor is then partially dried to condense the material and exposed to UV light for polymer crosslinking. This process may be repeated two to three times to reinforce the microneedle structure, followed by final drying and demolding.

Microneedles have recently been explored as delivery platforms for myocardial infarction (MI) therapy. Cheng's group developed a polyvinyl alcohol (PVA) microneedle patch with a

fibrin-gel basal layer encapsulating heart-derived cardiac stem cells (CSCs).[197] In this system, the PVA microneedles serve as microchannels connecting the basal layer with the host myocardium, enabling bidirectional molecular exchange. The implanted stem cells can receive essential nutrients from the host tissue while releasing paracrine factors that promote myocardial repair. This delivery strategy enhances angiomyogenesis, reduces scar size, and improves cardiac function. Compared with conventional intramyocardial injection, the microneedle-based delivery platform also enables more homogeneous and widespread distribution of therapeutic agents. In a related study, PVA microneedles crosslinked through multiple freeze–thaw cycles were used to deliver adeno-associated virus (AAV)-9 transgenic vectors for cardiac gene therapy.[198] The loading process involves precisely dispensing the AAV solution into the microneedle matrix. For in vivo delivery, the AAV-loaded microneedle patch is implanted into the heart using an endoscopic-assisted microthoracotomy approach. This delivery method significantly broadens the distribution of the viral vectors, alleviates adverse cardiac remodeling, and improves myocardial perfusion.

Recent studies have also demonstrated the therapeutic potential of mesenchymal stem cell–derived exosomes for cardiac repair. To enhance exosome delivery, our group developed two innovative microneedle-based platforms. The first system is a minimally invasive delivery device that integrates microneedles with a flexible kidney-stone retrieval grasper inspired by the biomechanics of a snake's jaw.[199] The implantation process mimics the mechanism of a snakebite. Once the device reaches the infarcted region, the grasper expands to encapsulate the heart and then closes to precisely deploy exosome-loaded microneedles into the target tissue. In another approach, our group developed a microneedle platform capable of delivering self-propelled nanorobots that are activated within the acidic microenvironment of myocardial infarction (Figure

15).[200] The nanorobots consist of ultrafine eggshell-derived calcium carbonate ($CaCO_3$) particles conjugated with therapeutic exosomes. In the acidic MI microenvironment, $CaCO_3$ reacts with protons to generate gas bubbles, producing a propulsive force that drives directional nanorobot movement. In addition, the basal layer of the microneedle patch is loaded with VEGF-encapsulated dual-complementary liposomes to further promote angiogenesis in the infarcted myocardium.

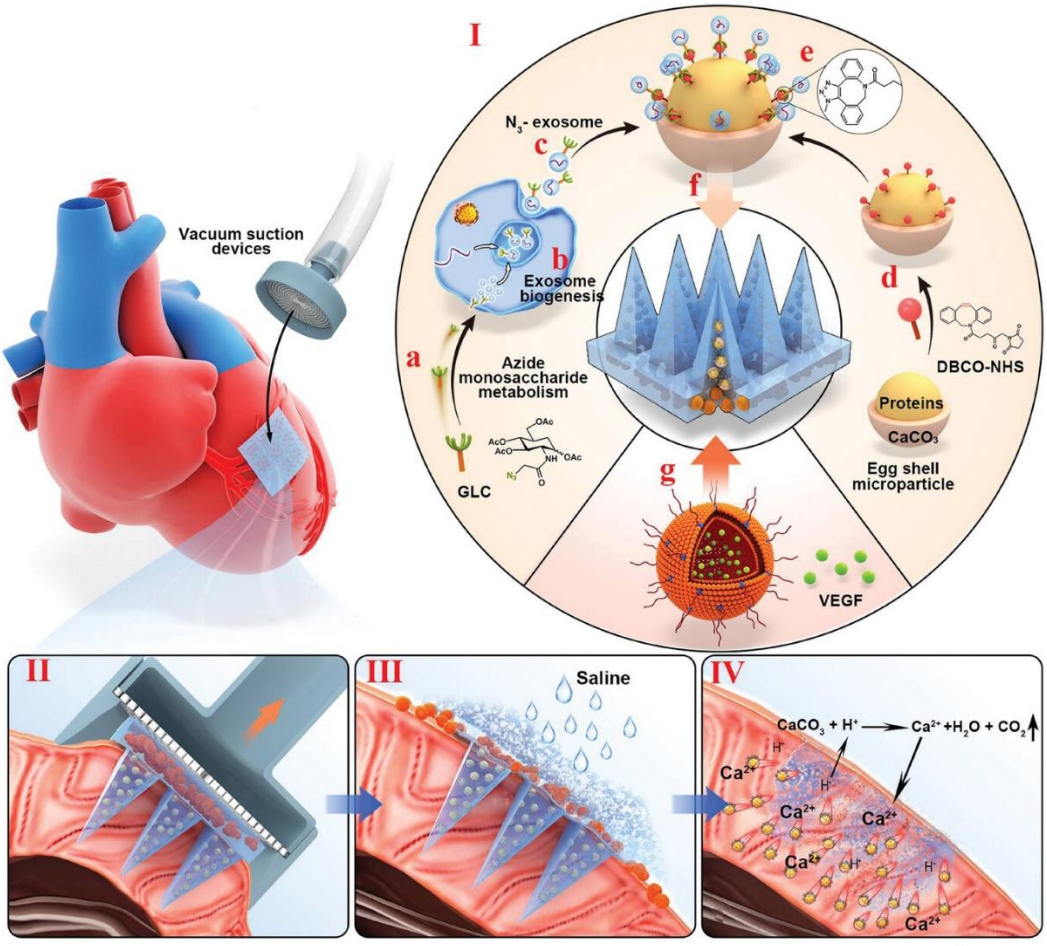

Figure 2-15 Schematic illustration of microneedle-based cardiac patches for MI repair.

Microneedle patch that delivers a self-propelling eggshell-exosome microrobot and VEGF-encapsulated dual-complementary liposome.[200] Reprinted with permission.

3 Chapter 3: Ultra-thin Graphene Oxide Membrane with Asymmetric Hydrophobicity/Hydrophilicity as Sensor, Actuator, and Conformable Cardiac Patch

3.1 Methods and Materials

3.1.1 Application of GO Ink for DIW

GO powder purchased from Tanfeng Tech Inc. (Suzhou, China) was dispersed in deionized (DI) water to prepare a GO solution with a concentration of 10 mg/ml. A probe-sonicator was used to make the solution homogeneous. The solution was homogenized using a probe sonicator. The GO solution was then heated at 95 °C for different durations under vigorous stirring to obtain GO colloidal gel inks. The GO colloidal ink was printed into designed patterns using a DIW printer (Geeetech, China). The spacing between adjacent printed lines was 1.5 mm, and the printing nozzle had an inner diameter of 0.21 mm. The GO colloidal ink was extruded onto polytetrafluoroethylene (PTFE) filter paper under a pressure of 10 kPa. The GO microlattices were subsequently reduced by soaking in hydroiodic acid for 2 h. The resulting reduced graphene oxide (rGO) microlattices were thoroughly washed with DI water, followed by ethanol. The GO microlattice was soaked in hydroiodic acid for 2 hours. The obtained rGO microlattice was washed with water and then with ethanol. To prepare PDA-coated rGO microlattices, dopamine was dissolved in Tris buffer (pH = 8.5) to obtain a solution with a concentration of 2 mg/ml. The rGO microlattices were immersed in the dopamine solution for 8 h to allow PDA deposition. For the preparation of DrGOM, GO microlattices printed using GO_{120} ink were first exposed to hydroiodic acid vapor for 30 min to induce partial reduction. The samples were then placed on the surface of a 2 mg/mL dopamine/Tris solution with the rGO surface facing the liquid to allow PDA deposition

for 8 h. During this process, the GO/rGO microlattices were maintained floating on the solution surface.

3.1.2 Application of GO Ink for "Masked Spin Coating"

Microscale and macroscale patterns were fabricated on copper tape using a commercial die-cutting machine (Cricut®, Spain). The patterned copper tape was then attached to a polytetrafluoroethylene (PTFE) substrate to serve as a mask. A 10 mg/ml GO solution was spin-coated onto the masked PTFE substrate at 1000 rpm for 10 s. After air-drying the GO coating for 2 h, the copper tape mask was carefully peeled off to obtain the patterned GO structure. The patterned GO films were subsequently exposed to hydroiodic acid vapor for different durations to induce reduction and achieve distinct functionalities.

3.1.3 Characterization

The rheological properties of GO inks prepared with different heating durations (30, 60, 90, and 120 min) were characterized using a Discovery Hybrid Rheometer (TA Instruments). For each measurement, 200 μL of GO ink was loaded onto the rheometer. Flow curves were obtained by performing a shear-rate sweep from 10^{-3} to 10^{2} s^{-1} at room temperature. The storage modulus (G') and loss modulus (G") were determined from stress sweep measurements conducted over a shear stress range of 10^{-2} to 10^{3} Pa at a constant oscillation amplitude of 1Hz. GO colloidal gel inks were freeze-dried before chemical characterization. Fourier transform infrared (FTIR) spectra of GO inks, rGO patches, DrGOM, and GO/rGO bilayers were obtained using an FTIR spectrometer. The sheet resistance of the membranes was measured using a four-point probe instrument (RTS-2, PROBES TECH®, China) with a probe spacing of 1 mm. The electrical resistance of the DIW-printed microlattices was measured using a four-wire method with a

benchtop digital multimeter (Keithley DMM6500, Tektronix®, USA). Surface wettability was evaluated by measuring the water contact angle using a goniometer (JY-PHA, Shengding, China). A 15 μL water droplet was dispensed onto the sample surface using the instrument platform, and images were recorded by the accompanying software. The contact angle was subsequently analyzed using ImageJ software. Uniaxial tensile tests were performed under ambient conditions to determine the mechanical properties of the films and DIW microlattices. The tests were conducted using a universal testing machine (MTS®, USA). GO_{120} was used to fabricate 15 mm x 15 mm DIW microlattices and 15 mm × 15 mm films for tensile tests. The tensile tests were performed at a crosshead speed of 1 mm/min, with an initial gauge length of 11 mm. The maximum stress was recorded as the ultimate tensile strength, while the slope of the stress–strain curve after the initial strain-hardening region was used to calculate the Young's modulus. The flexibility f of the samples was calculated from load F and extension x:

$$\boldsymbol{f = \frac{x}{F}} \qquad \textbf{Equation 3-1}$$

3.1.4 Sensitivity Test of GO/rGO Actuators

GO/rGO strips with dimensions of 12mm × 2mm were fabricated using a masked spin-coating method. The GO/rGO actuators were placed in sealed chambers containing saturated salt solutions to establish environments with controlled relative humidity (RH). Saturated lithium chloride (LiCl), potassium acetate (CH_3COOK), magnesium nitrate ($Mg(NO_3)_2$), and sodium chloride (NaCl) solutions were used to generate RH levels of 11%, 23%, 55%, and 75%, respectively. Photographs of the GO/rGO actuators were taken after they reached their maximum curvature at each humidity condition. The bending angles of the actuators were determined using ImageJ software. The curvature (k) of the actuator was calculated using the following equation:

$$\mathbf{k} = \frac{\mathbf{1}}{\boldsymbol{R}} = \frac{\mathbf{1}}{\frac{\boldsymbol{L}}{\boldsymbol{\theta}}} = \frac{\boldsymbol{\theta}}{\boldsymbol{L}} \qquad \textbf{Equation 3-2}$$

where R is the radius of the arc formed by the curved actuator, L is the length of the actuator, and θ is the bending angle of the curved actuator.

3.1.5 Temperature Sensing Performance

The temperature of a hot plate was set to 100 °C, and the real-time temperature was monitored using a handheld multimeter (Victor 86E) equipped with a thermocouple probe. The resistance change of the GO/rGO temperature sensing module was measured simultaneously using another handheld multimeter (Victor 86E). Both the temperature and resistance signals were recorded concurrently on two separate computers using the corresponding data acquisition software. The data acquisition rate on both systems was set to 2 Hz. During the measurement, the GO/rGO temperature sensing module and the thermocouple probe were placed together on the hot plate. To generate a low-temperature environment, the GO/rGO temperature sensing module and the thermocouple were placed on an ice-cooled metal plate. To evaluate the linearity of the temperature sensing module, the hot plate temperature was increased stepwise (30 °C, 50 °C, 70 °C, 90 °C, and 120 °C) and subsequently decreased stepwise. At each temperature point, the resistance of the GO/rGO sensing module and the temperature measured by the thermocouple were recorded once stable values were reached. All temperature-sensing experiments were conducted under ambient laboratory conditions.

3.1.6 pH Sensing Performance

The pH buffer solutions with pH values of 6, 7, and 8 were prepared using a phosphate buffer system (KH_2PO_4/NaOH). Buffer solutions with pH values of 4 and 5 were prepared using an acetic

acid/sodium acetate buffer system. The pH sensing performance of the GO/rGO sensing module was evaluated by measuring the open-circuit potential (OCP) relative to an Ag/AgCl reference electrode using a benchtop digital multimeter (Keithley DMM6500, Tektronix®, USA).

3.1.7 Strain Sensing Performance

Tensile strain was applied stepwise (1%, 2%, 3%, 4%, and 5%) to the rGO strain-sensing module using a universal testing machine (MTS®, USA). The resistance of the rGO strain sensor was simultaneously measured and recorded using a benchtop digital multimeter (Keithley DMM6500, Tektronix®, USA). After the sensor was stretched to each predefined strain level, its resistance value was recorded. The gauge factor (GF) of the rGO strain-sensing module was determined from the slope of the linear region of the relative resistance change ($\frac{\Delta R}{R_0}$) versus strain (ε) curve

$$\boldsymbol{GF = \frac{\delta \frac{\Delta R}{R_0}}{\delta \varepsilon}} \qquad \textbf{Equation 3-3}$$

where ΔR represents the change in resistance caused by stretching, R_0 is the initial resistance, $\varepsilon = \frac{\Delta L}{L_0}$, ΔL is the change in length due to stretching, L_0 is the initial length of the sensor.

3.1.8 Cell Culture

Neonatal rat CMs were isolated from the hearts of 1–3-day-old Sprague–Dawley (SD) rats according to a previously reported method.[201] Briefly, rat hearts were carefully excised and dissociated into a single-cell suspension using 0.25% Trypsin (GIBCO) digestion at 4 °C overnight, followed by digestion with 0.1% collagenase type II (YEASEN) at room temperature. CMs were enriched by pre-plating the cell suspension for 2 h to separate CMs from cardiac fibroblasts. The

obtained CMs were seeded onto the PDA-coated rGO surface of DrGOM at a density of 6×10^5 cells/cm^2 and onto glass slides at a density of 2×10^5 cells/cm^2. The cells were cultured in high-glucose Dulbecco's modified Eagle's medium (DMEM, GIBCO) supplemented with 15% fetal bovine serum (FBS, GIBCO), 100 U/mL penicillin, and 100 μg/mL streptomycin. The cells were maintained in a cell incubator (Thermo Scientific) at 37 °C with 5% CO_2. Human iPSCs-derived CMs (hCMs) were purchased from iPsyte Biosciences and cultured according to the manufacturer's instructions. The hCMs were seeded onto DrGOM at a density of 6×10^5 cells/cm^2 and cultured in a cell incubator at 37℃ with 5% CO_2. HUVECs (Shanghai Cell Bank, Chinese Academy of Sciences, China) were seeded onto DrGOM at a density of 1×10^5 cells/cm^2 and onto glass slides at a density of 2×10^4 cells/cm^2. The cells were cultured in RPMI 1640 medium (GIBCO) supplemented with 10% FBS, 100 μg/mL streptomycin, and 100 U/mL penicillin.

3.1.9 Cell Viability and Morphology of CMs Cultured on DrGOM

The cell viability of CMs cultured on DrGOM was evaluated using a live/dead cell staining kit (US EVERBRIGHT). After CMs were cultured on DrGOM for 1, 3, 7, and 14 days, the cells were washed three times with PBS and then stained with the live/dead working solution in the dark for 30 min at room temperature. The images were obtained using a laser scanning confocal microscope (LSM 880, Zeiss, Germany). Live cells were labeled with green fluorescence, while dead cells were labeled with red fluorescence. Cell viability was calculated as the ratio of live cells to the total number of cells. The cytoskeleton of CMs cultured on DrGOM was observed by F-actin staining. After CMs were cultured on DrGOM for 7 days, the cells were washed with PBS and fixed with 4% paraformaldehyde (PFA) at room temperature for 20 min. The cells were then stained with rhodamine-labeled phalloidin (AAT Bioquest). Fluorescence images of the stained

samples were captured using a laser scanning confocal microscope. For scanning electron microscopy (SEM) observation, CMs cultured on DrGOM for 7 days were washed with PBS and fixed with 2.5% glutaraldehyde overnight. The fixed cells were subsequently dehydrated using a graded ethanol series (50%, 60%, 70%, 80%, 90%, and 95% once each for 5 min, followed by 100% ethanol twice for 5 min) and then freeze-dried. The morphologies of CMs cultured on DrGOM were observed using SEM (ULTRA 55, Zeiss, Germany).

3.1.10 Immunofluorescence Staining for Cells Cultured on Different Substrates

At the scheduled time points, cells cultured on different substrates were fixed with 4% PFA for 20 min and then permeabilized with 0.2% Triton X-100 for 15 min. The samples were subsequently blocked with 2% bovine serum albumin (BSA) in PBS for 1 h and incubated with primary antibodies diluted in 2% BSA in a moist chamber at 4 °C overnight. The primary antibody combinations included mouse anti-cardiac troponin T (cTn) (1:200) and rabbit anti-nkx2.5 (1:200), mouse anti-α-actinin (1:200) and rabbit anti-CX-43 (1:200), or mouse anti-α smooth muscle actin (α-SMA) (1:200) and rabbit anti-vWF (1:200). After washing with PBS three times for 10 min each, the samples were incubated with secondary antibodies, including Alexa Fluor 488 donkey anti-mouse IgG (1:500) and Alexa Fluor 568 donkey anti-rabbit IgG (1:500), for 2 h in the dark at room temperature. Finally, the nuclei were stained with DAPI for 30 min, and the samples were imaged using a laser scanning confocal microscope. The positive staining areas were quantified using ImageJ software, and three independent samples were analyzed for each group.

3.1.11 Calcium Transient Assay and Synchronous Contraction of CMs Cultured on Different Substrates

To assess Ca^{2+} transients in CMs cultured on different substrates, a calcium indicator assay kit (DOJINDO Lab) was used. After 7 days of culture, all samples were stained with Fluo-4 AM reagent for 45 min at 37 °C according to the manufacturer's instructions. The cells were then washed with PBS, and calcium fluorescence signals were recorded using a fluorescence microscope (Olympus BX53, Japan). The fluorescence intensity (F) was normalized to the background intensity (F_0) during cell contraction, and the F/F_0 values were plotted over time using ImageJ software. Calcium transient parameters were calculated according to a previously reported method.[202] Ten consecutive F/F_0 peaks from three selected regions per sample were analyzed to determine the time-to-peak values, and peaks within three time periods (5 s per period) were quantified. Three independent samples were analyzed for each group. To evaluate the synchronous contraction behavior of CMs cultured on DrGOM, CMs were co-cultured with DrGOM for 7 days, and their synchronous contraction movements were recorded using a microscope (Nikon ECLIPSE Ts2R, Japan). To further verify the electrical conductivity of DrGOM, Matrigel-encapsulated CMs were first filled into the spaces of the DrGOM and cultured for 7 days, and the beating behavior of the CMs on DrGOM was then recorded using a video recording system.

3.1.12 Intravital Imaging of the Vasculature

On day 1 and day 7 after transplantation, mice were injected with a Rhodamine B isothiocyanate–dextran solution (Sigma, 1 g/L, red) through the tail vein and anesthetized with isoflurane. The fluorescent signals of the vascular structures within the dorsal window chambers were then captured using a multiphoton laser scanning microscope (Olympus FV1200MPE, Japan). On day 7 after transplantation, the mice were euthanized, and the dorsal skin tissues were harvested,

frozen, and embedded in O.C.T. (Sakura, China). The samples were subsequently sectioned into 6 μm slices for vWF immunofluorescence staining using the same protocol described above. The fluorescence signals were then imaged using a fluorescence microscope.

3.1.13 Implantation of Different Cardiac Patches in a Rat MI Model

Male SD rats (250 ± 20 g) were subjected to MI according to a previously reported method.[203] Briefly, all rats were anesthetized with isoflurane, followed by thoracotomy and ligation of the left anterior descending (LAD) artery. Fourteen days after LAD ligation, MI rats with a fractional shortening (FS) value of less than 30%, as evaluated by echocardiography, were selected and randomly divided into four groups: the MI group, the CMs injection group, the DrGOM group, and the DrGOM ECP group. For the sham group, rats underwent thoracotomy without LAD ligation. To prepare the DrGOM ECP, CMs were seeded onto DrGOM at a density of 6×10^5 cells/cm^2 and cultured for 7 days. The resulting DrGOM ECP was transplanted onto the epicardium in the infarct region, and the edges of the DrGOM were secured using 7-0 sutures. After surgery, the rats received intraperitoneal injections of penicillin sodium (2 mg/kg) and were monitored daily.

3.1.14 Echocardiographic Evaluation of Cardiac Function

The cardiac functions of all rats were evaluated using IE33 echocardiography (Vevo2100, Visual Sonics). The rats were anesthetized, and transthoracic echocardiography was performed. Short-axis views were recorded using a 40-MHz transducer and used to measure cardiac parameters. Cardiac functional parameters, including left ventricular internal diameter at end-diastole (LVIDd), left ventricular internal diameter at end-systole (LVIDs), FS, and EF, were obtained from M-mode tracings. The changes in cardiac function parameters (△FS, △EF,

△LVIDs, and △LVIDd) in different groups were calculated as the values at 4 weeks post-transplantation minus the corresponding values before transplantation.

3.1.15 Histology and Immunofluorescence Analysis

At four weeks after transplantation, all rats were euthanized, and the hearts were collected. The harvested hearts were fixed in 4% PFA overnight, frozen, and embedded in OCT (Sakura, China) for sectioning. Subsequently, 6 μm-thick sections were prepared using a Leica CM1950 cryostat. The sections were then stained with Masson's Trichrome staining kit (LEAGENE) according to the manufacturer's instructions to evaluate collagen deposition. Based on Masson's Trichrome staining images, the percentage of infarct area was defined as the ratio of the inner circumference of the fibrotic region (blue) to the total inner circumference of the left ventricle (LV). The wall thickness of the infarct region was measured using ImageJ software. Immunofluorescence staining of the cryosections was performed using the same protocol described above, and the fluorescence signals were captured using a fluorescence microscope.

3.2 Results and Discussion

3.2.1 Application of the GO ink for the DIW and the "Masked Spin Coating."

In this study, the rheological behavior of GO ink was modified through a simple heating process without the addition of any additives to enable its application in direct ink writing (DIW) (Figure 3-1). The GO macrolattice with nanoscale thickness fabricated by DIW was subsequently exposed to hydroiodic acid vapor to generate a hydrophobic rGO surface with high electrical conductivity. The combination of hydrophilic GO and hydrophobic rGO imparts humidity sensitivity to the structure. In addition, the GO ink can be directly applied in our "masked spin coating" process without further modification to fabricate microscale GO (hydrophilic)/rGO

(hydrophobic) wearable electronic devices capable of detecting multiple signals, including temperature, pH, and strain. The GO sheets in the GO powder used in this study have diameters ranging from 5 to 50 μm. The morphology of a representative GO sheet is shown in Figure 3-2, revealing an irregular two-dimensional sheet-like structure.

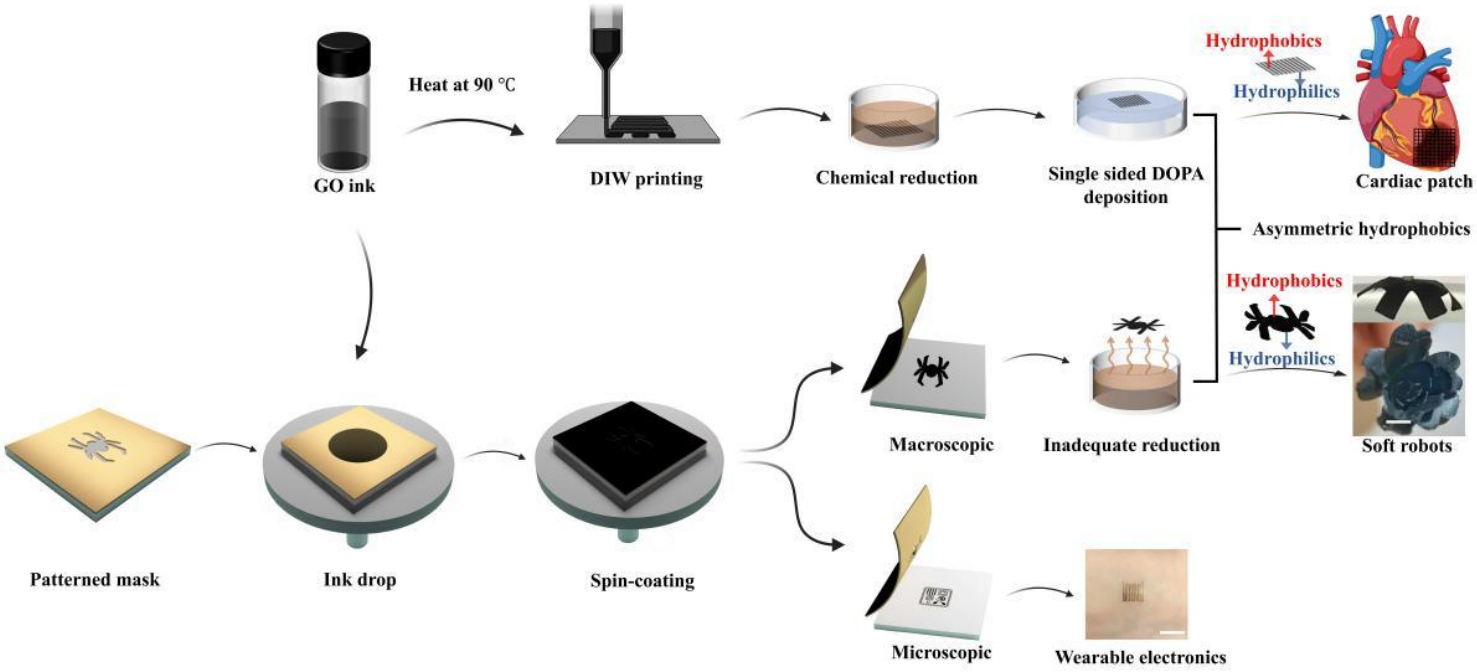

Figure 3-1 Macroscopic and microscopic graphene patterns prepared by the "masked spin coating" process.

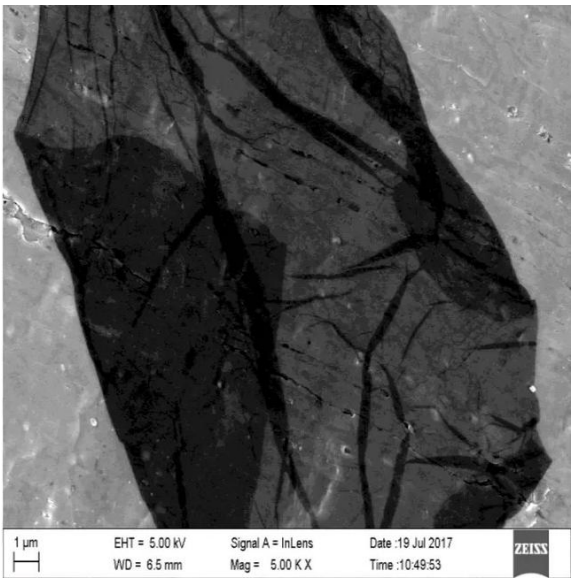

Figure 3-2 Scanning Electron Microscopy (SEM) image of a representative GO sheet.

The asymmetrical assembly strategy of integrating hydrophilic and hydrophobic interfaces into a single membrane provides a promising approach for developing actuators capable of gapless attachment to the epicardium. Considering the requirements of an ideal ECP, including high electrical conductivity and high loading capacity for CMs, a mussel-inspired PDA coating was applied to one side of the conductive rGO microlattice in this study, resulting in asymmetric surface wettability. The resulting PDA-coated (hydrophilic) rGO (hydrophobic)/GO (hydrophilic) macrolattice (DrGOM) exhibits high electrical conductivity, ultrathin thickness (~1 μm) (Figure 3-3), and excellent flexibility. The PDA coating increased the thickness of the rGO membrane from approximately 500 nm to 1 μm. The macrolattice architecture endows the DrGOM with sufficient flexibility to conform to the spherical geometry of the epicardium. Furthermore, the

humid environment of the epicardium triggers the spontaneous encapsulation of the moisture-responsive DrGOM, enabling seamless attachment to the curved epicardial surface.

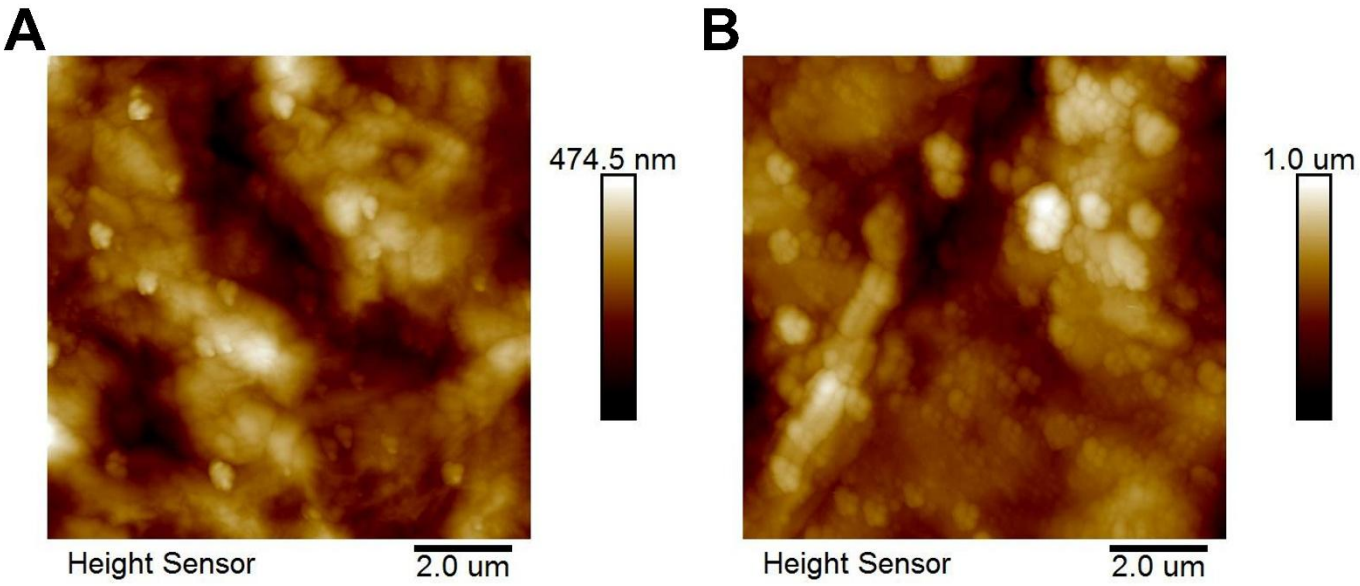

Figure 3-3 Atomic Force Microscope (AFM) images of (A) rGO microlattice and (B) PDA-coated rGO microlattice.

Appropriate rheological properties, including high viscosity (10^{-1}-10^{3} Pa·s) and shear-thinning behavior, are essential prerequisites for DIW inks.[155,204] To achieve these properties, the GO ink was heated at 90 °C for different durations to enhance the interactions between GO sheets. As a result, GO colloidal gel inks (GOCGIs) were formed, providing suitable printability for DIW. As shown in Figure 3-4A, the viscosities of all GOCGIs decreased with increasing shear rate, demonstrating their shear-thinning non-Newtonian fluid behavior. In addition, the viscosities of all GOCGIs were sufficiently high (>10^{-1} Pa·s) to allow the extruded ink to rapidly "set," thereby maintaining the printed structure. The viscosity of GOCGI increased with increasing heating time.

Longer heating durations also resulted in higher storage modulus and greater shear yield stress (Figure 3-4B). Among the tested inks, $GOCGI_{120}$ exhibited the highest viscosity, storage modulus, and shear yield stress, making it the most capable of resisting collapse of the extruded filaments caused by self-weight and surface tension, and thus showing the least smearing after extrusion. After air drying, the patterned GOCGI self-assembled into a free-standing DIW GO structure. The resulting DIW GO_{120} exhibited the finest printed line width (Figure 3-4C).

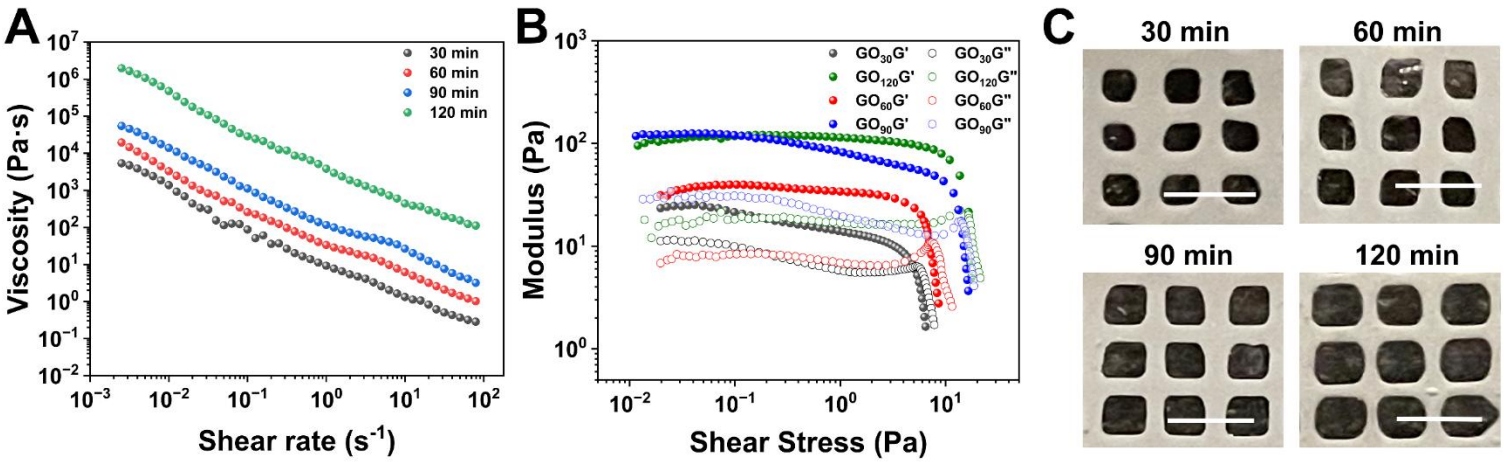

Figure 3-4 Rheological properties of graphene oxide colloidal gel inks (GOCGIs) and the resulting microlattices.

(A) Viscosity of GOCGIs as a function of shear rate. (B) Storage and loss moduli of GOCGIs as a function of the shear stress. (C) Images of direct ink writing reduced GO (DIW rGO) microlattices prepared by different GOCGIs. Scale bar: 2 mm.

In the FTIR spectrum of GO powder, the peaks at 1617 cm^{-1} corresponded to the C=C stretching vibrations of the aromatic domain (Figure 3-4A). The oxygen-containing groups (OCGs) of GO, including carboxyl, epoxy, and hydroxyl groups, contribute to several characteristic

absorption peaks: the peak at 1718 cm^{-1} corresponds to C=O stretching vibrations; the band at 1340 cm^{-1} is attributed to C–OH stretching vibrations; the peak at 1222 cm^{-1} is associated with C-O stretching vibrations; peak at 1039 cm^{-1} corresponds to C-O-C stretching vibrations; and the broad absorption band at 3360 cm^{-1} is attributed to O-H stretching vibrations. In the FTIR spectrum of GO colloidal ink, the O-H adsorption band shifted to 3198 cm^{-1} and was gradually broadened with increasing heating time. In addition, the C-OH band gradually shifted from 1340 cm^{-1} to 1374 cm^{-1} as the heating time increased. Moreover, the C-O twin peak at 1222 cm^{-1} gradually broadened, and the C-O-C band shifted from 1039 cm^{-1} to 1046 cm^{-1} during heating. These changes in the absorption characteristics related to carboxylic and hydroxyl groups, as well as O–H vibrations, indicate the formation of hydrogen bonding between hydroxyl groups on adjacent GO sheets. Therefore, the heat treatment promotes hydrogen bonding between GO sheets, contributing to the formation of GOCGIs.

The O-H peak of the DIW GO microlattice shifted to 3179 $cm^{-1,}$ and the C-O peak shifted to 1363 cm^{-1} (Figure 3-5A), indicating the presence of hydrogen bonding in the free-standing DIW GO structure. The DIW GO was chemically reduced to DIW rGO to restore electrical conductivity. In the FTIR spectrum of the DIW rGO film, the peaks at 3179 cm^{-1}, 1363 cm^{-1}, 1718 cm^{-1}, 1039 $cm^{-1,}$ and 1222 cm^{-1} associated with OCGs nearly disappeared (Figure 3-5B), indicating effective reduction. As a result, the resistance of the DIW rGO significantly decreased to 6.41 ± 0.33 **Ω** (Figure 3-5C). The chemical reduction had no significant effect on Young's modulus or flexibility but increased the ultimate strength. The Young's modulus and flexibility of the rGO film were comparable to those of the GO film (Figure 3-5D, E), while the rGO film exhibited a significantly higher ultimate strength than the GO film (Figure 3-5D). Although the DIW rGO microlattice displayed lower ultimate strength than the film structure, it exhibited higher flexibility (Figure 3-

5D, E). The high flexibility provided by the unique DIW microlattice architecture enables gapless encapsulation of spherical structures (Figure 3-5F). In contrast, the film structure cannot conform well to spherical surfaces despite its higher ultimate strength.

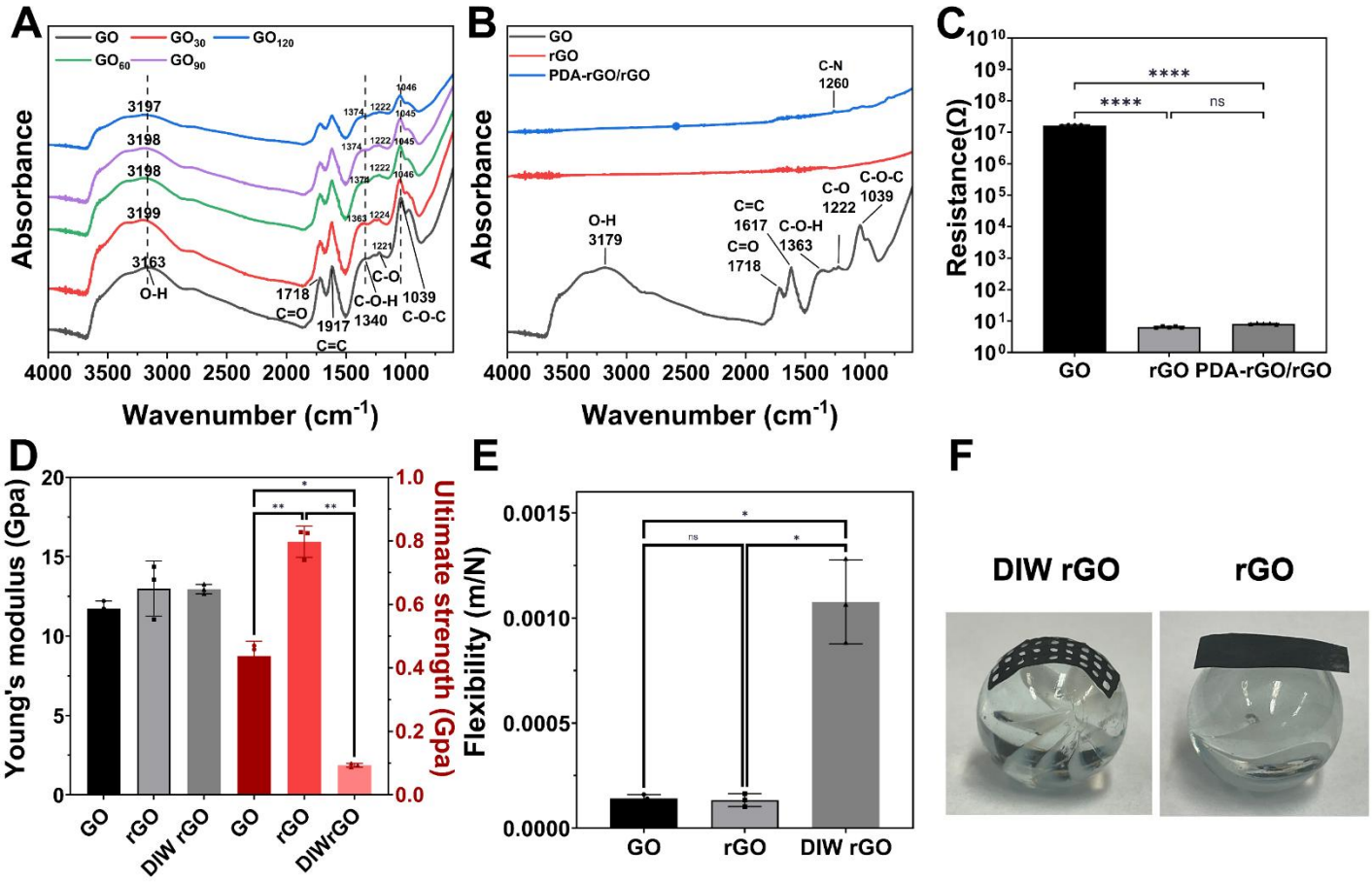

Figure 3-5 Characterization of graphene oxide colloidal inks, GO, rGO, PDA-rGO/GO films, and DIW printed microlattice

(A) FTIR spectra of GOCGIs. (B) FTIR spectra of DIW GO, DIW rGO, and PDA-rGO. (C) Resistances of DIW GO_{120}, DIW rGO, and PDA-rGO/rGO. (D) Young's moduli and ultimate strengths of the GO film, rGO film, and DIW rGO microlattices. (E) Flexibilities of the GO film,

rGO film, and DIW rGO microlattices. (F) Images showing the encapsulation of a wet sphere by a DIW rGO lattice and rGO film. (*p < 0.05, **p < 0.01, ***p < 0.001, ****P < 0.0001)

On the one hand, the removal of hydrophilic OCGs improved electrical conductivity; on the other hand, it reduced hydrophilicity.[205] Mussel-inspired dopamine can form strong adhesion on various surfaces through hydrogen bonding via its catechol groups and can spontaneously assemble into a PDA thin film through alkaline (pH = 8.5)-induced oxidation. Therefore, a PDA coating was deposited onto the rGO surface to restore the impaired hydrophilicity. High-energy hydrophilic surfaces are known to promote cell adhesion and proliferation.[206] In the FTIR spectrum of the PDA coated rGO film (PDA rGO), a new peak appeared at 1260 cm^{-1} corresponding to C-N stretching vibration, confirming the successful deposition of PDA (Figure 3-6B). As shown in Figure 3-6A, chemical reduction increased the water contact angle from 33.84° ± 1.95° to 80.34° ± 5.68°, while the PDA coating reduced the contact angle to 47.4° ± 9.81°, indicating that PDA significantly improved hydrophilicity. In addition, PDA modification enhanced hydrophilicity without significantly compromising conductivity. The resistance of PDA-rGO/rGO was 8.14 ± 0.37 Ω, which is not significantly different from that of DIW rGO (Figure 3-6C). The PDA coating slightly reduced the Young's modulus and ultimate strength of the rGO film (Figure 3-6B), while the flexibility of the rGO film was also moderately reduced after PDA coating (Figure 3-6C). Overall, the combination of GO ink-based DIW printing and subsequent PDA modification produced a soft, ultra-thin, flexible, conductive, and biocompatible cardiac patch suitable for MI repair.

The patterned mask plays an important role in screen printing and lithography. Inspired by this concept, we developed a "masked spin coating" method, in which both microscale and

macroscale patterns can be fabricated using a low-cost die-cutting machine. In this process, GO ink was spin-coated onto a mask-covered substrate to fabricate microscale wearable electronics as well as macroscale free-standing soft actuators. The patterned GO structures were subsequently exposed to hydroiodic acid vapor for different durations to create GO/rGO bilayers with tunable functionalities. In the masked spin-coating process, GO ink was directly deposited onto a substrate covered with a patterned mask without any preprocessing steps (Figure 3-1). Similar to GOCGIs, the GO ink self-assembled into a thin film on the substrate surface through hydrogen bonding and $\pi - \pi$ stacking interactions during air drying. The resulting thin film exhibited a chemical profile similar to that of the DIW GO film (Figure 3-5B and Figure 3-6D). The GO sheets forming the thin film displayed microscale wrinkles (Figure 3-6E), which arise from the stacking and collapse of GO sheets during air drying under non-pressurized conditions, unlike vacuum filtration. After drying, the mask was removed, leaving patterned GO thin films on the substrate. These films were then exposed to hydroiodic acid vapor for different durations to achieve varying degrees of reduction. In the FTIR spectra, the intensities of peaks associated with OCGs gradually decreased with increasing exposure time (Figure 3-6D), confirming the successful removal of OCGs. The removal of OCGs restored the graphene sp^2 domains, thereby increasing the conductivity of the reduced GO film. Consequently, the conductivity of the GO film reflects the extent of reduction. The sheet resistance of the GO film sharply decreased from 53.87 ± 1.74 KΩ/sq to 0.38 ± 0.06 KΩ/sq initially and then reached a plateau when the exposure time exceeded 120 min (Figure 3-6F). Since the exposure time had the greatest impact on conductivity when it was below 120 min, the actuation and sensing behaviors of GO/rGO_{10}, GO/rGO_{30}, GO/rGO_{60}, and GO/rGO_{90} were further investigated.

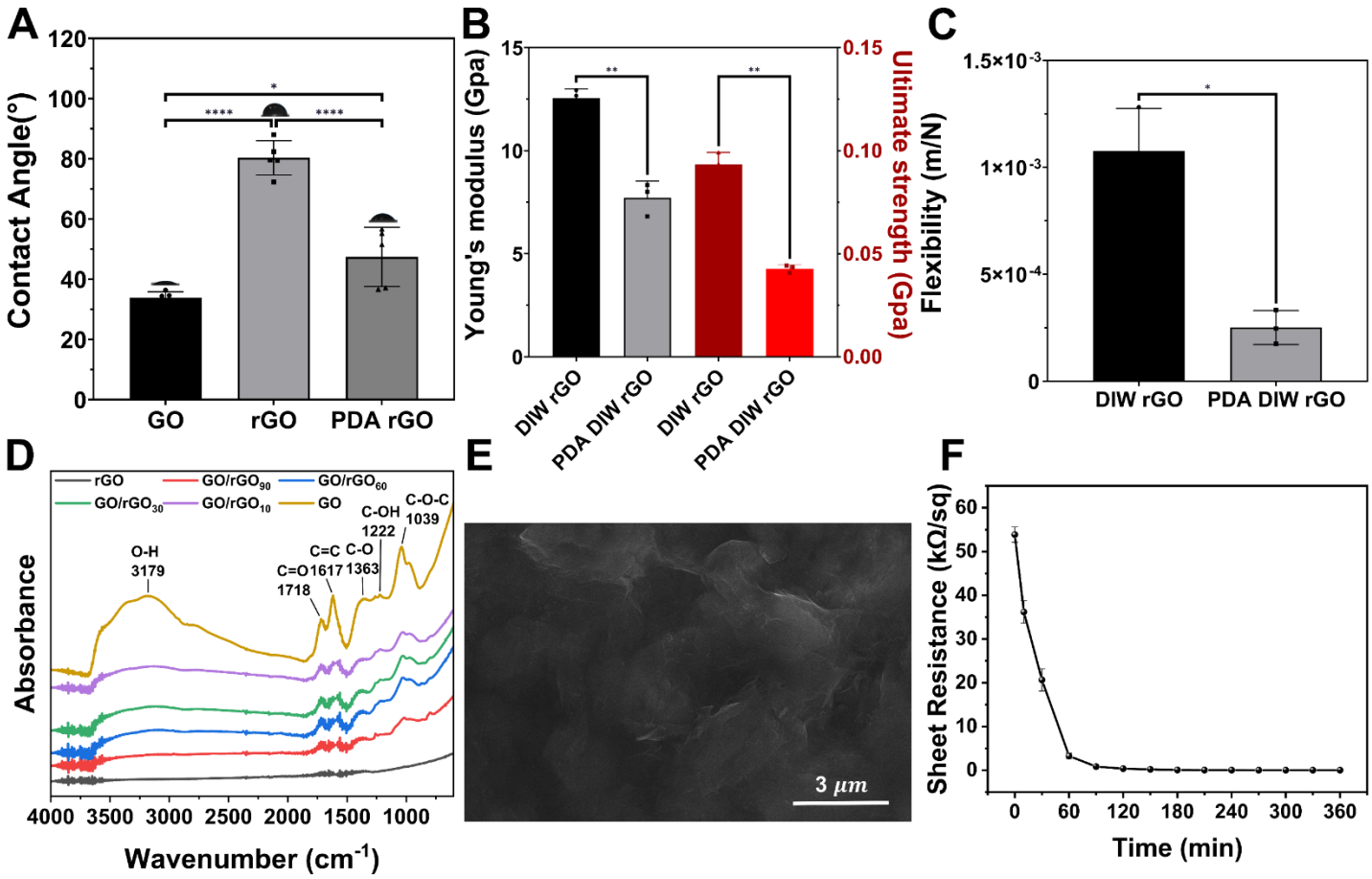

Figure 3-6 Characterization of GO, rGO, PDA-rGO, GO/rGO films, and DIW printed microlattice

(A) Water contact angles of DIW GO_{120}, DIW rGO, and PDA rGO. (B) Young's modulus and ultimate strength of DIW rGO and DIW PDA rGO. (C) Flexibility of DIW rGO and DIW PDA rGO. (D) FTIR spectra of GO, GO/rGO_{10}, GO/rGO_{30}, GO/rGO_{60}, GO/rGO_{90}, and rGO patterns. (E) SEM image of the GO pattern prepared by masked spin coating. (F) Sheet resistance of GO, GO/rGO_{10}, GO/rGO_{30}, $GO/_{rGO60}$, GO/rGO_{90}, and rGO patterns. (*p < 0.05, **p < 0.01, ***p < 0.001, ****P < 0.0001)

3.2.2 Soft Actuator Fabricated by "Masked Spin Coating"

Hydroiodic acid vapor required time to penetrate the GO film. Therefore, insufficient exposure time produced a unique anisotropic distribution of OCGs across the thickness of the GO film, resulting in the formation of a GO/rGO bilayer structure. While the hexagonal carbon lattice of graphene interacts weakly with water molecules through van der Waals forces, the OCGs can strongly adsorb water molecules via hydrogen bonding.[207] Water molecules adsorbed by OCGs increase the interlayer spacing between adjacent GO sheets, leading to an increase in the thickness of the GO layer. When the environmental relative humidity (RH) increases, the GO layer adsorbs water molecules and expands, whereas the rGO layer remains relatively unchanged because of its weak interaction with water molecules. As a result, moisture-driven deformation occurs in the GO/rGO bilayer. Ribbon-structured GO/rGO bilayers with different reduction extents were fabricated using the masked spin-coating technique. Saturated salt solutions were employed to establish different environmental RH levels, and the GO/rGO bilayers were placed in a closed chamber containing these solutions to evaluate their responses to RH changes. The bilayers responded rapidly to variations in RH and reached a stable state within approximately 150 min. Because the chamber also required time to reach equilibrium RH, the curvature of the GO/rGO bilayers was recorded 150 min after placement in the chamber, which included both the stabilization time of the chamber and the response time of the bilayers. As the environmental RH increased from 11% to 90%, the curvature of all GO/rGO bilayers increased (Figure 3-7A–D). In addition, bilayers with longer hydroiodic acid exposure times exhibited higher curvature at the same RH level, with the maximum curvature (628 m^{-1}) observed for GO/rGO_{90} at 99% RH (Figure 3-7E). When the RH decreased to a lower level, the GO/rGO bilayers returned to their original curvature. The actuation behavior remained stable over multiple bending and recovery cycles, with

GO/rGO_{10} and GO/rGO_{30} showing consistent curvature values at 55% RH, while GO/rGO_{60} and GO/rGO_{90} exhibited gradual upward shifts in curvature during repeated testing cycles (Figure 3-7F).

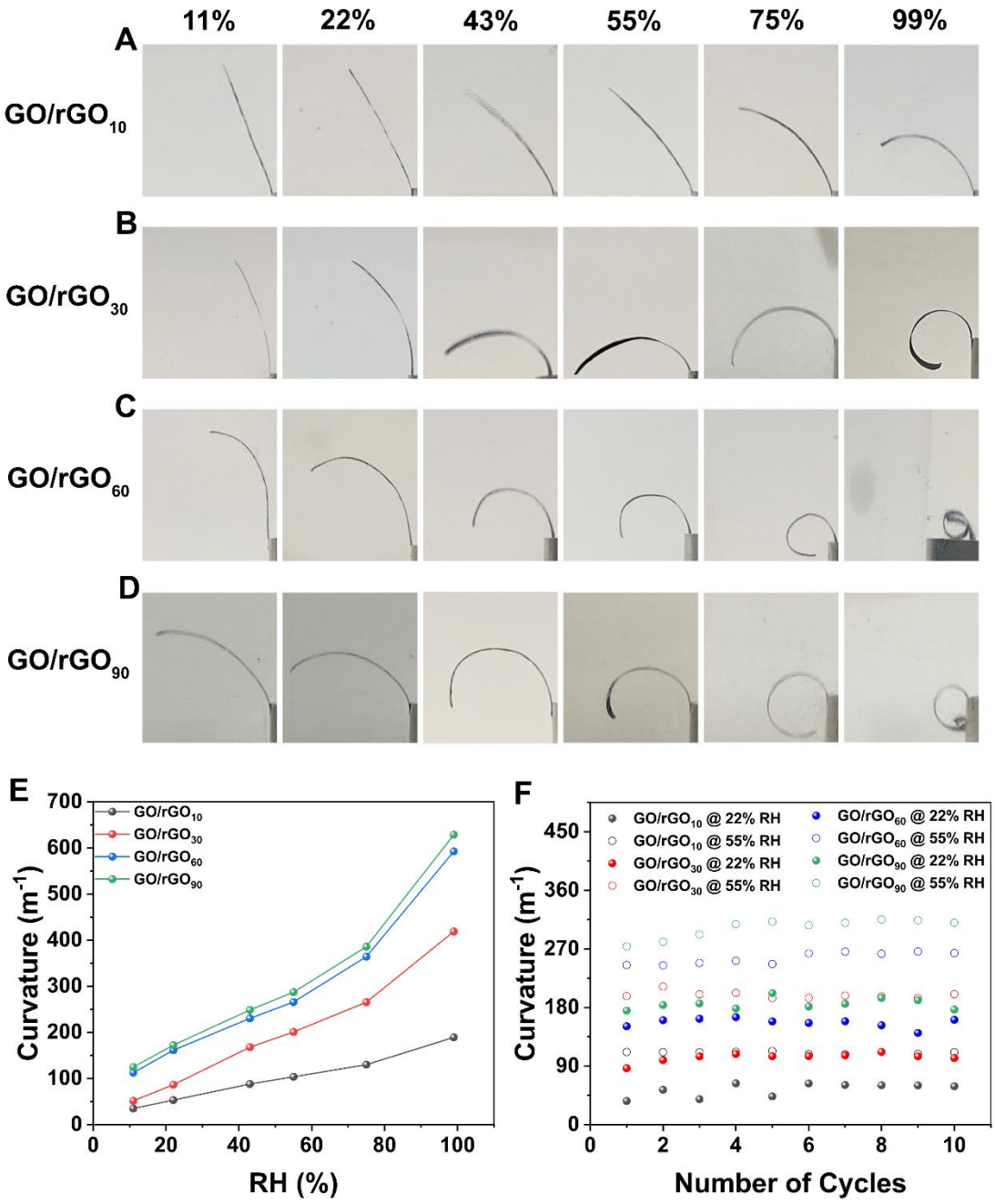

Figure 3-7 Moisture-driven actuation of GO/rGO bilayers.

(A-D) Response of different GO/rGO bilayers to different relative humidity levels. (E) Quantitative data obtained from A-D. (F) Cyclic stability of GO/rGO_{10}, GO/rGO_{30}, GO/rGO_{60}, and GO/rGO_{90} actuators.

The curvature of the GO/rGO bilayer could be precisely controlled by tuning the hydroiodic acid exposure time. The bending angle of GO/rGO30 at 99% RH ranged between 180° and 360°, which is suitable for robotic gripper applications. Accordingly, a GO/rGO_{30} gripper was fabricated through the masked spin coating method. The GO/rGO_{30} gripper was able to perform a series of tasks, including picking up, holding, and releasing objects (Figure 3-8A). In contrast, GO/rGO_{60} could bend by more than 360° at 99% RH. As shown in Figure 3-8B, the GO/rGO_{60} strap was able to retrieve objects in a manner similar to the prey-capturing motion of a frog's tongue. The humidity-responsive GO/rGO structure can also be incorporated into a DIW-printed GO microlattice, enabling the flexible microlattice to undergo spontaneous encapsulation when approaching the humid epicardium. The increase in local humidity generated by human skin can also induce curvature in the DIW GO/rGO macrolattice. As shown in Figure 3-9, when a human finger approached the GO surface of the GO/rGO90 macrolattice, the structure bent noticeably; however, no significant deformation occurred when the finger approached the rGO surface.

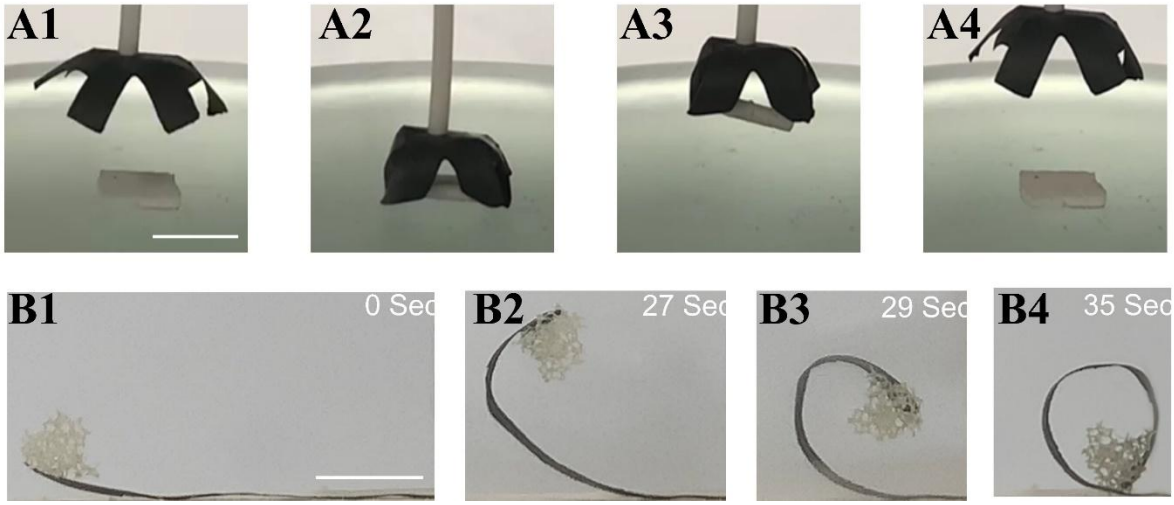

Figure 3-8 Application of different GO/rGO bilayers.

(A) Gripper made by GO/$rGO_{30,}$ grabbing and releasing a weight. Scale bar = 1cm. (B) Cargo lifting of GO/rGO_{60}. Scale bar = 2.5 mm

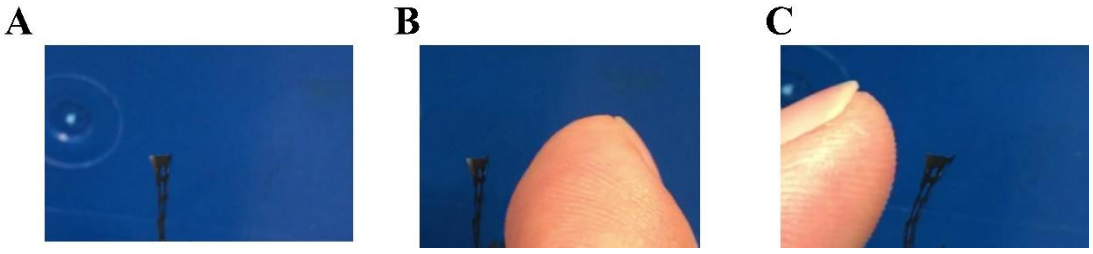

Figure 3-9 Photographs showing the actuation of DIW GO/rGO in response to human skin's humidity.

(A) Side view of DIW GO/rGO. (B) No response if an Index finger is approaching the rGO surface. (C) Bend if an index finger is approaching the GO surface.

3.2.3 Wearable Sensing Modules Fabricated by "Masked Spin Coating"

The response speed of the rGO and GO/rGO bilayer sensing modules to temperature changes was comparable to that of a commercial thermocouple (Figure 3-10A–F). The sensing modules and the thermocouple exhibited nearly identical response times to temperature variations. All sensing modules demonstrated high repeatability, as the resistance–temperature response curves remained highly consistent over five testing cycles (Figure 3-10A–D).

The temperature coefficient of resistance (TCR), which is commonly used to evaluate the sensitivity of temperature sensors,[208] is defined as

$$\boldsymbol{TCR = \frac{\Delta R}{R_0 \Delta T} \times 100\%} \qquad \textbf{Equation 3-4}$$

where $\Delta R = R - R_0$, R is the measured resistance, R_0 is the original resistance, and ΔT is the temperature change during measurement.

The rGO, GO/rGO$_{90}$, GO/rGO$_{60}$, and GO/rGO$_{30}$ exhibited negative temperature coefficients of resistance. As shown in Figure 3-10A-F, the resistance of these sensing modules decreased as the temperature increased. In contrast, the sensitivity of GO/rGO$_{10}$ to temperature was nearly two orders of magnitude higher than that of other sensing modules (Figure 3-10E and F). However, the real-time response of GO and GO/rGO$_{10}$ was not monotonic. During heating, the resistance of the GO and GO/rGO$_{10}$ sensing modules initially decreased slightly within the first 10–30 s, followed by an increase until reaching a stable value. During cooling, the resistance first decreased within approximately 5 s, then increased abruptly, and finally decreased again until stabilization. Based on the stabilized resistance values, GO and GO/rGO$_{10}$ showed a positive TCR. The sensitivity of the sensing modules decreased with increasing reduction extent (Figure 3-11A). Among the sensing modules with monotonic responses, GO/rGO30 exhibited the highest

sensitivity, with a TCR of 0.74% / °C, while also demonstrating good reliability. The sensitivity of GO/rGO30 during the cooling process differed from that during heating by only 0.02% / °C. In contrast, GO/rGO90 showed significant variation between heating and cooling cycles, indicating pronounced thermal hysteresis.

The conductivity (σ) of a material is given by

$$\boldsymbol{\sigma = |e| n u_e} \qquad \textbf{Equation 3-5}$$

where $|e|$ is the absolute quantity of one charge carrier (1.6×10^{-19} C), n is the charge carrier density, and u_e is the charge carrier mobility.[209]

For pristine graphene, rGO, and GO/rGO sensing modules, which behave as semiconductors, the intrinsic charge carrier concentration (n_i) depends on temperature and can be expressed as

$$\boldsymbol{n_i(T) = 2\left(\frac{2\pi KT}{h^2}\right)^{\frac{3}{2}}\left(m_n^* m_p^*\right)^{\frac{3}{4}} e^{\left(\frac{-E_g}{2KT}\right)}} \qquad \textbf{Equation 3-6}$$

where h is Planck's constant, K is the Boltzmann constant, m_n^* is the effective mass for an electron, m_p^* is the effective mass for a hole, and E_g is the bandgap energy.

Accordingly, the intrinsic carrier concentration increases with increasing temperature.[210] Carrier mobility in graphene is influenced by several scattering mechanisms, including Coulomb scattering, impurity scattering, and phonon scattering.[211] However, the exact relationship between the charge carrier mobility and temperature is ambiguous. Phonon scattering limits carrier mobility and leads to a linear temperature dependence of resistivity in single-layer graphene ($\rho \sim T, T \geq 50$ K) when the phonon scattering event is dominants. [212,213] The Coulomb scattering dominates in the bilayer/tri-layer graphene, and the charge carrier mobility increases with temperature when the

Coulomb scattering dominates at low carrier concentrations.[214] Impurity scattering decreases carrier mobility, and the interaction between carriers and impurities decreases along with temperature. Defect scattering due to an imperfect honeycomb structure also imposes a positive temperature-dependent hindrance on the mobility of carriers. The OCGs in rGO, GO/rGO, and GO impede the carrier mobility through defect scattering and impurity scatterings. In addition, the OCGs reduced the concentration of the intrinsic charge carrier. The paths for charge carriers of GO and GO/rGO were severely disrupted by the overwhelming amounts of OCGs, and the intrinsic charge carrier concentrations of GO and GO/rGO_{10} were extremely low because of the existence of OCGs. The temperature-dependent electron-phonon and defect scattering dominated the effect on conductivity. Thus, the GO and GO/rGO_{10} had a positive TCR. The unusual behavior of the initial response to the temperature change can be attributed to the short-time dominance of the temperature-dependent charge carrier concentration. The rGO and other GO/rGO sensing modules had fewer OCGs. Accordingly, the temperature-dependent carrier concentration dominated the effect on conductivity. Thus, the rGO and other GO/rGO sensing modules had a negative TCR. In contrast, OCGs such as carboxyl groups offer charged impurities, and the concentration increases along with the temperature. The effect of the temperature-dependent charged impurity concentration can cause an extra change in the conductivity of rGO and other GO/rGO sensing modules. Thus, the GO/rGO_{30} was the most sensitive among monotonic sensing modules because it contains the largest amount of OCGs. Linear fitting between relative resistance change and temperature showed limited accuracy. GO/rGO_{60} exhibited the best fitting during the cooling cycle (R^2 = 0.995), and the poorest fitting during the heating cycle (R^2 = 0.951). The TCR model is generally more suitable for conductors, such as metals, whose resistivity (ρ) varies linearly with temperature ($\rho = \rho_0 + \alpha T$) due to temperature-dependent defect and phonon scatterings.[209]

Therefore, the relationship between conductivity (σ) to temperature was further studied. The relationship between the conductivity and resistance can be expressed as

$$\frac{\Delta\sigma}{\sigma_0} \propto \frac{R_0}{R} - 1 \qquad \text{Equation 3-7}$$

where $\Delta\sigma = \sigma - \sigma_0$, σ is the conductivity at a given temperature, and σ_0 is the initial conductivity. As shown in Figure 3-11B, the linear fittings between relative conductivity change ($\frac{R_0}{R} - 1$) and temperature produced significantly better correlations.

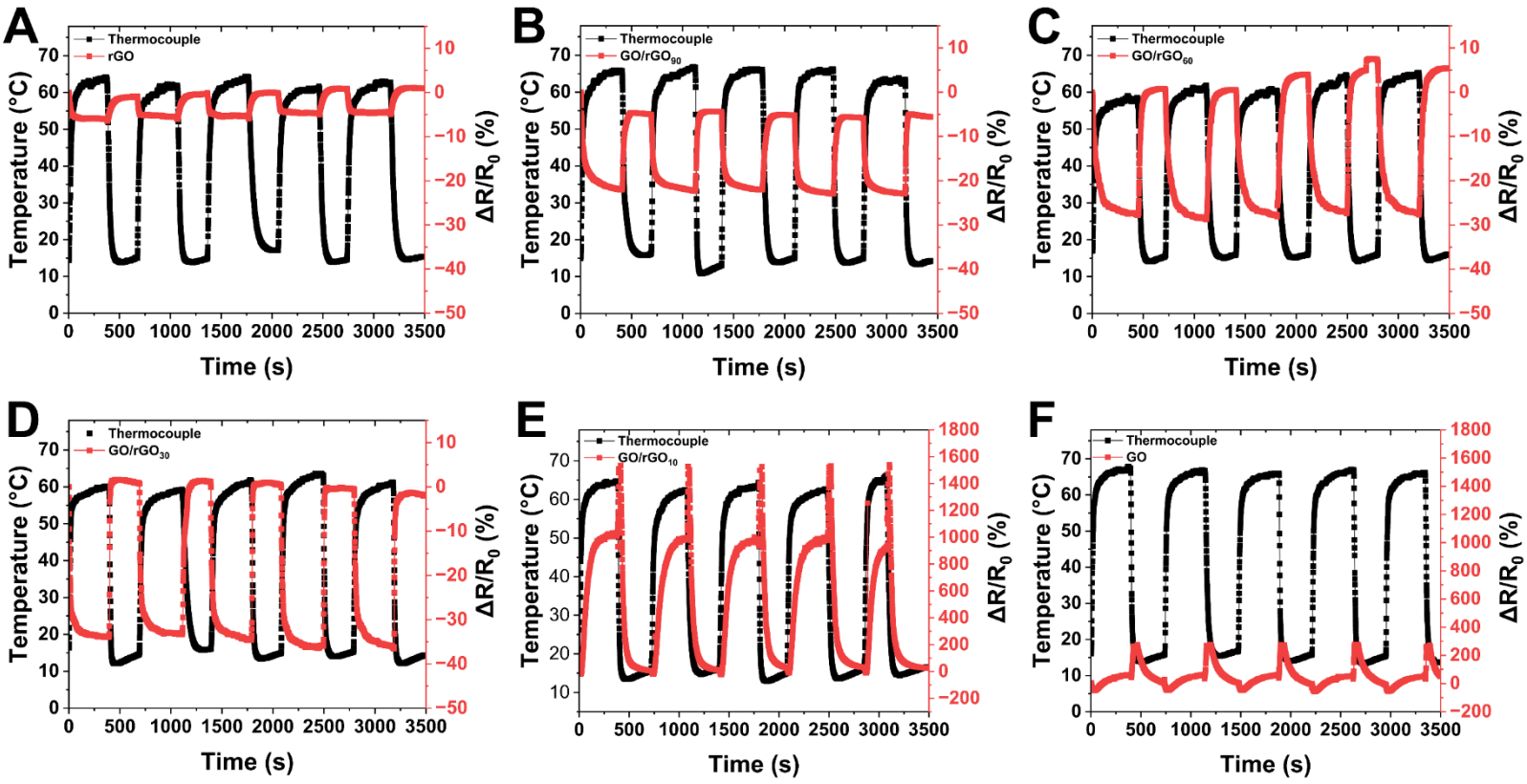

Figure 3-10 Temperature sensing of GO/rGO bilayers.

(A-F) Real-time responses of different GO/rGO bilayers and a commercial thermocouple to temperature changes from 13 °C to 66 °C.

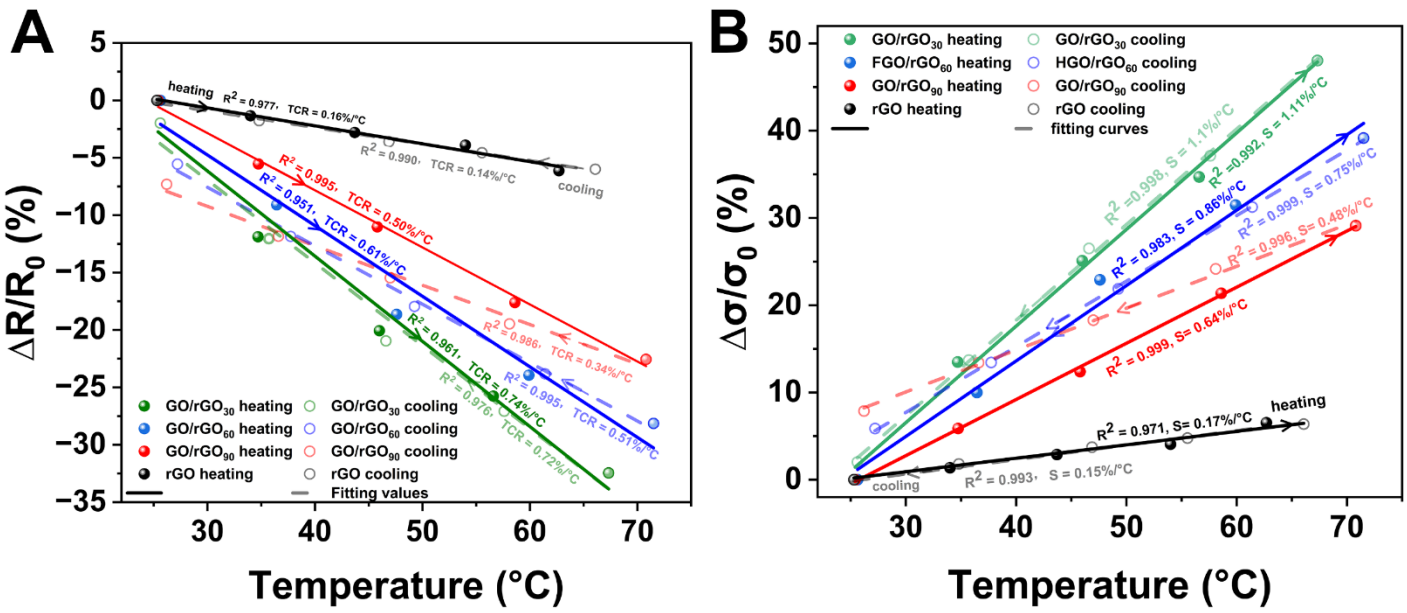

Figure 3-11 Linear fitting of temperature sensing performance of GO/rGO bilayers.

(A) Relative resistance responses of different GO/rGO bilayers to stepped temperature changes. (B) Relative conductivity responses of different GO/rGO bilayers to stepped temperature changes.

The carboxyl and hydroxyl groups on the pH-sensing module can react with H^+ ions in solution according to the following reaction:

$$-COO^-/-O^- + H^+ \rightleftharpoons -COOH/-OH \qquad \textbf{Equation 3-8}$$

According to the Nernst equation, the response of the pH-sensing module relative to the reference electrode is given by

$$E = E^{\ominus} + 0.0592\, lg[H^+] \qquad \textbf{Equation 3-9}$$

where $E^{\ominus}$ is the standard electrode potential of the pH sensing module, E is the measured potential of the sensing module relative to the reference electrode, and $[H^+]$ is the H^+ concentration.

The maximum theoretical sensitivity of the pH-sensing module is 0.0592 mV/pH. The rGO sensing module exhibited an undetectable response to pH (Figure 3-12A, B), as most oxygen-containing groups (OCGs) were removed during chemical reduction. GO/rGO_{90} exhibited the highest sensitivity (0.0443 mV/pH) and linearity (R^2 = 0.997), while GO/rGO_{60} showed a similar sensitivity (0.04358 mV/pH). Both GO/rGO_{90} and GO/rGO_{60} demonstrated near-Nernstian responses. In contrast, GO/rGO_{30} exhibited the lowest sensitivity and linearity. GO/rGO_{30} tended to partially disassemble in aqueous solution due to strong interactions between OCGs and water molecules. As a result, the standard electrode potential $E^{\ominus}$ of GO/rGO_{30}, which is expected to remain constant, may vary during the measurement. In comparison, GO/rGO_{90} remained more stable in aqueous solution and therefore exhibited the highest sensitivity and linearity. The strain sensitivity of the sensing modules increased with increasing reduction extent (Figure 3-12C, D). The strain response primarily originates from changes in conductivity caused by elastic deformation and variations in the contact interactions between rGO sheets. Sensing modules with higher reduction extents contain more rGO sheets and therefore exhibit greater sensitivity to strain. Among all sensing modules, the rGO sensor showed the highest strain sensitivity and displayed a linear response up to 4% strain with a gauge factor (GF) of 25.50.

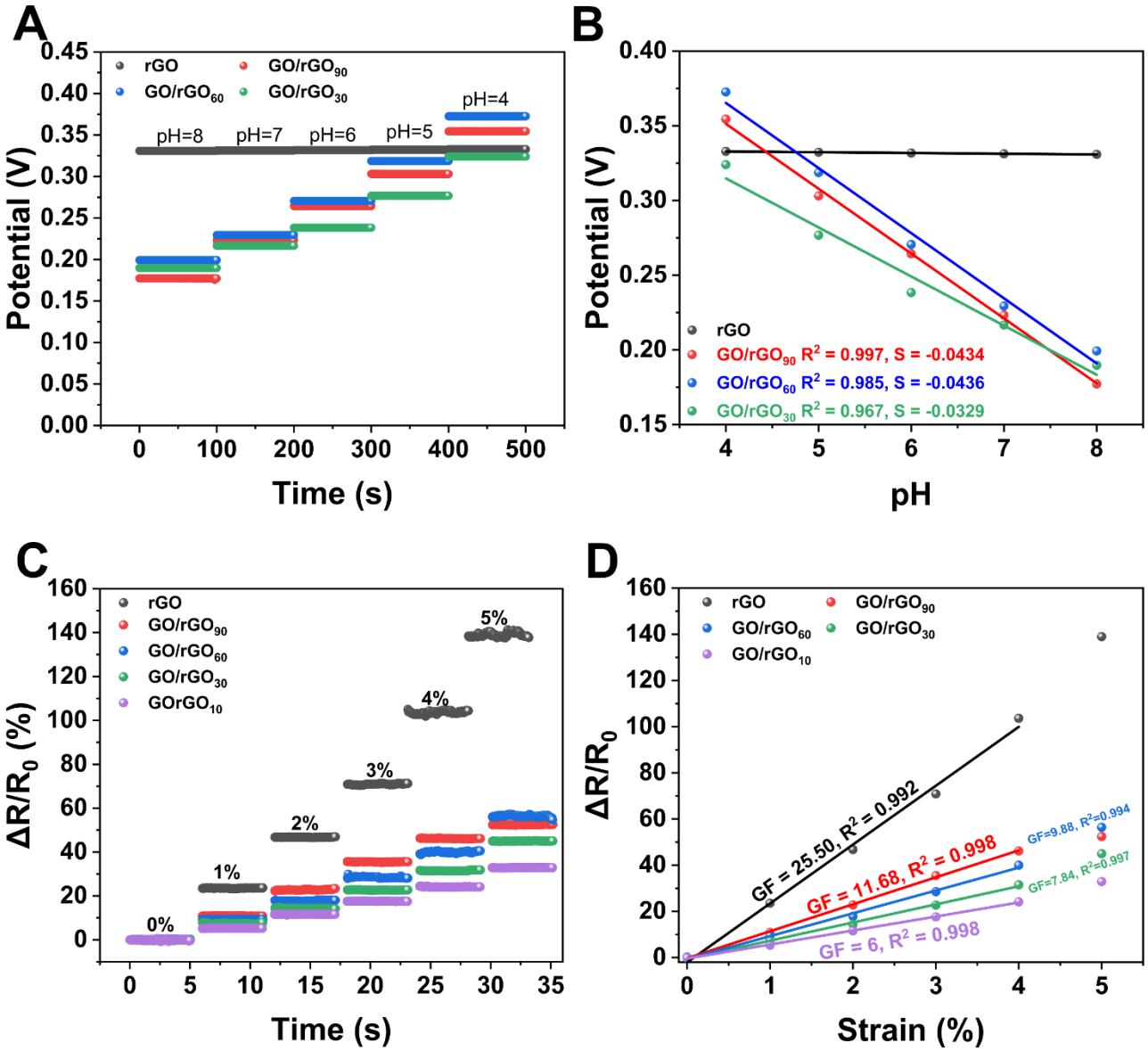

Figure 3-12 PH sensing of GO/rGO bilayers.

(A) Potentials of different GO/rGO bilayers immersed in different pH buffers measured relative to an Ag/AgCl reference electrode. (B) Linear relationships between the potential of different GO/rGO bilayers and pH. (C) Relative resistance changes of rGO under different applied strains. (D) Linear relationships between the relative resistance change of rGO and strain.

3.2.4 Cell Attachment, Viability, and Proliferation of CMs cultured on DrGOM

Because GO/rGO_{90} exhibited the highest sensitivity to moisture, and PDA deposition on the rGO surface had negligible effects on its conductivity and moisture sensitivity, GO/rGO_{90} was selected as the printing ink to fabricate the PDA-coated rGO/GO microlattice (DrGOM) cardiac patch for infarcted myocardium repair. CMs cultured on the PDA-coated rGO surface of DrGOM showed a high survival rate of over 80% during the 14-day culture period (Figure 3-13A). The high retention of CMs on DrGOM was mainly attributed to the hydrophilic interface and the strong adhesive properties of dopamine.[215] CMs cultured on DrGOM exhibited extensive cellular spreading within the first 24 h after seeding. By day 3, the CMs had spread across the entire field of view, demonstrating DrGOM's excellent capability to support CM adhesion, growth, and proliferation. This behavior primarily arises from dopamine acting as a robust anchoring mediator between the cells and the substrate.[201] Notably, 3D imaging of phalloidin-stained cytoskeletons revealed that the DrGOM surface supported the growth of a dense layer of CMs (Figure 3-13B), demonstrating the exceptional cell-loading capacity of this ultrathin conductive membrane. SEM analysis confirmed complete surface coverage by CMs on the DrGOM membrane after 7 days of culture (Figure 3-13C). In addition, myocardium-like tissue and intercellular junctions were clearly observed. Given the established use of iPSC-CMs in cardiac patches for MI treatment in both preclinical and clinical studies, we investigated DrGOM's effect on human iPSC-CM proliferation. Immunostaining confirmed the expression of characteristic cardiac proteins, including cardiac troponin T (cTn), which is a definitive marker for CMs, and nkx2.5, which is a cardiac progenitor marker (Figure 3-13D). The cells sustained a high proliferation rate at day 3 and day 7 after culturing (Figure 3-13E). Ideal ECPs preserve seeded cell viability and proliferation capacity,

thereby enhancing ventricular function while reducing fibrosis and scar formation in injured myocardium.[9] DrGOM demonstrated optimal performance by meeting these critical criteria, positioning it as a promising ECP for myocardial infarction (MI) repair. Furthermore, 3D imaging of phalloidin-stained cytoskeletons revealed that the DrGOM surface supported the formation of a dense CM layer (Figure 3-13B), highlighting the exceptional cell-loading capacity of this ultrathin conductive membrane. SEM analysis further confirmed that the DrGOM membrane was fully covered by CMs after 7 days of culture (Figure 3-13C), with myocardium-like tissue structures and intercellular junctions clearly observed. Considering the widespread use of induced pluripotent stem cell-derived cardiomyocytes (iPSC-CMs) in cardiac patches for MI treatment in both preclinical and clinical studies, the effect of DrGOM on human iPSC-CM proliferation was further investigated. Immunostaining confirmed the expression of characteristic cardiac proteins, including cardiac troponin T (cTn), a definitive CM marker, and nkx2.5, a cardiac progenitor marker (Figure 3-13D). The cells maintained a high proliferation rate at both day 3 and day 7 after culture (Figure 3-13E). An ideal epicardial cardiac patch (ECP) should maintain the viability and proliferative capacity of seeded cells, thereby improving ventricular function while reducing fibrosis and scar formation in injured myocardium.9 DrGOM satisfies these key requirements, highlighting its potential as a promising ECP for myocardial infarction (MI) repair.

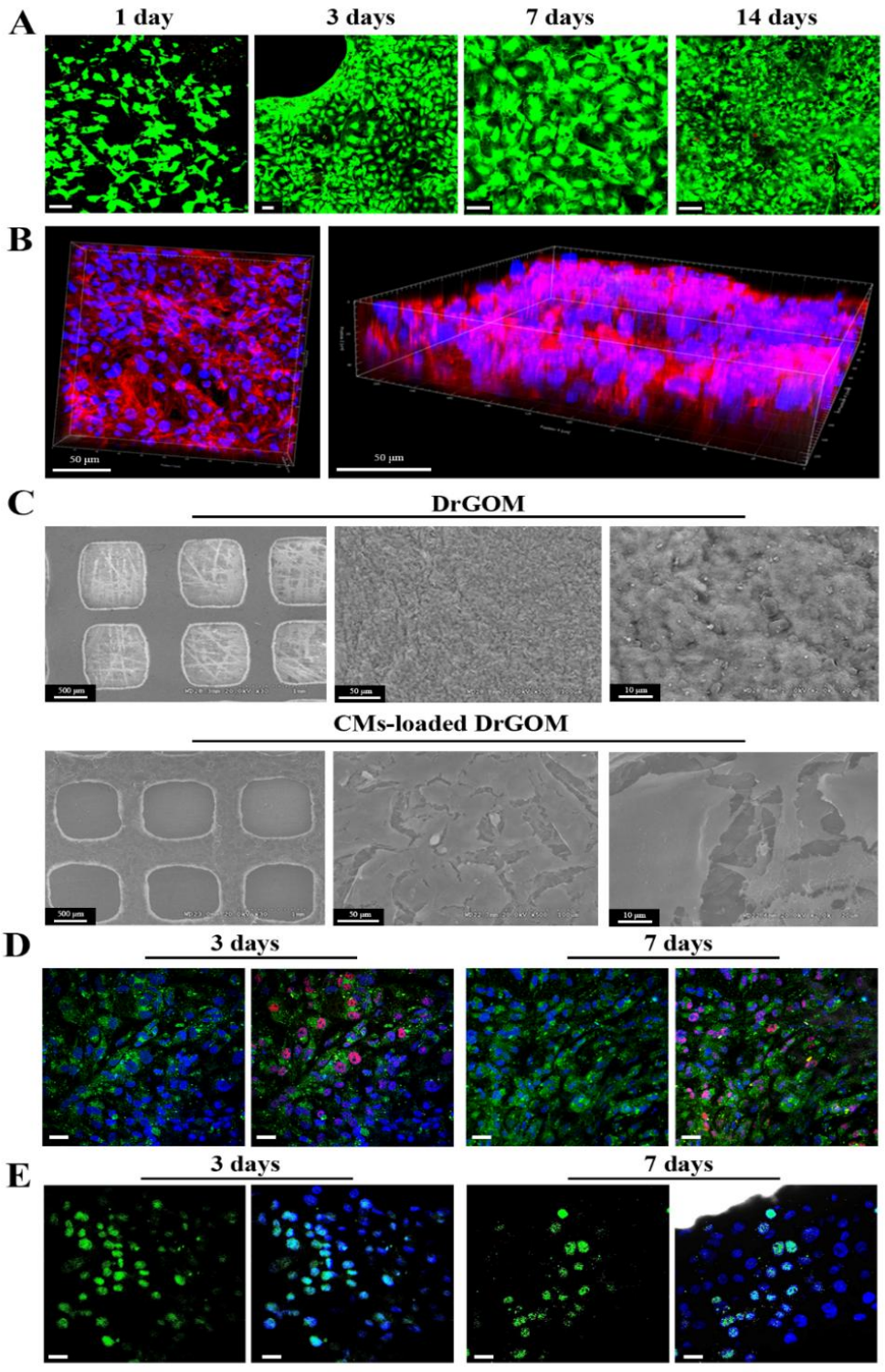
A
1 day
3 days
7 days
14 days
B
50 μm
50 μm
C
DrGOM
500 μm
50 μm
10 μm
CMs-loaded DrGOM
500 μm
50 μm
10 μm
D
3 days
7 days
E
3 days
7 days

Figure 3-13 PDA-coated rGO/GO microlattice (DrGOM) facilitates the adhesion, viability, and growth of CMs.

(A) Representative live/dead staining images of CMs cultured on DrGOM for 14 days. Scale bar: 50 μm. (B) Three-dimensional views of the cytoskeleton of CMs on DrGOM after 7 days of culture, stained with phalloidin (red) and DAPI (blue). (C) SEM images of pure DrGOM and CM-loaded DrGOM after 7 days of culture. (D) Fluorescence micrographs showing the expression of cardiac troponin T (cTn^+) (green) and $nkx2.5^+$ (red) hCMs cultured on DrGOM at days 3 and 7. The left images show the merged fluorescence of cTn and DAPI (blue), while the right images show the merged fluorescence of cTn, nkx2.5, DAPI, and the bright-field images. Scale bar: 20 μm. (E) Representative fluorescence micrographs of $Ki67^+$ (green) hCMs cultured on DrGOM at days 3 and 7. The right images show merged Ki67, DAPI (blue), and bright-field images. Scale bar: 20 μm.

3.2.5 DrGOM-Induced Calcium Transients in CMs and Electrical Signal Propagation Between CMs.

The functional maturation of CMs is characterized by the development of key electrophysiological properties, including the expression of cardiac-specific proteins, calcium current activity, and synchronous contraction behavior. Immunofluorescence analysis of cardiac-specific proteins, including α-actinin for sarcomeres and CX-43 for gap junctions, showed that CMs cultured on glass slides exhibited randomly dispersed sarcomeres on day 3, whereas CMs cultured on DrGOM displayed well-aligned sarcomeric bands and clearly defined intercellular junctions (Figure 3-14A). After 7 days of culture, CMs on DrGOM exhibited pronounced

sarcomeric anisotropy with well-defined striations and mature intercellular junction formation, and quantitative analysis revealed significantly higher expression levels of α-actinin and CX-43 in CMs on DrGOM compared with those on glass slides (Figure 3-14B, E). Intracellular calcium dynamics were monitored using the fluorescent Ca^{2+} indicator Fluo-4 AM, enabling real-time visualization of calcium transients in CMs cultured on different substrates. As shown in Figure 3-14C and D, CMs cultured on DrGOM exhibited synchronized and rhythmic Ca^{2+} transients by day 7, whereas CMs on glass substrates displayed asynchronous calcium puffs with spatially heterogeneous frequencies. Quantitative analysis further demonstrated that CMs cultured on DrGOM exhibited faster calcium transient kinetics, characterized by shorter time-to-peak values and higher transient frequencies within 5 s intervals compared with CMs on glass slides (Figure 3-14F, G). The alignment of sarcomeres, formation of intercellular junctions, and coordinated calcium transients are critical for efficient excitation–contraction coupling and CM maturation.[216] After CMs were co-cultured with DrGOM for 7 days, synchronous contractions were observed under a microscope (Figure 3-14H). Furthermore, Matrigel-encapsulated CMs co-cultured with DrGOM exhibited synchronized contraction across three spatially separated regions of the microlattice (Figure 3-14I), suggesting that electrical excitation generated in one region could be conducted through the rGO network of DrGOM to adjacent regions, thereby enabling coordinated contraction among CMs. Collectively, these results indicate that DrGOM enhances synchronized intracellular Ca^{2+} dynamics and promotes uniform electrical signal propagation between spatially distinct CM populations. The improved CM performance on DrGOM primarily arises from the electroactive properties of rGO, which provides a conductive substrate that supports electrical signal transmission between CMs, facilitates synchronized calcium transients, and strengthens intercellular electromechanical coupling.[217,218] Consequently, the high conductivity of DrGOM

enables coordinated contractile activity across different regions, suggesting that DrGOM has the potential to support electrical coupling between healthy and infarcted myocardium when applied as an ECP in vivo.

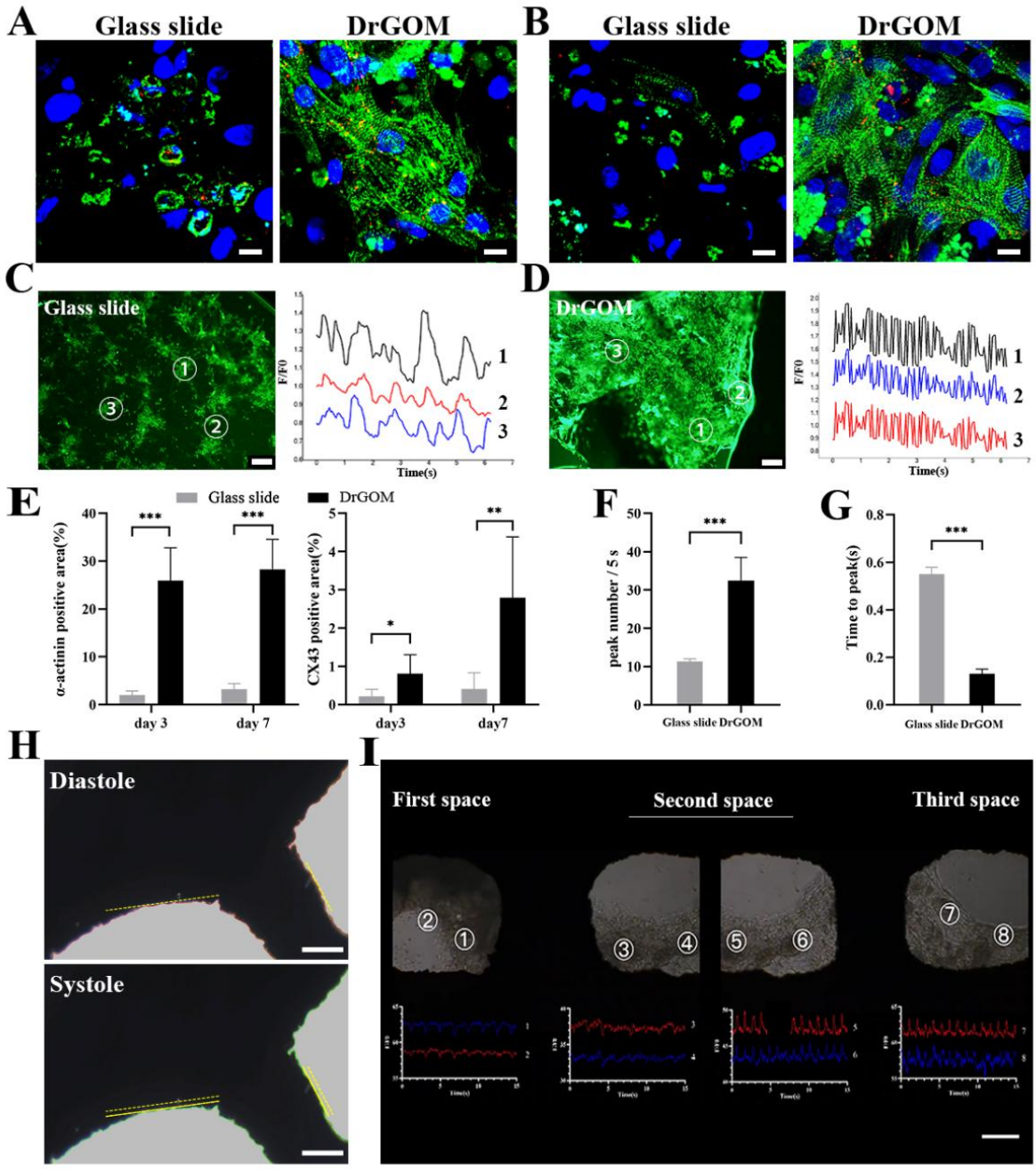

Figure 3-14 DrGOM facilitates the functionalization and synchronous contraction of CMs.

(A–B) Fluorescence images showing the expression of α-actinin (green) and CX-43 (red) in CMs cultured on different substrates on days 3 (A) and 7 (B). Scale bars: 20 μm. (C–D) Calcium transients (left) of CMs and the corresponding frequency signals (right) in different groups. Scale bars: 100 μm. (E) Quantification of the positive areas of α-actinin and CX-43 in CMs based on the fluorescence images. (F–G) Statistical analysis of peak number per 5 s (F) and time to peak (G) calculated from the calcium transient frequency signals. All data in (E–G) are presented as mean ± SD. *P < 0.05, **P < 0.01, ***P < 0.001. (H) Synchronous contraction of CM-loaded DrGOM observed under a microscope after 7 days of culture. The yellow dotted line indicates the displacement between diastole and systole. Scale bar: 100 μm. (I) Synchronous beating behavior of Matrigel-encapsulated CMs in the three spaces of DrGOM observed under a microscope. The beating signals extracted from two randomly selected spots in each space are shown as curves. Scale bar: 250 μm.

3.2.6 DrGOM Enhances Angiogenesis in vitro and in vivo

Previous studies have demonstrated that rGO possesses pro-angiogenic properties both in vitro and in vivo, representing a crucial mechanism for MI repair.[12,219-221] In this section, the pro-angiogenic capability of DrGOM was evaluated both in vitro and in vivo. Long, tubular, and mature microvessels formed by HUVECs were observed on DrGOM (Figure 3-15A). These microvessels exhibited strong α-smooth muscle actin (α-SMA) expression along their walls, confirming the formation of functional arteriole-like vessels capable of contractile activity. In contrast, HUVECs cultured on glass substrates formed only sparse and primitive vascular-like structures. To further evaluate the angiogenic effect in vivo, a dorsal window chamber assay was

performed in nude mice (Figure 3-15B). Intravital multiphoton microscopy showed no significant difference in blood vessel density in the Matrigel group between day 1 and day 7 after subcutaneous transplantation (Figure 3-15C, D). In contrast, the DrGOM group exhibited a significant increase in blood vessel density on day 7 compared with day 1. Furthermore, von Willebrand factor (vWF) staining of dorsal skin cross-sections revealed that the DrGOM group had a significantly higher microvessel density than the Matrigel group (Figure 3-15E). These results confirm that DrGOM possesses strong pro-angiogenic capability both in vitro and in vivo. Previous studies have attributed the pro-angiogenic activity of rGO to the activation of phosphorylated endothelial nitric oxide synthase (phospho-eNOS)–dependent nitric oxide (NO) signaling.

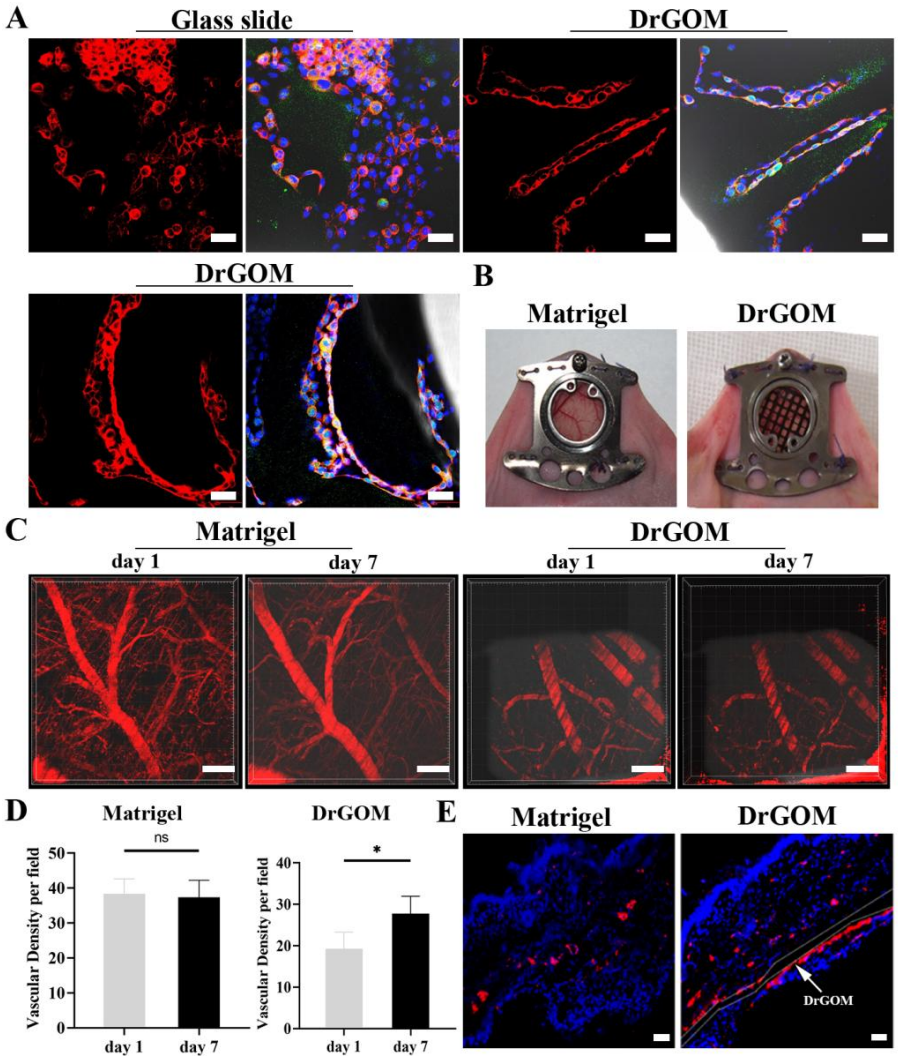

Figure 3-15 Effect of DrGOM on angiogenesis in vitro and in vivo.

(A) Tube formation assay of human umbilical vein endothelial cells (HUVECs) cultured on a glass slide and on DrGOM for 24 h. Scale bars: 50 μm. (B) Representative photographs of the transplanted Matrigel and DrGOM in the dorsal skinfold window chambers of nude mice. (C) Fluorescent images showed the blood vessel structure taken by multi-photon microscopy in the dorsal skinfold chambers. Scale bars: 200 μm. (D) Fold changes of the blood vessel density according to multi-photon microscopy images in different groups on day 7 relative to that on day 1. All data are presented as the mean ± SD. ***P < 0.001. (E) vWF immunostaining (red) in the

matrigel- or DrGOM-implanted dorsal skin cross-section 14 d after the implantation. The nucleus was stained by DAPI (blue). Scale bars: 100 μm.

3.2.7 Therapeutic Efficacy of DrGOM-based Cardiac Patches in Rat MI Models

As mentioned above, DrGOM significantly enhanced CM functional maturation. In this section, the therapeutic effect of DrGOM-based cardiac patches was evaluated in a rat MI model. Owing to the synergistic effects of its flexibility and hydrophilic/hydrophobic surface properties, DrGOM was expected to achieve conformal contact with the epicardial surface. Pure CMs, pure DrGOM, and DrGOM ECPs, which consist of CMs and DrGOM, were cultured for 7 days before being transplanted onto infarcted myocardium for 4 weeks. Subsequently, hearts from each group were harvested, and the infarct size and vascularization level were assessed in cardiac tissue sections using Masson's Trichrome and immunofluorescence staining. As shown in Figure 3-16A, fibrous tissue filled the infarct region in the MI group, and the infarct area reached 52.71% ± 3.73%. All treatment groups showed significant reductions in infarct size accompanied by increased wall thickness in the infarcted region. The infarct areas in the CM, DrGOM, and DrGOM ECP groups were 32.69% ± 11.08%, 26.01% ± 8.28%, and 14.33% ± 3.66%, respectively (Figure 3-16A, C). Compared with CM transplantation alone, pure DrGOM transplantation resulted in a smaller infarct area and a thicker left ventricular wall, while the DrGOM ECP group exhibited the smallest infarct area and the greatest wall thickness among all treatment groups (Figure 3-16C, D). Immunofluorescence staining further revealed α-actinin-positive neo-myocardium in the infarct regions of the DrGOM and DrGOM ECP groups, and substantial expression of CX-43, which

indicates electrical coupling between cardiac tissues (Figure 3-16B). Quantitative analysis showed that the DrGOM ECP group exhibited the highest percentages of α-actinin-positive and CX-43-positive areas among all infarcted hearts (Figure 3-16F). Regarding vascularization, only limited angiogenesis was observed in the CM group, whereas abundant vWF^+ microvessels and vWF^+/α-SMA^+ arterioles were detected in the infarct regions of the DrGOM and DrGOM ECP groups, with the DrGOM ECP group showing the highest vascularization level (Figure 3-16G). Merged bright-field images of the marginal zones in the DrGOM and DrGOM ECP groups further showed that DrGOM was surrounded by fibrous tissue with numerous newly formed microvessels (Figure 3-16G). These results demonstrate that DrGOM-based cardiac patches effectively promote MI repair by reducing infarct size and enhancing vascularization in the damaged myocardium. The conformable conductive scaffold facilitates electrical integration between the patch and the infarcted heart, enabling the conductive ECP to function as an electrical bridge that improves signal propagation between healthy and damaged myocardial tissues.[222] Restoration of cardiac electrical signal conduction improves cardiac function and contributes to myocardial recovery.[223] Furthermore, enhanced angiogenesis provides oxygen and nutrients to the infarcted region and reduces fibrosis, which is critical for effective MI repair.[223]

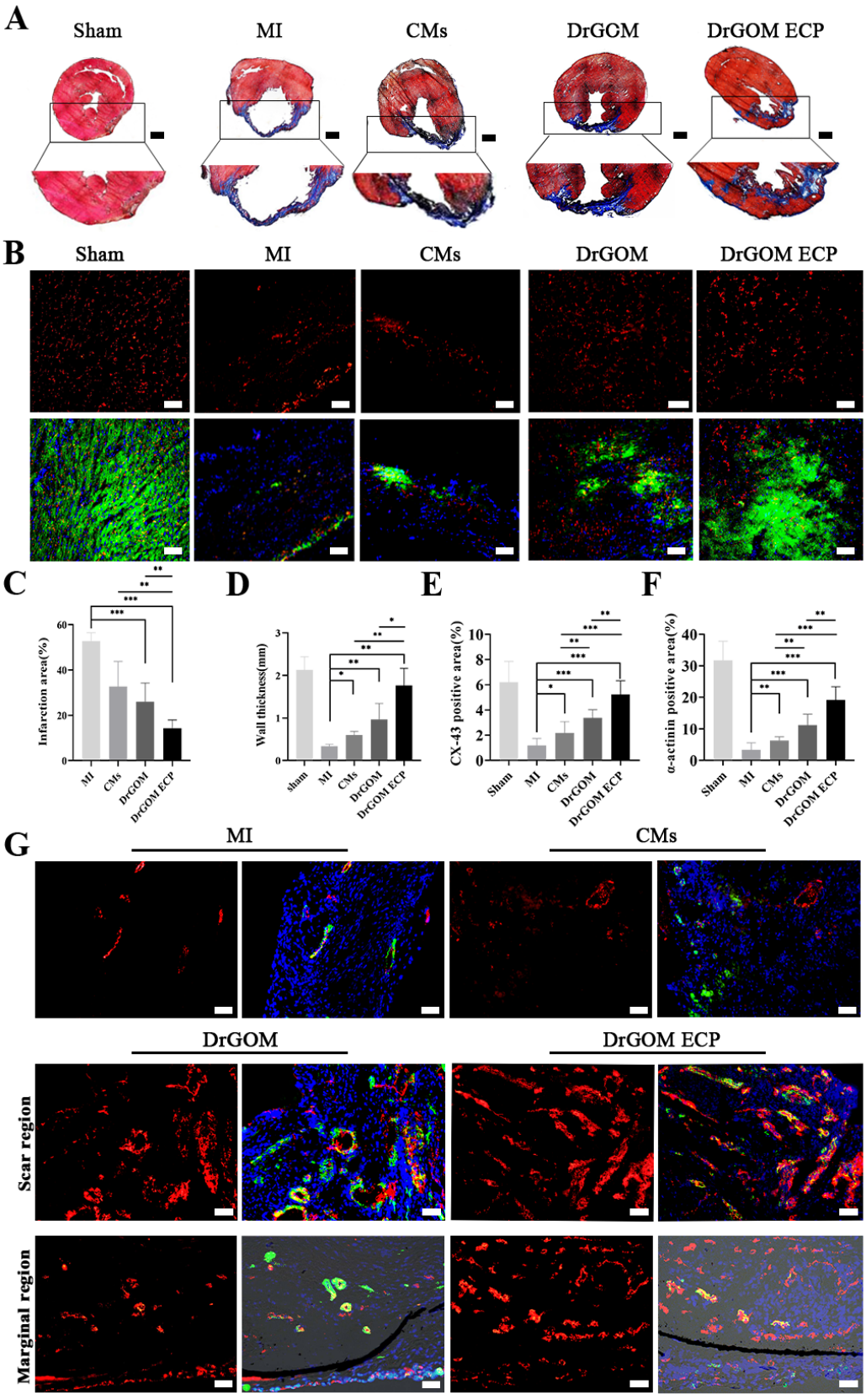
A
Sham
MI
CMs
DrGOM
DrGOM ECP
B
Sham
MI
CMs
DrGOM
DrGOM ECP
C
Infarction area(%)
MI
CMs
DrGOM
DrGOM ECP
D
Wall thickness(mm)
sham
MI
CMs
DrGOM
DrGOM ECP
E
CX-43 positive area(%)
Sham
MI
CMs
DrGOM
DrGOM ECP
F
α-actinin positive area(%)
Sham
MI
CMs
DrGOM
DrGOM ECP
G
MI
CMs
DrGOM
DrGOM ECP
Scar region
Marginal region

Figure 3-16 Detection of infarct area and vascularization levels in different groups in rat myocardial infarction (MI) models after patch transplantation for 4 weeks.

(A) Representative Masson's Trichrome staining images showing myocardium (red) and fibrous tissue (blue) in heart sections from different groups. Scale bar: 1 mm. (B) Immunofluorescence images showing α-actinin-positive myocardial tissue (green) and CX-43 proteins (red) in the infarct regions of different groups. Scale bar: 50 μm. (C–D) Statistical analysis of infarct area (C) and wall thickness (D) based on Masson's Trichrome staining images in different groups. *P < 0.05, **P < 0.01, ***P < 0.001. (E–F) Quantitative analysis of CX-43-positive area (E) and α-actinin-positive area (F) based on immunofluorescence staining images. *P < 0.05, **P < 0.01, ***P < 0.001. (G) Immunofluorescence staining of vWF (red) and α-SMA (green) in heart sections from different groups. Images in the MI and CMs groups correspond to infarct regions. The upper images in the DrGOM and DrGOM ECP groups correspond to infarct regions, while the lower images show merged bright-field images of marginal regions surrounding the DrGOM and DrGOM ECP patches. Scale bar: 50 μm.

3.2.8 DrGOM-Based Cardiac Patches Improve Cardiac Function in Rat MI Models

Echocardiography was performed before transplantation and 4 weeks after transplantation to evaluate changes in cardiac function. As shown in Figure 3-17A, weak and stiff contractions were observed in the MI and CM groups, whereas the DrGOM and DrGOM ECP groups exhibited enhanced contractile activity in the left ventricle. Key cardiac functional parameters, including fractional FS, EF, LVIDs, and LVIDd, were analyzed from the echocardiographic images (Figure

3-17B, C). The results showed that the △FS% and △EF% values in the DrGOM and DrGOM ECP groups, as well as the △EF% value in the CM injection group, were significantly higher than those in the MI group, indicating improved cardiac pumping function in these treatment groups (Figure 3-17C). Furthermore, both DrGOM and DrGOM ECP transplantation significantly reduced the △LVIDs values compared with the MI group, suggesting that these treatments could inhibit pathological left ventricular (LV) dilation after MI (Figure 3-17C). Among all treatment groups, the DrGOM ECP group exhibited the best cardiac functional recovery. Collectively, these results demonstrate that DrGOM-based cardiac patches have strong therapeutic potential for MI repair through synergistic effects on electrical integration, revascularization, and inhibition of fibrosis and LV dilation in the infarcted heart. In addition, the combined effects of paracrine signaling from both DrGOM and CMs enabled the DrGOM ECP to achieve better repair outcomes than pure DrGOM. Specifically, DrGOM-based cardiac patches effectively alleviated LV dilation and improved cardiac function in the infarcted heart, which could not be achieved by CM transplantation alone.

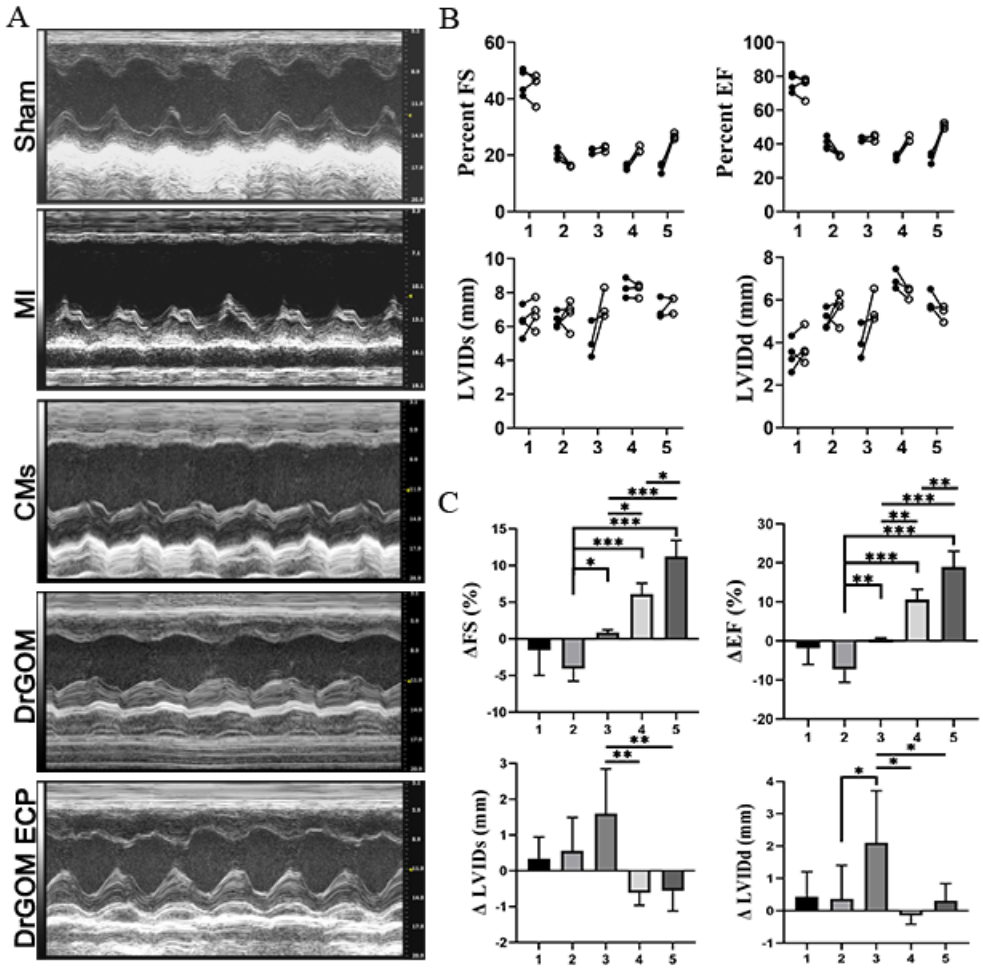

Figure 3-17 Left ventricular functions evaluated by echocardiography 4 weeks after transplantations.

(A) Representative echocardiographic images from different groups. (B) Changes in fractional FS, EF, LVIDs, and LVIDd for each rat measured by echocardiography. (C) Statistical analysis of the changes in FS, EF, LVIDs, and LVIDd in different groups during the 4-week transplantation period. Data are presented as mean ± SD. *P < 0.05, **P < 0.01, ***P < 0.001. Line 1: Sham group; Line 2: MI group; Line 3: CMs group; Line 4: DrGOM group; Line 5: DrGOM ECP group.

3.3 Conclusions

This study demonstrates the multifunctional implementation of a moisture-driven soft actuator and the fabrication of multifunctional wearable electronics with different sensing modules by tuning the reduction time and pattern design. In this work, asymmetrical hydrophilicity was applied to a DIW-printed microlattice to prepare a DrGOM ECP. The DrGOM exhibited excellent conformability to curved surfaces owing to its unique microlattice architecture and moisture-responsive actuation behavior. The GO/rGO sensing modules fabricated using the "masked spin-coating" technique, which possess asymmetrical hydrophilicity, demonstrated potential for sensing cardiac physiological signals, including temperature, pH, and strain. The results further showed that the biocompatible DrGOM promotes the adhesion and growth of CMs. In addition, DrGOM enhances the expression of cardiac-specific proteins in CMs, improves CM communication, facilitates synchronous contraction, and promotes vascularization both in vitro and in vivo. As a moisture-responsive actuator and conformable cardiac patch, both pure DrGOM and CM-loaded DrGOM significantly improved cardiac function and reduced infarct size in rat MI models.

4 Chapter 4: A Trinity Triboelectric Nanogenerator as Cardiac Patch Repairs and Monitors Infarcted Myocardium

4.1 Methods and Materials

4.1.1 Materials

The live/dead cell staining kit was purchased from Molecular Probes (USA). Primary antibodies against α-actinin, connexin-43 (CX-43), von Willebrand factor (vWF), and α-smooth muscle actin (α-SMA) were purchased from Abcam (UK). Alexa Fluor 568 donkey anti-rabbit IgG (H&L) and Alexa Fluor 488 donkey anti-mouse IgG (H&L) secondary antibodies were obtained from Life Technologies (USA). Polylactic acid (PLA) was purchased from XYZ Printing (USA). Graphene oxide (GO) was purchased from Tanfeng Tech., Inc. (Suzhou, China). Dopamine (DOPA) was purchased from Sigma-Aldrich (Canada). Ecoflex 00-50 was purchased from Smooth-On, Inc. (USA). Polyvinylpyrrolidone (PVP, Mw = 130,000) was purchased from Shanghai Aladdin Bio-Chem Technology Co., Ltd. (China). Tris-HCl and dimethylformamide (DMF) were purchased from Sigma-Aldrich (USA). Hexane was purchased from Anachemia Canada, Inc. (Canada). Sylgard 184 silicone elastomer kit was purchased from Dow Corning (USA). Acetone was purchased from Thermo Scientific (USA). The silver epoxy kit H20E was purchased from Epoxy Technology, Inc. (USA).

4.1.2 Preparation of Leaf Vein Template

Leaves were harvested from boldo (*Peumus boldus*). The cuticle and mesophyll cells were removed by immersing the leaves in hexane for 24 h to obtain leaf vein templates.

4.1.3 Preparation of Molds

PLA round molds (diameter = 8 mm, height = 0.5 mm) were fabricated for the preparation of rGO electrodes, PDA-rGO electrodes, and the bottom packaging layer. PLA hollow cylindrical molds (inner diameter = 6.5 mm, outer diameter = 8 mm, height = 5 mm) were fabricated for the preparation of Ecoflex spacers. All molds were produced using a da Vinci Junior 1.0 3D printer (XYZprinting, Inc.). To prepare the leaf vein molds, the two components of the Sylgard 184 silicone elastomer kit were mixed at a 10:1 ratio and spin-coated onto a coverslip at 3500 rpm for 30 s. The mixture was then cured at 120 °C for 30 min to form a cured elastomer layer. After cooling to room temperature, another layer of the elastomer mixture was spin-coated onto the cured layer at 3500 rpm for 30 s. A piece of the leaf vein template was then placed onto the uncured elastomer layer. The elastomer was subsequently cured at 120 °C for 30 min, after which the leaf vein template was peeled off to obtain the leaf-vein-patterned mold.

4.1.4 Preparation of rGO and PDA-rGO Electrodes.

GO powder was dispersed in DI water and sonicated using a probe sonicator (SK92-IIN) for 60 min to obtain a uniform aqueous GO dispersion (8 mg/mL). Subsequently, 90 μL of the GO dispersion was drop-cast onto 8 mm PLA round molds and allowed to evaporate at room temperature to form GO thin films. The GO films were then thermally reduced at 300 °C for 12 h to obtain rGO electrodes. Dopamine (DOPA) was dissolved in Tris buffer (pH 8.5) to prepare a 2 mg/mL DOPA solution. The rGO electrodes were immersed in the DOPA solution for 8 h to form a PDA coating on the rGO electrodes.

4.1.5 Preparation of PVDF Membrane with Leaf Vein Structure

Poly(vinylidene fluoride) (PVDF) was dissolved in a mixed solvent of DMF and acetone (DMF: acetone = 2:1) under vigorous stirring for 30 min to obtain a homogeneous solution with a

concentration of 10% (w/v). Subsequently, 150 μL of the PVDF solution was drop-cast onto the leaf vein mold. After vacuum drying to remove the solvent, a PVDF membrane with a leaf vein structure was obtained.

4.1.6 Assembly of TENG

Polyvinylpyrrolidone (PVP) was dissolved in ethanol at 90 °C under vigorous stirring to prepare a 10% (w/v) ethanolic PVP solution. The PVP solution was spin-coated onto a PLA round mold at 2000 rpm for 60 s. After evaporation of ethanol, a PVP sacrificial layer was formed. Part A and Part B of Ecoflex 00-50 were then mixed at a 1:1 ratio, and the mixture was spin-coated onto the PVP sacrificial layer at 3500 rpm for 60 s. The Ecoflex layer was cured at 60 °C for 30 min. Another Ecoflex mixture was subsequently spin-coated onto the cured Ecoflex layer at 3500 rpm for 60 s. The rGO electrodes were placed onto the uncured Ecoflex layer, followed by the curing of the Ecoflex. The PVDF membrane was then placed on top of the rGO electrode. Subsequently, 25 mg of the Ecoflex mixture was drop-cast into a PLA hollow cylindrical mold, which was then positioned on the PVDF layer with the uncured Ecoflex facing the PVDF surface. The Ecoflex mixture was cured at 60 °C for 30 min to form the Ecoflex spacer, after which the hollow cylindrical mold was removed. Next, the PDA-rGO electrode was placed on top of the spacer, and another Ecoflex spacer layer was assembled on top of the PDA-rGO electrode using the same procedure. Finally, the entire device was immersed in DI water to dissolve the PVP sacrificial layer, enabling the release of the TENG device.

4.1.7 Assembly of TENG Array

A 4 cm × 4 cm PLA mold was used as the initial spin-coating substrate for fabricating the TENG array, while 1 cm × 1 cm PLA molds were used for the preparation of rGO and PDA-rGO

electrodes. A 4 cm × 4 cm grid-patterned PLA mold with a line width of 1.5 mm was used to prepare the Ecoflex spacer, and a 4 × 4 configuration was adopted for the TENG array. Electrical connections between every two neighboring rGO electrodes and PDA-rGO electrodes were established using air-dried PEDOT:PSS/GelMA hydrogel as conductive solder. GelMA was synthesized following a previously reported method: briefly, 10 g of gelatin was dissolved in 100 mL PBS at 50 °C under vigorous stirring to obtain a 10% (w/v) solution, followed by the addition of 2 mL methacrylic anhydride (MAA). The reaction proceeded at 50 °C for 2 h, and the pH was maintained at 7.4 using 10 M NaOH. The product was dialyzed against deionized (DI) water at 50 °C for 3 days and subsequently lyophilized. To prepare the conductive hydrogel solder, 100 mg PEDOT:PSS, 100 mg GelMA, and 2 mg Irgacure® were dissolved in 2 mL DI water at 50 °C under vigorous stirring to obtain a homogeneous precursor solution. A small amount (5–10 mg) of the precursor solution was placed at each connection point and cured under UV irradiation for 30 min, followed by air drying. For TENG devices with external leads, rGO and PDA-rGO electrodes were integrated with a connection structure prepared using a PLA round mold with an extended connection region, and insulated wires were attached using silver epoxy.

4.1.8 Characterization of the TENG

The cyclic compressive mechanical input used to drive the TRI-TENG was provided by an MTS® universal testing machine. The electrical signals were recorded using a benchtop digital multimeter (Keithley DMM6500, Tektronix®). For in vitro characterization of the TENG devices, the rGO electrode of the TENG was connected to the digital multimeter. A PDMS cube (2 cm × 2 cm × 2 cm) was affixed to the top compression platen of the universal testing machine to act as the contact material. Cyclic compression of the testing machine enabled periodic contact and separation

between the PDMS cube and the TRI-TENG device. Fourier transform infrared spectroscopy (FTIR) was used to characterize the presence of specific functional groups. FTIR spectra were recorded using an infrared spectrophotometer (Nicolet 6700, Thermo Fisher Scientific Inc., USA) over a spectral range of 400–4000 cm^{-1} with a resolution of 4 cm^{-1} and an average of 64 scans.

4.1.9 Neonatal Rat CMs Culture.

Sprague–Dawley (SD) rats (newborns aged 1–3 days or adults weighing 250 ± 20 g) were purchased from the Animal Center of Southern Medical University, and Bama minipigs were obtained from Longgui Xingke Animal Breeding Farm (Baiyun District, Guangzhou, China). All animal procedures were approved by the Animal Ethics Committee of Southern Medical University and performed in accordance with the Regulations on the Administration of Laboratory Animals of China.

Hearts from 1–3-day-old neonatal SD rats were rapidly excised, carefully dissected, and washed three times with PBS to remove blood clots. The heart tissues were dissociated in trypsin overnight at 4 °C and subsequently digested with 0.1% collagenase type II (Sigma) to obtain a single-cell suspension. The isolated cells were pre-plated for 2 h to remove cardiac fibroblasts, and the non-adherent cells were seeded onto different scaffolds at a density of 5×10^6 cells/cm^2. Cardiomyocytes (CMs) were cultured in high-glucose Dulbecco's modified Eagle's medium (DMEM, GIBCO) supplemented with 15% fetal bovine serum (FBS, GIBCO), 100 U/mL penicillin, and 100 μg/mL streptomycin. All cells were maintained in an incubator at 37 °C with 5% CO_2, and the culture medium was replaced every 2 days.

4.1.10 SEM

The microstructure of the scaffolds and the micromorphology of CMs seeded on the scaffolds were observed using SEM. After 7 days of culture, the CM-loaded scaffolds were rinsed with PBS, fixed with glutaraldehyde at 4 °C overnight, dehydrated through a graded ethanol series, and dried using the critical point drying method. The samples were then sputter-coated with gold and imaged using a scanning electron microscope (ULTRA55, Zeiss).

4.1.11 Sensing Signal Detection

Minipigs were anesthetized by intramuscular injection of ketamine hydrochloride (10 mg/kg) and sumianxin (1 mg/kg). A thoracotomy was performed between the fourth and fifth ribs, and the fourth intercostal space was widened using a rib spreader. After opening the pericardium, a TRI-TENG patch with a connecting wire was placed between the ventricle and the pericardium. The voltage signal was recorded using a digital multimeter (DMM7510, Keithley), and the electrocardiogram (ECG) was recorded using a signal acquisition system (BL-420F, Chengdu Techman Software Co., Ltd.).

For the Langendorff perfusion experiment, rats were injected with heparin (3125 U/kg) for 10 min to prevent blood coagulation and were then euthanized using pentobarbital sodium. The hearts were rapidly excised and rinsed in Krebs–Henseleit (KH) buffer containing 128 mM NaCl, 4.7 mM KCl, 20 mM $NaHCO_3$, 1.05 mM $MgCl_2$, 1.19 mM NaH_2PO_4, 1.3 mM $CaCl_2$, and 11.1 mM D-glucose. The hearts were then retrogradely perfused using a Langendorff apparatus with KH buffer bubbled with 95% O_2 and 5% CO_2 and stabilized for 15 min at 37 ± 0.5 °C. The flow rate and perfusion pressure were maintained at 8–10 mL/min and 60–70 mmHg, respectively. The TRI-TENG patch with wire was placed on the left ventricle, and the voltage signal of the sinus rhythm was recorded using the multimeter. Electrical stimulation (7 Hz) was then applied beneath

the left atrial appendage using an electronic stimulator, and the voltage signal was recorded. ECG electrodes were positioned on the right atrium and left ventricle to continuously monitor the ECG signals.

For the wireless sensing experiment, male SD rats were anesthetized and ventilated, followed by thoracotomy. The TRI-TENG connected to an external wireless device (Pokit meter) was placed on the rat heart to collect the open-circuit voltage (V_{oc}) under both normal and ischemic conditions. After receiving the wireless signal, the waveform of V_{oc} was displayed on a mobile phone, while the ECG signals were simultaneously recorded using the signal acquisition system.

4.1.12 Implantation of Different Cardiac Patches into the Rat MI Model

Male SD rats were used to establish the MI model and were randomly divided into five groups: sham, MI, PDMS, rGO-PDMS, and TRI-TENG groups. Briefly, all rats were anesthetized, ventilated, and subjected to thoracotomy. Rats in the sham group underwent thoracotomy only, whereas rats in the other groups underwent ligation of the left anterior descending (LAD) coronary artery after thoracotomy. Electrocardiographic monitoring showed a significant elevation of the ST segment, indicating successful establishment of the MI model. Fifteen minutes after LAD ligation, PDMS, rGO-PDMS, or TRI-TENG patches were implanted onto the surface of the infarcted myocardium, and the edges of the patches were sutured to the epicardium at the border of the infarct region using 7-0 polypropylene sutures.

4.1.13 Immunofluorescence Staining

For immunofluorescence staining, CMs were co-cultured with different matrices for 3 and 7 days. The samples were fixed with 4% paraformaldehyde (PFA) at 4 °C overnight and washed three times with PBS. Subsequently, the samples were permeabilized with 0.2% Triton X-100 for

15 min at room temperature and blocked with 2% bovine serum albumin (BSA) in PBS for 30 min. The samples were then incubated with primary antibodies, including rabbit anti-α-actinin (1:100) and mouse anti-CX43 (1:500), diluted in 2% BSA/PBS at 4 °C overnight. After removal of the primary antibodies, the samples were incubated with secondary antibodies for 2 h at room temperature, including Alexa Fluor 488 donkey anti-rabbit IgG (H&L) (1:500) and Alexa Fluor 568 donkey anti-mouse IgG (H&L) (1:500). F-actin organization was analyzed by staining with fluorescein isothiocyanate (FITC)-conjugated phalloidin (1:500; Yeasen Biotechnology, Shanghai, China) for 1 h at room temperature. Finally, all samples were counterstained with DAPI (Santa Cruz) and imaged using a fluorescence microscope (BX53O, Olympus).

4.1.14 Cardiac Stimulus Threshold and Contraction Force of Ventricular Tissue

Rats were euthanized 10 min after heparin administration, and the hearts were rapidly excised. The hearts were perfused and stabilized for 15 min to remove residual blood until a normal cardiac rhythm resumed, while ECG signals were continuously monitored. Electrical pulses were delivered by an electronic stimulator positioned beneath the left auricle. The pacing voltage was initially set at 1 V and increased in increments of 0.5 V until ECG capture was achieved. The recorded ECG signal was defined as the stimulus threshold of the normal heart. After attaching PDMS, rGO-PDMS, or TRI-TENG patches to the left ventricle, ECG signals were recorded again to determine the stimulus threshold of the patched hearts. To further evaluate the effects of different patches under ischemic conditions, myocardial ischemia was induced by ligation of the left anterior descending (LAD) artery, which resulted in ST-segment elevation in the ECG. PDMS, rGO-PDMS, or TRI-TENG patches were then applied, and ECG signals from the ischemic and patched hearts were recorded.

For contraction force measurements, hearts were rapidly excised, and intact ventricular tissues were isolated in Krebs–Henseleit (KH) buffer. The ventricular tissue was secured between two vascular clamps and stimulated using a 1 Hz electrical pulse applied at the ventricular apex. The contractile force of the ventricular tissue was first recorded using the mechanical sensing module of the signal acquisition system. Subsequently, PDMS, rGO-PDMS, and TRI-TENG patches were sequentially attached to the ventricular tissue, and the corresponding contraction forces were recorded. In addition, four weeks after patch transplantation (PDMS, rGO-PDMS, or TRI-TENG) in rats, ventricular tissues from each group were collected and tested for contractile force using the same method.

4.1.15 Electrical Mapping and Optical Mapping

Rats were anticoagulated with heparin and subsequently sacrificed. After opening the chest and exposing the heart, the lungs were clamped, and the heart was rapidly excised by cutting along the posterior side of the lungs. The isolated hearts were immediately mounted on a Langendorff perfusion system and perfused with Krebs–Henseleit (KH) buffer at a flow rate of 10 mL min^{-1} at 37 ± 0.5 °C. After residual blood was flushed out, the hearts were allowed to stabilize for 15 min before experimental procedures. A 64-electrode array (8 × 8 grid, 0.55 mm spacing) was positioned at the border zone between healthy and infarcted myocardium. Electrical stimulation (2 mV, 5 Hz) was applied to the epicardium beneath the left atrial appendage. ECG electrodes were placed on the right atrium and left ventricle, respectively, pacing from the right atrium while ECG signals were continuously recorded.

For optical mapping, hearts were perfused with KH solution containing 10 μM blebbistatin to suppress contractions and minimize motion artefacts. Dye loading was facilitated by pre-

perfusion with Pluronic F-127 (20% w/v in DMSO). The calcium indicator Rhod2-AM (1 mg mL^{-1}) and the voltage-sensitive dye Rh237 (1 mg mL^{-1}) were sequentially added to the perfusion solution to measure intracellular Ca^{2+} transients and membrane potential. The heart was illuminated with 530 nm excitation light from LEDs (MGL-III-532-100 mW) and imaged using a 50-mm camera lens. Fluorescence emission was collected at >700 nm for Rh237 and 590 ± 15 nm for Rhod2-AM. The emitted signals were recorded simultaneously using two CMOS cameras (01-KINETIX-M-C, Teledyne Photometrics) with a spatial resolution of 350 × 350 pixels and a sampling rate of 100 Hz.

4.1.16 Echocardiography of Rats

Left ventricular function in all animal groups was evaluated using echocardiography (Vevo 2100, VisualSonics). At two and four weeks after patch transplantation, rats were anesthetized and subjected to transthoracic echocardiography. M-mode images were acquired using a 40-MHz transducer, and short-axis views were obtained to assess cardiac parameters. The functional parameters measured included the LVIDd, LVIDs, EF (defined as the ratio of stroke volume to left ventricular end-diastolic volume), and FS, which were used to evaluate left ventricular function after patch transplantation.

4.1.17 Morphology, Histology, and Immunofluorescence Assay for Cardiac Sections

At week 4 after implantation, rats were sacrificed, and the hearts were collected. The harvested hearts were sliced into three sections and immediately fixed in 4% paraformaldehyde overnight at 4 °C. Images of the gross cross-sectional morphology of the hearts were captured. The tissue slices were then dehydrated sequentially in 15% and 30% sucrose solutions and

embedded in OCT at −20 °C. Cryosections with a thickness of 6 μm were prepared and mounted onto slides for histological analysis. Masson's Trichrome staining was performed to evaluate the infarct area and ventricular wall thickness. The infarct size was calculated as the ratio of the inner perimeter of the scar region to the total inner perimeter of the left ventricular wall. The thickness of the scar region was measured at three different locations and averaged. Immunofluorescence staining of the cryosections was performed using the same procedure described above. Primary antibodies, including rabbit anti-vWF (1:200) with mouse anti-α-SMA (1:100), and rabbit anti-α-actinin (1:100) with mouse anti-CX43 (1:500), were used. All stained samples were imaged using a fluorescence microscope (Olympus BX53), and the images were analyzed using ImageJ software (v2.0.0).

4.1.18 Minipigs Model of MI and TRI-TENG Array Implantation

Minipigs were housed at a constant temperature of 22–25 °C for one week to acclimate to the environment and were randomly assigned to the Sham, MI, and TRI-TENG groups. Thoracotomy was performed as described previously. The fourth intercostal space was expanded to expose the left anterior descending (LAD) coronary artery, which was ligated using a 5-0 polypropylene suture (Prolene, Ethicon) for 10 min, followed by two reperfusion cycles before permanent ligation. The myocardial infarction (MI) model was confirmed by ST-segment elevation on the electrocardiogram and cyanosis of the myocardial surface during surgery. In the Sham group, the same thoracotomy procedure was performed without LAD ligation. The chest of the MI group was then closed, while in the TRI-TENG group, the infarcted myocardial region was covered with the TRI-TENG array before chest closure. Electrocardiogram, body temperature,

blood pressure, and arterial oxygen saturation were continuously monitored throughout the operation. Body weight and overall physiological status were monitored daily after surgery.

After four weeks, ex vivo electrical signal propagation in the infarcted region was evaluated by ECG measurement using a signal acquisition system. Following euthanasia, the hearts were excised and immersed in Krebs–Henseleit (KH) solution. One end of the infarcted region was connected to stimulating electrodes, while ECG electrodes were used to detect electrical signals using a two-lead configuration. Electrical stimulation was applied at a frequency of 2 Hz.

4.1.19 Echocardiography of Minipigs

Echocardiographic measurements of minipigs were obtained using a portable echocardiograph before LAD occlusion and at 2 and 4 weeks after surgery. The anesthetized minipigs were placed in the left lateral decubitus position, and warmed ultrasound gel was applied to the chest to ensure proper acoustic coupling. Echocardiographic images were acquired to measure LVIDs, left ventricular internal diameter at end-diastole (LVIDd), EF, and FS from M-mode tracings at the mid-papillary level.

4.1.20 Histology and Immunofluorescence of Tissue Sections of Minipigs

Minipigs were euthanized 4 weeks after surgery. Portions of major organs (lung, liver, spleen, and kidney) were harvested, washed with PBS, and fixed in 10% formalin. The hearts were rapidly excised, and balloons filled with 20 mL of formalin were inserted into the left ventricle to prevent ventricular collapse during fixation. The hearts were then sectioned into four slices (1 cm thickness) from the apex to the atrium and fixed in 10% formalin. After fixation for 48 h, the tissues were sequentially dehydrated in 20% sucrose solution for 24 h and 30% sucrose solution for 24 h at 4 °C. Masson’s Trichrome staining and immunofluorescence staining of cardiac tissue

sections were performed following the same procedures described above. Tissue sections of the lung, liver, spleen, and kidney were embedded in paraffin and stained with hematoxylin and eosin (H&E) for histopathological examination.

4.1.21 RNA Sequencing of Heart Tissues and Bioinformatics Analysis

Rats were euthanized 4 weeks after myocardial infarction (MI), and heart tissues were rapidly collected from the infarct and border regions. RNA extraction and quality assessment were performed by Annoroad Gene Technology Co., Ltd. (Beijing, China). RNA degradation and contamination were evaluated using 1% agarose gel electrophoresis. RNA purity was measured using a NanoPhotometer® spectrophotometer (IMPLEN, CA, USA), and RNA integrity was assessed using the RNA Nano 6000 Assay Kit on a Bioanalyzer 2100 system (Agilent Technologies, CA, USA). For library preparation, 2 μg of RNA from each sample was used as the input material. Sequencing libraries were constructed using the NEBNext® Ultra™ RNA Library Prep Kit for Illumina® (NEB, USA) following the manufacturer's protocol. The clustering of index-coded samples was performed on a cBot Cluster Generation System using the TruSeq PE Cluster Kit v3-cBot-HS (Illumina) according to the manufacturer's instructions. After cluster generation, the libraries were sequenced on an Illumina NovaSeq platform.

For bioinformatics analysis, the reference genome and gene annotation files were obtained from the genome database. Gene Ontology (GO) enrichment analysis of differentially expressed genes was conducted using the clusterProfiler R package, and enrichment of Kyoto Encyclopedia of Genes and Genomes (KEGG) pathways was also analyzed using the clusterProfiler R package to identify significantly enriched biological processes and signaling pathways.

4.2 Results and Discussions

4.2.1 Assembly and Characterization of TRI-TENG CCP

A typical contact–separation mode triboelectric nanogenerator (TENG) consists of two metal plates serving as electrodes and a dielectric layer.[224] In conventional TENG designs, the dielectric and electrode surfaces are often engineered with nanoscale structures through specialized surface modification to increase the effective contact area and surface roughness. Such approaches usually involve costly fabrication techniques, including plasma dry etching[225], spin coating on lithographic patterned mold[226], NaOH wet-etching[195], and gold nanoparticle deposition.[227] Furthermore, the therapeutic electrodes integrated with implantable TENGs (I-TENGs), such as elastomer-encapsulated ionic hydrogel patches[228], ultrathin Au film deposited by electron-beam evaporation,[229] flexible metallic electrode fabricated through lithography[230], and elastomer-encapsulated interdigital Au electrodes, also require complex and expensive processing procedures. For MI treatment and diagnosis, our I-TENG conductive cardiac patch (CCP) employs a PDA-modified rGO membrane as a substitute for conventional metallic electrodes. A unique double-spacer design is adopted in the TRI-TENG CCP, enabling the PDA-rGO membrane to function simultaneously as the conductive cardiac patch, the triboelectric electrode that generates triboelectric charges, and the therapeutic electrode that establishes an electric field on the myocardium, thereby eliminating the need for an additional therapeutic electrode. Although the myocardium itself exhibits relatively poor triboelectric charge generation capability, the double-spacer design allows the electrical potential between the myocardium and the PDA-rGO electrode to be governed by the potential generated between the PDA-rGO electrode and the triboelectric layer through electrostatic induction. In addition, a mold-casting strategy was employed to introduce a leaf-vein microstructure into the polyvinylidene fluoride (PVDF) triboelectric layer.

Both the leaf-vein microstructure and the PDA coating on the rGO electrode are nature-inspired surface features that enhance the triboelectric effect by increasing surface roughness and effective contact area in a cost-efficient manner. Consequently, the TRI-TENG CCP integrates three functions into a single device: (1) serving as a therapeutic electrode that delivers electrical stimulation to infarcted tissue and facilitates electrical signal propagation between healthy and infarcted myocardium, (2) converting biomechanical energy into electrical energy, and (3) acting as a potential wireless diagnostic sensor.

As illustrated in Figure 4-1, the TRI-TENG conductive cardiac patch mainly consists of an elastomer bottom package, an rGO electrode, a PVDF triboelectric layer with a leaf-vein microstructure, two elastomer spacers, and a PDA-rGO electrode. The biocompatible elastomer Ecoflex 00-50 was used as both the spacer and encapsulation layer to further enhance the triboelectric effect and prevent electrical leakage. During cardiac contraction and relaxation, the TRI-TENG CCP undergoes cyclic contact and separation with the heart surface, generating opposite charges on the PDA-rGO electrode and the epicardial surface. Consequently, the PDA-rGO electrode performs a dual role, functioning both as a triboelectric electrode for energy conversion and as a therapeutic electrode for delivering electrical stimulation to the epicardium. Wireless monitoring of cardiac activity was achieved by connecting the rGO electrode to a Bluetooth-enabled device that communicates with a smartphone application. To ensure compatibility with hearts possessing relatively large surface areas, a TENG array design was implemented to improve conformability and coverage.

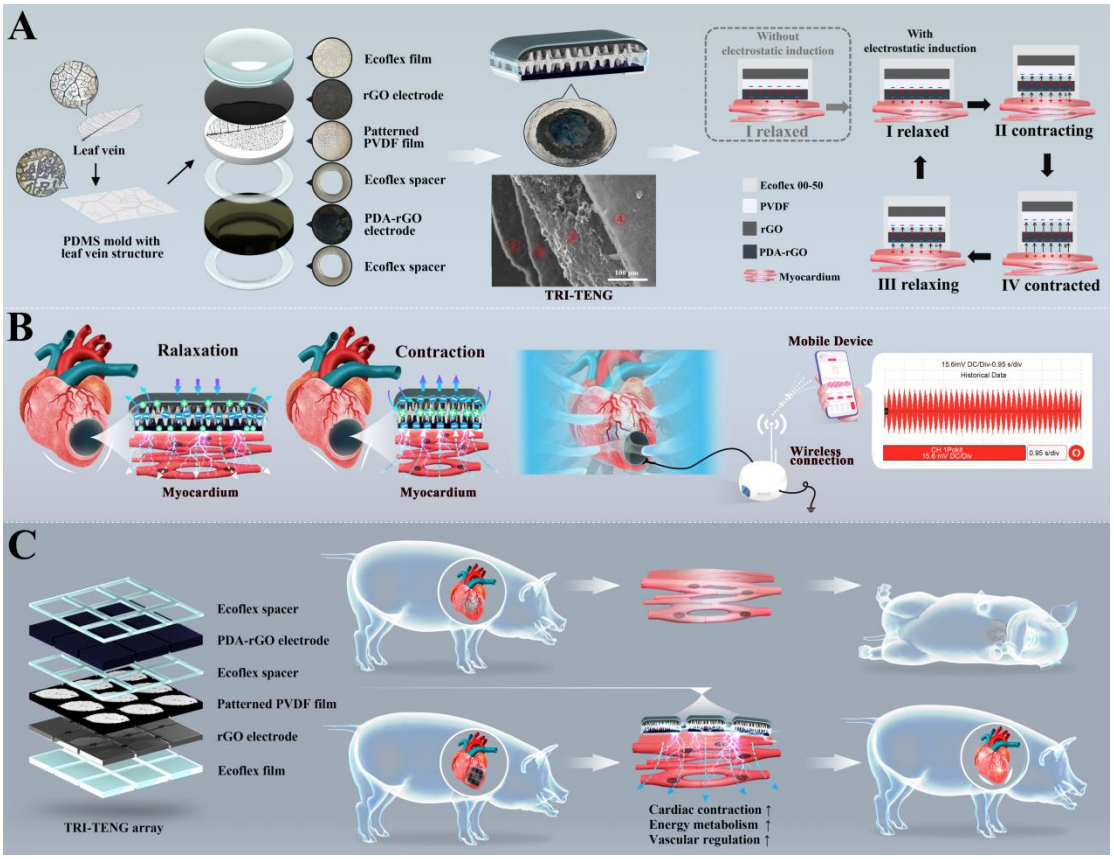

Figure 4-1 The schematic illustration of the composition of TRI-TENG CCP and its repair effect for MI.

(A) The TENG cardiac patch generates alternating current (AC) driven by relaxation and contraction of the heart. (B) Real-time communication of the TENG, a smartphone for *in vivo* monitoring of cardiac rhythm. (C) TENG array repairs extensive infarcted myocardium in minipigs.

The bottom package (1), rGO electrode (2), leaf-vein structured PVDF triboelectric layer (3), and PDA–rGO electrode (4) are clearly illustrated in the cross-sectional SEM image of the TRI-TENG CCP (Figure 4-2A). The bottom elastomer package was fabricated through spin coating followed by curing. To prepare the rGO and PDA–rGO electrodes, graphene oxide (GO)

electrodes were first fabricated by drop-casting a GO aqueous solution onto templates. During solvent evaporation, GO sheets underwent self-assembly at the air–liquid interface and eventually formed a uniform GO film. The surface morphology of the resulting GO electrode is shown in Figure 4-2B, where individual GO sheets can be clearly identified. The GO sheets appear bumpy and loosely packed, which is attributed to the distortion of the GO sheets caused by the presence of OCGs.[231,232] Energy-dispersive spectroscopy (EDS) analysis was performed to determine the elemental composition, showing a C/O ratio of 2.1 for the GO film (Figure 4-3). Fourier-transform infrared (FTIR) spectroscopy was further used to characterize the OCGs in the GO film (Figure 4-4A). Characteristic peaks of GO were observed at 3159 cm^{-1} corresponding to the stretching vibration of C–OH groups, 1718 cm^{-1} corresponding to the stretching vibration of C=O in carboxyl groups, and 1030 cm^{-1} attributed to the stretching vibration of C–O–C in epoxide groups. The peak at 1617 cm^{-1} is associated with the in-plane vibration of sp^2-hybridized C=C bonds. These results are consistent with previous studies.[233,234] To obtain the rGO electrode, the GO film was thermally annealed at 300 °C. After reduction, rGO sheets became more densely packed within the electrode (Figure 4-2C), indicating the removal of OCGs and the partial restoration of the sp^2-hybridized graphene lattice structure.[235,236] Correspondingly, the C/O ratio increased to 4.2 (Figure 4-3), providing further evidence of GO reduction. In addition, OCG-related peaks disappeared in the FTIR spectrum of rGO, confirming successful reduction. The sheet resistance of the rGO electrode was measured to be 0.420 ± 0.047 kΩ/sq (Figure 4-4B), and the improved conductivity further verified the reduction process. The rGO electrode was subsequently modified by PDA coating deposition. After treatment, PDA granules aggregated and anchored on the surface of the rGO electrode (Figure 4-2D). Elemental analysis showed that the PDA coating increased the oxygen content and introduced nitrogen elements on the electrode surface (Figure 4-3). In the FTIR

spectrum of the PDA–rGO electrode, a broad band appeared at 3220 cm^{-1} corresponding to the stretching vibrations of N–H and O–H, while two new peaks at 1508 cm^{-1} and 1050 cm^{-1} corresponded to the stretching vibrations of C=N and C–N, respectively,[237] confirming the successful deposition of PDA (Figure 4-4A). The sheet resistance of the PDA–rGO electrode (0.484 ± 0.153 MΩ sq^{-1}) was slightly higher than that of the rGO electrode (Figure 4-4B). Finally, PVDF dissolved in a DMF/acetone mixture was drop-cast onto a PDMS mold to fabricate the PVDF triboelectric layer with leaf-vein microstructures. As shown in Figure 4-2E, the surface of the resulting PVDF layer exhibits well-defined leaf-vein patterns.

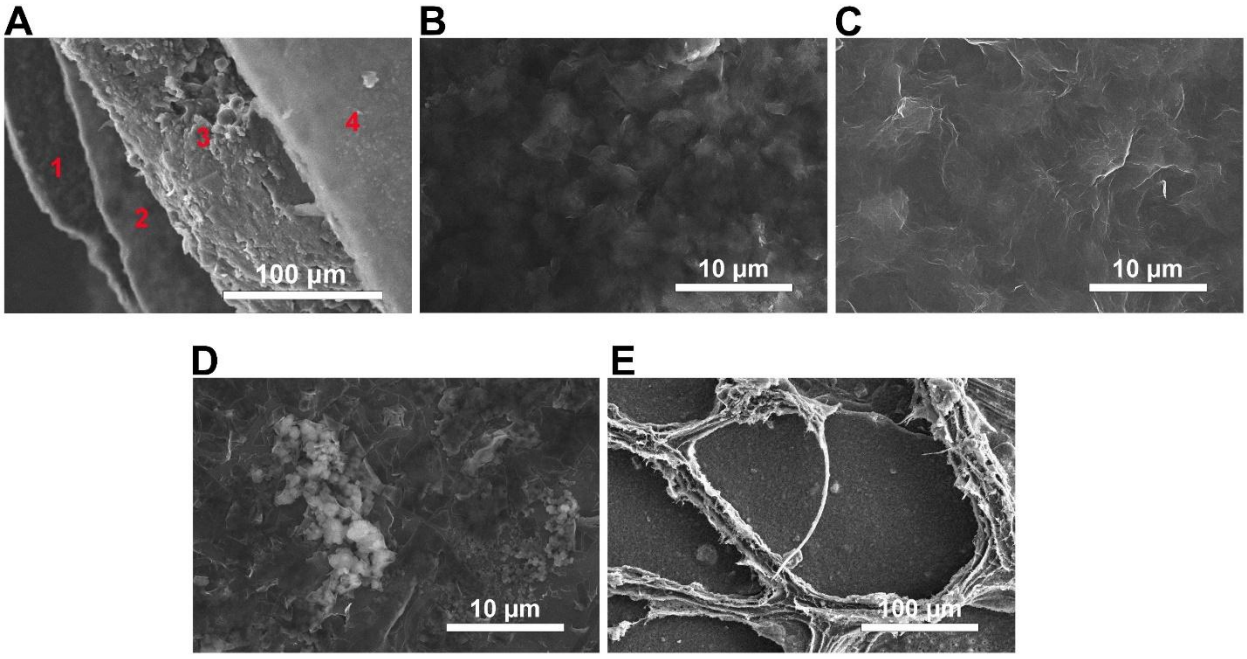

Figure 4-2 Characterization of TRI-TENG CCP and microscopic surface structures of different components.

SEM image of (A) TRI-TENG CCP cross-section; (B) GO electrode; (C) the surface rGO electrode; (D) PDA-rGO electrode; (E) PVDF triboelectric layer.

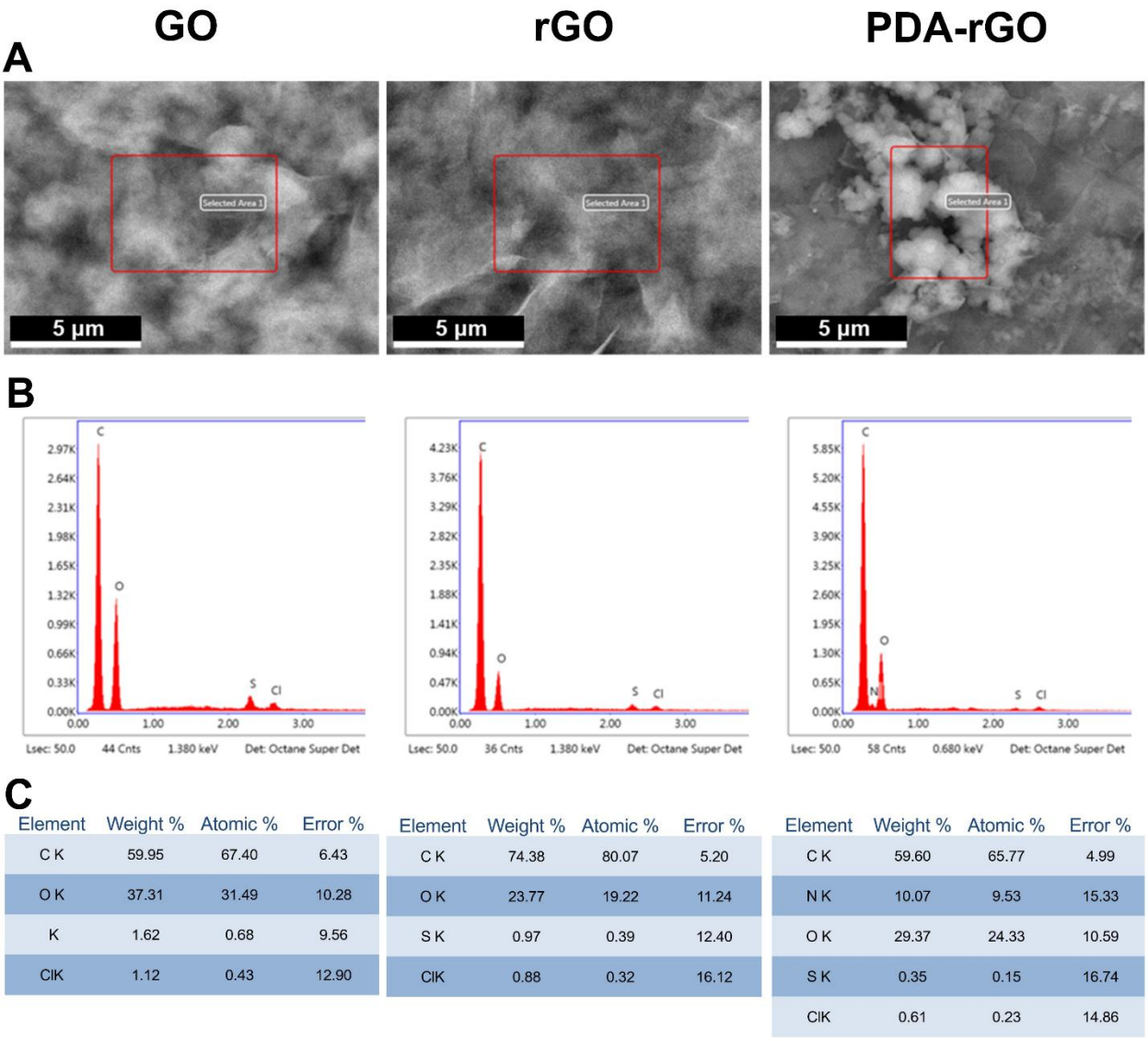

Element	Weight %	Atomic %	Error %
C K	59.95	67.40	6.43
O K	37.31	31.49	10.28
K	1.62	0.68	9.56
ClK	1.12	0.43	12.90

Element	Weight %	Atomic %	Error %
C K	74.38	80.07	5.20
O K	23.77	19.22	11.24
S K	0.97	0.39	12.40
ClK	0.88	0.32	16.12

Element	Weight %	Atomic %	Error %
C K	59.60	65.77	4.99
N K	10.07	9.53	15.33
O K	29.37	24.33	10.59
S K	0.35	0.15	16.74
ClK	0.61	0.23	14.86

Figure 4-3 Chemical characterization of the GO electrode, rGO electrode, and PDA-rGO electrode.

(A) Backscattered electron (BSE) SEM image of different electrodes. (B) Energy-dispersive X-ray spectroscopy analysis (EDS) spectra of the selected area in (A). (C) Table of the chemical composition of the EDS analysis.

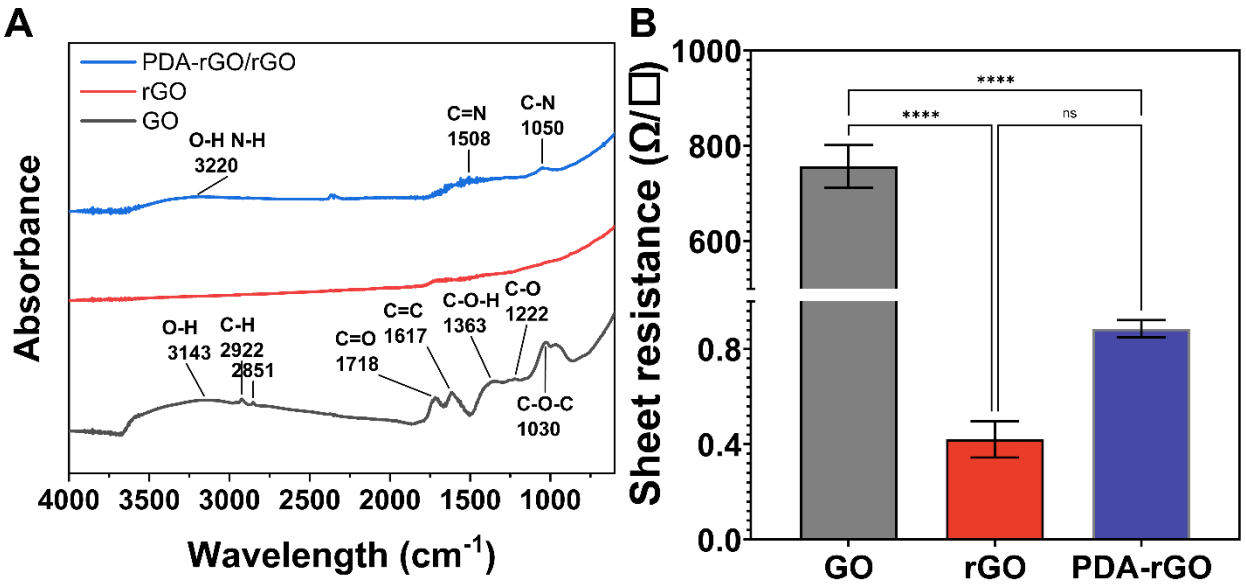

Figure 4-4 (A) Chemical and electrical characterization of different electrodes. (A) FTIR spectra of different electrodes. (B)The sheet resistance of different electrodes.

4.2.2 The Performance of TRI-TENG CCP as Energy Converter and Sensor In Vitro

To harvest the mechanical energy generated by cardiac contraction and relaxation for electrical stimulus generation, the TRI-TENG operates in a contact–separation mode. The working mechanism of the TRI-TENG is illustrated in Figure 4-5A. In the initial state, when the heart is contracted, no contact occurs between the PDA–rGO electrode and the PVDF layer due to the presence of the Ecoflex spacer. As the heart begins to relax, the TRI-TENG is stretched, forcing simultaneous contact between the upper surface of the PDA–rGO electrode and the PVDF layer, as well as between the lower surface of the PDA–rGO electrode and the epicardium.

According to Figure 4-5C and D, the PVDF layer has a stronger tendency to gain electrons than the PDA–rGO electrode, while the PDA–rGO electrode has a stronger tendency to gain

electrons than the myocardium. Consequently, electrons transfer from the upper surface of the PDA–rGO electrode to the PVDF layer during contact, leaving positive charges on the electrode surface. Meanwhile, electrons are injected from the myocardium to the bottom surface of the PDA–rGO electrode, generating negative charges on the bottom surface of the PDA–rGO electrode and positive charges on the epicardium. Owing to electrostatic induction, the triboelectric charges generated on the upper and lower surfaces of the PDA–rGO electrode are equal. When the heart is fully relaxed, the three layers come into close contact, resulting in negligible separation between oppositely charged surfaces and thus minimal potential difference. As the heart begins to contract, the separation distance between oppositely charged surfaces gradually increases, leading to the establishment of electric potentials between the PDA–rGO electrode and the epicardium, as well as between the PDA–rGO electrode and the PVDF layer. These potentials reach their maximum when the heart is fully contracted. The first spacer enables the PDA–rGO electrode not only to participate in triboelectric charge generation but also to function as a therapeutic electrode that builds an electric field across the myocardium. The second spacer further amplifies the generated electric field to a magnitude comparable to that established between the PDA–rGO electrode and the PVDF layer.

To enable sensing functionality, the output voltage between the rGO electrode of the TRI-TENG CCP and ground was measured using either an electrometer or a wireless sensing module (Figure 4-5B). During heart contraction, to balance the potential difference generated between the PDA–rGO electrode and the PVDF layer, the rGO electrode develops a higher electric potential relative to ground. When the rGO electrode and ground are electrically connected, electrons flow from the rGO electrode to ground. The potential difference between the rGO electrode and ground

continues to increase until the heart reaches full contraction. During heart relaxation, as the layers return to contact and the spatial separation decreases, the rGO electrode acquires a lower electric potential than ground, driving electrons to flow back from ground to the rGO electrode when the circuit is closed. Consequently, cyclic cardiac contraction and relaxation generate an alternating current voltage between the rGO electrode and ground, enabling the TRI-TENG CCP to function as a self-powered cardiac sensor.

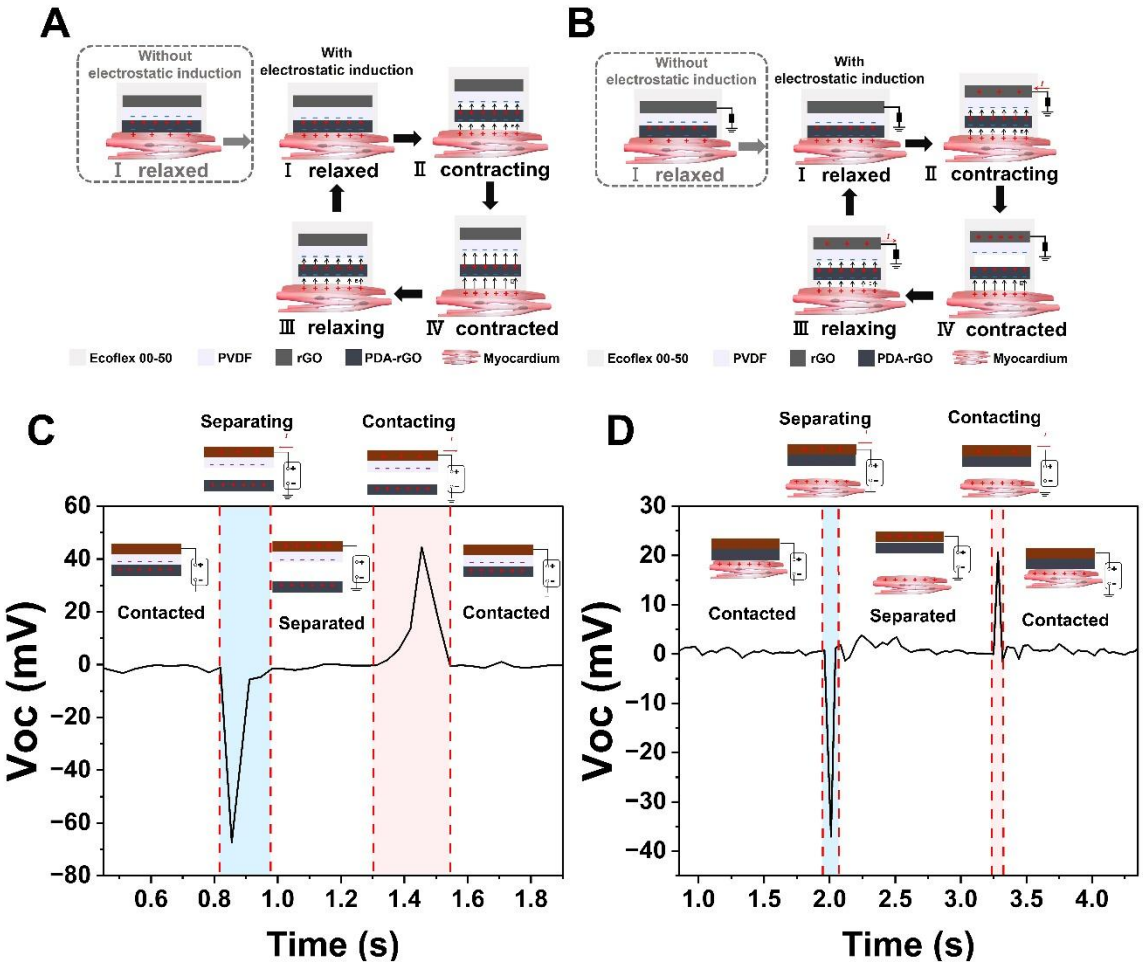

Figure 4-5 Working mechanisms of the TRI-TENG CCP.

TRI-TENG as (A) electric stimulus-generating cardiac patch, and (B) Working mechanism of sensor. Voltage measured from a copper electrode (C) attached to the PVDF contacting with and

separating from PDA-rGO and (D) attached to the PDA-rGO contacting with and separating from the myocardium.

Nature-inspired surface structures were employed to improve the electrical output performance of the TRI-TENG CCP. The patterned PVDF layer (P-PVDF) adopts a leaf-vein-inspired structure. In natural leaves, veins branch from a primary vein with a large diameter into secondary veins and eventually into microcapillaries with extremely small diameters (Figure 4-6A). This hierarchical branching architecture produces multilevel surface modulation at the macroscopic scale (Figure 4-6B). A mussel-inspired PDA coating was deposited on the rGO electrode to improve its biocompatibility. In addition to enhancing biocompatibility, the PDA coating increased the surface roughness of the PDA-rGO electrode. Both the average roughness (Ra) and root-mean-square roughness (Rq) of PDA-rGO were higher than those of rGO (Figure 4-6C, D). Overall, nature-inspired surface modifications were introduced at both the macroscopic multilevel scale and the microscopic scale to optimize the surface characteristics of the TRI-TENG CCP.

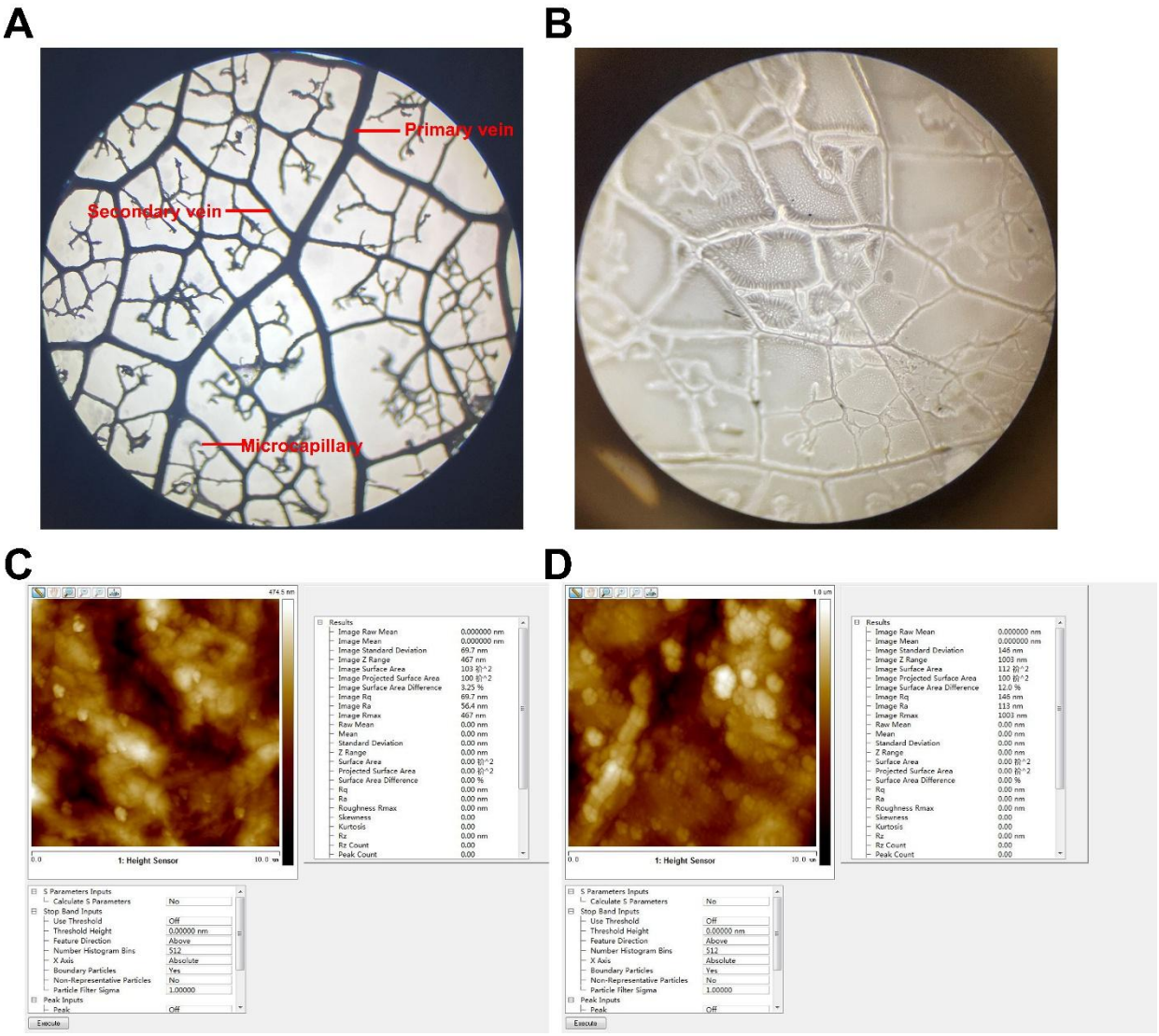

Figure 4-6 Nature-inspired structures.

Optical microscopy images of A) a natural leaf-vein structure and B) the surface of Patterned PVDF. Atomic force images (AFM) and the corresponding quantitative analysis of C) rGO and D) PDA-rGO

The effect of nature-inspired surface modification on TENG performance was further investigated. An electrometer was connected between the PDA-rGO electrode and the rGO electrode to evaluate the performance of TENGs with different components under controlled pressure and loading rates. The leaf-vein structure on the P-PVDF layer significantly improved the open-circuit voltage, short-circuit current, and transferred charge (Figure 4-7A). The PDA coating on the PDA-rGO electrode further increased the open-circuit voltage, short-circuit current, and transferred charge to 21.98 mV, 2.23 nA, and 0.22 nC, respectively. To investigate the output power of the TENGs, resistors ranging from 1 kΩ to 1 GΩ were connected as external loads. The output voltages and currents of all TENGs remained relatively stable when the external load was below 1 MΩ (Figure 4-7B). When the external load exceeded 1 MΩ, the voltages increased markedly with increasing resistance, while the currents decreased significantly due to Ohmic loss. Consequently, the instantaneous output power of all TENGs reached their maximum values at an external load of 10 MΩ. The instantaneous output power was further enhanced by the nature-inspired leaf-vein structure and the PDA modification, and the TENG incorporating both the P-PVDF layer and the PDA-rGO electrode achieved the highest maximum instantaneous output power of 0.16 $\mu W/m^2$.

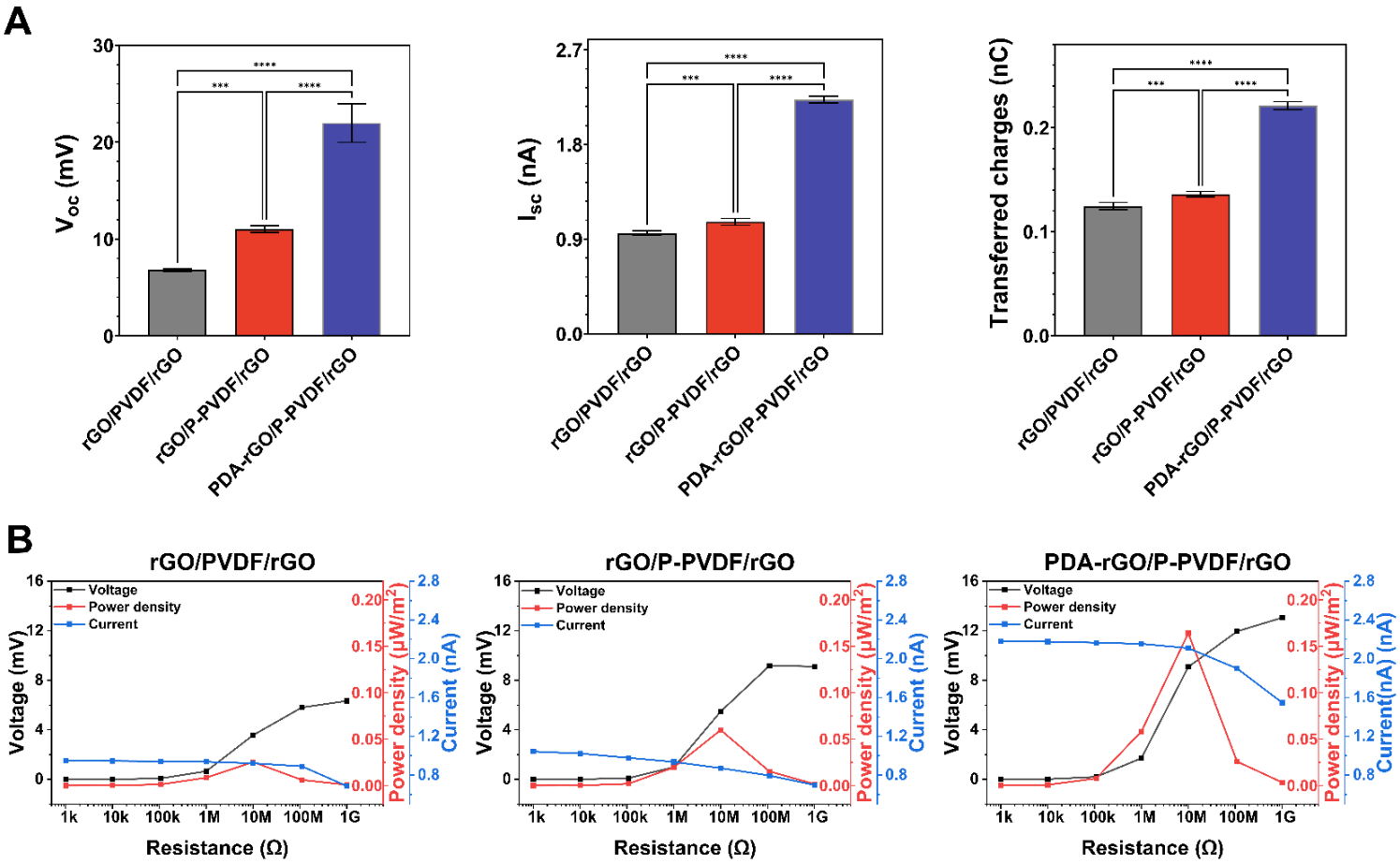

Figure 4-7 The in vitro output performance of different TENGs.

(A) V_{oc}, I_{sc}, and transferred charge of different TENGs. (B) Peak voltage and power density of different TENGs at different external loading resistances. (*p < 0.05, **p < 0.01, ***p < 0.001, ****P < 0.0001)

The contraction and relaxation of the heart occasionally exhibit irregularities in both strength and frequency. Since the amplitude, frequency, and waveform of TENG output signals are highly dependent on external mechanical stimuli, the voltage output of the TRI-TENG CCP was evaluated under different strains, compression frequencies, and compression pressures. The amplitude of the output voltage increased as the compression frequency increased from 1 to 5 Hz, and the frequency of the output voltage corresponded well with the applied compression frequency (Figure 4-8A). The amplitude of the output voltage also increased with increasing compressive pressure (Figure 4-8B). The relationship between the relative change in voltage amplitude and pressure is shown in Figure 4-8D. The pressure response can be divided into two regions: a high-sensitivity region (Region I) and a low-sensitivity region (Region II). In Region I, where the pressure was below 5.9 kPa, the TRI-TENG CCP sensor exhibited a sensitivity of 6.74 mV/kPa ($R^2 = 0.979$). In Region II, the sensitivity decreased to 2.54 mV/kPa ($R^2 = 0.991$). The voltage amplitude of the TRI-TENG sensor depends on the change in spatial distance between the P-PVDF layer and the PDA-rGO electrode, the rate of change in this distance, and the triboelectric charge density.[238] In Region I, increasing compressive pressure caused a substantial increase in the separation change between the two layers, resulting in a pronounced increase in voltage amplitude. Near the transition between Region I and Region II, the spatial distance between the layers approached zero, and further pressure mainly increased the contact area between the two layers, exerting a limited influence on the output voltage. In contrast, the voltage amplitude of the TRI-TENG CCP sensor decreased with increasing applied strain (Figure 4-8C). Due to the positive Poisson's ratio of the elastomer spacer, the spatial distance between the two layers decreases as strain increases. Consequently, the voltage amplitude of the TRI-TENG CCP sensor decreased

with increasing strain, showing a sensitivity of −2.65 mV per 1% strain (R^2 = 0.970) (Figure 4-8E).

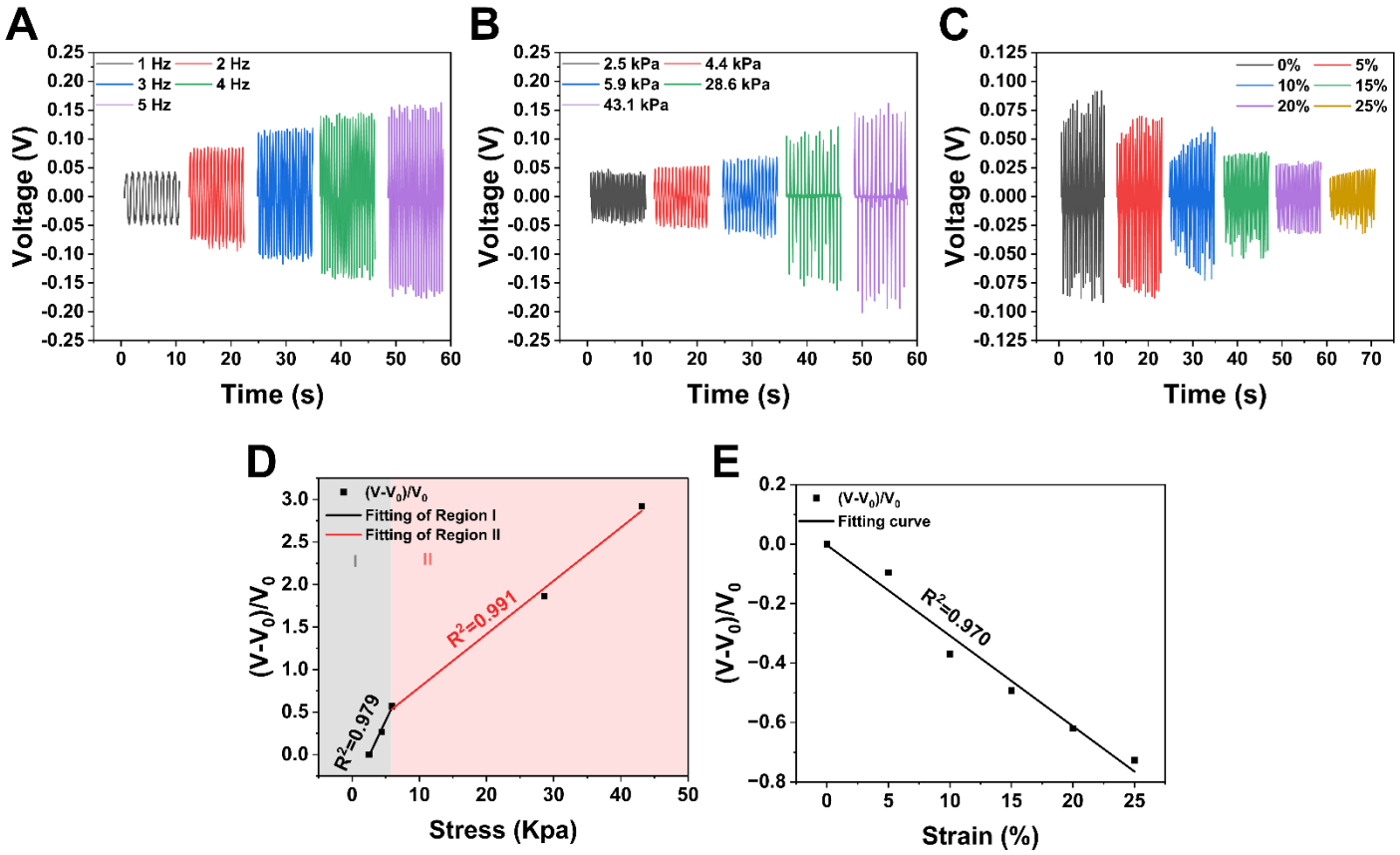

Figure 4-8 The response of TRI-TENG CCP sensor to different stimuli.

The output voltage of the TRI-TENG sensor at (A) different frequencies, (B) different pressures, and (C) different strains. (D) Linear fitting and the relationship between the relative change in voltage amplitude and the applied pressure. (E) Linear fitting and the relationship between the relative change in voltage amplitude and the applied strain.

A single variation in the strain or pressure of mechanical stimuli results in a corresponding change in output voltage, while the frequency of the output voltage reflects the frequency of the mechanical stimulus. The potential of the TRI-TENG CCP as an activity monitoring sensor was therefore evaluated. The TRI-TENG CCP sensor was attached to different locations of the human body using tape to monitor various human activities. The motion of the throat involves small-strain vibrations occurring at specific frequencies; therefore, particular throat movements produced distinct changes in spatial distance between layers, resulting in unique output voltage waveforms (Figure 4-9A). Larger mechanical deformations, such as the bending of the index finger, could also be effectively monitored by the TRI-TENG CCP sensor (Figure 4-9B). The peak output voltage increased with increasing bending angle. The increase in bending angle from 30° to 60° resulted in a greater increase in peak output voltage than that from 60° to 90°, suggesting that the change in spatial distance may approach saturation when the bending angle exceeds 60°. Despite variations in bending angles, finger bending followed a similar motion pattern, resulting in consistent output voltage waveforms. In addition, when the TRI-TENG CCP was attached to the ankle, it was able to monitor the intensity of human activity (Figure 4-9C). As the level of activity increased, both the amplitude and frequency of the output voltage increased accordingly.

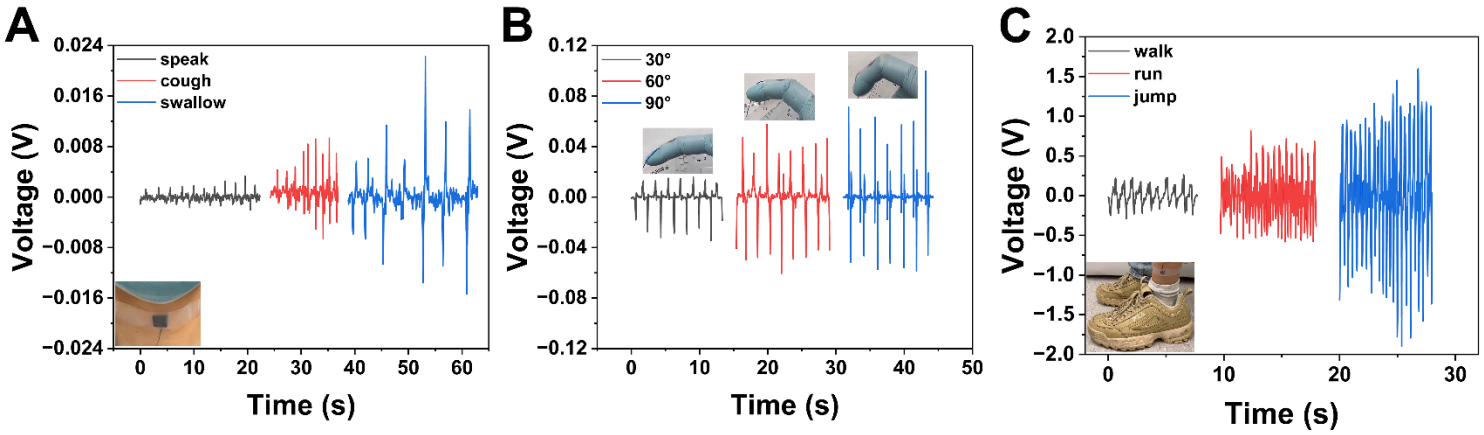

Figure 4-9 Demonstration of the TRI-TENG CCP sensor detecting different mechanical motions.

The TENG is (A) attached to the throat for the detection of speaking, coughing, and swallowing; (B) attached to the fingers for the detection of finger joint movements; and (C) attached to the ankle for the detection of walking, running, and jumping.

4.2.3 TRI-TENG as an Implantable Sensor for *In vivo* Monitoring

The TRI-TENG was implanted between the apex cordis and the pericardium of a minipig to evaluate its in vivo sensing performance (Figure 4-10A, B). The V_{oc} output of the TRI-TENG and electrocardiogram (ECG) signals were recorded simultaneously. The R–R interval of the ECG signal, representing the ventricular rate, was found to correspond to the peak-to-peak interval of the V_{oc} signal (Figure 4-10C). In addition, the number of marked peaks in the V_{oc} signal was equal to that observed in the ECG signal over the same 5 s interval. These observations demonstrate a strong correspondence between the frequency of the ECG signal and the frequency of the TRI-TENG output voltage. The heartbeat of a healthy porcine heart produced an average V_{oc} amplitude of 6.24 ± 1.55 mV.

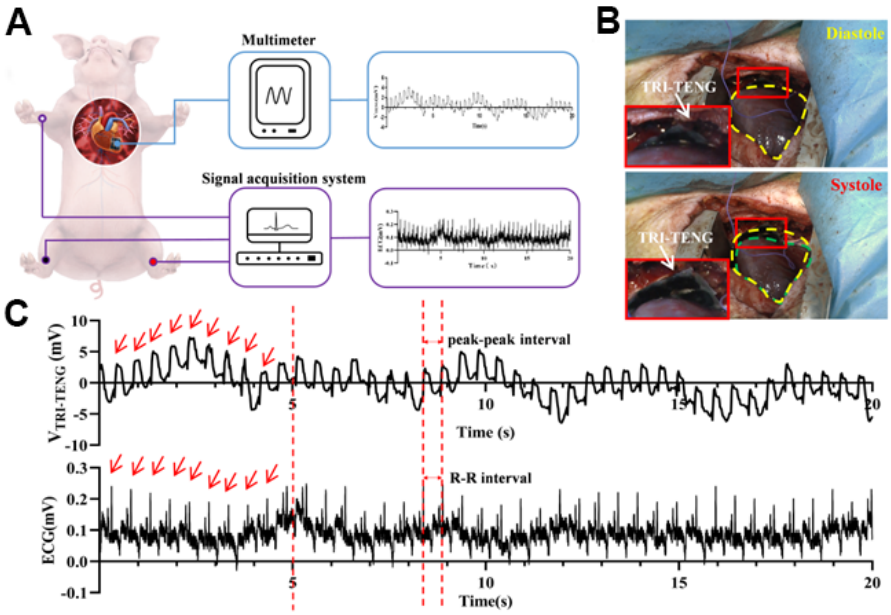

Figure 4-10 The potential application of the TRI-TENG as a real-time *in vivo* cardiac sensor. (A) Schematic illustration of the simultaneous recording of the ECG signals and the V_{oc} output from the TRI-TENG. (B) Photography depicting a TRI-TENG array transplanted between the apex cordis and the pericardium of a minipig under the activities of the heart. The area encircled by the yellow dashes represents the diastolic cardiac contour, and the area enclosed by the green dashes represents the systolic cardiac contour. (C) The simultaneously recorded V_{oc} output of TRI-TENG and the 2-lead ECG signal from the minipig.

The TRI-TENG was transplanted onto an isolated Langendorff-perfused rat heart model to investigate the effects of contractile force and heart rate on the V_{oc} of the TRI-TENG (Figure 4-11A, B). The V_{oc} amplitude of the TRI-TENG on isolated Langendorff-perfused rat hearts that had returned to sinus rhythm was 1.739 ± 0.118 mV (Figure 4-11C). Electrical pacing at 7 Hz was applied to elevate the heart rate to 420 bpm. The V_{oc} frequency of the TRI-TENG implanted on

the isolated heart with an elevated heart rate increased correspondingly and remained consistent with the ECG signals (Figure 4-11A, B). Moreover, the V_{oc} amplitude of the TRI-TENG under elevated heart rate was greater than that observed during sinus rhythm (Figure 4-11C). These results are consistent with the in vitro testing of the TRI-TENG, which demonstrated that increasing the compression frequency increased both the frequency and amplitude of V_{oc}. To further investigate the effect of myocardial infarction on the V_{oc} output of the TRI-TENG, ligation of the left anterior descending (LAD) coronary artery was performed on isolated rat hearts under both sinus rhythm and elevated heart rate conditions. The ischemic injury induced by LAD ligation resulted in a decrease in V_{oc} amplitude (Figure 4-11C), regardless of whether the isolated heart exhibited sinus rhythm or elevated heart rate before ischemia. The loss of contractile myocardium following ischemic injury leads to an acute reduction in cardiac contractility.[239] Since the voltage amplitude of the TRI-TENG mainly depends on the change in spatial distance between the P-PVDF layer and the PDA-rGO electrode, reduced cardiac contractility results in a smaller variation in this distance. Consequently, the V_{oc} amplitude generated by ischemic hearts was lower than that of non-injured hearts (Figure 4-11D). These results suggest that the TRI-TENG array holds significant potential as an implantable sensor for monitoring heart rate and abnormal cardiac contractility.

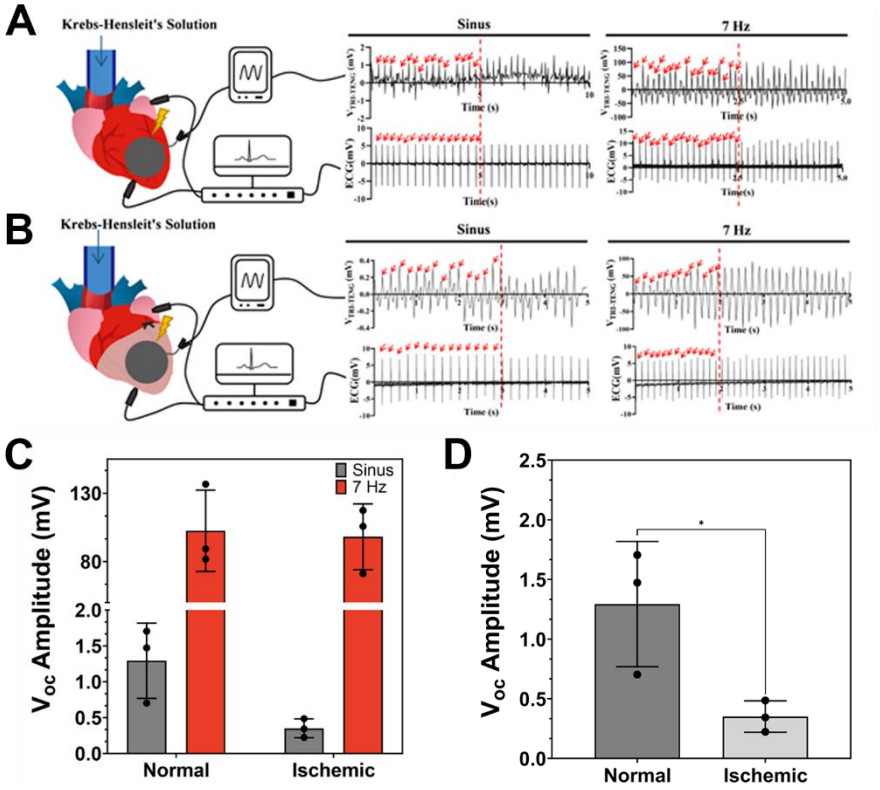

Figure 4-11 Heart rate and myocardial infarction sensing.

The simultaneously recorded V_{oc} output and ECG signals from Langendorff-perfused isolated (A) normal heart (B) heart with ischemic injuries. (C) The statistical analysis of the V_{oc} amplitude of TRI-TENG transplanted on a normal heart ischemic heart with sinus rhythm and 7 Hz spacing. (D) Comparison of the V_{oc} amplitude from the normal heart versus the ischemic heart with sinus rhythm. (*$p < 0.05$)

4.2.4 Effects of TRI-TENG on CM Structure and Maturation

Our previous studies suggest that the surface topography and conductivity of cardiac patches can remodel cardiomyocyte (CM) phenotype and function in vitro, which may play an important role in activating endogenous repair after transplantation. In this study, the cell morphology and cardiac-specific protein expression of neonatal rat CMs cultured on Ecoflex, PDA-rGO/Ecoflex, and TRI-TENG substrates were examined. By day 3 of culture, F-actin staining revealed a greater number of CMs and larger cell spreading areas in the PDA-rGO/Ecoflex and TRI-TENG groups compared with the Ecoflex group (Figure 4-12A, D, E). By day 7, CMs cultured on PDA-rGO/Ecoflex and TRI-TENG exhibited denser and more elongated myofibrils with abundant parallel-aligned actin filaments compared to those on Ecoflex, indicating structural characteristics of enhanced differentiation and maturation. SEM imaging further showed that CMs on PDA-rGO/Ecoflex and TRI-TENG formed confluent myocardial-like structures with clearly visible cell–cell contacts and intercellular connections (Figure 4-12B). Immunostaining of cardiac-specific markers, sarcomeric α-actinin and CX43, demonstrated more developed sarcomeric organization and increased CX43 expression in CMs cultured on PDA-rGO/Ecoflex and TRI-TENG compared with Ecoflex controls at both day 3 and day 7 (Figure 4-12C). Quantitative analysis further showed that the highest α-actinin and CX43 coverage areas were observed in the TRI-TENG group (Figure 4-12F, G). CX43, the main component of gap junctions, plays a crucial role in transmitting electrical excitation signals between CMs.[240] Collectively, these results demonstrate that the PDA-rGO/Ecoflex conductive cardiac patch promotes cardiomyocyte maturation and enhances synchronous electrical excitation. The PDA-rGO composite also exhibited excellent water stability and biocompatibility, enabling enhanced protein adsorption through multiple molecular interactions, including hydrophobic interactions, electrostatic

attraction, and π–π stacking, which contributed to higher cardiomyocyte density on the substrate.[241] Moreover, PDA-rGO demonstrated electrophysiological advantages by reducing cardiomyocyte excitation thresholds and accelerating intercellular electrical signal propagation.[242] When combined with the electrical stimulation generated by TRI-TENG, the system further promoted cardiomyocyte maturation and functional development.

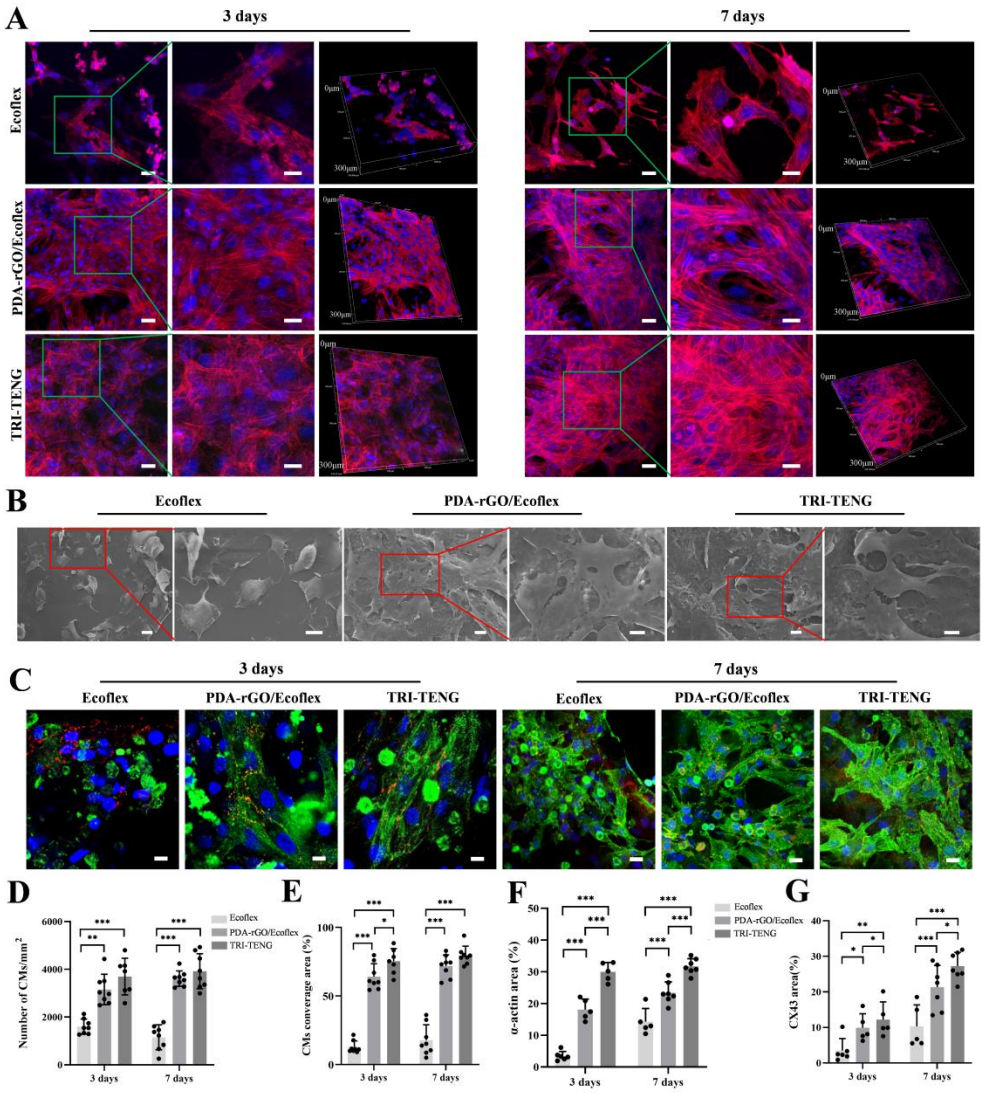

Figure 4-12 Morphology and specific protein expression of neonatal rat CMs on different scaffolds.

(A) The 2D and 3D views of phalloidin (red) and DPAI (blue) staining in CMs in different CPs on days 3 and 7 of culture. Scale bars: 10 μm. (B) Scanning electron microscopy images of CMs on the Ecoflex, PDA-rGO/Ecoflex, and TRI-TENG. (C) Expressions of α-actinin (green) and CX43 (red) proteins in CMs in different CPs on days 3 and 7 of culture. (D, E) Quantification of CMs number (D) and CMs coverage area (E) based on the fluorescence images of phalloidin staining (Ecoflex n=6, PDA-rGO/Ecoflex n=8, TRI-TENG n=7 fields from 5 distinct samples on day 3, Ecoflex n=8, PDA-rGO/Ecoflex n=8, TRI-TENG n=8 fields from 5 distinct samples on day 7). (F, G) Quantitative analyses of α-actinin (F) and CX43 (G) fluorescent intensity (Ecoflex n=6, PDA-rGO/Ecoflex n=5, TRI-TENG n=5 fields from 5 distinct samples on day 3; Ecoflex n=5, PDA-rGO/Ecoflex n=7, TRI-TENG n=7 fields from 5 distinct samples on day 7). The data were presented as mean ± SD. One-way ANOVA, *P < 0.05, **P < 0.01, ***P < 0.001.

4.2.5 TRI-TENG Improves Cardiac Electroactivity in Rat MI Models

The effects of TRI-TENG on the electrical properties of the injured myocardium were further investigated. Infarcted myocardium exhibits impaired contractile function due to excitation–contraction uncoupling, which can lead to decompensated hypertrophy and progressive deterioration of cardiac function.[243] Enhanced electrical sensitivity and contractility can restore functional activity in the injured myocardium and prevent further cardiac dysfunction.[244] s shown in Figure 4-13A–C, ligation of the left anterior descending (LAD) coronary artery induced myocardial injury and reduced electrical excitability in Langendorff-perfused rat hearts, as indicated by increased pacing thresholds. Notably, transplantation of the TRI-TENG reduced the pacing threshold of the rat heart, meaning that lower stimulus voltage pulses were sufficient to

trigger synchronous pacing of the entire heart in both TRI-TENG-transplanted normal hearts and TRI-TENG-transplanted injured hearts (Figure 4-13A–C). We further examined whether the TRI-TENG-mediated enhancement of electrical sensitivity was accompanied by improved myocardial contractility (Figure 4-13D–I). Under identical electrical stimulation, left ventricular (LV) contractility increased by approximately twofold after TRI-TENG transplantation onto the rat LV compared with the contractility before transplantation (Figure 4-13F, G). Furthermore, after TRI-TENG transplantation onto infarcted hearts in rat MI models for four weeks, the contractility of the infarcted LV was significantly greater than that in the MI group without treatment (Figure 4-13H, I). These results indicate that the microcurrent generated by TRI-TENG exerts both immediate and sustained effects on electrical excitation in injured hearts, which can be coupled with myocardial contraction to enhance the contractility of infarcted hearts. In contrast, the conductive patch alone appeared to have minimal influence on immediate electrical excitation and contractility. We propose that the conductive patch improves contractility indirectly by promoting structural and functional myocardial recovery during the four-week post-transplantation remodeling process.[245]

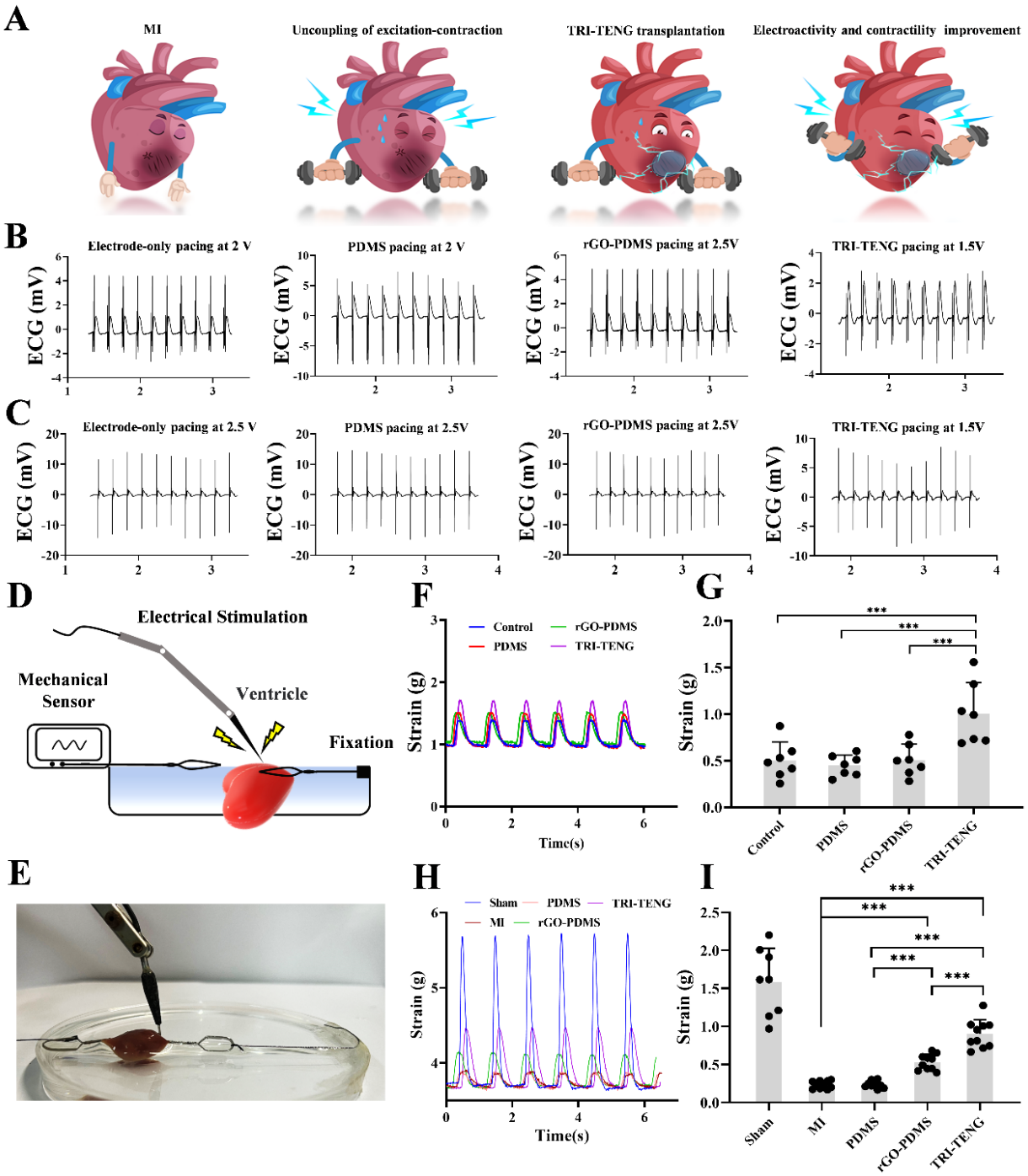

Figure 4-13 The impact of TRI-TENG transplantations on the excitation-contraction coupling of rat hearts.

(A) Schematic illustrating the augmented effects of TRI-TENG transplantation on excitation-contraction coupling in the infarcted rat heart. (B, C) Pacing thresholds of the Langendorff-

perfused whole heart in different groups under various normal conditions (B) and ischemic conditions (C). (D, E) Schematic representation (D) and Profile display (E) of contractility measurements in ventricular tissue. (F to I) Contraction waves (F, H) and contractility analyses (G, I) of the ventricular tissues were assessed under 1 Hz pulse stimulation in different groups following the patches' transient transplantation on the normal heart (F, G) or patches' transplantation on the infarcted heart for a duration of 4 weeks (H, I). The data were presented as mean ± SD. ***P < 0.001.

Electrical mapping and optical mapping were performed to further investigate electrophysiological reconstruction of the infarcted heart after 4 weeks of patch transplantation. Epicardial electrical mapping collected and analyzed the electrical activity of the left ventricular (LV) free wall to generate electrical conduction velocity (CV) maps spanning from non-infarcted to infarcted myocardium.[246] As shown in Figure 4-14A, the MI and PDMS groups exhibited inhomogeneous conduction and delayed electrical propagation. In contrast, transplantation of rGO-PDMS or TRI-TENG significantly accelerated excitation propagation between healthy and infarcted myocardium, with the TRI-TENG group showing the highest CV among all transplantation groups (Figure 4-14A–D). Surface electrocardiogram (ECG) signals were simultaneously recorded during electrical mapping (Figure 4-14B). Consistent with the CV maps, prolonged QRS durations in ECG recordings indicated abnormal ventricular conduction in the MI and PDMS groups (Figure 4-14B, E).[247] Transplantation of rGO-PDMS or TRI-TENG shortened the QRS duration, and notably, the QRS duration in the TRI-TENG group was comparable to that in the sham group (Figure 4-14B, E). Field potentials in remote, border, and scar regions were also measured using the electrical mapping system. As shown in Figure 4-14C, PDMS transplantation

had little effect on the global field potential of the infarcted heart. Although the border/remote and scar/remote field potential amplitude ratios increased in the rGO-PDMS group compared with the MI group, the increase in the border/remote ratio was not statistically significant (Figure 4-14C, F, G). The TRI-TENG-treated hearts exhibited the highest border/remote and scar/remote field potential amplitude ratios among all transplantation groups, suggesting that both conductive patches and conductive patches integrated with self-powered nanogenerators can enhance regional electrical activity and improve global electrical impulse propagation in infarcted hearts, with TRI-TENG showing the most pronounced effect.

Optical mapping was subsequently conducted to evaluate transmembrane action potentials (V_m) and Ca^{2+} handling dynamics in Langendorff-perfused isolated hearts from different groups. Electrical propagation and calcium transient fluorescence signals were recorded from RH237 (voltage-sensitive dye) and Rhod-2 AM (Ca^{2+} indicator)-stained hearts during 5 Hz point stimulation (Figure 4-14H). As expected, myocardial infarction disrupted action potential propagation and caused Ca^{2+} handling abnormalities in the left ventricular myocardium (Figure 4-14I, J). In contrast, TRI-TENG transplantation markedly improved action potential propagation and Ca^{2+} dynamics in the infarcted left ventricle (Figure 4-14H–J). Disordered electrical propagation and calcium transient patterns typically lead to repolarization heterogeneity in the myocardium.[248] As shown in Figure 4-14K, L, myocardial infarction prolonged both the action potential duration at 90% repolarization (APD_{90}) and the calcium transient duration at 90% (CaD_{90}). After 4 weeks of TRI-TENG treatment, these prolonged APD_{90} and CaD_{90} values were significantly reduced, indicating recovery of electrophysiological function in the infarcted myocardium. These results suggest that TRI-TENG transplantation accelerates repolarization of

injured ventricular myocardium and reduces the risk of calcium-dependent gap junction uncoupling and malignant arrhythmias in infarcted hearts.

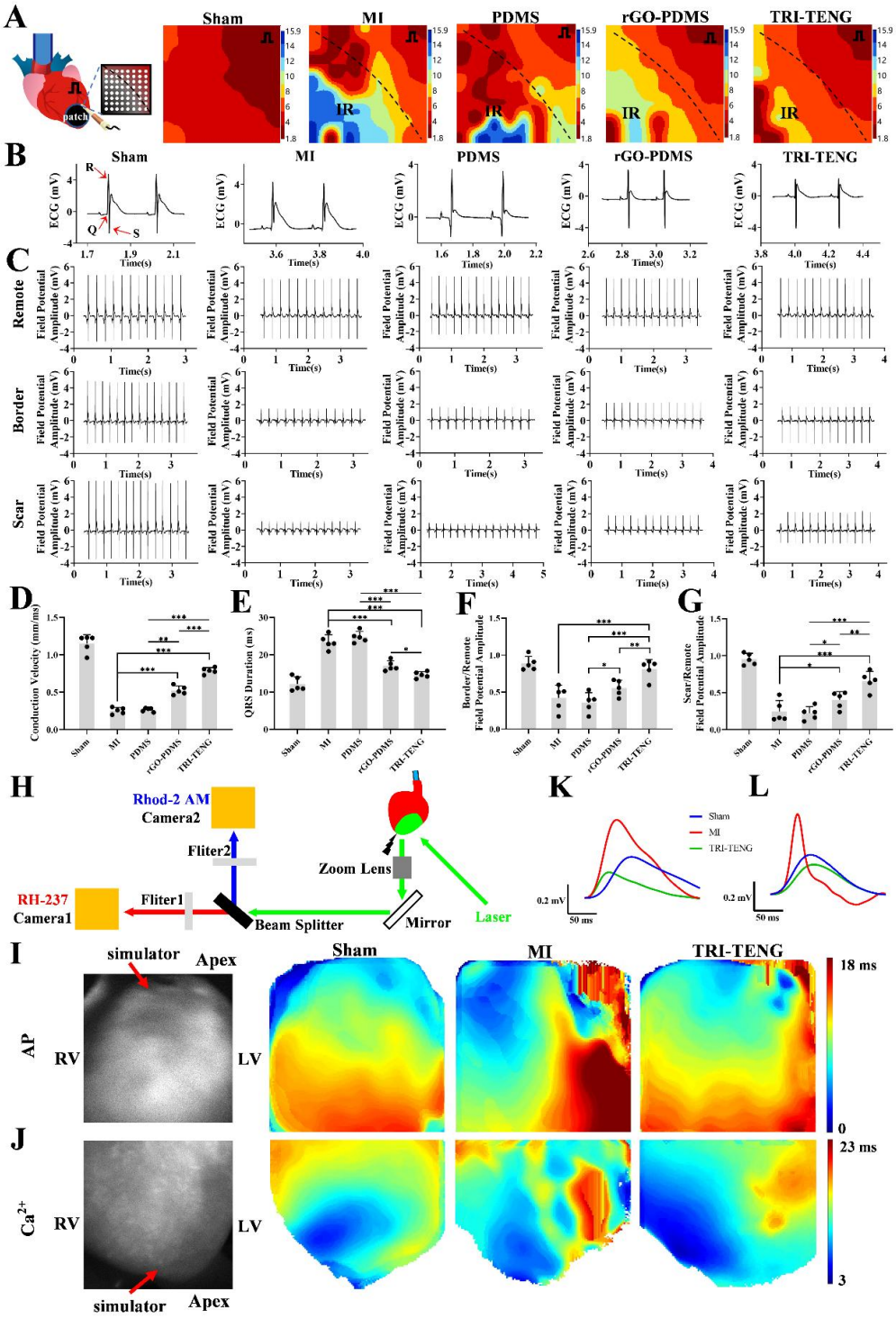

Figure 4-14 Electrical mapping and optical mapping for the Langendorff-perfused hearts at week 4 after patches' transplantation.

(A) The schematic diagram of electrical mapping from Langendorff-perfused hearts in different groups at week 4 post-transplantation. The stimulating electrode was positioned inferior to the right atrial appendage, while an electrode array consisting of 64 electrodes was placed at the border zone. Representative epicardial activation maps in all groups were displayed. The dark lines demarcated the boundary between the non-infarcted and infarcted myocardium. IR means infarcted region. The red color indicates the earliest activation, while blue represents the latest activation. The numerical values on the heat map scale correspond to the time of activation in milliseconds. (B) Representative ECG traces of different groups. c, The field potential amplitude of the remote area, border area, and scar area in different groups at week 4 post-transplantation. (D) The conduction velocity of different groups based on the electrical mapping heat maps was calculated. The data were presented as mean ± SD. **P <0.01， ***P < 0.001. The QRS duration of different groups was calculated from the ECG. The data were presented as mean ± SD. *P <0.05 ， ***P < 0.001. (F, G) The statistical analysis of the border/remote field potential amplitude (f) and the scar/remote field potential amplitude (g) ratios in different groups. The data were presented as mean ± SD. *P <0.05， **P <0.01， ***P < 0.001. (H) Schematic of a setup for dual optical mapping of Rhod-2 AM-reported Ca^{2+} transients and RH237-reported transmembrane voltage in Langendorff-perfused rat hearts. (I, J) The optical mapping images of action potential (AP) (I) and ventricular Ca^{2+} transients initiation (J) from the Langendorff-perfused hearts in different groups at week 4 post-transplantation. (K, L) Representative optical traces of V_m (K) and Ca2+ transient (L) in the different groups.

4.2.6 TRI-TENG therapy for infarcted heart in rat and porcine MI models

The enhanced electroactivity provided by the TRI-TENG CCP suggests a promising reparative effect for injured myocardial tissue. Accordingly, the therapeutic efficacy of the TRI-TENG CCP was evaluated in rat and minipig MI models at 4 weeks after transplantation. Masson's trichrome staining of cardiac sections from rat experiments showed that the infarcted myocardium in the MI group was almost completely replaced by fibrotic scar tissue, accompanied by the largest infarct area and the thinnest LV wall thickness. The PDMS group showed negligible differences compared with the MI group in terms of infarct size and LV wall thickness, whereas the rGO-PDMS and TRI-TENG groups exhibited a pronounced reduction in fibrosis within the infarct region, characterized by significantly decreased infarct size and increased LV wall thickness (Figure 4-15A–C). Consistent with Masson's staining results, immunostaining revealed strong expression of α-actinin and CX43 in the infarct regions of rats treated with rGO-PDMS and TRI-TENG, while minimal expression was detected in the MI and PDMS groups (Figure 4-15D). Notably, the TRI-TENG group displayed the highest positive expression density of α-actinin and CX43 within the infarct area. Cardiac function was further evaluated using echocardiography at 2 and 4 weeks after transplantation. Echocardiographic images revealed severe ventricular dilation and reduced LV anterior wall motion in both the MI and PDMS groups. In contrast, the rGO-PDMS group exhibited partially improved pumping activity, while the TRI-TENG–treated hearts demonstrated more pronounced wall motion (Figure 4-15E). Quantitative echocardiographic analysis showed decreased EF and FS, along with increased LVIDd and LVIDs, indicating deteriorated cardiac function in the MI and PDMS groups (Figure 4-15F). In contrast, rGO-PDMS and TRI-TENG transplantation improved cardiac function, as evidenced by increased ΔFS% and ΔEF% and decreased LVIDs (Figure 4-15F, G), indicating enhanced cardiac pumping ability and

reduced compensatory ventricular dilation. Among all groups, the TRI-TENG group exhibited the highest ΔFS% and ΔEF%, resulting in the most significant recovery of cardiac function. Collectively, these results demonstrate for the first time that the TRI-TENG CCP, which integrates electrical stimulation and conductivity within a single cardiac patch, is superior to traditional conductive cardiac patches in promoting myocardial repair and restoring cardiac function.

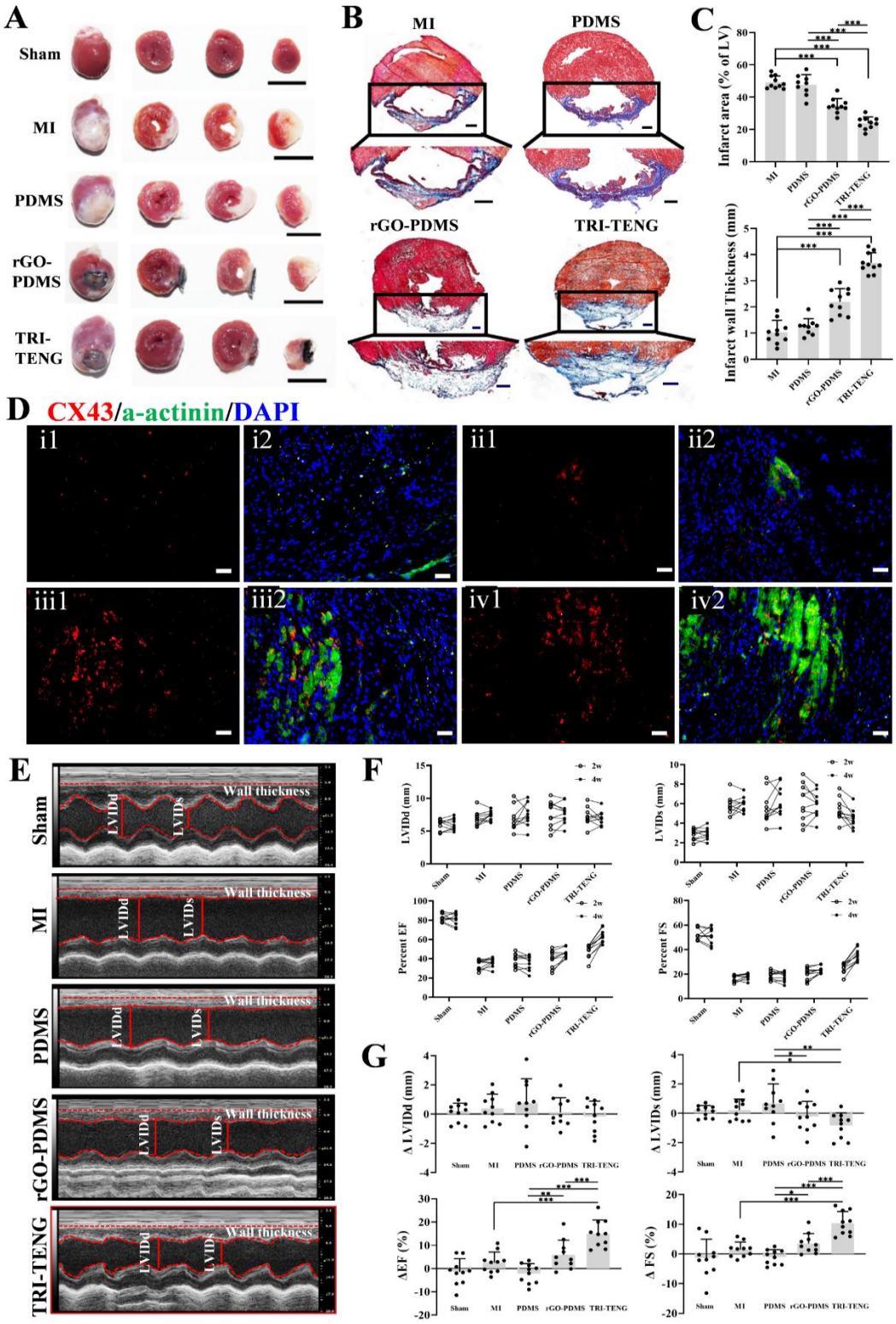

Figure 4-15 The histological examination and assessment of cardiac function on rat hearts from different groups at week 4 after transplantation.

(A) Gross observations of the whole heart and three cross sections of the heart in different groups. Scale bars: 1cm. (B) Masson's Trichrome staining for cardiac sections in different groups. Blue: fibrosis tissue; red: myocardium. Scale bars: 1mm. (C) The quantitative comparisons of the infarct area and infarct wall thickness among the study groups. (D) Immunofluorescent staining of CX43 (red) and α-actinin (green) proteins in the infarct areas in different groups. Scale bars: 10 μm. (E) The echocardiograms of LV contraction in different groups. (F) Changes of FS, EF, LVIDs, and LVIDd in different groups were determined by echocardiography at 2 weeks and 4 weeks after transplantation. (G) The statistical results of the changes of the FS, EF, LVIDs, and LVIDd in different groups measured by echocardiography. The data were presented as mean ± SD. *P < 0.05, **P < 0.01, ***P < 0.001.

Given that the structure and physiological function of porcine hearts closely resemble those of human hearts,[12] we further evaluated the therapeutic efficacy of TRI-TENG in a minipig MI model after 4 weeks of transplantation (Figure 4-16A). A TRI-TENG array (3 cm × 3 cm) was designed to match the clinically relevant size of the Bama minipig heart.[249] At 4 weeks post-transplantation, the hearts were harvested for morphometric and histological analyses (Figure 4-16A, B). Gross examination showed that hearts treated with the TRI-TENG array exhibited smaller infarct areas and thicker anterior ventricular walls compared with untreated MI hearts (Figure 4-16B). Masson's Trichrome staining further revealed extensive fibrotic tissue formation in the infarct region of the MI group, whereas TRI-TENG array transplantation reduced myocardial fibrosis and promoted the formation of new myocardium (Figure 4-16C). Consistently, immunofluorescence staining demonstrated that TRI-TENG–treated hearts exhibited more mature myocardial tissue and increased CX43 expression (Figure 4-16D). In addition, ex vivo electrical

signal propagation was evaluated in freshly excised porcine hearts from the sham, MI, and TRI-TENG array groups, which were immediately immersed in KH solution to maintain physiological activity, using ECG measurements with a signal acquisition system (Figure 4-16E). Under identical electrical stimulation, the local field potential amplitude of the MI group was significantly reduced, whereas the TRI-TENG array group exhibited approximately a fivefold increase in local field potential amplitude compared with the MI group (Figure 4-16F, G). The enhanced electroactivity improved contractile synchrony in the injured myocardium, contributing to functional recovery of cardiac performance. Accordingly, echocardiography was performed before MI induction and again at 4 weeks after surgery to evaluate cardiac functional changes among the groups. While the MI group displayed impaired contractility of the left ventricular anterior wall, hearts treated with the TRI-TENG array exhibited restored wall motion and contractile function (Figure 4-16H). Quantitative analysis showed that FS and EF derived from the short-axis view of the left ventricle were significantly reduced in the MI group at 4 weeks after surgery but were markedly increased in the TRI-TENG array group compared with the MI group (Figure 4-16I–L).

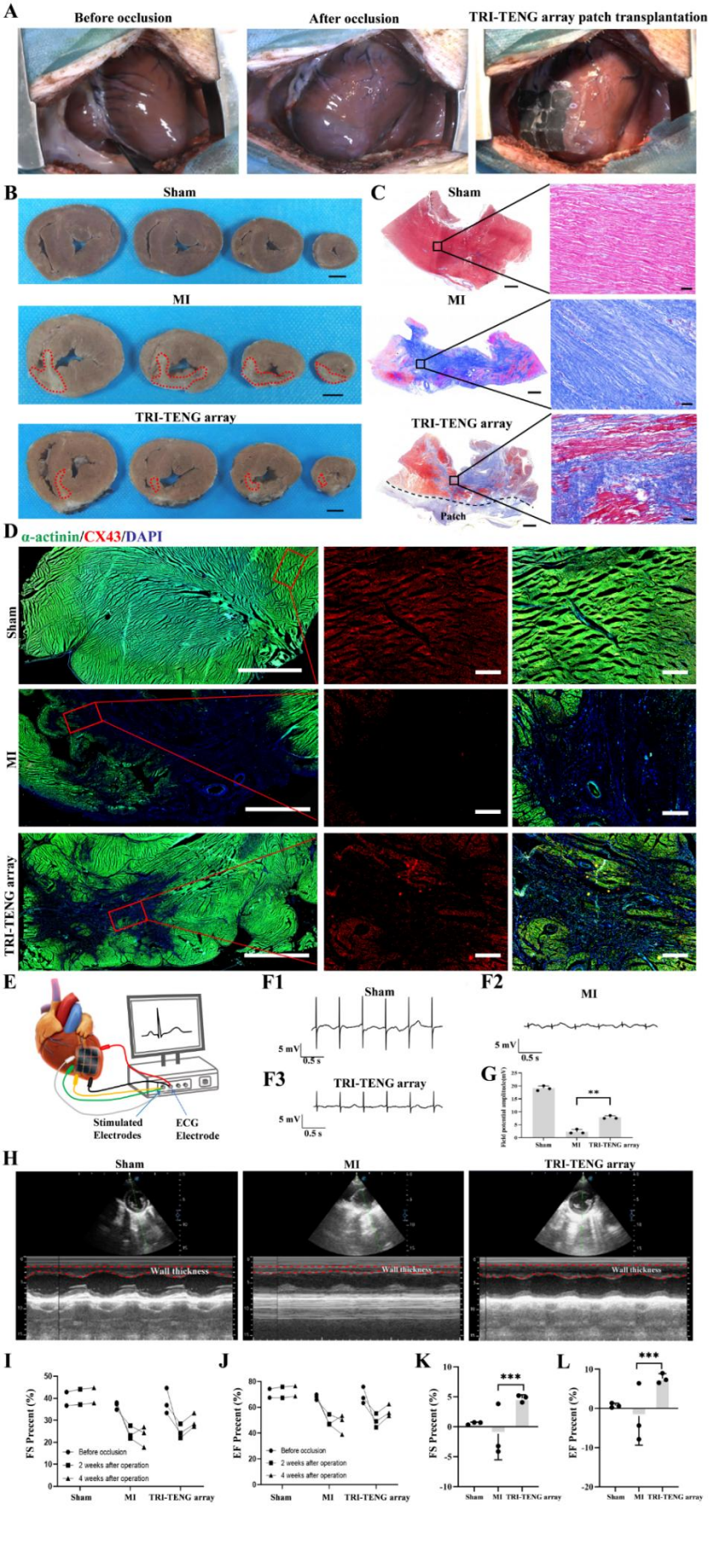
A
Before occlusion
After occlusion
TRI-TENG array patch transplantation
B
Sham
MI
TRI-TENG array
C
Sham
MI
TRI-TENG array
Patch
D
α-actinin/CX43/DAPI
Sham
MI
TRI-TENG array
E
Stimulated Electrodes
ECG Electrode
F1
Sham
5 mV
0.5 s
F2
MI
5 mV
0.5 s
F3
TRI-TENG array
5 mV
0.5 s
G
Field potential amplitude(mV)
**
Sham
MI
TRI-TENG array
H
Sham
MI
TRI-TENG array
Wall thickness
Wall thickness
Wall thickness
I
FS Precent (%)
Before occlusion
2 weeks after operation
4 weeks after operation
Sham
MI
TRI-TENG array
J
EF Precent (%)
Before occlusion
2 weeks after operation
4 weeks after operation
Sham
MI
TRI-TENG array
K
FS Precent (%)
***
Sham
MI
TRI-TENG array
L
EF Precent (%)
***
Sham
MI
TRI-TENG array

Figure 4-16 The treatment effect of TRI-TENG array for the infarcted heart in porcine MI models.

(A) Representative macroscopic images of the minipig hearts pre- and post-occlusion, as well as following transplantation of the TRI-TENG array onto the heart. (B) Representative transverse sections of hearts from sham, MI, and TRI-TENG array transplantation groups after 4 weeks. The heart was cut into four layers from apex to the level of ligation. The scar region was highlighted in the sections. Scale bars, 2 cm. (C) Representative images showing myocardial fibrosis stained with Masson's Trichrome of cardiac sections in different groups. Scale bars, 2000 μm (left) and 50 μm (right). (D) The expressions of α-actinin (green) and CX43(red) proteins in porcine cardiac sections from various groups. Scale bars, 5000 μm (left) and 500 μm (mid and right). (E) Schematic representation of the assessment of electrical responses in infarcted myocardium in ex vivo porcine hearts using a signal acquisition system. (F) Representative ECG traces of the stimulation signal from ex vivo hearts in the sham (F1), MI (F2), TRI-TENG array (F3) groups. (G) The amplitude of the local field potential was subjected to statistical analysis across various groups. Data were presented as mean ± SD. **$P < 0.01$. (H) Echocardiographic parasternal short-axis views of the minipigs' LV in different groups at the papillary-muscle level at 4 weeks after operation. (I, J) The change of FS (I) and EF (J) in different groups before occlusion, as well as at 2 and 4 weeks post-operation. (K, L) Statistical analysis of the changes of FS (K), EF (L) in different groups at 4 weeks after transplantation. The data were presented as mean ± SD. ***$P < 0.001$.

4.2.7 Whole-Transcriptome RNA Sequencing Analysis of Gene Expression Changes in Different Regions of Infarcted Heart

TRI-TENG exhibits remarkable reparative effects on infarcted hearts in both rat and pig models, which are primarily attributed to its ability to enhance the electroactivity of the infarcted myocardium. However, further investigation is required to elucidate the underlying mechanisms at the genetic level. After 4 weeks of transplantation, rat hearts from the sham, MI, PDMS, rGO-PDMS, and TRI-TENG groups were harvested, and tissues from the infarct region (IR) and border region (BR) were dissected for RNA sequencing (RNA-seq) to evaluate changes in gene expression. Principal component analysis (PCA) showed that samples from the IR or BR of the PDMS and MI groups were tightly clustered, indicating minimal differences in gene expression between these two groups (Figure 4-17A). In contrast, clear separations were observed between the rGO-PDMS and MI groups as well as between the TRI-TENG and MI groups, suggesting significant transcriptional differences. Consistently, pyramid diagrams and volcano plots of differentially expressed genes (DEGs) demonstrated that the TRI-TENG and rGO-PDMS groups exhibited a much greater number of DEGs compared with the MI group, whereas the PDMS group showed gene expression patterns similar to those of the MI group (Figure 4-17B, C). Cluster analysis of perturbed genes using the TCseq package identified two major gene clusters (cluster 1 and cluster 2), and hierarchical clustering heatmaps were generated based on the gene expression patterns within these clusters (Figure 4-17D–F). Genes in cluster 1 exhibited low expression in the sham group but were upregulated in the MI group; following treatment, their expression levels decreased, with TRI-TENG showing the most pronounced downregulation toward levels comparable to the sham group. In contrast, genes in cluster 2 showed high expression in the sham group but were downregulated in the MI group; therapeutic interventions restored their expression,

with TRI-TENG showing the strongest upregulation toward the sham level. Furthermore, the gene expression heatmap revealed marked upregulation of genes associated with cardiac conduction (*Dsc2, Hrc, Kcna5, Scn4b, Tnni3k*), calcium handling (*Cxcl11, Dhrs7c, Fhl2, Gbp1, Pdk2, Stc2*), cardiac muscle contraction (*Asb15, Atp2a2*, *Fgf13, Myh6, Scn5a, Tmem38a*), angiogenesis (*Angpt1, Igf2, Il1a, Rgcc, Vegfb*) and wound healing (*Celsr1, Gp1ba, Habp2, Klkb1, Ppara, Prkce*) in the IR of the TRI-TENG and rGO-PDMS groups compared with the MI and PDMS groups, with the TRI-TENG group exhibiting the highest expression levels (Figure 4-17G). These results indicate that TRI-TENG and rGO-PDMS transplantation significantly modulate signaling pathways related to cardiac contraction, energy metabolism, extracellular matrix–receptor interactions, and inflammatory responses, reflecting molecular-level adaptations to the ischemic/hypoxic microenvironment and demonstrating their reparative effects on MI. Notably, the superior reparative effect of TRI-TENG compared with rGO-PDMS is largely attributed to its intrinsic self-powered property, which enables the conversion of cardiac mechanical activity into electrical stimulation that activates infarcted tissue. Through this mechanism, TRI-TENG enhances cardiac conduction, calcium handling, energy metabolism, myocardial contractility, and angiogenesis, thereby promoting the repair and regeneration of infarcted myocardium.

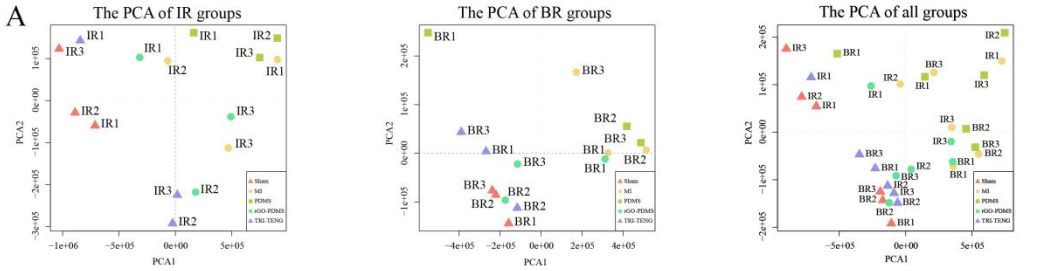

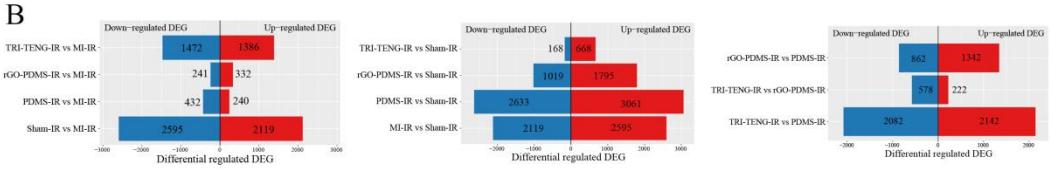

	Down-regulated	Up-regulated	Total DEGs
TRI-TENG-IR vs MI-IR	1473	1386	2859
rGO-PDMS-IR vs MI-IR	241	332	573
PDMS-IR vs MI-IR	432	240	672
Sham-IR vs MI-IR	2595	2119	4714

	Down-regulated	Up-regulated	Total DEGs
TRI-TENG-IR vs Sham-IR	168	668	836
rGO-PDMS-IR vs Sham-IR	1019	1795	2814
PDMS-IR vs Sham-IR	2633	3061	5694
MI-IR vs Sham-IR	2119	2595	4714

	Down-regulated	Up-regulated	Total DEGs
rGO-PDMS-IR vs PDMS-IR	862	1342	2204
TRI-TENG-IR vs rGO-PDMS-IR	578	222	800
TRI-TENG-IR vs PDMS-IR	2082	2142	4224

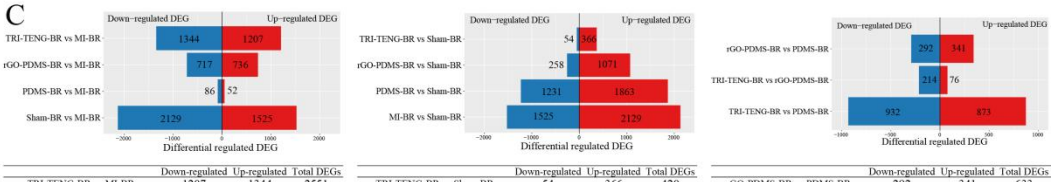

	Down-regulated	Up-regulated	Total DEGs
TRI-TENG-BR vs MI-BR	1207	1344	2551
rGO-PDMS-BR vs MI-BR	717	736	1472
PDMS-BR vs MI-BR	86	52	138
Sham-BR vs MI-BR	2129	1525	3654

	Down-regulated	Up-regulated	Total DEGs
TRI-TENG-BR vs Sham-BR	54	366	420
rGO-PDMS-BR vs Sham-BR	258	1071	1329
PDMS-BR vs Sham-BR	1231	1863	3094
MI-BR vs Sham-BR	1525	2129	3654

	Down-regulated	Up-regulated	Total DEGs
rGO-PDMS-BR vs PDMS-BR	292	341	633
TRI-TENG-BR vs rGO-PDMS-BR	214	76	290
TRI-TENG-BR vs PDMS-BR	932	873	1805

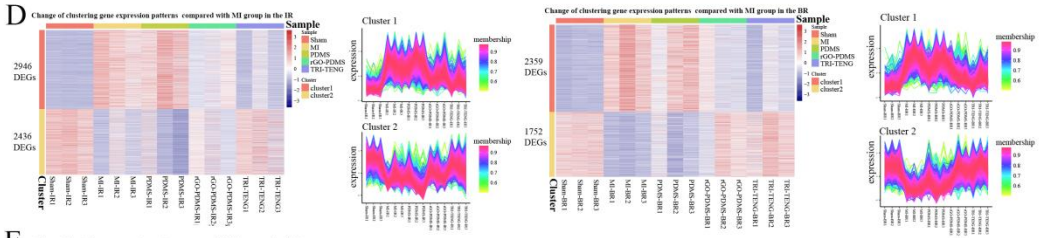

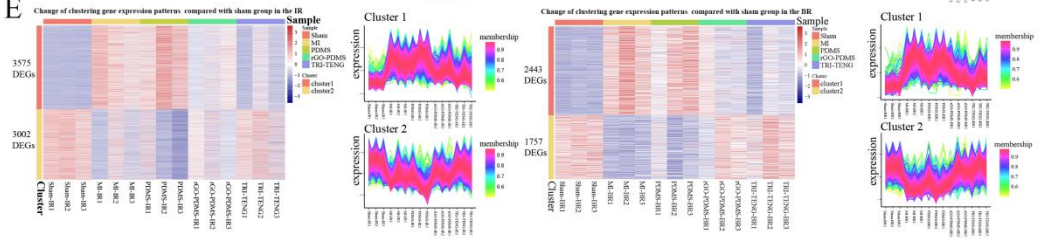

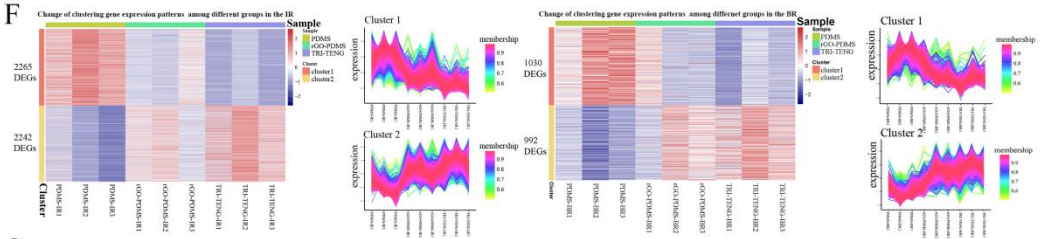

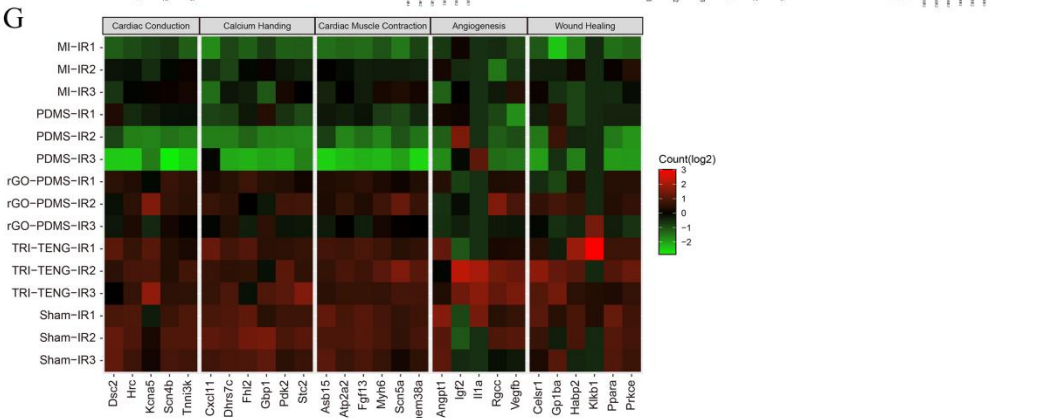

Figure 4-17 Gene expression pattern analysis for the infarct region (IR) and border region (BR) of rats in different groups at 4 weeks after transplantation by RNA-Seq.

(A) Principal component analysis (PCA) of the IR samples (left), the BR samples (middle), and all samples (right). (B, C) Differentially expressed genes (DEGs) in each pairwise comparison in the IR (B) and the BR (C). Upper: pyramid diagrams of the number of DEGs. Red represents the number of upregulated genes, blue represents the number of downregulated genes. Lower: the tables of the number of down-regulated genes, up-regulated genes, and total DEGs. (D) Clustering trend analysis based on the union of differential genes comparing the groups (sham, Ecoflex, PDE, and TRI-TENG) vs the MI group in the IR (left) and the BR (right). (E) Clustering trend analysis based on the union of differential genes comparing the groups (MI, Eco f lex, PDE, and TRI-TENG) vs the sham group in the IR and the BR. (F) Clustering trend analysis based on the union of differential genes comparing TRI-TENG vs Ecoflex, TRI-TENG vs PDE, and PDE vs Ecoflex in the IR and the BR. Left: Hierarchical clustering heatmap, right: gene expression trend diagram in the (D–F). (G) Gene expression heatmap of the specified function-related genes in different groups. Green, low expression. Red, high expression.

4.3 Conclusions

In this study, a biomimetic TRI-TENG was developed. Through a unique double-spacer design, the TRI-TENG integrates energy harvesting, therapeutics, and sensing within a single cardiac patch. In this configuration, the first spacer layer directly establishes an electrical potential on the myocardium, while the second spacer layer further amplifies the generated potential. Inspired by natural structures, surface modifications including a leaf-vein structure and PDA coating were introduced to increase the surface roughness of the TRI-TENG components, thereby enhancing triboelectric charge generation during contact electrification. Multiple TRI-TENG units were connected using tiny PEDOT: PSS/GelMA solder and organized into an array configuration to enable conformal integration with large-area curved surfaces. The TRI-TENG demonstrated potential as a wearable sensor for monitoring various human strain activities and as an implantable sensor for monitoring heart rate and abnormal cardiac contractility in an isolated Langendorff-perfused rat heart model.

5 Chapter 5: Summary and Future Work

5.1 Summary

The candidacy proposal reports two CCPs designed to achieve repair and sensing of infarcted myocardium: (I) an ultra-thin and highly conformable GO membrane with asymmetric hydrophobicity/hydrophilicity that exhibits moisture-responsive actuation and sensitivity to multiple stimuli, and (II) a TRI-TENG capable of directly generating electrical stimulation and detecting cardiac abnormalities. The development of these two CCP systems successfully addressed all the challenges outlined in Chapter 1.

In Project I, a multifunctional GO ink was developed. After simple thermal treatment, the GO ink could be used for direct ink writing (DIW) printing to fabricate an ultra-thin GO microlattice. In addition, the GO ink could be applied in a "masked spin coating" technique to fabricate wearable electronic devices. Controlled chemical reduction was used to generate an asymmetric hydrophilic/hydrophobic GO/rGO structure in both the microlattice and wearable electronics. A PDA coating was deposited on the rGO surface of the GO/rGO microlattice to enhance cell adhesion. The ultrathin thickness, DIW-printed microlattice geometry, and asymmetric GO/rGO structure endowed the DrGOM with moisture-responsive actuation, enabling it to spontaneously attach to and encapsulate the myocardium. The DrGOM promoted the growth, adhesion, maturation, communication, and synchronous contraction of cardiomyocytes (CMs). In addition, the DrGOM enhanced vascularization both in vitro and in vivo. In the rat myocardial infarction model, the DrGOM improved cardiac function and reduced the infarct size. Furthermore, the GO/rGO structure enabled the wearable GO/rGO sensing modules to detect multiple cardiac physiological signals.

In Project II, a TRI-TENG was developed based on drop-cast rGO electrodes. PDA coating was applied to modify the rGO electrode surface and improve its biocompatibility. The triboelectric PVDF layer was patterned with a leaf-vein structure using mold casting. Both the PDA coating and the leaf-vein structure are nature-inspired surface modifications that increase surface roughness and effective contact area cost-effectively. In the double-spacer design, the first spacer allows the PDA-rGO electrode to function simultaneously as a triboelectric electrode that generates triboelectric charges and as a therapeutic electrode that establishes an electrical potential on the myocardium. Moreover, the excellent conductivity of the PDA-rGO electrode facilitates electrical signal propagation within ischemic myocardium. The second spacer further amplifies the potential generated between the PDA-rGO electrode and the myocardium to a level comparable to that between the PDA-rGO electrode and the leaf-vein-structured PVDF layer. The V_{oc} of the TRI-TENG is highly sensitive to variations in the frequency and magnitude of applied mechanical stress. Consequently, the TRI-TENG can monitor myocardial infarction by detecting changes in heart rate and cardiac contractility.

The two cardiac patches share several similarities; however, the TRI-TENG cardiac patch demonstrates more advanced capabilities than the DrGOM patch in myocardial infarction repair and sensing. Both systems are biocompatible and electrically conductive, with their conductivity and biocompatibility derived from the incorporation of PDA/rGO. Both patches are also highly conformable, although their conformability arises from different design strategies. The conformability of the DrGOM results from its ultrathin thickness and 4D-printed mesh architecture, whereas the conformability of the TRI-TENG patch originates from its array-based structural design.

Both systems can repair myocardial infarction through distinct mechanisms. The therapeutic efficacy of the DrGOM relies on the integration of cardiomyocytes and their conductive network, which facilitates electrical signal propagation across the infarcted region. In contrast, the TRI-TENG patch not only provides electrical conductivity but also actively generates electrical stimulation, enabling significant therapeutic effects without requiring stem cell loading. Therefore, in terms of myocardial repair, the TRI-TENG patch represents a more advanced and cost-effective strategy than the DrGOM patch.

In addition to their therapeutic functions, both systems possess sensing capabilities. The sensing function of the DrGOM is based on the stimulus-responsive behavior of GO/rGO sensing modules toward multiple environmental cues. In comparison, the sensing capability of the TRI-TENG patch relies on variations in its V_{oc} in response to mechanical stimuli. The TRI-TENG cardiac patch demonstrates the potential for wireless, real-time cardiac health monitoring. In contrast, the sensing study of the DrGOM is limited to calibration of the GO/rGO bilayer under various external stimuli.

5.2 Limitation

A key limitation of the two cardiac patches is their lack of injectability, which necessitates open surgical implantation to deliver them to the infarcted myocardium. This requirement increases procedural invasiveness and reduces their clinical practicality. In addition, neither cardiac patch enables three-dimensional high-resolution spatiotemporal cardiac mapping. The degradation behavior of both patches was not evaluated, leaving their long-term in vivo performance unclear. Although both cardiac patches demonstrated good biocompatibility, a

systematic assessment of the host immune response was not conducted. To function effectively as a therapeutic platform, the DrGOM must be loaded with CMs, whereas the cell-free TRI-TENG patch presents different challenges. Specifically, the TRI-TENG requires suturing for fixation onto the myocardium, which introduces additional surgical trauma and complexity. Furthermore, the electrical field generated by the TRI-TENG is primarily confined to the myocardial surface and does not effectively penetrate deeper tissue layers. The GO/rGO bilayer also exhibits simultaneous responses to multiple external stimuli, requiring specialized packaging strategies to enable selective sensing of a single stimulus. In addition, the wireless sensing capability of the TRI-TENG currently relies on a relatively bulky wireless module, which could be further miniaturized through optimized circuit design and system integration.

5.3 Future Work

Microneedles can penetrate the superficial skin layer, enabling minimally invasive transdermal drug delivery.[250] Future work will therefore focus on developing microneedle electrodes integrated with a TENG system. In this design, each TENG element will consist of two microneedle electrodes and two triboelectric layers. Such an integrated platform could generate localized penetrative electric fields within infarcted myocardial tissue for targeted electrotherapy. High-resolution spatiotemporal monitoring of electrophysiological signals is also critical for cardiac healthcare.[251] The proposed system will adopt a modular TENG array architecture in which each independently addressable unit incorporates wireless communication capabilities, enabling spatiotemporal mapping of cardiac electrical signals. Reducing the device thickness from the millimeter scale to the micrometer scale can significantly decrease device rigidity.[190] Lithography-

based fabrication will therefore be employed to construct the TENG array and minimize device thickness. In addition, specialized structural designs, such as spring-like helical structures, mesh-shaped arrays, and kirigami-inspired configurations, can further enhance device flexibility.[252] The TENG system will be arranged in a cross-shaped configuration, and the ultrathin structure combined with this unique design will allow the array to be injectable. This injectable TENG array is expected to enable real-time spatiotemporal mapping of infarcted myocardial regions while maintaining minimally invasive operation.

Reference

1 Thygesen, K. *et al.* Fourth universal definition of myocardial infarction (2018). **72**, 2231-2264 (2018).

2 Reed, G. W., Rossi, J. E. & Cannon, C. P. J. T. L. Acute myocardial infarction. **389**, 197-210 (2017).

3 Libby, P. J. N. E. J. M. Mechanisms of acute coronary syndromes and their implications for therapy. **368**, 2004-2013 (2013).

4 Van Den Borne, S. W. *et al.* Myocardial remodeling after infarction: the role of myofibroblasts. **7**, 30 (2010).

5 Sutton, M. G. S. J. & Sharpe, N. J. C. Left ventricular remodeling after myocardial infarction: pathophysiology and therapy. **101**, 2981-2988 (2000).

6 Huang, K., Hu, S. & Cheng, K. A New Era of Cardiac Cell Therapy: Opportunities and Challenges. *Advanced healthcare materials* **8**, e1801011 (2019). https://doi.org/10.1002/adhm.201801011

7 Tang, J. N. *et al.* Concise Review: Is Cardiac Cell Therapy Dead? Embarrassing Trial Outcomes and New Directions for the Future. *Stem cells translational medicine* **7**, 354-359 (2018). https://doi.org/10.1002/sctm.17-0196

8 Huang, K. *et al.* An off-the-shelf artificial cardiac patch improves cardiac repair after myocardial infarction in rats and pigs. *Science translational medicine* **12** (2020). https://doi.org/10.1126/scitranslmed.aat9683

9 Jackman, C. P. *et al.* Engineered cardiac tissue patch maintains structural and electrical properties after epicardial implantation. *Biomaterials* **159**, 48-58 (2018). https://doi.org/10.1016/j.biomaterials.2018.01.002

10 Malki, M., Fleischer, S., Shapira, A. & Dvir, T. Gold Nanorod-Based Engineered Cardiac Patch for Suture-Free Engraftment by Near IR. *Nano letters* **18**, 4069-4073 (2018). https://doi.org/10.1021/acs.nanolett.7b04924

11 Jabbour, R. J. *et al.* In vivo grafting of large engineered heart tissue patches for cardiac repair. *JCI insight* **6** (2021). https://doi.org/10.1172/jci.insight.144068

12 Wang, L. *et al.* Injectable and conductive cardiac patches repair infarcted myocardium in rats and minipigs. *Nature biomedical engineering* **5**, 1157-1173 (2021). https://doi.org/10.1038/s41551-021-00796-9
13 Song, C. *et al.* An injectable conductive three-dimensional elastic network by tangled surgical-suture spring for heart repair. *ACS nano* **13**, 14122-14137 (2019).
14 Castilho, M. *et al.* Melt electrowriting allows tailored microstructural and mechanical design of scaffolds to advance functional human myocardial tissue formation. **28**, 1803151 (2018).
15 Cui, H. *et al.* 4D physiologically adaptable cardiac patch: a 4-month in vivo study for the treatment of myocardial infarction. **6**, eabb5067 (2020).
16 Yang, Y. *et al.* Elastic 3D-printed hybrid polymeric scaffold improves cardiac remodeling after myocardial infarction. **8**, 1900065 (2019).
17 Gaetani, R. *et al.* Epicardial application of cardiac progenitor cells in a 3D-printed gelatin/hyaluronic acid patch preserves cardiac function after myocardial infarction. **61**, 339-348 (2015).
18 Ajdary, R. *et al.* Multifunctional 3D-printed patches for long-term drug release therapies after myocardial infarction. **30**, 2003440 (2020).
19 Xu, L. *et al.* 3D multifunctional integumentary membranes for spatiotemporal cardiac measurements and stimulation across the entire epicardium. **5**, 1-10 (2014).
20 Feiner, R. *et al.* Engineered hybrid cardiac patches with multifunctional electronics for online monitoring and regulation of tissue function. **15**, 679-685 (2016).
21 Neto, A. C., Guinea, F., Peres, N. M., Novoselov, K. S. & Geim, A. K. J. R. o. m. p. The electronic properties of graphene. **81**, 109 (2009).
22 Li, J. *et al.* Efficient inkjet printing of graphene. **25**, 3985-3992 (2013).
23 Torrisi, F. *et al.* Inkjet-printed graphene electronics. **6**, 2992-3006 (2012).
24 Wang, F. *et al.* Inter-flake quantum transport of electrons and holes in inkjet-printed graphene devices. **31**, 2007478 (2021).
25 Jabari, E. & Toyserkani, E. J. C. Micro-scale aerosol-jet printing of graphene interconnects. **91**, 321-329 (2015).
26 Ali, M. A. *et al.* Sensing of COVID-19 antibodies in seconds via aerosol jet nanoprinted reduced-graphene-oxide-coated 3D electrodes. **33**, 2006647 (2021).
27 Zhou, G.-X. *et al.* 3D Printing Graphene Oxide Soft Robotics. **16**, 3664-3673 (2022).
28 Hyun, W. J., Secor, E. B., Hersam, M. C., Frisbie, C. D. & Francis, L. F. J. A. M. High-resolution patterning of graphene by screen printing with a silicon stencil for highly flexible printed electronics. **27**, 109-115 (2015).
29 Pan, K. *et al.* Sustainable production of highly conductive multilayer graphene ink for wireless connectivity and IoT applications. **9**, 1-10 (2018).
30 Secor, E. B. *et al.* Gravure printing of graphene for large-area flexible electronics. **26**, 4533-4538 (2014).
31 Vaithilingam, J. *et al.* Multifunctional bioinstructive 3D architectures to modulate cellular behavior. *Advanced Functional Materials* **29**, 1902016 (2019).
32 Brevet, A., Pinto, E., Peacock, J. & Stockdale, F. E. Myosin synthesis increased by electrical stimulation of skeletal muscle cell cultures. *Science* **193**, 1152-1154 (1976).

33 McDonough, P. M. & Glembotski, C. Induction of atrial natriuretic factor and myosin light chain-2 gene expression in cultured ventricular myocytes by electrical stimulation of contraction. *Journal of Biological Chemistry* **267**, 11665-11668 (1992).
34 Guo, Z. J. & Guo, Z. Non-excitatory electrical stimulation attenuates myocardial infarction via homeostasis of calcitonin gene-related peptide in myocardium. *Peptides* **65**, 46-52 (2015). https://doi.org/10.1016/j.peptides.2015.01.010
35 Jiang, W. *et al.* Fully bioabsorbable natural-materials-based triboelectric nanogenerators. *Advanced Materials* **30**, 1801895 (2018).
36 Zhao, L. *et al.* Promoting maturation and contractile function of neonatal rat cardiomyocytes by self-powered implantable triboelectric nanogenerator. *Nano Energy* **103**, 107798 (2022).
37 Zheng, Q. *et al.* In vivo self-powered wireless cardiac monitoring via implantable triboelectric nanogenerator. *ACS nano* **10**, 6510-6518 (2016).
38 Zhao, D. *et al.* Eco-friendly in-situ gap generation of no-spacer triboelectric nanogenerator for monitoring cardiovascular activities. *Nano Energy* **90**, 106580 (2021).
39 Liu, Z. *et al.* Transcatheter self-powered ultrasensitive endocardial pressure sensor. *Advanced Functional Materials* **29**, 1807560 (2019).
40 Long, Y., Li, J., Yang, F., Wang, J. & Wang, X. Wearable and implantable electroceuticals for therapeutic electrostimulations. *Advanced science* **8**, 2004023 (2021).
41 Cheng, T., Shao, J. & Wang, Z. L. Triboelectric nanogenerators. *Nature Reviews Methods Primers* **3**, 39 (2023). https://doi.org/10.1038/s43586-023-00220-3
42 Thygesen, K. *et al.* Fourth Universal Definition of Myocardial Infarction (2018). *Journal of the American College of Cardiology* **72**, 2231-2264 (2018). https://doi.org/https://doi.org/10.1016/j.jacc.2018.08.1038
43 Johns hopkinsmedicine. *Anatomy and Function of the Coronary Arteries*, <https://www.hopkinsmedicine.org/health/conditions-and-diseases/anatomy-and-function-of-the-coronary-arteries> (n.d).
44 Reed, G. W., Rossi, J. E. & Cannon, C. P. Acute myocardial infarction. *The Lancet* **389**, 197-210 (2017).
45 Sutton, M. G. S. J. & Sharpe, N. Left ventricular remodeling after myocardial infarction: pathophysiology and therapy. *Circulation* **101**, 2981-2988 (2000).
46 Azevedo, P. S., Polegato, B. F., Minicucci, M. F., Paiva, S. A. & Zornoff, L. A. Cardiac remodeling: concepts, clinical impact, pathophysiological mechanisms and pharmacologic treatment. *Arquivos brasileiros de cardiologia* **106**, 62-69 (2015).
47 Bhatt, A. S., Ambrosy, A. P. & Velazquez, E. J. Adverse remodeling and reverse remodeling after myocardial infarction. *Current cardiology reports* **19**, 1-10 (2017).
48 Berezin, A. E. & Berezin, A. A. Adverse cardiac remodelling after acute myocardial infarction: old and new biomarkers. *Disease Markers* **2020** (2020).
49 Cleutjens, J. P., Blankesteijn, W. M., Daemen, M. J. & Smits, J. F. The infarcted myocardium: simply dead tissue, or a lively target for therapeutic interventions. *Cardiovascular research* **44**, 232-241 (1999).
50 Cleutjens, J. P., Kandala, J. C., Guarda, E., Guntaka, R. V. & Weber, K. T. Regulation of collagen degradation in the rat myocardium after infarction. *Journal of molecular and cellular cardiology* **27**, 1281-1292 (1995).

51 Pfeffer, M. A. & Braunwald, E. Ventricular remodeling after myocardial infarction. Experimental observations and clinical implications. *Circulation* **81**, 1161-1172 (1990).
52 Hutchins, G. M. & Bulkley, B. H. Infarct expansion versus extension: two different complications of acute myocardial infarction. *The American journal of cardiology* **41**, 1127-1132 (1978).
53 Lew, W., Chen, Z., Guth, B. & Covell, J. W. Mechanisms of augmented segment shortening in nonischemic areas during acute ischemia of the canine left ventricle. *Circulation research* **56**, 351-358 (1985).
54 Jessup, M. & Brozena, S. Heart failure. *N Engl J Med* **348**, 2007-2018 (2003). https://doi.org/10.1056/NEJMra021498
55 Porter, K. E. & Turner, N. A. Cardiac fibroblasts: at the heart of myocardial remodeling. *Pharmacology & therapeutics* **123**, 255-278 (2009).
56 Van Den Borne, S. W. *et al.* Myocardial remodeling after infarction: the role of myofibroblasts. *Nature Reviews Cardiology* **7**, 30-37 (2010).
57 Ongstad, E. & Kohl, P. Fibroblast–myocyte coupling in the heart: Potential relevance for therapeutic interventions. *Journal of molecular and cellular cardiology* **91**, 238-246 (2016).
58 Camelliti, P., Borg, T. K. & Kohl, P. Structural and functional characterisation of cardiac fibroblasts. *Cardiovascular research* **65**, 40-51 (2005).
59 Wang, Y. *et al.* Fibroblasts in heart scar tissue directly regulate cardiac excitability and arrhythmogenesis. *Science* **381**, 1480-1487 (2023).
60 Kamihata, H. *et al.* Implantation of bone marrow mononuclear cells into ischemic myocardium enhances collateral perfusion and regional function via side supply of angioblasts, angiogenic ligands, and cytokines. *Circulation* **104**, 1046-1052 (2001).
61 Hench, L. L. Biomaterials. *Science* **208**, 826-831 (1980). https://doi.org/doi:10.1126/science.6246576
62 Hench, L. L. & Polak, J. M. Third-Generation Biomedical Materials. *Science* **295**, 1014-1017 (2002). https://doi.org/doi:10.1126/science.1067404
63 Peppas, N. A. & Langer, R. New Challenges in Biomaterials. *Science* **263**, 1715-1720 (1994). https://doi.org/doi:10.1126/science.8134835
64 Weinberger, F., Mannhardt, I. & Eschenhagen, T. Engineering cardiac muscle tissue: a maturating field of research. *Circulation research* **120**, 1487-1500 (2017).
65 Zhang, J., Zhu, W., Radisic, M. & Vunjak-Novakovic, G. Can we engineer a human cardiac patch for therapy? *Circulation research* **123**, 244-265 (2018).
66 Fink, C. *et al.* Chronic stretch of engineered heart tissue induces hypertrophy and functional improvement. *The FASEB Journal* **14**, 669-679 (2000).
67 Zimmermann, W. H. *et al.* Three-dimensional engineered heart tissue from neonatal rat cardiac myocytes. *Biotechnology and bioengineering* **68**, 106-114 (2000).
68 Zimmermann, W.-H. *et al.* Tissue engineering of a differentiated cardiac muscle construct. *Circulation research* **90**, 223-230 (2002).
69 Pelham Jr, R. J. & Wang, Y.-l. Cell locomotion and focal adhesions are regulated by substrate flexibility. *Proceedings of the national academy of sciences* **94**, 13661-13665 (1997).
70 Discher, D. E., Janmey, P. & Wang, Y.-l. Tissue cells feel and respond to the stiffness of their substrate. *Science* **310**, 1139-1143 (2005).

71 Guo, M. *et al.* Cell volume change through water efflux impacts cell stiffness and stem cell fate. *Proceedings of the National Academy of Sciences* **114**, E8618-E8627 (2017).
72 Zanotelli, M. R. *et al.* Regulation of ATP utilization during metastatic cell migration by collagen architecture. *Molecular biology of the cell* **29**, 1-9 (2018).
73 Guilak, F. *et al.* Control of stem cell fate by physical interactions with the extracellular matrix. *Cell stem cell* **5**, 17-26 (2009).
74 Engler, A. J., Sen, S., Sweeney, H. L. & Discher, D. E. Matrix elasticity directs stem cell lineage specification. *Cell* **126**, 677-689 (2006).
75 Roy, D. *et al.* Programmed ventricular stimulation in survivors of an acute myocardial infarction. *Circulation* **72**, 487-494 (1985).
76 Gilbert, P. M. *et al.* Substrate elasticity regulates skeletal muscle stem cell self-renewal in culture. *Science* **329**, 1078-1081 (2010).
77 Yang, C., Tibbitt, M. W., Basta, L. & Anseth, K. S. Mechanical memory and dosing influence stem cell fate. *Nature materials* **13**, 645-652 (2014).
78 Lo, C.-M., Wang, H.-B., Dembo, M. & Wang, Y.-l. Cell movement is guided by the rigidity of the substrate. *Biophysical journal* **79**, 144-152 (2000).
79 Tse, J. R. & Engler, A. J. Stiffness gradients mimicking in vivo tissue variation regulate mesenchymal stem cell fate. *PloS one* **6**, e15978 (2011).
80 Tzahor, E. & Dimmeler, S. A coalition to heal—the impact of the cardiac microenvironment. *Science* **377**, eabm4443 (2022).
81 Chaudhuri, O., Cooper-White, J., Janmey, P. A., Mooney, D. J. & Shenoy, V. B. Effects of extracellular matrix viscoelasticity on cellular behaviour. *Nature* **584**, 535-546 (2020).
82 Chaudhuri, O. *et al.* Substrate stress relaxation regulates cell spreading. *Nature communications* **6**, 6365 (2015).
83 Chaudhuri, O. *et al.* Hydrogels with tunable stress relaxation regulate stem cell fate and activity. *Nature materials* **15**, 326-334 (2016).
84 Cameron, A. R., Frith, J. E. & Cooper-White, J. J. The influence of substrate creep on mesenchymal stem cell behaviour and phenotype. *Biomaterials* **32**, 5979-5993 (2011).
85 Wisdom, K. M. *et al.* Matrix mechanical plasticity regulates cancer cell migration through confining microenvironments. *Nature communications* **9**, 4144 (2018).
86 Lee, H.-p., Gu, L., Mooney, D. J., Levenston, M. E. & Chaudhuri, O. Mechanical confinement regulates cartilage matrix formation by chondrocytes. *Nature materials* **16**, 1243-1251 (2017).
87 Schultz, K. M., Kyburz, K. A. & Anseth, K. S. Measuring dynamic cell–material interactions and remodeling during 3D human mesenchymal stem cell migration in hydrogels. *Proceedings of the National Academy of Sciences* **112**, E3757-E3764 (2015).
88 Tandon, N. *et al.* Electrical stimulation systems for cardiac tissue engineering. *Nature protocols* **4**, 155-173 (2009).
89 Radisic, M. *et al.* Functional assembly of engineered myocardium by electrical stimulation of cardiac myocytes cultured on scaffolds. *Proceedings of the National Academy of Sciences* **101**, 18129-18134 (2004).
90 Yang, X., Pabon, L. & Murry, C. E. Engineering adolescence: maturation of human pluripotent stem cell–derived cardiomyocytes. *Circulation research* **114**, 511-523 (2014).
91 Karbassi, E. *et al.* Cardiomyocyte maturation: advances in knowledge and implications for regenerative medicine. *Nature Reviews Cardiology* **17**, 341-359 (2020).

92 Nunes, S. S. *et al.* Biowire: a platform for maturation of human pluripotent stem cell–derived cardiomyocytes. *Nature methods* **10**, 781-787 (2013).
93 Andrade, J. & Hlady, V. Protein adsorption and materials biocompatibility: a tutorial review and suggested hypotheses. *Biopolymers/Non-Exclusion HPLC*, 1-63 (2005).
94 Tziampazis, E., Kohn, J. & Moghe, P. V. PEG-variant biomaterials as selectively adhesive protein templates: model surfaces for controlled cell adhesion and migration. *Biomaterials* **21**, 511-520 (2000).
95 McClary, K. B., Ugarova, T. & Grainger, D. W. Modulating fibroblast adhesion, spreading, and proliferation using self-assembled monolayer films of alkylthiolates on gold. *Journal of Biomedical Materials Research: An Official Journal of The Society for Biomaterials, The Japanese Society for Biomaterials, and The Australian Society for Biomaterials and the Korean Society for Biomaterials* **50**, 428-439 (2000).
96 Shen, M. & Horbett, T. A. The effects of surface chemistry and adsorbed proteins on monocyte/macrophage adhesion to chemically modified polystyrene surfaces. *Journal of Biomedical Materials Research: An Official Journal of The Society for Biomaterials, The Japanese Society for Biomaterials, and The Australian Society for Biomaterials and the Korean Society for Biomaterials* **57**, 336-345 (2001).
97 Anderson, J., Defife, K., McNally, A., Collier, T. & Jenney, C. Monocyte, macrophage and foreign body giant cell interactions with molecularly engineered surfaces. *Journal of Materials Science: Materials in Medicine* **10**, 579-588 (1999).
98 Iuliano, D. J., Saavedra, S. S. & Truskey, G. A. Effect of the conformation and orientation of adsorbed fibronectin on endothelial cell spreading and the strength of adhesion. *Journal of Biomedical Materials Research* **27**, 1103-1113 (1993).
99 Keselowsky, B. G., Collard, D. M. & García, A. J. Surface chemistry modulates fibronectin conformation and directs integrin binding and specificity to control cell adhesion. *Journal of Biomedical Materials Research Part A: An Official Journal of The Society for Biomaterials, The Japanese Society for Biomaterials, and The Australian Society for Biomaterials and the Korean Society for Biomaterials* **66**, 247-259 (2003).
100 Michael, K. E. *et al.* Adsorption-induced conformational changes in fibronectin due to interactions with well-defined surface chemistries. *Langmuir* **19**, 8033-8040 (2003).
101 Garcıa, A. J., Vega, M. a. D. & Boettiger, D. Modulation of cell proliferation and differentiation through substrate-dependent changes in fibronectin conformation. *Molecular biology of the cell* **10**, 785-798 (1999).
102 Keselowsky, B. G., Collard, D. M. & García, A. J. Surface chemistry modulates focal adhesion composition and signaling through changes in integrin binding. *Biomaterials* **25**, 5947-5954 (2004).
103 Brodbeck, W. G. *et al.* Biomaterial adherent macrophage apoptosis is increased by hydrophilic and anionic substrates in vivo. *Proceedings of the National Academy of Sciences* **99**, 10287-10292 (2002).
104 Hallab, N. J., Bundy, K. J., O'Connor, K., Moses, R. L. & Jacobs, J. J. Evaluation of metallic and polymeric biomaterial surface energy and surface roughness characteristics for directed cell adhesion. *Tissue engineering* **7**, 55-71 (2001).
105 Laflamme, M. A. & Murry, C. E. Heart regeneration. *Nature* **473**, 326-335 (2011).
106 Beltrami, A. P. *et al.* Adult cardiac stem cells are multipotent and support myocardial regeneration. *cell* **114**, 763-776 (2003).

107 Anversa, P. & Kajstura, J. Ventricular myocytes are not terminally differentiated in the adult mammalian heart. *Circulation research* **83**, 1-14 (1998).
108 Messina, E. *et al.* Isolation and expansion of adult cardiac stem cells from human and murine heart. *Circulation research* **95**, 911-921 (2004).
109 Chimenti, I. *et al.* Relative roles of direct regeneration versus paracrine effects of human cardiosphere-derived cells transplanted into infarcted mice. *Circulation research* **106**, 971-980 (2010).
110 Makkar, R. R. *et al.* Intracoronary cardiosphere-derived cells for heart regeneration after myocardial infarction (CADUCEUS): a prospective, randomised phase 1 trial. *The Lancet* **379**, 895-904 (2012).
111 Takahashi, K. & Yamanaka, S. Induction of pluripotent stem cells from mouse embryonic and adult fibroblast cultures by defined factors. *cell* **126**, 663-676 (2006).
112 Nussbaum, J. *et al.* Transplantation of undifferentiated murine embryonic stem cells in the heart: teratoma formation and immune response. *The FASEB Journal* **21**, 1345-1357 (2007).
113 Ye, L. *et al.* Cardiac repair in a porcine model of acute myocardial infarction with human induced pluripotent stem cell-derived cardiovascular cells. *Cell stem cell* **15**, 750-761 (2014).
114 Laflamme, M. A. *et al.* Cardiomyocytes derived from human embryonic stem cells in pro-survival factors enhance function of infarcted rat hearts. *Nature biotechnology* **25**, 1015-1024 (2007).
115 Mummery, C. L. *et al.* Differentiation of human embryonic stem cells and induced pluripotent stem cells to cardiomyocytes: a methods overview. *Circulation research* **111**, 344-358 (2012).
116 Lian, X. *et al.* Directed cardiomyocyte differentiation from human pluripotent stem cells by modulating Wnt/β-catenin signaling under fully defined conditions. *Nature protocols* **8**, 162-175 (2013).
117 Ieda, M. *et al.* Direct reprogramming of fibroblasts into functional cardiomyocytes by defined factors. *Cell* **142**, 375-386 (2010).
118 Efe, J. A. *et al.* Conversion of mouse fibroblasts into cardiomyocytes using a direct reprogramming strategy. *Nature cell biology* **13**, 215-222 (2011).
119 Caplan, A. I. & Dennis, J. E. Mesenchymal stem cells as trophic mediators. *Journal of cellular biochemistry* **98**, 1076-1084 (2006).
120 Gnecchi, M. *et al.* Evidence supporting paracrine hypothesis for Akt-modified mesenchymal stem cell-mediated cardiac protection and functional improvement. *The FASEB Journal* **20**, 661-669 (2006).
121 Gnecchi, M. *et al.* Paracrine action accounts for marked protection of ischemic heart by Akt-modified mesenchymal stem cells. *Nature medicine* **11**, 367-368 (2005).
122 Berry, M. F. *et al.* Mesenchymal stem cell injection after myocardial infarction improves myocardial compliance. *American Journal of Physiology-Heart and Circulatory Physiology* **290**, H2196-H2203 (2006).
123 Saldin, L. T., Cramer, M. C., Velankar, S. S., White, L. J. & Badylak, S. F. Extracellular matrix hydrogels from decellularized tissues: Structure and function. *Acta biomaterialia* **49**, 1-15 (2017).

124 Wolf, M. T. *et al.* A hydrogel derived from decellularized dermal extracellular matrix. *Biomaterials* **33**, 7028-7038 (2012).
125 Giobbe, G. G. *et al.* Extracellular matrix hydrogel derived from decellularized tissues enables endodermal organoid culture. *Nature communications* **10**, 5658 (2019).
126 Reing, J. E. *et al.* Degradation products of extracellular matrix affect cell migration and proliferation. *Tissue Engineering Part A* **15**, 605-614 (2009).
127 Badylak, S. F. in *Seminars in cell & developmental biology.* 377-383 (Elsevier).
128 Huleihel, L. *et al.* Matrix-bound nanovesicles within ECM bioscaffolds. *Science advances* **2**, e1600502 (2016).
129 Singelyn, J. M. *et al.* Naturally derived myocardial matrix as an injectable scaffold for cardiac tissue engineering. *Biomaterials* **30**, 5409-5416 (2009).
130 Park, S.-J. *et al.* Dual stem cell therapy synergistically improves cardiac function and vascular regeneration following myocardial infarction. *Nature communications* **10**, 3123 (2019).
131 Song, K. *et al.* Heart repair by reprogramming non-myocytes with cardiac transcription factors. *Nature* **485**, 599-604 (2012).
132 Jayawardena, T. M. *et al.* MicroRNA induced cardiac reprogramming in vivo: evidence for mature cardiac myocytes and improved cardiac function. *Circulation research* **116**, 418-424 (2015).
133 Wolfram, J. A. & Donahue, J. K. Gene therapy to treat cardiovascular disease. *Journal of the American Heart Association* **2**, e000119 (2013).
134 Cao, N. *et al.* Conversion of human fibroblasts into functional cardiomyocytes by small molecules. *Science* **352**, 1216-1220 (2016).
135 Jin, Y. *et al.* Three-dimensional heart extracellular matrix enhances chemically induced direct cardiac reprogramming. *Science advances* **8**, eabn5768 (2022).
136 Huang, K. *et al.* An off-the-shelf artificial cardiac patch improves cardiac repair after myocardial infarction in rats and pigs. *Science translational medicine* **12**, eaat9683 (2020).
137 Hodgkinson, C. P., Bareja, A., Gomez, J. A. & Dzau, V. J. Emerging concepts in paracrine mechanisms in regenerative cardiovascular medicine and biology. *Circulation research* **118**, 95-107 (2016).
138 Marbán, E. A mechanistic roadmap for the clinical application of cardiac cell therapies. *Nature biomedical engineering* **2**, 353-361 (2018).
139 Zhu, D. *et al.* Minimally invasive delivery of therapeutic agents by hydrogel injection into the pericardial cavity for cardiac repair. *Nature communications* **12**, 1412 (2021).
140 Derakhshanfar, S. *et al.* 3D bioprinting for biomedical devices and tissue engineering: A review of recent trends and advances. *Bioactive materials* **3**, 144-156 (2018).
141 Lewis, J. A. & Gratson, G. M. Direct writing in three dimensions. *Materials today* **7**, 32-39 (2004).
142 Calvert, P. Inkjet printing for materials and devices. *Chemistry of materials* **13**, 3299-3305 (2001).
143 De Gans, B. J., Duineveld, P. C. & Schubert, U. S. Inkjet printing of polymers: state of the art and future developments. *Advanced materials* **16**, 203-213 (2004).
144 Le, H. P. Progress and trends in ink-jet printing technology. *Journal of imaging science and technology* **42**, 49-62 (1998).

145 Singh, M., Haverinen, H. M., Dhagat, P. & Jabbour, G. E. Inkjet printing—process and its applications. *Advanced materials* **22**, 673-685 (2010).
146 Saunders, R. E. & Derby, B. Inkjet printing biomaterials for tissue engineering: bioprinting. *International Materials Reviews* **59**, 430-448 (2014).
147 Barui, S. 3D inkjet printing of biomaterials: Principles and applications. *Medical Devices & Sensors* **4**, e10143 (2021).
148 Kruth, J. P., Mercelis, P., Van Vaerenbergh, J., Froyen, L. & Rombouts, M. Binding mechanisms in selective laser sintering and selective laser melting. *Rapid prototyping journal* **11**, 26-36 (2005).
149 Serra, P. & Piqué, A. Laser-induced forward transfer: fundamentals and applications. *Advanced Materials Technologies* **4**, 1800099 (2019).
150 Delaporte, P. & Alloncle, A.-P. Laser-induced forward transfer: A high resolution additive manufacturing technology. *Optics & Laser Technology* **78**, 33-41 (2016).
151 Armon, N. *et al.* Laser-based printing: from liquids to microstructures. *Advanced Functional Materials* **31**, 2008547 (2021).
152 Melchels, F. P., Feijen, J. & Grijpma, D. W. A review on stereolithography and its applications in biomedical engineering. *Biomaterials* **31**, 6121-6130 (2010).
153 Billiet, T., Vandenhaute, M., Schelfhout, J., Van Vlierberghe, S. & Dubruel, P. A review of trends and limitations in hydrogel-rapid prototyping for tissue engineering. *Biomaterials* **33**, 6020-6041 (2012).
154 Kawata, S., Sun, H.-B., Tanaka, T. & Takada, K. Finer features for functional microdevices. *Nature* **412**, 697-698 (2001).
155 Lewis, J. A. J. A. F. M. Direct ink writing of 3D functional materials. **16**, 2193-2204 (2006).
156 Miller, J. S. *et al.* Rapid casting of patterned vascular networks for perfusable engineered three-dimensional tissues. *Nature materials* **11**, 768-774 (2012).
157 Ye, X. *et al.* A biodegradable microvessel scaffold as a framework to enable vascular support of engineered tissues. *Biomaterials* **34**, 10007-10015 (2013).
158 Bae, H. *et al.* Building vascular networks. *Science translational medicine* **4**, 160ps123-160ps123 (2012).
159 Koffler, J. *et al.* Improved vascular organization enhances functional integration of engineered skeletal muscle grafts. *Proceedings of the National Academy of Sciences* **108**, 14789-14794 (2011).
160 Choi, N. W. *et al.* Microfluidic scaffolds for tissue engineering. *Nature materials* **6**, 908-915 (2007).
161 Gaebel, R. *et al.* Patterning human stem cells and endothelial cells with laser printing for cardiac regeneration. *Biomaterials* **32**, 9218-9230 (2011).
162 Ye, X. *et al.* Scalable Unit for Building Cardiac Tissue. *Advanced Materials (Deerfield Beach, Fla.)* **26**, 7202 (2014).
163 Wang, Y., Ameer, G. A., Sheppard, B. J. & Langer, R. A tough biodegradable elastomer. *Nature biotechnology* **20**, 602-606 (2002).
164 Wu, W., Allen, R. A. & Wang, Y. Fast-degrading elastomer enables rapid remodeling of a cell-free synthetic graft into a neoartery. *Nature medicine* **18**, 1148-1153 (2012).
165 Engelmayr Jr, G. C. *et al.* Accordion-like honeycombs for tissue engineering of cardiac anisotropy. *Nature materials* **7**, 1003-1010 (2008).

166 Chen, Q.-Z. *et al.* Characterisation of a soft elastomer poly (glycerol sebacate) designed to match the mechanical properties of myocardial tissue. *Biomaterials* **29**, 47-57 (2008).
167 Bettinger, C. J., Bruggeman, J. P., Borenstein, J. T. & Langer, R. In vitro and in vivo degradation of poly (1, 3-diamino-2-hydroxypropane-co-polyol sebacate) elastomers. *Journal of Biomedical Materials Research Part A: An Official Journal of The Society for Biomaterials, The Japanese Society for Biomaterials, and The Australian Society for Biomaterials and the Korean Society for Biomaterials* **91**, 1077-1088 (2009).
168 Bettinger, C. J., Bruggeman, J. P., Borenstein, J. T. & Langer, R. S. Amino alcohol-based degradable poly (ester amide) elastomers. *Biomaterials* **29**, 2315-2325 (2008).
169 McCall, A. S. *et al.* Mechanisms of corneal tissue cross-linking in response to treatment with topical riboflavin and long-wavelength ultraviolet radiation (UVA). *Investigative ophthalmology & visual science* **51**, 129-138 (2010).
170 Heo, J. *et al.* Riboflavin-induced photo-crosslinking of collagen hydrogel and its application in meniscus tissue engineering. *Drug delivery and translational research* **6**, 148-158 (2016).
171 Jang, J. *et al.* Tailoring mechanical properties of decellularized extracellular matrix bioink by vitamin B2-induced photo-crosslinking. *Acta biomaterialia* **33**, 88-95 (2016).
172 Jang, J. *et al.* 3D printed complex tissue construct using stem cell-laden decellularized extracellular matrix bioinks for cardiac repair. *Biomaterials* **112**, 264-274 (2017).
173 Gao, L. *et al.* Myocardial tissue engineering with cells derived from human-induced pluripotent stem cells and a native-like, high-resolution, 3-dimensionally printed scaffold. *Circulation research* **120**, 1318-1325 (2017).
174 Streeter Jr, D. D., Spotnitz, H. M., Patel, D. P., Ross Jr, J. & Sonnenblick, E. H. Fiber orientation in the canine left ventricle during diastole and systole. *Circulation research* **24**, 339-347 (1969).
175 Pijnappels, D. A. *et al.* Forced alignment of mesenchymal stem cells undergoing cardiomyogenic differentiation affects functional integration with cardiomyocyte cultures. *Circulation research* **103**, 167-176 (2008).
176 Miao, S. *et al.* 4D printing of polymeric materials for tissue and organ regeneration. *Materials Today* **20**, 577-591 (2017).
177 Cui, H. *et al.* 4D physiologically adaptable cardiac patch: A 4-month in vivo study for the treatment of myocardial infarction. *Science advances* **6**, eabb5067 (2020).
178 Pashakhanloo, F. *et al.* Myofiber architecture of the human atria as revealed by submillimeter diffusion tensor imaging. *Circulation: arrhythmia and electrophysiology* **9**, e004133 (2016).
179 Rohmer, D., Sitek, A. & Gullberg, G. T. Reconstruction and visualization of fiber and laminar structure in the normal human heart from ex vivo diffusion tensor magnetic resonance imaging (DTMRI) data. *Investigative radiology* **42**, 777-789 (2007).
180 Mao, M. *et al.* Leaf-venation-directed cellular alignment for macroscale cardiac constructs with tissue-like functionalities. *Nature Communications* **14**, 2077 (2023).
181 Contessotto, P. *et al.* Elastin-like recombinamers-based hydrogel modulates post-ischemic remodeling in a non-transmural myocardial infarction in sheep. *Science translational medicine* **13**, eaaz5380 (2021).

182 Fan, C. *et al.* Myocardial-infarction-responsive smart hydrogels targeting matrix metalloproteinase for on-demand growth factor delivery. *Advanced materials* **31**, 1902900 (2019).
183 Chen, W. *et al.* A matrix-metalloproteinase-responsive hydrogel system for modulating the immune microenvironment in myocardial infarction. *Advanced materials* **35**, 2209041 (2023).
184 Mihic, A. *et al.* A conductive polymer hydrogel supports cell electrical signaling and improves cardiac function after implantation into myocardial infarct. *Circulation* **132**, 772-784 (2015).
185 Wang, L. *et al.* Injectable and conductive cardiac patches repair infarcted myocardium in rats and minipigs. *Nature Biomedical Engineering* **5**, 1157-1173 (2021).
186 He, Y. *et al.* A smart adhesive Janus hydrogel for non-invasive cardiac repair and tissue adhesion prevention. *Nature Communications* **13**, 7666 (2022).
187 DiFrancesco, D. The role of the funny current in pacemaker activity. *Circulation research* **106**, 434-446 (2010).
188 Kleinman, M. E. *et al.* Part 14: pediatric advanced life support: 2010 American Heart Association guidelines for cardiopulmonary resuscitation and emergency cardiovascular care. *Circulation* **122**, S876-S908 (2010).
189 Hong, Y. J., Jeong, H., Cho, K. W., Lu, N. & Kim, D. H. Wearable and implantable devices for cardiovascular healthcare: from monitoring to therapy based on flexible and stretchable electronics. *Advanced Functional Materials* **29**, 1808247 (2019).
190 Yu, K. J. *et al.* Bioresorbable silicon electronics for transient spatiotemporal mapping of electrical activity from the cerebral cortex. *Nature materials* **15**, 782-791 (2016).
191 Kim, D.-H. *et al.* Epidermal electronics. *science* **333**, 838-843 (2011).
192 Zhang, L. *et al.* 3D morphable systems via deterministic microfolding for vibrational sensing, robotic implants, and reconfigurable telecommunication. *Science Advances* **8**, eade0838 (2022).
193 Sim, K. *et al.* An epicardial bioelectronic patch made from soft rubbery materials and capable of spatiotemporal mapping of electrophysiological activity. *Nature Electronics* **3**, 775-784 (2020).
194 Hwang, J. C. *et al.* In situ diagnosis and simultaneous treatment of cardiac diseases using a single-device platform. *Science advances* **8**, eabq0897 (2022).
195 Zheng, Q. *et al.* In vivo self-powered wireless cardiac monitoring via implantable triboelectric nanogenerator. **10**, 6510-6518 (2016).
196 Qiu, R. *et al.* E-cardiac patch to sense and repair infarcted myocardium. *Nature Communications* **15**, 4133 (2024).
197 Tang, J. *et al.* Cardiac cell–integrated microneedle patch for treating myocardial infarction. *Science advances* **4**, eaat9365 (2018).
198 Shi, H. *et al.* Microneedle-mediated gene delivery for the treatment of ischemic myocardial disease. *Science advances* **6**, eaaz3621 (2020).
199 Mei, X. *et al.* Minimally invasive snakebite inspired microneedle delivery system for internal organs. *Bioactive Materials* **49**, 576-585 (2025).
200 Wang, F. *et al.* Cardiac Organoid Model Inspired Micro-Robot Smart Patch to Treat Myocardial Infarction. *Advanced Materials*, 2417327 (2025).

201 Ye, G. *et al.* Mussel-inspired conductive Ti(2)C-cryogel promotes functional maturation of cardiomyocytes and enhances repair of myocardial infarction. *Theranostics* **10**, 2047-2066 (2020). https://doi.org/10.7150/thno.38876
202 Jensen, L. *et al.* Integrated molecular, biochemical, and physiological assessment unravels key extraction method mediated influences on rat neonatal cardiomyocytes. *Journal of cellular physiology* **233**, 5420-5430 (2018). https://doi.org/10.1002/jcp.26380
203 Landa, N. *et al.* Effect of injectable alginate implant on cardiac remodeling and function after recent and old infarcts in rat. *Circulation* **117**, 1388-1396 (2008). https://doi.org/10.1161/circulationaha.107.727420
204 Truby, R. L. & Lewis, J. A. J. N. Printing soft matter in three dimensions. **540**, 371-378 (2016).
205 Han, D. D. *et al.* Moisture-responsive graphene paper prepared by self-controlled photoreduction. **27**, 332-338 (2015).
206 Ishizaki, T., Saito, N. & Takai, O. J. L. Correlation of cell adhesive behaviors on superhydrophobic, superhydrophilic, and micropatterned superhydrophobic/superhydrophilic surfaces to their surface chemistry. **26**, 8147-8154 (2010).
207 Guo, L. *et al.* Two-beam-laser interference mediated reduction, patterning and nanostructuring of graphene oxide for the production of a flexible humidity sensing device. **50**, 1667-1673 (2012).
208 Liu, Q. *et al.* A high-performances flexible temperature sensor composed of polyethyleneimine/reduced graphene oxide bilayer for real-time monitoring. **4**, 1800594 (2019).
209 Callister, W. D. & Rethwisch, D. G. *Materials science and engineering: an introduction*. Vol. 9 (Wiley New York, 2018).
210 Novoselov, K. S. *et al.* Electric field effect in atomically thin carbon films. **306**, 666-669 (2004).
211 Ensslin, K. (Nature Publishing Group, 2019).
212 Hwang, E. & Sarma, S. D. J. P. R. B. Acoustic phonon scattering limited carrier mobility in two-dimensional extrinsic graphene. **77**, 115449 (2008).
213 Bolotin, K. I., Sikes, K. J., Hone, J., Stormer, H. L. & Kim, P. Temperature-Dependent Transport in Suspended Graphene. *Physical Review Letters* **101**, 096802 (2008). https://doi.org/10.1103/PhysRevLett.101.096802
214 Zhu, W., Perebeinos, V., Freitag, M. & Avouris, P. J. P. R. B. Carrier scattering, mobilities, and electrostatic potential in monolayer, bilayer, and trilayer graphene. **80**, 235402 (2009).
215 Song, C. *et al.* An injectable conductive three-dimensional elastic network by tangled surgical-suture spring for heart repair. **13**, 14122-14137 (2019).
216 He, K. *et al.* Long-distance intercellular connectivity between cardiomyocytes and cardiofibroblasts mediated by membrane nanotubes. **92**, 39-47 (2011).
217 Norahan, M. H. *et al.* Electroactive cardiac patch containing reduced graphene oxide with potential antibacterial properties. *Materials science & engineering. C, Materials for biological applications* **104**, 109921 (2019). https://doi.org/10.1016/j.msec.2019.109921
218 Li, X. P. *et al.* Electrical stimulation of neonatal rat cardiomyocytes using conductive polydopamine-reduced graphene oxide-hybrid hydrogels for constructing cardiac

microtissues. *Colloids and surfaces. B, Biointerfaces* **205**, 111844 (2021). https://doi.org/10.1016/j.colsurfb.2021.111844
219 Song, C. *et al.* An Injectable Conductive Three-Dimensional Elastic Network by Tangled Surgical-Suture Spring for Heart Repair. *ACS nano* **13**, 14122-14137 (2019). https://doi.org/10.1021/acsnano.9b06761
220 Mukherjee, S. *et al.* Graphene Oxides Show Angiogenic Properties. *Advanced healthcare materials* **4**, 1722-1732 (2015). https://doi.org/10.1002/adhm.201500155
221 Rehman, S. R. U. *et al.* Reduced Graphene Oxide Incorporated GelMA Hydrogel Promotes Angiogenesis For Wound Healing Applications. *International journal of nanomedicine* **14**, 9603-9617 (2019). https://doi.org/10.2147/ijn.S218120
222 Mihic, A. *et al.* A Conductive Polymer Hydrogel Supports Cell Electrical Signaling and Improves Cardiac Function After Implantation into Myocardial Infarct. *Circulation* **132**, 772-784 (2015). https://doi.org/10.1161/circulationaha.114.014937
223 van Zyl, M. *et al.* Injectable conductive hydrogel restores conduction through ablated myocardium. *Journal of cardiovascular electrophysiology* **31**, 3293-3301 (2020). https://doi.org/10.1111/jce.14762
224 Wang, Z. L. On the expanded Maxwell's equations for moving charged media system–General theory, mathematical solutions and applications in TENG. *Materials Today* **52**, 348-363 (2022).
225 Zhu, G. *et al.* Triboelectric-generator-driven pulse electrodeposition for micropatterning. **12**, 4960-4965 (2012).
226 Wang, S., Lin, L. & Wang, Z. L. J. N. l. Nanoscale triboelectric-effect-enabled energy conversion for sustainably powering portable electronics. **12**, 6339-6346 (2012).
227 Zhu, G. *et al.* Toward large-scale energy harvesting by a nanoparticle-enhanced triboelectric nanogenerator. **13**, 847-853 (2013).
228 Jeong, S.-H. *et al.* Accelerated wound healing with an ionic patch assisted by a triboelectric nanogenerator. *Nano Energy* **79**, 105463 (2021).
229 Long, Y. *et al.* Effective wound healing enabled by discrete alternative electric fields from wearable nanogenerators. *ACS nano* **12**, 12533-12540 (2018).
230 Lee, S. *et al.* Development of battery-free neural interface and modulated control of tibialis anterior muscle via common peroneal nerve based on triboelectric nanogenerators (TENGs). *Nano Energy* **33**, 1-11 (2017).
231 Chen, C. M. *et al.* Self-assembled free-standing graphite oxide membrane. (2009).
232 Eda, G. & Chhowalla, M. Chemically derived graphene oxide: towards large-area thin-film electronics and optoelectronics. *Advanced materials* **22**, 2392-2415 (2010).
233 Sudesh, Kumar, N., Das, S., Bernhard, C. & Varma, G. Effect of graphene oxide doping on superconducting properties of bulk MgB2. *Superconductor Science and Technology* **26**, 095008 (2013).
234 Wang, L. *et al.* Ultralight conductive and elastic aerogel for skeletal muscle atrophy regeneration. *Advanced functional materials* **29**, 1806200 (2019).
235 Feng, H., Cheng, R., Zhao, X., Duan, X. & Li, J. A low-temperature method to produce highly reduced graphene oxide. *Nature communications* **4**, 1539 (2013).
236 Eluyemi, M. *et al.* Synthesis and characterization of graphene oxide and reduced graphene oxide thin films deposited by spray pyrolysis method. *Graphene* **5**, 143-154 (2016).

237 Zangmeister, R. A., Morris, T. A. & Tarlov, M. J. Characterization of polydopamine thin films deposited at short times by autoxidation of dopamine. *Langmuir* **29**, 8619-8628 (2013).
238 Yang, B. *et al.* A fully verified theoretical analysis of contact-mode triboelectric nanogenerators as a wearable power source. *Advanced Energy Materials* **6**, 1600505 (2016).
239 Zhang, H. *et al.* Increasing cardiac contractility after myocardial infarction exacerbates cardiac injury and pump dysfunction. *Circulation research* **107**, 800-809 (2010).
240 De Smet, M. A. *et al.* Cx43 hemichannel microdomain signaling at the intercalated disc enhances cardiac excitability. **131** (2021).
241 Li, X.-P. *et al.* Electrical stimulation of neonatal rat cardiomyocytes using conductive polydopamine-reduced graphene oxide-hybrid hydrogels for constructing cardiac microtissues. **205**, 111844 (2021).
242 Mayourian, J. *et al.* Physiologic, pathologic, and therapeutic paracrine modulation of cardiac excitation-contraction coupling. **122**, 167-183 (2018).
243 Heusch, G. J. B. R. i. C. Coronary blood flow in heart failure: cause, consequence and bystander. **117**, 1-24 (2022).
244 Fukui, H. *et al.* Bioelectric signaling and the control of cardiac cell identity in response to mechanical forces. **374**, 351-354 (2021).
245 Liang, S. *et al.* Paintable and rapidly bondable conductive hydrogels as therapeutic cardiac patches. **30**, 1704235 (2018).
246 Pedrotty, D. M. *et al.* Three-dimensional printed biopatches with conductive ink facilitate cardiac conduction when applied to disrupted myocardium. **12**, e006920 (2019).
247 Gardner, R. *et al.* Targeting protein tyrosine phosphatase σ after myocardial infarction restores cardiac sympathetic innervation and prevents arrhythmias. **6**, 1-9 (2015).
248 Gao, L. *et al.* Large cardiac muscle patches engineered from human induced-pluripotent stem cell–derived cardiac cells improve recovery from myocardial infarction in swine. **137**, 1712-1730 (2018).
249 Shadrin, I. Y. *et al.* Cardiopatch platform enables maturation and scale-up of human pluripotent stem cell-derived engineered heart tissues. *Nat Commun* **8**, 1825 (2017). https://doi.org/10.1038/s41467-017-01946-x
250 Zheng, M., Sheng, T., Yu, J., Gu, Z. & Xu, C. Microneedle biomedical devices. *Nature Reviews Bioengineering* **2**, 324-342 (2024).
251 Kanemaru, K. *et al.* Spatially resolved multiomics of human cardiac niches. *Nature* **619**, 801-810 (2023).
252 Ha, T. *et al.* A chest-laminated ultrathin and stretchable E-tattoo for the measurement of electrocardiogram, seismocardiogram, and cardiac time intervals. *Advanced Science* **6**, 1900290 (2019).